DX243025

Application of Circulation Control Aerofoils to Wind Turbines

---

by

Conrad Trevelyan

Doctoral Thesis

Submitted in partial fulfilment of the requirements

for the award of

Doctor of Philosophy of Loughborough University

November 2002

Abstract

Circulation control aerofoils potentially offer an additional means of load and power control for horizontal axis wind turbines by virtue of their rapid response time. Their suitability for these tasks has been assessed with respect to the power which they absorb, their interaction with aerofoils used on modern wind turbines, the infrastructure or hardware which they require and the degree to which they can affect the loads experienced by the turbine blades and other major components. It has been determined that the type of circulation control aerofoil most suited to use on wind turbine blades are those of the jet flap type and it has been realised that an ability to shed, as well as increase loads is advantageous in this application. To this end the behaviour of both negatively and positively deflected jets have been investigated with a two-dimensional computational fluid dynamics code, validated in the course of this work for such modelling. Particular emphasis has been placed on minimising the input power requirements of the circulation control aerofoils and in proposing an overall system that has the required level of robustness and reliability. A 2MW turbine has been modelled with a blade element momentum theory code in order to compare performance with and without circulation control aerofoils. These initial results show that there may be some positive benefits to be gained, but that the energy demands of the system place a hard limit on the degree to which circulation control aerofoils can determine the forces experienced by the turbine.

Acknowledgements

This work was aided by many people and their support is gratefully acknowledged. Firstly, I would like to thank my supervisor, David Sharpe, for his guidance during the course of this project. Particular acknowledgement and thanks are given to Jess A. Michelsen who answered my CFD questions unceasingly and helped me in understanding some of the details of the EllipSys2D code. Also, I would like to thank Martin O.L. Hansen for inviting me to DTU to familiarise myself with the code in the first place and to Niels N. Sorenson for allowing me access to the HypGrid2D mesh generator and providing guidance in its use. A special thank you is also sent to Ernie Rogers for the priceless (and often unpublished) information he gave me on various aspects of circulation control as applied to rotors and Jim McGuirk for his welcome advice on various topics. I would also like to say a thank-you to all the numerous friends and colleagues who have helped in various direct or indirect ways throughout the course of this work. Finally, I want to thank my partner Clare for her patience and support and my son Jarrow for the inspiration he provides.

Contents

Appendices

Appendices

0.1 Nomenclature

$A =$ area, m^2

$C_d =$ two-dimensional drag coefficient, dimensionless

$C_T =$ rotor thrust coefficient, dimensionless

$\Delta C_{d_T} = \Delta C_{d_P} + \Delta C_{d_D} =$ total change in two-dimensional drag coefficient due to circulation control jet(s), dimensionless

$\Delta C_{d_D} = C_\mu \cos\tau =$ change in two-dimensional drag coefficient due to direct jet reaction of circulation control jet(s), dimensionless

$\Delta C_{d_P} = \Delta C_d =$ change in two-dimensional drag coefficient due to circulation control jet(s), dimensionless

$C_l =$ two-dimensional lift coefficient, dimensionless

$\Delta C_{l_T} = \Delta C_{l_P} + \Delta C_{l_D} =$ total change in two-dimensional lift coefficient due to circulation control jet(s), dimensionless

$\Delta C_{l_D} = C_\mu \sin\tau =$ change in two-dimensional lift coefficient due to direct jet reaction of circulation control jet(s), dimensionless

$\Delta C_{l_P} = \Delta C_l =$ change in two-dimensional lift coefficient due to circulation control jet(s), dimensionless

$C_n =$ coefficient of aerofoil forces normal to the chordline, dimensionless

$C_t =$ coefficient of aerofoil forces tangential to the chordline, dimensionless

$C_x = C_{n_{rotor}} =$ coefficient of blade forces normal to the rotor plane, dimensionless

$C_y = C_{t_{rotor}} =$ coefficient of blade forces tangential to the rotor plane, dimensionless

$C_\mu = \frac{\rho V_j^2 \delta}{\frac{1}{2}\rho U_\infty^2 c} =$ two-dimensional momentum coefficient, dimensionless

$C_\mu = \frac{\dot{m} V_j}{\rho A V_t^2} =$ rotor craft definition of the momentum coefficient, dimensionless

$c =$ chord length, metres

$d =$ diameter, metres

$d' =$ hydraulic diameter, metres

D_{rotor} = rotor diameter, metres

$f = \frac{0.25}{\left[\log\left(\left(\frac{k}{3.7\times d'}\right)+\left(\frac{5.74}{\mathrm{Re}^{0.9}}\right)\right)\right]^2}$ = friction factor, dimensionless

$G = \frac{\Delta C_{l_T}}{C_\mu \sin\tau} = \frac{C_{l_p}}{C_\mu}$ = lift gain factor for jet flap and Coanda CCAs respectively, dimensionless

$G = \frac{C_T}{C_\mu}$ = rotor craft definition of the gain factor, dimensionless

h = slot height for Coanda CCAs (equivalent to δ for jet flap CCAs), metres

h/c = slot height to chord ratio, dimensionless

h/r = slot height to trailing edge radius ratio, dimensionless

I = turbulence intensity, dimensionless

$k = \omega c/2U_\infty$ = reduced frequency, dimensionless

k = turbulent kinetic energy, m^2/s^2

k = pipe roughness factor, metres

k = head loss coefficient, dimensionless

$k_j = \omega_j c/2U_\infty$ = jet reduced frequency, dimensionless

m = mass, kilogrammes

$\dot{m}$= mass flow rate, kg/s

Q = volume flow rate, m^3/s

r = radius, metres

r/c = trailing edge radius to chord ratio, dimensionless

Re = Reynolds number based on aerofoil chord and freestream velocity (unless otherwise stated), dimensionless

U_∞ = freestream velocity, m/s

v = velocity, m/s

V_j = jet velocity, m/s

V_t = rotor blade tip velocity, m/s

α = aerofoil angle of attack, degrees

α_{stall} = aerofoil angle of attack at stall, degrees

δ = slot width for jet flap CCAs (equivalent to h for Coanda CCAs), metres

δ/c = slot height or width to chord ratio, dimensionless

θ = blade set angle, degrees

ρ = density kg/m^3

τ = initial jet deflection angle, degrees

τ_w = wall shear stress, N/m^2

υ = kinematic viscosity, m^2/s

ω = rotational speed, radians per second

ω = pitching frequency, radians per second

ω = rate of dissipation of turbulent energy, s^{-1}

ω_j = jet oscillation frequency, radians per second

Chapter 1

Introduction

1.1 Wind Turbine Operating Conditions and Load Scenarios

Horizontal axis wind turbines (HAWTs) have two fundamental operating regimes: below rated power, where maximum power (and hence energy) capture is of prime importance, and above rated power where the amount of energy harnessed from the wind must be restricted in order to limit loads and keep the various components of the machine within their operating limits.

These two basic requirements (*energy capture* and *survival*) combined with the need to generate energy in a *cost effective* manner, have resulted in the fundamental design types which are found today. These are power regulation by blade stall (passive or active) and blade pitching (normally to feather), either of which can be combined with the use of dual or variable speed rotor operation for increased energy capture below rated power and alleviation of transient loads.

Both of these approaches have implications for the design of the turbine components. For example, a passively stall regulated turbine must have blades of a greater structural stiffness than those of a pitch regulated machine, due to the fact that above the cut-out wind speed the blades of the former cannot be pitched to full feather to present the smallest possible area to the on coming wind and hence reduce out of rotor plane loading and deflection.

It is fair to say that the traditionally simplest design approach of a fixed pitch, passively stall regulated turbine has become progressively usurped as the dominant design by pitch regulated (predominantly to feather but also to stall), often in combination with variable speed capability, as machines have grown in size. This is partly due to the fact that the forces experienced by passive stall machines are larger than those experienced by a pitch control HAWT and have become problematic with turbine up-scaling, but has also been driven by the ever present need to produce energy more cost effectively. It also shows an unsurprising trend within the industry toward employing greater complexity and sophistication in return for improved control over the turbine's behaviour. At the same time any added sophistication must prove to be reliable, due to the nature of the HAWT operating environment. This is one in which servicing and routine maintenance are minimal (typically, twice yearly), while the machine must continue to operate reliably in all meteorological conditions.

The atmospheric wind field (and hence the loading scenario) in which HAWTs operate is by nature stochastic; long term (>1 hour) variations are driven by the prevalent wind climate, while short term (<10 minutes) variations are determined by the turbulent content of the wind. In addition to these random fluctuations, a HAWT also imposes a cyclic load variation upon itself due to rotational sampling of the wind field, which varies across the rotor diameter due to phenomenon such as wind shear and tower shadow/yaw misalignment. As such the structure, and in particular the blades, must be capable of surviving a huge number ($>10^9$) of fatigue cycles over a lifetime (of typically 20 years) as well as the extreme load cases that arise. The control system used (be it active or passive) must, at all costs, avoid amplifying these loads unnecessarily and will be dependent on the machine design and its particular characteristics (e.g. pitch or stall regulated) and it's structural response, defined primarily by the flexibility of the structure. One way of making wind turbines more cost effective is to reduce the initial cost of the major components and this can be achieved by reducing the amount of material used and hence the tower-top mass. Weight reduction, particularly of the blades, then increases structural flexibility and hence the degree of aeroelastic interaction of the machine with the wind. Alternatively, if the lifetime of the structure can be extended or the reliability improved, the ratio of the initial investment against the income generated over the machines lifetime can be decreased. It is proposed in this thesis, that in order to achieve either of these goals, it is worth exploring new possibilities for active control of the loads experienced by a HAWT as well as control of the turbine's power output. In particular, the suitability of circulation control aerofoils will be investigated for this role.

1.2 The Circulation Control Concept

Circulation is an aeronautical concept developed in order to analyze the forces experienced by a body placed in a fluid stream. The force associated with the circulation concept is referred to as lift and this, in turn, is defined as the component of the total force which is aligned perpendicular to the direction of the fluid flow (from here on referred to as the freestream). The lift force (indeed the total force) generated by an aerofoil section is a function of its particular shape and the angle between its chordline and the freestream (known as the angle of attack). Circulation control refers to the ability to vary the forces produced by the aerofoil without having to change either its angle of attack or geometry. This is generally achieved by expelling or drawing in air through an aperture in the aerofoil surface.

The ability to vary aerofoil forces by expelling air from the trailing edge was first documented in 1938 by Hagedorn and Ruden; it was noted that the presence of a jet of air emanating from the lower surface of the aerofoil trailing edge increased the lift force on the aerofoil. Over the sixty years since its discovery this technique for adjusting the lift experienced by an aerofoil section, wing or rotor blade has received attention from both academic researchers and engineers for a variety of different reasons and purposes. In the early 1950s the idea received much attention due to the increased use of the jet engine, and in both Britain (at the National Gas Turbine Establishment - NGTE) and France (at the Office National d'Etudes et Recherches Aeronautiques - ONERA) the concept of integrating the lifting and propulsive elements of future jet engine propelled aeroplanes was concurrently proposed. The term 'jet flap' was coined due to the obvious analogy the jet stream provided with a mechanical flap and the idea received much interest, particularly academically, although it was never realised.

The idea for a circulation control aerofoil utilising the Coanda effect to obtain the required jet deflection originated with Cheeseman in the mid 1960's. In this revision the jet stream is expelled tangentially to the aerofoil surface, from a slot on the upper (rather than lower) surface slightly forward of a blunt, rounded trailing edge. Provided the wall jet has adequate kinetic energy, it will remain attached to the rounded trailing edge due to the pressure difference that exists across the jet, from the wall to its outer edge (the Coanda effect). The jet detaches from the trailing edge at a point determined primarily by its initial velocity and the geometry of the trailing edge, and impinges on the freestream at an angle to it. The concept gained popularity within the helicopter community and then in the X-wing (a prototype, rotating to fixed wing aircraft) project, as both these applications already used, or could justify using, aerofoils with the blunt, rounded trailing edge required to gain jet deflection. In this field the primary aim was to use it to provide cyclic (1P) variation of the blade forces, such that it could be used to replace the swash plate, although other secondary benefits such as the use of higher harmonic control to reduce blade load excursions, became apparent in the large scale test programs that were commissioned. It was also the subject of extended research for application to fixed wing craft, in particular for use with Short Take-Off and Landing (STOL) aircraft, and in this area much work was done on aërofoil design and in particular ways of reducing the drag penalty associated with the required blunt trailing edge.

1.3 Synopsis

The primary aim of this work is to assess the suitability of the circulation control concept for use on wind turbine rotors, particularly in respect to identifying potential areas of useful application, quantifying the behaviour of circulation control aerofoils (CCAs) at the very low momentum coefficients suitable for use with HAWTs, reducing the energy input required by virtue of maximising the energy specific CCA gain and reducing the overall required system complexity to an acceptable level. The investigation takes the format outlined below.

Chapter 2 begins with an overview of the relevant literature, with respect to the development and use of circulation control aerofoils in both fixed wing and rotor craft. This is followed by a critical review of previous attempts to utilise pneumatic and other aerodynamic devices on wind turbine blades. Lastly, a speculative look at research in the field of sensors, including the newly emerging field of micro-electrical-mechanical (MEMS) devices, potentially suitable for use with wind turbines is taken with an eye to the possibilities these open up for adaptive control strategies to be implemented.

Chapter 3 assesses and describes the aerofoil requirements of wind turbine blades, as well as the characteristics of both jet flap and Coanda Circulation Control Aerofoils (CCAs). An exercise in the synthesis of these two parameters is carried out, leading to a clear set of design requirements for a CCA section for wind turbine blades.

Chapter 4 introduces the Computational Fluid Dynamics (CFD) code used to assess two dimensional CCA sections for HAWTs. The reasons for limiting the CFD investigation to two dimensional analysis are described and the modelling work carried out to assess the suitability of the code for simulating the behaviour of CCAs is presented. Finally, conclusions are drawn as to the code's ability to correctly predict the effect of trailing edge jets of different types on the flowfield surrounding a CCA, including the quantitative accuracy of the solver with respect to the changes in lift coefficient.

Chapter 5 develops the CFD modelling consistent with the design requirements developed in Chapter 3. Three aerofoils are modelled in detail: the NACA 4415 in order to determine characteristics needed as an input to the HAWT modelling subsequently presented in Chapter 7; the NACA 63415 (and other sections from the same family) due to its widespread use on HAWTs; and the FX77w153, an aerofoil purpose designed for use on HAWTs. As well as exploring the different behaviours of these three sections when used as CCAs and drawing conclusions as to their suitability, other parameters are also investigated such as slot position, slot size and jet efflux angle.

Chapter 6 makes a detailed assessment of the required 'infrastructure' for the application of CCAs to HAWTs, such as fan/blower/compressor sizing and duct work design. The energy requirements are quantified by means of example to a 2MW turbine and an optimisation procedure carried out with respect to the maximum aerodynamic effect achieved for minimum energy input. The potential for using 'passively' raised pressure due to the centrifugal 'self-pumping' action of the rotor is discussed, and the likely resulting pressure gradient in the blade duct and energy extraction from the rotor due to Coriolis force are quantified.

Chapter 7 introduces the principles and assumptions behind Blade Element Momentum theory (BEM) and relevant details of the particular BEM code used, FAST_AD(4). An adequately detailed model of the Tjaerborg 2MW wind turbine is developed and validated against existing data. The two-dimensional CCA data derived in Chapter 5 is then used to simulate the effect of CCAs fitted to the Tjaerborg turbine and identify potential areas of useful application within the constraints of the system outlined in Chapter 6.

Conclusions and further research areas are presented in Chapter 8.

Chapter 2

LITERATURE SURVEY

2.1 Introduction

Circulation Control Aerofoils (CCAs) have been have been the subject of investigation for almost 50 years and, as such, there is a large body of work detailing fundamental research and various applications. The first section of the literature study is devoted to outlining the physical nature and types of CCAs, as well as making the reader aware of the aspects of previous research pertinent to their potential for application to Horizontal Axis Wind Turbines (HAWTs). The second section presents a short synopsis of the previous work that has been conducted in applying additional devices to HAWT blades, some of which are pneumatic, and summarises the type of sensors currently used for HAWT control. Additionally, recent research that has developed sensor systems, which are considered to have potential for facilitating advances in HAWT control are identified.

2.2 Circulation Control Aerofoils (CCAs)

Control of the circulation around an aerofoil can be achieved by either suction or ejection of air from different locations on the aerofoil surface. For the purpose

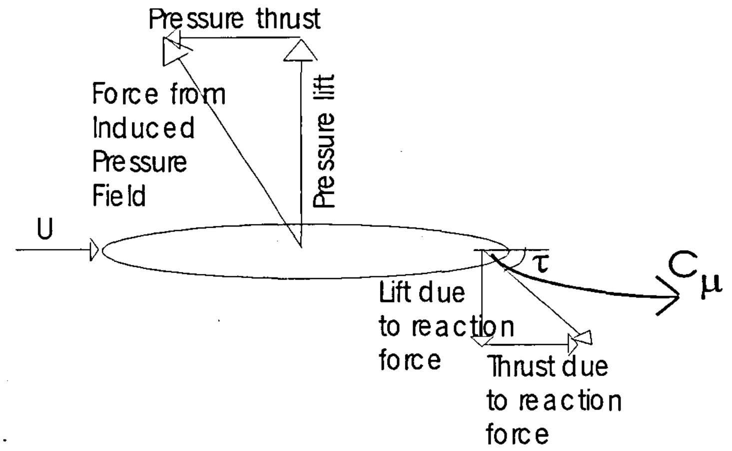

Figure 2.1: Schematic showing variables and forces for a jet flap aerofoil

of this work, however, circulation control aerofoils are defined by the presence of a sheet of air expelled from a thin, spanwise slot in the region of the trailing edge. The primary effect of this jet sheet is to cause an asymmetry of the flowfield around the aerofoil, thereby inducing lift due to circulation much as a mechanical flap does, although the nature of the interaction of the jet sheet with the freestream (and the aerofoil boundary layers) is fluidic, and the jet sheet can possess a significant amount of energy which produces a direct, reaction force on the aerofoil. The two primary variables which determine the degree of lift created by the jet sheet are the momentum coefficient, C_μ, given in its two-dimensional form by Equation 2.1 and the angle between the chordline and the initial jet deflection angle, τ, as shown in Figure 2.1. In Figure 2.1 where the jet emanates from the lower surface of the aerofoil, the jet deflection angle, τ, is defined as positive.

$$C_\mu = \frac{\rho V_j^2 \delta}{\frac{1}{2}\rho U_\infty^2 c} \tag{2.1}$$

where δ is the height (or width) of the slot and hence the initial thickness of the jet, V_j is the mean velocity of the jet relative to the aerofoil and c is the chord.

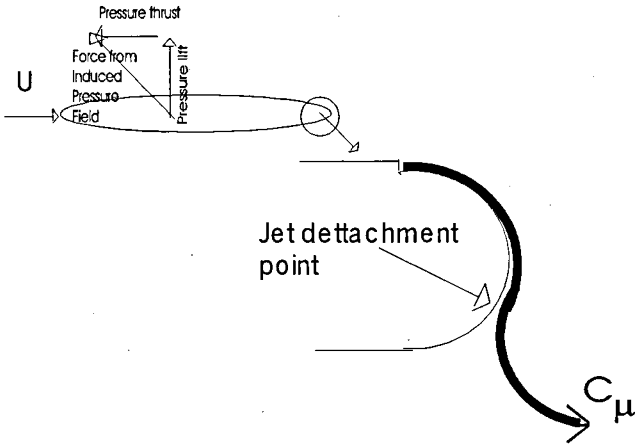

Figure 2.2: Schematic showing principle of Coanda Circulation Control Aerofoil

Two main variants of the CCA idea exist, being the jet flap, where the jet is initially ejected at an angle to the aerofoil chord (from a point somewhere on the lower surface to increase lift, as indicated by Figure 2.1), and the Coanda CCA in which the jet is expelled tangentially to the upper surface, some short distance forward of a blunt, rounded trailing edge and achieves a downward deflection into the freestream by virtue of the attachment of the jet to the trailing edge due to the Coanda effect (shown in Figure 2.2).

2.2.1 The Jet Flap

As mentioned in the introduction, the 'jet flap' effect was first observed in 1938 by Hagedorn and Ruden [1]. However, it was not until the establishment of the jet engine as a viable means of aeronautical propulsion that the idea received serious experimental attention, as its name suggests. Early efforts to quantify the effect were made at the National Gas Turbine Establishment (NGTE) [2] [3] [4] and the Office National d'Etudes et Recherches Aeronautiques (ONERA) [5] [6]. These tests, although fairly extensive, were restricted by the use of low Reynolds numbers ($3 - 6x10^5$), small test models and, for obvious reasons, a limited understanding of the preferred test techniques (and were deemed to be 'of an exploratory nature' by both parties).

Both NGTE and ONERA determined similar performance characteristics in tests with quasi two-dimensional, symmetrical profiles, most notably an increase in $C_{l\,\mathrm{max}}$, a decrease in stalling incidence and an increase in $dC_l/d\alpha$ with increasing momentum coefficient, as well as an increase in nose down pitching moment and a decrease in drag greater than the direct jet thrust contribution of the jet. The former points only become highly pronounced at momentum coefficients which are beyond the range of interest in this work due to the high energy input required, although this is not to say that the effect will not be present to a lesser degree at lower ranges of C_μ. A clear linear relationship was found to exist between $\sin\tau$ and ΔC_l due to blowing, although for $C_\mu > 0.1$ the experimental data progressively deviates from this relationship, becoming applicable only for $\tau < 65°$ at $C_\mu = 1$ [5] [6].

The use of the momentum coefficient, C_μ, as the appropriate dimensionless coefficient was determined by the ONERA team by varying the slot height to chord ratio, δ/c, from 0.0068 to 0.189, thus changing the jet velocity for a given momentum coefficient. It was found that the results from all δ/c configurations fell on the same line when ΔC_l was plotted against C_μ. There is a small caveat to this finding, in that as δ/c was increased it was found that the desired initial jet deflection angle was harder to maintain; as ΔC_l increases with increasing τ, this suggests that slighter greater ΔC_l may be achievable with larger slot heights for a given C_μ.

For the symmetrical aerofoil section (NACA 0018) and the range of momentum coefficients tested by ONERA ($C_\mu = 0.02 - 1$), the empirical relationship given by Equation 2.2 was found to hold

$$\Delta C_{l_T} = 3.9\sqrt{C_\mu}.\sin\tau \tag{2.2}$$

where ΔC_{l_T} is the total change in two-dimensional lift coefficient due to the jet flap, including both the direct jet reaction and the primary lift contribution from the change created in surface pressure.

It follows that the lift gain factor, G, (also referred to as the augmentation ratio or magnification factor), a measure of the efficiency of the circulation control in producing lift, defined by Equation 2.3, increases as C_μ is decreased. For the ONERA tests with the NACA 0018 section G varied between 3.5 and 25 as C_μ was decreased from 1.0 to 0.02.

$$G = \frac{\Delta C_{l_T}}{C_\mu \sin\tau} \tag{2.3}$$

The increase in nose down pitching moment is caused by the 'saddleback' pressure distribution present on a jet flap aerofoil, which has suction peaks at both the leading and trailing edges, as well as a small region of positive pressure on the lower surface of the aerofoil at the trailing edge; the direct jet reaction also contributes. It is the extent of the leading edge suction peak caused by the jet flap which is primarily responsible for producing a thrust greater than the direct jet reaction, $C_\mu \cos\tau$ or, viewed alternatively, a reduction in profile drag. This characteristic attracted much attention in light of the 'propulsive wing' concept, although it was not found possible to achieve close to 100% 'thrust recovery' (that is, full jet thrust in the chordwise direction, irrespective of the initial jet deflection angle), except at low jet deflection angles ($\tau < 30°$) in the NGTE and ONERA tests. Later experimental work by Foley [7] indicated that substantial (approximately 94%) jet flap thrust recovery could be achieved using deflection angles up to 60° and $C_\mu < 1$. Bevilaqua et al. [8] [9] provided greater detail on the thrust losses which can occur at both high ($C_\mu > 1$) and low ($C_\mu < 0.2$) momentum coefficients. Based on their experimental findings they proposed that at low momentum coefficients thrust recovery was lost due to the jet entrainment (which is partly responsible for the low pressure region developed on the upper surface of the trailing edge), while at higher momentum coefficients the loss was due to a leading edge separation bubble bursting and growing. The former point is applicable to the work presented here, while the latter is not.

Finally, further experimental work was carried out by Yuan [10], although the experimental procedure (model type and size, Reynolds number etc.) was not significantly different to that of the NGTE experiments and reasonable agreement was found between the two data sets.

Theoretically the most important contribution to the analysis of jet flaps was made by Spence [11] [12] who built on work published by Helmbold [13] which treated the jet flap problem in a formulation based on thin aerofoil theory. In this the jet sheet is represented by an infinitesimally thin vortex sheet with the boundary condition on the jet being defined in terms of a proportionality between the pressure difference across the jet and its curvature. The numerical solutions to the problem presented by Spence [12] were defined in relation to the results from the NGTE experiments, as were those of a later analytical approach [14] presented in a further paper. Two methods for determining the pressure distribution over a jet flapped aerofoil were also developed separately by Spence [15] and Kuchemann [16]; the former method provides the pressure distribution on a thin, symmetrical aerofoil except in the vicinity of the trailing edge, while the latter includes thickness and camber effects, but requires that the lift coefficient produced by a given momentum coefficient be known *a priori*. Both methods are validated against the NGTE experimental data [2] [3], which is presented in Chapter 4.

Various other researchers developed the methodology of Spence in order to make the solutions amenable to different situations, such as the behaviour of the jet flap in ground effect [17] and its interaction with a fully developed jet stream [18]. Later, Leamon and Plotkin [19] presented an iterative solution method based on determining the actual jet path (rather than one coincident with the freestream as in the fully linearised approach), as did Halsey [20] who also included an inverse design method which could cope with thin or thick aerofoils of arbitrary shape. Sato [21] and O'Mahoney and Smith [22] used conformal mapping techniques to provide solutions to the jet flap problem that were also capable of providing a solution for an arbitrary aerofoil profile; the latter also provided an additional, empirically based, means of including the viscous interaction at the trailing edge. Tang and Tinkler [23] presented a further iterative solution technique which provided the correct jet path as well as allowing for a finite jet thickness - their results suggested that increasing the jet thickness led to a slight increase in lift coefficient for a given momentum coefficient and jet deflection angle, in agreement with the ONERA findings, although they do not appear to have been aware of this work. Finally, Mateescu and Newman [24] developed a means of analysing the jet flap problem for thin aerofoils using velocity singularities.

Apart from the viscous interaction at the trailing edge of the aerofoil provided by O'Mahoney and Smith [22], all of the above techniques utilise an inviscid approach for treatment of the jet. The only analysis known to this author to fully incorporate viscous effects is that of Chen and Shaw [25], who used the commercial Computational Fluid Dynamics (CFD) code Phoenics (with the $k-\epsilon$ turbulence model) to simulate the NGTE jet flapped aerofoil, although the rigour of the work is, in this author's opinion, somewhat less than thorough, even lacking proof of mesh independency for the results presented. It is, therefore, clear that no previously developed methods are capable of tackling the jet flap aerofoil problem with the appropriate inclusion of viscous flow effects. Further, all the work conducted to date has relied, for verification, on one series of experiments, which by the researchers' own admission, was of 'an exploratory nature'.

2.2.2 Coanda Circulation Control

The idea for a circulation control aerofoil utilising the Coanda effect to obtain the required jet deflection, as shown in Figure 2.2, originated with Davidson [26] and was initially explored by Kind and Maul [27] [28]. Cheeseman [29] [30] and Dunham [31] [32] proposed its application to helicopter rotors and made initial investigations in this context. Accordingly, the concept has been extensively investigated in the helicopter community (and in the X-wing project - a rotating to fixed wing craft concept), as these applications already used (or could justify using) aerofoils with the blunt, rounded trailing edge required to gain jet deflection. Fixed wing applications have also been considered and in this area of application much of the emphasis has been on reducing the trailing edge radius required for effective jet deflection.

The Coanda effect which is used to achieve the jet deflection occurs as the result of a pressure differential which exists across the curved wall jet, between the solid surface and the free shear layer [33]. It is not essential for the jet to be initially attached to the wall as the creation of a small starting vortex between the jet and wall will often encourage attachment, and very localised separation with reattachment has been seen to occur in some Coanda CCA tests [34], presumably due to a similar effect. The degree of jet attachment is determined primarily by the jet velocity and local surface curvature and therefore its behaviour is sensitive to both the height of the slot (which defines the jet velocity for a given momentum coefficient) and the shape of the trailing edge. The three dominant design variables in this respect are the slot height to chord ratio, h/c, the ratio of the slot height to trailing edge radius, h/r, and the trailing edge radius to chord ratio, r/c. The slot position with respect to chord and the exact trailing edge geometry are also important.

The lift augmentation caused by the jet on a Coanda aerofoil is due to two separate phenomena. The first is the boundary layer control that occurs downstream of the jet slot on the upper surface and the second is the circulation control achieved by the movement of the stagnation point at the trailing edge. Placing the slot forward as far as 92% of the chord has been shown [34] to increase the range of unstalled operation within the low momentum coefficient range ($C_\mu < 0.05$) due to the upper surface boundary control, although this occurs at the expense of reduced augmentation at higher momentum coefficients owing to decreased Coanda turning efficiency. Wherever the slot is placed, Coanda CCAs display the same tendency to reduce the stall angle as jet flap CCAs at higher momentum coefficients.

Drag is found to decrease for Coanda CCAs, in a similar manner to that of the jet flap CCA, in cases where the trailing edge radius is truncated and flattened on the lower surface [35] [36], or too small to enable significant jet turning [34], and a significant direct thrust component is present. Again, similar to jet flap behaviour, the presence of a large leading edge suction peak also plays a significant role in drag reduction, until jet induced leading edge separation occurs. Where the trailing edge radius is large enough to ensure significant jet turning, drag is initially reduced from the unblown state as blowing is initiated and the momentum coefficient increased. However, when the jet pressure becomes high enough to produce large jet turning angles, the drag is increased due to the increasing size of the viscous wake created by the jet.

For Coanda CCAs the deflection angle is not defined *a priori* (the degree of jet attachment being a strong function of C_μ) and so the $\sin\tau$ term is neglected in the definition of the two-dimensional augmentation ratio, given by Equation 2.4.

$$G = \frac{C_{l_p}}{C_\mu} \tag{2.4}$$

Decreasing the slot height initially improves lift augmentation for a given C_μ, due to the decreased mass flow and increased kinetic energy in the jet [37], which improves the jet turning capability. However, this augmentation reaches a maximum at an h/c ratio of approximately 0.0015, and it has been suggested that the reduced performance witnessed with $h/c < 0.0015$ is possibly due to the size of the boundary layers in the nozzle becoming significant in relation to the slot dimension [34]. There is also a dependency of the lift on the slot height to trailing edge radius (h/r), which strongly affects the jet turning capabilities due to loss of jet attachment. For a given slot height, lift is found to reduce slightly as h/r is increased [35] and there is the potential for loss of the Coanda attachment of the jet to the trailing edge.

For application to fixed wing craft, Coanda CCAs have been investigated, primarily by Englar, for use with Short Take-Off and Landing (STOL) aircraft leading to full-scale flight testing [38]. The low drag requirement during cruise led researchers firstly to explore ways of mechanically converting from the blunt rounded trailing edge (required to provide the jet deflection for high lift production at take off and landing) to a sharp trailing edge [37]. Later, to avoid mechanical complexity, efforts were directed at reducing the radius of the rounded trailing edge as much as possible, and attempts to incorporate the Coanda surface within the contour of an existing supercritical aerofoil (a NASA 17% thick section) were largely successful [35]. In this case r/c was reduced to 0.009 (just over twice the trailing edge thickness of the baseline aerofoil) without significantly degrading CCA performance compared with larger r/c configurations, or increasing drag compared to the baseline aerofoil. An even smaller ($r/c = 0.0045$) trailing edge was tested less successfully with another aerofoil section (that already fitted to the A-6 flight tested CCW). This highlighted the limitations on reducing the trailing edge radius, as it suffered from a set of lift maxima imposed at a relatively low momentum coefficient of 0.04 [36], presumably due to an upper limit on the jet turning capability with increasing jet velocity. Even with the successes of [35] taken into consideration it is clear from the emphasis of later work (where a degree of mechanical complexity is traded for the ability to have a sharp trailing edge during cruise, by use of a dual radius CCA design [39]) that the use of Coanda surfaces is not fully compatible with modern mono-element, low drag aerofoils. A final point worthy of note from Englar's work is the detrimental effect wing bending can have on maintaining a consistent (and open) slot gap for a Coanda CCA, where the slot is normal to the chordline [38].

Wood [40] investigated the effect that sweep and finite aspect ratio might have on Coanda CCA wings, in order to ascertain the validity of using two-dimensional sectional data in the design of rotor blades, which experience highly three-dimensional flow. The CC wing section was found to behave in the same way as a conventional (non-blown) wing would, with regard to both sweep (up to 45°) and finite aspect ratio, and it was suggested by Wood that standard aerodynamic correction factors could be used with confidence. In particular, flow visualisation studies showed that the interaction between the jet and upper surface boundary layer was not affected by the sweep present. At the same time, highly three-dimensional flows were found to be present at the interfaces between the CCA and unblown wing sections (at both root and tip), which induced downwashes that could reach the same order of magnitude as those produced by the conventional (non-blown) tip vortex (momentum coefficients up to $C_\mu = 0.08$ were used). Englar reports similar shed vorticity in 3D wing tests [37].

The possible advantages of providing Coanda jets from two slots positioned sequentially in the chordwise sense, was investigated by Harvell and Franke [41] using an appropriately equipped 20% thick, cambered ellipse. It was found that significant increases in lift coefficient can be achieved for a given total momentum coefficient in the range $0 < C_\mu < 0.08$ when the secondary jet is positioned such that it is close to the point at which the primary jet would otherwise separate. To this author's knowledge there has been no further application of this idea, presumably due to the extra complexity incurred in the design and variability of the optimum slot position over the operating range.

Various theoretical approaches to the Coanda CCA problem have been developed for both analysis and design purposes. Initially these used potential flow solutions matched to the separation points on the aerofoil, which were determined using empirical formulae to define the velocity profile of the curved wall jet and its likely point of separation [28] [42]. Later, Gibbs and Ness [43] and Dvorak and Kind [44] developed more fully coupled viscid-inviscid methods that require no empirical input; of the two, the latter seems to have been more widely adopted. For example, Tai et al. [45] coupled the analytical method of Dvorak and Kind [44] with an optimisation routine in order to predict the trailing edge design that would, for a given aerofoil and momentum coefficient, produce the greatest lift coefficient subject to certain constraints. Improvements of the order of 15% over the baseline case are predicted for the lift coefficient from this design procedure. Soliman also produced an analysis method based on a discrete vortex model [46]. Shrewsbury [47] found considerable success using compressible, Reynolds averaged Navier-Stokes (RANS) CFD methods (with an eddy-viscosity turbulence model) to predict the performance of two-dimensional Coanda CCAs. However, it should be noted that additional empiricism was required in the turbulence model in order to represent the effect flow curvature has on turbulence levels in the Coanda wall jet. This took the form of a scaling constant that varied with the local radius of curvature and local streamwise velocity, as well as a constraint placed on the points in which the eddy viscosity was actually calculated (the region around the point of jet detachment being ignored and later interpolated from the bounding (calculated) values). This modelling was later extended to unsteady flow conditions pertinent to rotorcraft application [48] and in the development of Englar's CCAs for fixed wing applications [39].

Although a small amount of work explored the potential for the application of jet-flap CCAs to rotors [49] [50] [51], the majority of such work has involved Coanda CCAs. The idea of a stoppable rotor was first developed by Dunham [31] [32] and Cheeseman [29] [30] using circular sections with pressurised air supplied to tip-jets for propulsion and 'trailing edge' jets for circulation control. The latter could be throttled cyclically in the hub to provide the control conventionally provided by a swash plate, although the results of these tests were not published. Kretz [51], however, does show, by means of two-dimensional and model rotor tests, that higher order control (both open and closed-loop) can be used to significantly reduce stresses and vibrations as well as replacing the 1P swash plate. This work used various configurations including a jet flap, a mechanical flap and a rotor with individually pitched blades. For the two-dimensional tests closed loop control was achieved using integrated pressure readings from the section. Higher harmonic control has also been successfully used to control blade flap loads on X-wing test rotors. Potthast [52] used closed-loop control based on measurement of hub moments for reduction of 2P blade loadings, as did Abramson and Rogers [53] (although in a non-automated fashion) and Reader [54] (in an open-loop fashion). All three approaches used Coanda CCAs and hub-mounted, cyclically variable valving, which also acted as a replacement for the swash plate. In all of these experiments a phase lag between setting the air flow at the hub and the corresponding change in blade forces had to be accounted for. Experimental and analytical work by Watkins et al. [55] clearly identified this pneumatic time lag as being sonic in nature and independent of the frequency of the cyclic input at the valve mechanism.

Finally, it should be noted that the rotor craft definition of C_μ is different to fixed wing 2D definition

$$C_\mu = \frac{\dot{m}\, V_j}{\rho A V_t^2} \tag{2.5}$$

where A is the rotor disc area and V_t is the rotor blade tip velocity.

The rotor gain or augmentation is given by equation 2.6 and typically has values lower than for the two-dimensionally defined gain (for example, the rotor tested by Schartz and Rogers [56] was considered to have had an unusually high augmentation ratio, being 29), due to the induced flow through the rotor driving down the angle of attack and the uneven C_μ distribution along the blade (greatest at the root, due to the variation of the tangential velocity).

$$G = \frac{C_T}{C_\mu} \tag{2.6}$$

where C_T is the rotor thrust coefficient.

2.2.3 Unsteady Aerodynamics

Spence's analytical approach used for the steady state case [12] [14] was extended to include the effect of an oscillating jet flap [57] [58] as well as of the jet flap aerofoil in pitching and plunging motion. For the case of a jet flap oscillating at the trailing edge a constant lift coefficient (equal to the steady state value) was predicted for reduced frequencies ($k = \omega c/2U_\infty$) up to 1, after which the lift coefficient was predicted to rise, with the lift leading the jet deflection. However, later experiments by Simmons in which a jet flap was oscillated at reduced frequencies between 0.053 to 2.36, do not verify these results [59]; rather it is reported that the lift coefficient reduces with increased frequency, with the lift coefficient lagging the jet deflection. It is interesting to note that in these experiments the jet flap aperture comprised discrete round holes ($d/c = 0.0025$) rather than a continuous slot, which was responsible for an (unquantified) reduction in steady state, jet induced lift coefficient, compared to the results from the NGTE tests - reducing the spacing between holes was found to ameliorate this. It is also interesting to note that the sinusoidal oscillation of the jet flap was achieved both mechanically and fluidically, with the novel fluidic actuation system able to vary jet deflection by $\pm 80°$. Similar findings to those in [59] were made in a later test [60] using a different aerofoil with a mechanically oscillated jet flap ($\tau = \pm 15°$); in this case a continuous slot was used and the lift increment improved correspondingly.

Further work by Simmons with a jet flapped aerofoil with $\tau = 0°$, in pitching and translational movement, found better agreement with the theory of Theodorsen [61] for unsteady aerodynamics of plain aerofoils, than that of Spence [58] (although it should be stated for completeness that the reduced frequency range was lower than that deemed by Spence to be applicable to his approach). Simmons et al. [62] later developed a quasi-steady, thin aerofoil model of the unsteady jet flap problem, which incorporated experimental results for the velocity profile evolution of an oscillating plane jet [63]. Although this model correctly predicts the trend of an increasing phase lag of aerofoil lift in relation to jet oscillation with increasing reduced frequency, it underpredicts the extent of the phase lag, particularly at the lower momentum coefficients studied. After further development Simmons and Pullin [64] concluded that the thin aerofoil model of unsteady jet flap aerodynamics suffered from difficulties associated with inherent numerical instabilities.

Shrewsbury used an in-house CFD code to model the time dependent characteristics of a Coanda CCA in an oscillatory pitching motion [47]. The CCA section modelled was the XW103 developed in the course of the previously mentioned X-wing project, although only static data was available for comparison (where good agreement was found). The mean angle of attack and the pitching amplitude for the simulations were both 4 degrees, with a constant momentum coefficient of 0.05, which seems a low angle of incidence until one realises that the $C_{l\max}$ value of 2.83 occurs at less than 4 degrees in this configuration (although unsteady vortex shedding does not occur until 6 degrees). The reduced frequency was varied from 0.1 to 1.0. In general, it was found that, unlike a conventional aerofoil undergoing dynamic stall, lift starts to collapse as soon as a separation vortex appears at the leading edge and only starts to recover after it has convected off the trailing edge. Further, the time required for circulation recovery after vortex convection was found to be almost independent of pitching frequency, while the characteristic time for convection of the separation vortex decreased with increasing reduced frequency. However, the precise behaviour was found to be highly dependent on the rate of aerofoil oscillation. At reduced frequencies equal to or less than 0.2, a deep stall hysteresis was found to exist, with large loss of lift at higher angles of attack until recovery occurs after the vortex convection is completed. With the exception of the reduced frequency of 0.5, for values above 0.3 a bimodal behaviour was found in the hysteresis loops due to the circulation recovery time being longer than the time required to return to the minimum angle of attack. At values above 0.5 the loops do not fall to the significantly low lift coefficient values seen at lower frequencies, as is common to conventional aerofoils. It should be noted that the Coanda jet remained attached at all times in the cycles, continuing to cause flow curvature at the lower surface trailing edge.

Ghee and Leishman [65] conducted wind tunnel tests on a circular cylinder with a circulation control jet positioned at 90° to the freestream and aligned tangential to the local surface. Benchmark tests were conducted to establish the pressure induced force coefficients over a range of steady momentum coefficients, before the blowing was varied in an oscillatory manner about selected mean values, over a range of reduced jet frequencies. It was found that in all cases elliptic hysteresis loops were produced, which advanced in a counter-clockwise sense, that is, a phase lag was found to exist producing lift coefficients which were greater when decreasing momentum coefficient, compared to those on the increasing part of the cycle. At higher mean values of momentum coefficient (around $0.11 - 0.13$) the mean, unsteady normal force coefficients and augmentation values were consistently higher than those obtained under steady conditions. At lower mean values ($0.05 - 0.06$) this was found to be dependent on the reduced jet frequency with values lower than 0.26 producing higher performance coefficients. In various cases higher harmonics originating in the valving were seen to affect the precise shape of the hysteresis loops. In all cases the phase lag increased with increased reduced frequency, reaching approximately $-70°$ by $k = 0.5$. It is also worth noting that for the cases of moderate blowing where the unsteady values were less than those of the steady blowing tests (i.e. at higher reduced frequencies) the jet detachment point was found to be sensitive to the condition of the upstream boundary layer and could be affected by the use of transition strips.

2.3 Wind Turbine Technology

2.3.1 Supplementary Devices for Wind Turbine Blades

Gurney flaps are small (<4% chord) flat plates, positioned on the pressure surface, either at the trailing edge or just forward of it, and aligned at some steep (>45°) angle to the chordline, but usually normal to it. Divergent Trailing Edges (DTEs) are similar in the effect they have and can be viewed as a Gurney flap with fairing. Liebeck [66] first documented the effect of Gurney flaps when added to a plain aerofoil, which is primarily to increase the lift coefficient, while slightly decreasing the stall angle although at a higher lift coefficient. The lift increment over the plain aerofoil grows with increasing flap height, although not proportionally (smaller flaps being the more effective).

Gurney flaps have been used on racing cars to assist in providing the aerodynamic down force necessary for high speed handling [67], as well as being assessed for use on HAWT blades [68] [69]. They were experimentally investigated on a NACA 4412 aerofoil section by Storms and Jang who found that, although they increased the lift coefficient, the lift to drag ratio was decreased at low to moderate lift coefficients. This finding is borne out by all further experimental work, for example [70] [71], although it is contrary to the original claims of Liebeck. It is for this reason that they have not found favour in HAWT applications and to the author's knowledge have never been utilised on production machines. This is not the case for vortex generators, another device tested by Storms and Jang [72] and Timmer and Rooy [71], which have been utilised on the inboard blade sections of large (>300kW) stall regulated turbines for some time. Vortex generators are small, often V-shaped, protruberances mounted on the suction side of an aerofoil at around 20-30% chord. They have the effect of energising the boundary layer and delaying the angle of attack at which stall occurs by as much as 10° with a commensurate increase in maximum lift coefficient.

Oliver [73] [74] explored the possibility of incorporating pneumatic vortex generators on the mid to outer-span blade sections of a stall regulated HAWT, activating them as the turbine operated just below rated power, increasing power capture at a operating point where stall controlled machines are less efficient than pitch regulated ones. Full scale field tests [75] indicated some increased net power capture was possible, but this was not shown conclusively and, although academic interest has been maintained, the idea has not been implemented on commercial HAWTS.

Other pneumatic devices have been designed for wind turbines, both vertical and horizontal axis. Rao and Perera [76] [77] designed a novel vertical axis machine utilising tangential wall jets for improved power control, while Bannister et al. [78] [79] [80] developed a 'pneumatic spoiler' for rotational speed control of a relatively small wind turbine (a Rutland 1800). This consisted of three rows spanwise of holes, placed aft of the half-chordline which, when activated ejected air normal to the chord, disturbing the boundary layer. This was found to have the required effect, although not of a large enough magnitude to prevent rotor runaway.

2.3.2 Sensors

At present, HAWT control is primarily concerned with the regulation of power above rated wind speed, with the aim of producing a smooth power output irrespective of changes in the wind field, without incurring damaging load cases due to the control action. The controllers employed are generally of the PI or PID type [81] [82] and the sensors used in the control loops are generally power transducers, and rotational speed sensors in the case of variable speed machines. Additionally, HAWTs have wind vanes and anemometers fitted on the nacelle to allow for performance monitoring, wind speed estimation and wind direction sensing for the control input to the yaw drive.

Recently, Bossayani [83] has suggested that control algorithms be designed with a second explicit purpose, that of reducing loads. In this vein the use of tower accelerometers is suggested, as they provide a robust sensing mechanism and tower acceleration (and hence velocity and displacement) is an important structural load, dependent primarily on the rotor thrust, while tower oscillations can also be indicative of turbulence and rapid blade pitching. Such ideas have been voiced by other parties [84] [85], but the requirement for sensor robustness is the primary feature which has to date prevented additional instrumentation of wind turbines. Strain gauges are used for experimental work and prototype assessment (as in the Garrad Hassan T-mon system), but suffer from excessive drift with time and are extremely fragile in installation and operation. Some work has been reported in the literature regarding the potential for embedding fibre-optic strain gauges in blades at the point of manufacture, but the results were not particularly encouraging and the author has no evidence of the technique being used to date with HAWTs. However, it should be noted that within the sensor industry such integrated fibre-optic sensors are thought to hold potential for similar applications [86].

Other than these previously documented sensors, two quite different, but promising devices have been identified in the literature. The first is a series of MEMS based devices developed by Sarcos [87], known as a UAST, BiAST and MAST (Uni-, Bi- and Multi-Axis Strain Transmitter) and the second is a low cost fibre-optic laser radar device named LIDAR [88]. The former is a strain gauge (or more accurately an extensometer) with a two part design, being a silicon base with an array of field detectors and a companion array of electrostatic field emitters on a quartz armature. This allows for relative movement between the two parts to be measured within an accuracy of 3.5nm for a gauge length of 10mm. Most importantly for application on HAWTs, the Sarcos devices do not suffer from drift and a rotational equivalent (the RDT) has been tested successfully over a lifetime of 2×10^8 cycles.

LIDAR, which can be mounted in the hub of a HAWT, is able to measure discrete points in the approaching wind field at a sampling rate of up to 100 readings per second and will return readings of high accuracy up to distances of 200m. By sweeping the laser in a cone in front of the turbine it is possible to rapidly build a picture of the wind incident to the entire rotor area, several seconds before the wind arrives at the rotor plane.

It is considered that both the Lidar and Sarcos devices have potential for use in HAWT control, in the field, as well as for R&D purposes.

Chapter 3

Circulation Control Aerofoils Suitable for Wind Turbine Blades

3.1 Introduction

The aerofoils that are used on HAWT blades are chosen, or designed for, specific properties which enhance the performance of the blades and hence, the turbine behaviour in general. At the same time, CCAs clearly display certain unique characteristics and introduce another set of parameters to be incorporated in the design/choice process. Also, the use of CCA sections may enable new or enhanced possibilities in terms of rotor response. In a similar way to which CCAs have been adapted for certain flight specific purposes (for example, the Englar adaptation of a super critical aerofoil for sub-sonic transport aircraft [39]), it should be possible to refine the CCA approach to the requirements of wind turbines.

The chapter begins with an overview of some aspects of the behaviour required of HAWT rotors and then proceeds to explore the ways in which the characteristics of the aerofoil sections chosen can assist in achieving the desired rotor behaviour. The characteristics common to both jet flap and Coanda CCAs, as well as those particular to each design, are then examined. The suitability of each of the two distinct variants to the requirements of a wind turbine CCA is then assessed, in the light of the HAWT aerofoil characteristics previously discussed and the necessary energy input required in such a system. An assessment of the most appropriate means of achieving force coefficient variation (by variation of jet deflection angle, τ, or momentum coefficient, C_μ) for a HAWT CCA is also discussed.

It is the purpose of this chapter to examine the different requirements and characteristics of HAWT aerofoils and CCAs, highlight the areas in which they are complementary and those in which they are conflicting and to define a clear set of design requirements for a HAWT CCA, which will direct the subsequent CFD investigation.

3.2 HAWT Requirements and CCAs

As mentioned in Chapter 1 the three requirements of a wind turbine are that it produces energy at as low a cost as possible, that it provides high reliability (as downtime increases the cost of energy through the loss of potential loss of power production, as well as the additional cost of replacement parts and repair) and survivability, that is the turbine must be able to survive (or avoid) the extreme loading cases which would cause catastrophic failure. In addition, there is the emerging demand for HAWTs to provide electrical power in an increasingly controllable fashion i.e. to be able to act as generators capable of providing grid support [89] [90].

In the light of these statements it must be asked, what are the potential uses (and the inherent limitations) of CCAs in application to HAWTs. It is known from previous work as presented in Chapter 2, that CCAs (at least in positive jet deflection) do not increase the angle of attack at which large scale flow separation and stall occurs as can other devices positioned forward on the aerofoil; in fact, at high momentum coefficients they are known to substantially reduce it. This immediately limits their application to pitch controlled machines if they are to be used in operating conditions above rated power and fitted over any significant portion of the blade. Even on a pitch regulated machine the inboard (>35% span) sections will regularly operate at angles of attack greater than 14° (i.e. beyond stall) in non-yawed flow conditions, while in asymmetric flow fields the angle becomes time dependent over the course of a rotor revolution and increases over that experienced in non-yawed conditions over certain azimuth angles. This then restricts their application to blade spans greater than approximately 50% if they are to be effective under a wide range of operating conditions. These restrictions imply that their function will not be one of supplying the primary means of power control, although it is not necessary at this point to rule out the possibility of their use as an additional means of, for example, power smoothing by virtue of their potential for an extremely rapid response time.

It is this potential for quick response which may make them suitable as a device for response to load excursions placed upon the blades, and the turbine in general, due to the (sometimes) fast changing nature of the wind field or the highly turbulent nature of the wind field when a turbine is operating in the wake of another, a common occurrence in wind farms. Further, the cyclic sampling of the wind field which occurs in both yawed and non-yawed states is primarily responsible for the highly demanding fatigue life which blades must endure. A significant amelioration of any of these loads has the potential to extend component lifetimes, add further freedoms to an initial turbine design and reduce component weight.

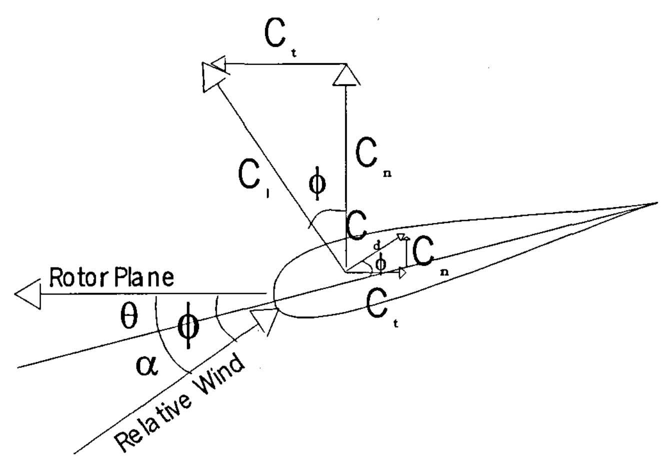

Figure 3.1: Blade element schematic showing resolution of lift and drag forces onto rotor plane

3.3 Desirable Aerofoil Characteristics for Outer Span Wind Turbine Blades

3.3.1 Lift to Drag ratio

Below rated power the power capture of any turbine is strongly influenced by the lift to drag ratio (C_l/C_d) of the aerofoil sections used over the outer 50% of the blade span and low drag aerofoils are required. The C_l/C_d ratio is of such importance over this part of the blade for two reasons: firstly, due to the increasing swept area and torque arm, the outer regions of the blade span play a disproportionate role in power capture, and, secondly, as one moves outward along the blade span, the chord line becomes aligned more closely to the rotor plane, due to the twist of the blades. As can be seen in Figure 3.1, the lower the angle ϕ, the greater the effect the drag has on the force tangential to the rotor plane given by Equation 3.2. ϕ, in defined by the blade set angle, θ (composed of the local blade twist and the pitch angle at the root), and the angle of attack, α.

$$C_{n_{rotor}} = C_x = C_l \cos\phi + C_d \sin\phi \tag{3.1}$$

$$C_{t_{rotor}} = C_y = C_l \sin\phi - C_d \cos\phi \tag{3.2}$$

In order to achieve low drag, it is necessary to design the aerofoil such that the boundary layer remains laminar for as long as possible (i.e. extended laminar flow caused by a rearward position of minimum pressure), thereby reducing skin friction. The lift to drag ratio of an aerofoil suitable for use with a large, modern HAWT should be greater than 140 [91]. Location of the low drag range is also important and should preferably extend over as much of the attached flow region over which significant lift is produced. An entirely sharp trailing edge is not a strict requirement for the design of a low drag aerofoil and with respect to wind turbine blades, the commonly used construction method of manufacture for glassfibre blades makes the fabrication of a very sharp trailing edge extremely hard to achieve.

3.3.2 Roughness insensitivity

HAWT blades, especially the outer span, are susceptible to accumulation of dirt and other airborne matter due to their unattended nature and their passing proximity to the ground. Insensitivity to leading edge roughness caused by either fouling or manufacturing imperfections is therefore a requirement of HAWT aerofoils [92]. This is inconsistent with the need for low drag aerofoils, as these are more susceptible to performance degradation due to roughness.

3.3.3 Structural Requirements

An important element in HAWT aerofoil design is the requirement for a sufficiently structurally stiff blade whilst minimising the amount material and hence weight of the blade. It is for this reason that thicker aerofoils are favoured as they allow the main structural element, the spar, to possess an increased cross sectional area. HAWT blades are far more structurally compliant in the flatwise sense than they are torsionally or in the edgewise direction.

3.3.4 Stall behaviour

As HAWT blades will always encounter stall due to the rapidly changing wind environment, whether they are on pitch or stall regulated machines, the aerofoils used on HAWT blades should preferably not suffer from a sudden and dramatic loss of lift at stall. A progressive loss of lift helps reduce the severity of losing aerodynamic damping on the blades at stall, and of the negative effect this can have on both the blades and the support structure. In order to achieve this characteristic, stall should come from the trailing edge. It should be added that field measurements on HAWTs indicate that the stall characteristic of aerofoils on the outer part of the blade will generally be less severe in the rotating environment than measured in two dimensional testing [91].

3.4 Desirable Circulation Control Aerofoil Characteristics for Wind Turbine Blades

3.4.1 Maximum ΔC_l for a given C_μ

As one of the potential uses of CCAs is as a means of reducing cyclic force variations on the blades, drive train and support structure, the HAWT CCA design should attempt to maximise the range of lift coefficient (ΔC_l) possible for a given momentum coefficient, C_μ. This suggests that use of a negatively deflected (or upper surface jet in the case of a jet flap CCA), as well as a positively deflected jet (or lower surface jet), should be considered if the former is equally effective at producing a negative lift increment as the latter is at producing a positive increment. A jet expelled towards the suction side of an aerofoil is termed 'negative jet deflection' in the context of this work, in line with the convention used for physical flaps. In this way the C_l range can be effectively doubled for a given maximum C_μ. Further, as air at raised pressure has to be provided for the CCAs to operate, and the energy for this must be provided by the turbine (if only indirectly), as well as the fact that the blower(s) etc. that supply this will add to the tower top weight, the ΔC_l range should preferably be delivered with the lowest possible energy input.

3.4.2 Lift to Drag ratio in Unblown Configuration

As mentioned in the previous section, the C_l/C_d ratio is extremely important for aerofoil sections present on the outer blade span. As such, and assuming that energy considerations will dictate that the CCAs operate without jets present under some conditions (e.g. below rated power), excessively thick trailing edges will not be desirable due to the high lift to drag ratio requirement of HAWT aerofoils. In fact, it is thought that a HAWT CCA in its unblown state must be capable of C_l/C_d ratios similar to that of modern wind turbine aerofoil sections.

3.4.3 Stall behaviour

For positive jet deflection (and from the literature survey, this is all that is known *a priori*) an increased adverse pressure gradient exists on the forward sections of a CCA, in conjunction with a favourable pressure gradient at the trailing edge, which explains why these aerofoils can suffer from leading edge stall at higher values of C_μ. This implies that at high momentum coefficients they will not meet the criteria that stall should come from the trailing edge and that they will not be suitable for operation at higher angles of attack under these operating conditions. It is also the case that momentum coefficients high enough to significanttly affect stall angle are unlikely to be encountered in this application due to energy considerations. It is difficult to say at this point to what degree a negative jet will affect stall angle.

3.4.4 Reliability and Structural Integrity

As reliability under extremely adverse operating conditions is a prerequisite of successful wind turbine design, any new or additional devices employed should be robust and not require servicing more regularly than standard wind turbine components. Further, any components that do require servicing should, preferably, be readily accessible to maintenance crews.

Additionally, CCAs require a continuous slot to be present at the trailing edge, in the spanwise sense. This slot should be such that its effect on the blade's structural integrity is minimised and positioned so that it suffers from as little a variation in aperture size as possible during the expected deformation of the blade under loading.

3.5 Initial Design Decisions

It is clear from the information presented in Chapter 2 that there are two primary means of varying the lift coefficient on a CCA, that is, by adjustment of the jet deflection angle, τ, or by changing the momentum coefficient, C_μ. It is also apparent that there are two sub-types of CCA, namely those that work by utilising the Coanda effect and those that use the jet flap approach. It is, therefore, necessary to make an initial decision on the preferred configuration for a wind turbine CCA, based on the requirements presented in the previous sections.

The desirable features for a HAWT CCA design are listed in Table 3.1 and the compatibility of each feature with the four primary choices (Coanda, jet flap, variable τ or C_μ) is graded between 1 and 5, a higher value indicating greater compatibility. Explanation of the various features and discussion of the most important points shown in Table 3.1, are then presented in the following subsections.

Feature	**Coanda**	**Jet Flap**	**Variable τ**	**Variable C_μ**
Dual deflection sense	4	5	5	5
Large slot size, δ or t.	1	5	3	5
High lift augmentation	5	3	N/A	N/A
High unblown L/D	3	5	3	5
Fast response time	N/A	N/A	5	4
Reliability	N/A	N/A	4	5
Structural Integrity	2	4	3	4
Ruggedness	N/A	N/A	3	4
Roughness Sensitivity	2	4	N/A	N/A
Good stall behaviour	2	2	N/A	N/A

Table 3.1: showing relative scoring of primary design options with respect to desirable features for a HAWT CCA.

3.5.1 Relative Suitability of Jet Flap and Coanda CCAs

In relation to the first requirement for a CCA suitable for use with wind turbines, that is, providing the maximum ΔC_l for a given C_μ, or more correctly, for a given energy input, there are two factors to consider. Firstly, can the design provide for a dual sense of deflection i.e. can the jet be deflected in such a way as to decrease as well as increase the lift coefficient? This should be equally achievable with either a Coanda or jet flap CCA as in either case the only requirement is for an additional slot on the opposite surface to that provided for the positively deflected jet, although optimisation of the Coanda surface trailing edge for one sense of deflection would not be possible. Secondly, the lift augmentation created by the jet should be as high as possible; in this Coanda CCAs are known to be superior to jet flap CCAs [42]. However, it is the energy specific augmentation which is of prime importance for the application to wind turbines, and in this respect the possibility of using larger slot to chord ratios than have previously been used (typically δ/c=0.001-0.0025) is a potential means of increasing this energy specific augmentation. In the first instance the energy or power required to provide a given momentum coefficient can be assessed by applying Bernoulli's equation and equating the static pressure in the duct with the dynamic pressure of the jet i.e. an isentropic expansion is assumed. Treating any density differences between the jet and external air flow as negligible, the required jet velocity for a given momentum coefficient, C_μ, and slot height to chord ratio, δ/c, is given by Equation 3.3

$$V_j = \sqrt{\frac{C_\mu U_{rel}^2}{2}\frac{c}{\delta}} \tag{3.3}$$

where U_{rel} is the relative windspeed seen at the blade.

The jet velocity and slot height are then used to define the volume flow rate per unit span as given by Equation 3.4

$$Q_j = V_j\delta \tag{3.4}$$

The dynamic pressure is defined by the jet velocity and the product of dynamic pressure and volume flow rate yields the fluid power per unit span as given by Equations 3.5 and 3.6

$$P_f = \frac{1}{2}\rho V_j^3\delta \tag{3.5}$$

$$P_f = \frac{1}{2}\rho\left(\frac{C_\mu c}{2}\right)^{\frac{3}{2}}\frac{U_{rel}^3}{\sqrt{\delta}} \tag{3.6}$$

It can be seen that the fluid power can be reduced for a given momentum coefficient by increasing the slot dimension, δ. Of the two CCA approaches, only the jet flap will allow significantly increased slot sizes to be used as the effectiveness of the Coanda jet turning is highly dependent on jet velocity and δ/c values greater than 0.003 are extremely detrimental to performance [34].

In order to achieve a design which has a suitable lift to drag ratio when the CC jets are not being powered an aerofoil with a reasonably sharp trailing edge must be used - this is not possible with a Coanda CCA. The Coanda CCA design with the smallest trailing edge diameter known to the author still had a substantial trailing edge diameter ($d/c = 0.018$) in terms of low drag design.

Jet flap CCAs are thought to be more suitable to HAWT blades with regard to maintaining structural integrity and being less likely to suffer from 'pinching' of the aperture as the slots will be nominally parallel to the chord rather than normal to it. As previously noted, HAWT blades are subject to much greater bending in the flatwise sense.

Neither Coanda or jet flap CCAs have desirable stall behaviour with a positively deflected jet as the increased circulation produced tends to increase the gradient of the post-stall lift slope.

3.5.2 Merits and Demerits of a Variable Deflection Angle Operating Strategy

As the clearest, identified application of CCAs to wind turbines is to produce a system whereby blade forces can be varied rapidly in response to either periodic or random fluctuations of the relative wind, it is appropriate to consider using a device capable of changing the jet deflection angle controlled and driven using modern electronics. This would certainly provide a system with a faster response time than one in which the aerofoil force coefficients are adjusted by variation of the mass flow and pressure in the duct and hence velocity of the jet stream.

However, there are serious drawbacks with such an approach that can be envisaged even before a particular type of device is defined as suitable. Firstly, in order for the jet stream to be expelled over a significant range of positive and negative angles, the deflection device would need to be mounted at the trailing edge, with the likely introduction of an excessively blunt trailing edge with regard to the aerofoil's drag coefficient when no jet is present (this is also incompatible with the potential use of larger slot sizes). Secondly, as the device would be hard to access for either maintenance or repair with the blades in place on the turbine, it would pose a serious reliability problem and would need to be capable of surviving a high ($> 10^9$) number of cycles without substantial degradation of performance. Finally, wind turbines are exposed to a harsh environment and the device would have to be rugged enough to survive the elements, most particularly lightning strikes.

3.5.3 Merits and Demerits of a Variable Momentum Coefficient Operating Strategy

In considering a CCA design which effects a change in force coefficients by use of a variable momentum coefficient it is at once possible to envisage a design which retains the desirable aerofoil feature of a reasonably sharp trailing edge. The sharp trailing edge, and associated low drag coefficient, can be retained by placing the jet efflux slots forward of the trailing edge. In this case it does not make any sense to use anything but the efflux angle which causes greatest increment in force coefficients and this is likely to be orthogonal to the aerofoil surface and hence, the local flow vector. Tests with Gurney flaps [69] have shown that no performance improvement is achieved when the flap is set at an acute angle i.e. more than 90° to local flow direction.

The response time of such a system is unlikely to be on par with one in which the deflection angle is adjusted by electronic actuators, but such systems have been successfully applied to helicopter rotors [53] [54] [52] and research [55] has shown that the time delay apparent in such systems is defined by the time required for pressure wave propagation i.e. a sonic lag.

Problems with component reliability are significantly reduced with such a system, primarily because it can comprise fairly standard and robust components but also because the valves required can be situated in the hub or at the root of the blade to which access can be gained for maintenance and repair. If a permanently open pair of slots is used there is no need to have any moving parts over the blade span which is fitted with CCAs although this may introduce a problem with the intrusion of rain water and possibly airborne debris, in which case slow moving sleeves may be required to seal the slots.

3.6 Summary

- The most likely use for CCAs of whatever type has been identified as a means by which cyclic and transient load fluctuations may be reduced.

- The desired characteristics of the aerofoil sections used on HAWTs, namely a high lift to drag ratio, roughness insensitivity, trailing edge stall characteristic and a reasonably large thickness to chord ratio, have been described in the light of the behaviour of the rotor.

- The requirements of a CCA for wind turbine use have been presented and have led to an initial design choice of a fixed jet deflection angle, variable momentum coefficient jet flap CCA. This is expected to provided the simplest and most reliable system with the further advantage of being capable of using larger slot sizes and hence effecting a greater force variation for a given energy input.

- It has been realised that if the largest variation of aerofoil forces is to be achieved for a given momentum coefficient, then a two-jet system should be used. That is, one in which jet slots are placed on both the upper and lower aerofoil surfaces, enabling a lift reduction as well as a lift increase to be achieved.

Chapter 4

Modelling CCAs using Computational Fluid Dynamics

4.1 Introduction

The Computational Fluid Dynamics (CFD) code EllipSys2D (E2D) [93] has been used to investigate aerofoil sections suitable for use with wind turbines with circulation control capabilities. The code is written and maintained in a collaboration between the Danish Technical University (DTU), Lyngby and the Risoe National Laboratory, Denmark. It is used in conjunction with a hyperbolic mesh generator, HypGrid2D (HG2D) [94], and a preprocessor, Basis2D (B2D) [95], which were developed at Risoe and DTU respectively, as well as the commercial post-processor TecPlot. This code (E2D) was chosen for its proven track record in the modelling of two dimensional aerofoils suitable for wind turbines [96] and a description of the most relevant aspects of E2D is the first item to be presented in this chapter. CFD was chosen as an appropriate tool as it allows for a fairly free selection of aerofoil profiles and operating conditions to be simulated, as well as providing details of the flow field, in particular the slot characteristics, unavailable with older viscid/inviscid jet flap solvers [20] [19]. The same conclusion was reached by Englar [39] on the applicability of different modelling approaches to CCAs, although it should be said that reliable CFD modelling of *Coanda* CCAs is not a fully established design practice, largely due to the difficulty in accurately predicting the detachment point of the wall jet. Also, to the best of this author's knowledge, such approaches would not have allowed for the assessment of other parameters, for example slot position and width. Finally, as no aerofoil design procedure was to be undertaken, there was no requirement for the significantly faster run time of such viscid/inviscid solvers.

This Chapter continues by presenting a justification for using a two dimensional (sectional) modelling approach and then proceeds to describe the validation tests used to confirm the code's suitability for the task tackled within the course of this work. This includes a discussion of the problems encountered when attempting to use the available jet flap experimental data and the reasons for modelling a Coanda circulation aerofoil. Quantitative results are presented which confirm the code's suitability for the task.

It is intended that this chapter will present a brief but adequate overview of the code used, a convincing argument for the adequacy of two-dimensional modelling of CCAs in the light of the current design tools for wind turbines and, finally, evidence that the CFD code, E2D, is capable of accurately predicting the quantitative effect CC jets have on aerofoil performance coefficients.

4.2 EllipSys2D

E2D is an incompressible, multiblock, multigrid CFD code for solution of the Reynolds Averaged Navier Stokes (RANS) equations, based on the finite-volume methodology . In order to apply boundary conditions coincident with the geometry of the problem, E2D solves the discretised RANS equations on grids defined in a Body Fitted Coordinate (BFC) system. As such, the governing equations are transformed from a Cartesian form to a curvilinear coordinate system, this transformation being achieved by use of Jacobian matrices, resulting in a strong conservation form of the governing equations [93] [97]. It uses a co-located variable arrangement in order to minimise storage requirements for the variables and employs the interpolated cell face fluxes to prevent velocity-pressure decoupling in the manner of Rhie and Chow [98]. Under-relaxation of the discretised equations is carried out in the usual manner, in order to ensure computational stability and avoid solution divergence.

The multiblock grid approach allows for geometrically flexible body-fitted grids to be used in connection with a structured grid as well as enabling use of parallel processor architecture where required. For simple geometries such as a two-dimensional aerofoil in an unconfined external flow this is not particularly important but, as seen in the following Chapter where the flow upstream of the slot exit is modelled, when defining a grid for a more complex geometry it provides much needed flexibility. The rules for defining meshes compatible with the pre-processor, B2D, are fairly strict, in that any mesh must be decomposable into an arbitrary number of blocks, all of $n \times n$ cells, and each block must be fully coincident with its neighbours, i.e. grid lines are continuous across block faces, but this does help to produce a computationally efficient and transparent code. Communication between blocks is achieved using ghost cells which surround the periphery of each block and hold the current values of the variables in each neighbouring block's corresponding cells.

The multigrid facility provides an effective means of solution acceleration. The highest level mesh, as initially defined during the generation process, is taken as the finest mesh to be used (grid level 1) and a maximum of four progressively coarser grid levels (to grid level 5) may be employed, although two are often adequate. The grid coarsening is carried out such that two cells in each direction are merged to form a single cell on the next grid level.

Wall and inlet boundaries are defined as Dirichlet conditions with the no-slip condition applied to the velocity in the case of the wall. For outlet velocity boundaries the assumption of a near parabolic flow is made and a Neumann condition is applied with the gradient normal to the outlet boundary being set equal to zero. The cell face fluxes on the inlet and outlet boundaries are also used for mass balance to ensure global conservation of mass entering and exiting the domain. No adjustments are made for circulation present at the farfield boundaries in the case of aerofoil computations and solution independency checks have to be made in order to ensure that they are sufficiently far away from the aerofoil body.

A choice of interpolation schemes is available for the discretisation of the convective terms in the transport equations, although the Second Order Upwind Difference Scheme (SUDS) is consistently used in the simulations presented here. The first order Upwind Difference Scheme (UDS) is routinely applied to the interpolation of the turbulence variables while the Central Difference Scheme (CDS) is always applied to the interpolation of second order derivatives and the pressure gradient terms. The SIMPLE algorithm is used for pressure correction [99].

In all the simulations which are presented in the following chapters the $k-\omega$ SST turbulence model of Menter [100] is used. This is a variation of the $k-\omega$ model of Wilcox [101] developed particularly for flows with adverse pressure gradients, such as those experienced by aerofoils, which applies the $k-\omega$ model close to the surface of the body (in the sub layer and log-law region) while using a blending function to allow the model to change into the high Reynolds number $k-\epsilon$ model (transformed to a $k-\omega$ formulation) in the outer boundary layer and wake region and out into the freestream. This is said to remove the dependency of the solution on the freestream turbulence values used [100], although in conjunction with aerofoil computations with the E2D code this dependency was not found to be of any significance [102], and it is the SST adaptation which makes the model of use in aerofoil calculations. This further adaptation enforces Bradshaw's observation on the proportionality of the turbulent kinetic energy to the principal turbulent shear stress in the wake region of the boundary layer. This is achieved by means of a maximum value constraint placed on the turbulent viscosity. The net effect of this is to produce a turbulence model which is much more sensitive to the separation induced by adverse pressure gradients as it realistically constrains the value of the turbulent viscosity in the boundary layer in such situations and as such is well suited to aerofoil flows. It is suggested by Menter [100] that, for accurate resolution of the low Reynolds number region, the near wall grid should be constructed such that the distance from the first cell to the wall will correspond to values of y^+ less than 2. This has been adhered to in all the simulation results presented in this and the following chapter; y^+ is defined by Equation 4.1:

$$y^+ = \sqrt{\frac{\tau_w}{\rho}}\frac{\Delta y}{\nu} \tag{4.1}$$

where τ_w is the shear stress at the wall (calculated at the near wall cell node), Δy is the distance from the wall to the first cell node and other symbols have their usual meaning.

The suitability of this turbulence model for representation of the jet itself and the shear layers which form the interface between it and the external flow, is less clear.

No means of transition modelling is currently implemented in E2D, although both the Michel criteria and the Orr-Sommerfield equations have been tested with the code [103] and the former is currently in development [104]. As such the boundary layer is treated as fully turbulent along the entire surface of the aerofoil. This has been shown to lead to an over-prediction of the drag coefficient due to the increased skin friction and can lead to under-prediction of the lift coefficient at lower Reynolds numbers [103]. However, at the Reynolds numbers suitable for the purposes of this application (i.e. 3-6 million) this deficit in the physics being modelled should only lead to inaccuracies in respect to the drag. Even in this, however, relative variations in the pressure drag due to the presence of the jet should be valid.

The code is written in Fortran90 and has been supplied as source code, which has provided for changes to be made in order to include the additional jet parameters, by way of user defined inlet boundary conditions.

The hyperbolic grid generator, H2D, provides meshes possessing good orthogonality and mesh expansion rates for use with appropriate geometries, such as aerofoils. Variables which are user defined include a choice of C or O-mesh, the number of vertices and their distribution around the body, height of the first cell, tanh or sinh type cell expansion away from the body, extent of the domain, wake angle and wake contraction. Examples of the meshes used are presented in the course of this Chapter and the next.

4.3 Two-Dimensional Modelling

There are two primary reasons why two-dimensional CFD modelling of CCAs for wind turbines is considered sufficient for the purposes of this study. Firstly, the only engineering method available for the evaluation of wind turbine behaviour, both in terms of power output and structural response, is based on the blade element momentum theory (BEM). Thus, in order to assess the potential for

CCAs on HAWT blades, the only available tools are BEM codes and these use two dimensional aerofoil data as part of their primary input. Secondly, although a CFD code may fairly readily be used for two-dimensional aerofoil analysis, it is not at all a trivial matter to extend this to a rotating, three dimensional model. CFD modelling of wind turbine rotors is in a highly developmental stage at present [105] and, at least as far as the EllipSys3D code is concerned, can only be sensibly carried out on large, parallel processor work stations. Even with such hardware available, run times are on the order of 36 hours, running on 8 processors.

Further to the above points, it is known that over blade regions which experience a predominantly attached flow, BEM codes, used with appropriate two-dimensional data, yield good results [106] [107]. As it is also known, *a priori*, that circulation control devices do not extend an aerofoil's incidence operating range and are likely to be less effective in detached flow conditions, it is sensible to limit their installation on the blade to spanwise regions which experience attached flow under most operating conditions and the two-dimensional flow assumption of BEM is most valid.

The highly three-dimensional nature of circular jets in a crossflow is well documented [108] [109] [110], however, with a near continuous and long slot, the flow can, in the absence of any contradictory data and for the purpose of a first approximation, be considered two-dimensional. Clearly any requirements (e.g. manufacturing or structural) which necessitate the inclusion of small struts or the like to support the slot will interfere with the truly continuous nature of the slot and introduce an increased three-dimensionality to the jet/external flow interaction. This, however, is unquantified at present and may be best treated as an adjustment to the two-dimensionality of the flow, with the predictions made here adjusted for accordingly.

4.4 Validation of the Suitability of the Flow Solver and Turbulence Model

4.4.1 Jet Flap CCA

In order to validate the code it is necessary to have reasonably detailed data. This must include, at a minimum, global lift data over a range of operating conditions and surface pressure measurements for some of the corresponding operating conditions. Only one such data set exists for jet flap aerofoils; being that of the NGTE experiments [2] [3]; this presents global lift and drag data for a range of jet deflection angles, momentum coefficients and incidences as well as representative pressure profiles for the same, although only at zero incidence. Published results from the ONERA [5] [6] test program and others [7] only give global values. There is some later experimental work by Yuan [10], but as this uses effectively the same test equipment and techniques and claims good agreement with the work done at NGTE and the theoretical work based on it, there seems no need to consider the data in addition to the NGTE work.

Experimental data set

The quasi two-dimensional experimental investigation which was of 'an exploratory nature' [2] was conducted with a 12.5% thickness/chord ellipse with an aspect ratio of 1.5. The trailing edge, with a full-span blowing slot on the lower surface, was detachable so as to allow three different jet efflux angles (nominally 30°, 60°and 90°) to be studied. The slot height to chord ratio was nominally 0.00225. The model was fitted with 26 mid-span static pressure taps, 17 on the upper surface and 9 on the lower surface and the jet total pressure was recorded inside the model. The model was also mounted on a thrust/drag balance, the wind tunnel side walls being clamped to the model when taking readings from the pressure taps.

The momentum coefficient was determined (with the wind tunnel off) by aligning the aerofoil so that the jet efflux was horizontal, measuring the thrust from the balance and subtracting the integrated surface pressure readings (resolved parallel to the jet direction) from it. This was calibrated against the jet total pressure reading inside the aerofoil body. The efflux angle was determined visually with the use of wool tufts placed along the span.

The majority of the testing (and all that is considered here) was conducted at a chord based Reynolds number of $4.25x10^5$ and so transition effects were present. For the majority of the testing, trip wires were fitted at roughly 85% chord from the leading edge, although different configurations were tried, which had a marked effect on the surface pressures, as shown in Appendix 1.

CFD Predictions

An O-mesh is used which extends approximately 15 chord lengths from the aerofoil in all directions. There are two reasons for using an O-mesh rather than a C-mesh for these simulations. Firstly, a fixed wake angle behind the aerofoil does not exist in the same way as with a plain aerofoil, so the benefit of defining a wake cut angle as can be done with a C-mesh is not apparent. Secondly, in this instance, the shape of the trailing edge interacts more comfortably with an O-mesh than a C-mesh.

Mesh independency was achieved with 384 cells around the aerofoil and 128 cells defined in the direction normal to the surface (as can be seen in Figure 4.4). The surface vertices are highly concentrated in the trailing edge region, encompassing the slot position on the lower surface, and at the leading edge to a lesser extent; a typical cell distribution is shown in Figure 4.6 for the Coanda CCA model which is also representative of the grid used for the jet flap simulations. The distance of the first cell from the wall is $1x10^{-5}c$ and the farfield boundaries are approximately

15 chord lengths away from the aerofoil boundary in all directions. This distance was found to adequate and the change in lift coefficient with increasing distance is also shown in Figure 4.4.

The slot is defined as an inlet of the same dimensions as used experimentally and appropriate velocity and turbulence values (k and ω) are defined over the 24 cells which comprise it. It is impossible to know, *a priori*, what the turbulence intensity of the jet at the slot exit will be for a given configuration as this will be dependant on the upstream flow conditions in the duct etc. However, it is possible to set realistic upper and lower bounds on the value [111] and for this reason the jet turbulence intensity, I, defined by Equation 4.2, was varied between 1 and 6%.

$$I = \frac{u'}{\bar{U}} \tag{4.2}$$

where u' is the r.m.s. magnitude of the turbulent velocity fluctuations and $\bar{U}$ is the (appropriate) mean flow velocity (in this case that of the jet). Solutions were found to be virtually independent of the value used, although the convergence could be affected slightly. All results presented here use a value of 3% for I, unless otherwise stated.

Knowing the turbulence intensity, the turbulent inlet boundary conditions for the jet can be defined in terms of turbulent kinetic energy, k, and the rate of dissipation of this energy, ω, using Equations 4.3 and 4.4,

$$k = (U_{jet} \times I)^2 \tag{4.3}$$

and

$$\omega = \frac{\sqrt{k}}{C_{\mu}^{1/4} \times \kappa \times l} \tag{4.4}$$

where l is the characteristic length scale of the turbulence (defined in this instance by the slot dimension, δ), κ is the Von Karman constant $= 0.41$ and C_{μ} is a dimensionless empirical constant derived during the original turbulence model calibration process [101]= 0.09. This should not be confused with the momentum coefficient used elsewhere.

In all cases presented, the simulated jet velocity was defined with reference to Equation 2.1 and the desired value of C_{μ}.

Results

The CFD results presented below for the lift coefficient are for the total lift, that is, the pressure lift as deduced by the solver plus the direct lift component due to jet thrust given by Equation 4.5

$$C_{l_d} = C_{\mu} \sin(\tau + \alpha) \tag{4.5}$$

Agreement between simulated and experimentally derived results is generally poor and there is a fairly constant error for the global lift coefficient between $C_{\mu} = 0.1 - 0.5$, as shown in Figure 4.1.

The CFD results presented are the result of extensive variation of cell density and distribution and jet inlet boundary conditions and are believed to be final, that is, apart from attempting to model the actual experiment three-dimensionally (i.e. including tunnel walls etc.) this represents the best approximation that this solver and turbulence model will provide. Hence, if the discrepancy can be

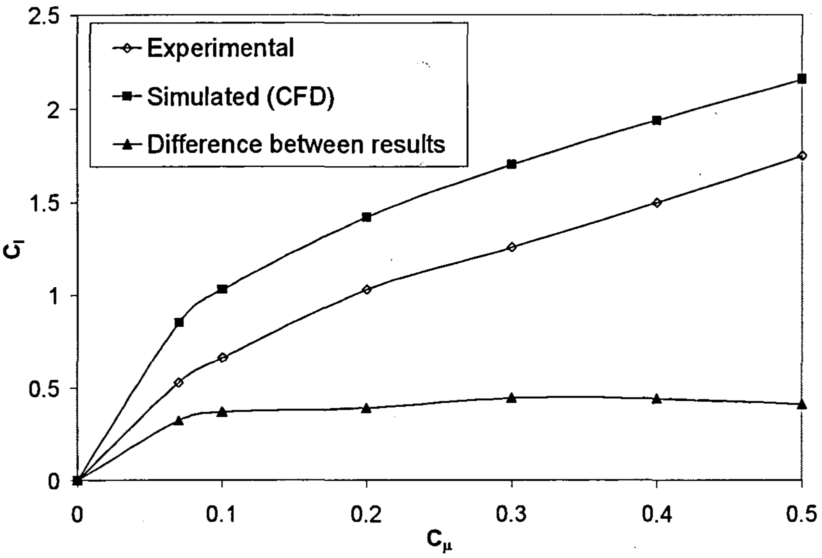

Figure 4.1: Experimental and CFD predicted lift coefficients for NGTE jet flap ellipse with jet deflection angle of 30 degrees (incidence=0 degrees)

argued to be due primarily to the poor quality of the experiment, the most likely cause of this is tunnel effects (most notably wall boundary layer separation and induced flow angles) with a second possible factor being incorrect quantification of the momentum flux exiting the slot. Greater insight into the possible cause of experimental inaccuracies (or modelling errors) can be gained by studying the pressure profiles for a range of momentum coefficients (C_μ=0.1, 0.2 and 0.3) as shown in Figures 4.2, 4.3 and 4.4 respectively. Also shown in the Figures is an attempt to match the pressure profile for a given momentum coefficient by adjusting the angle of attack to account for the induced flow effects which are thought to occur for reasons detailed later.

It is clearly seen that accounting for an induced angle produces a better agreement, at least over the forward portion of the aerofoil. The existence of a strong induced flow effect is indicated in the original pressure plots for C_μ=0.056, reproduced in Appendix 1, where the stagnation point is clearly seen to lie on the

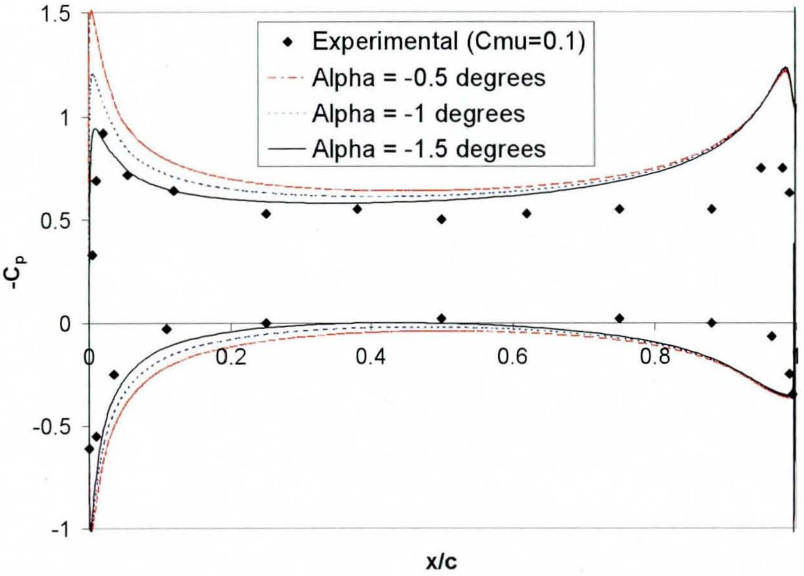

Figure 4.2: Experimental and predicted pressure profiles for NGTE jet flap ellipse (momentum coefficient=0.1, geometric angle of attack=0 degrees) showing effect of including various induced angles of attack in simulation

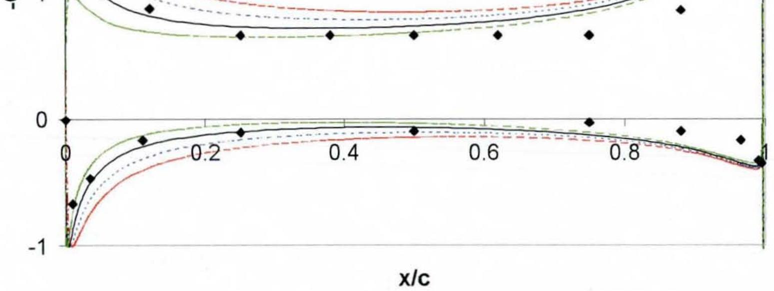

Figure 4.3: Experimental and predicted pressure profiles for NGTE jet flap ellipse (momentum coefficient=0.2, geometric angle of attack=0 degrees) showing effect of including various induced angles of attack in simulation

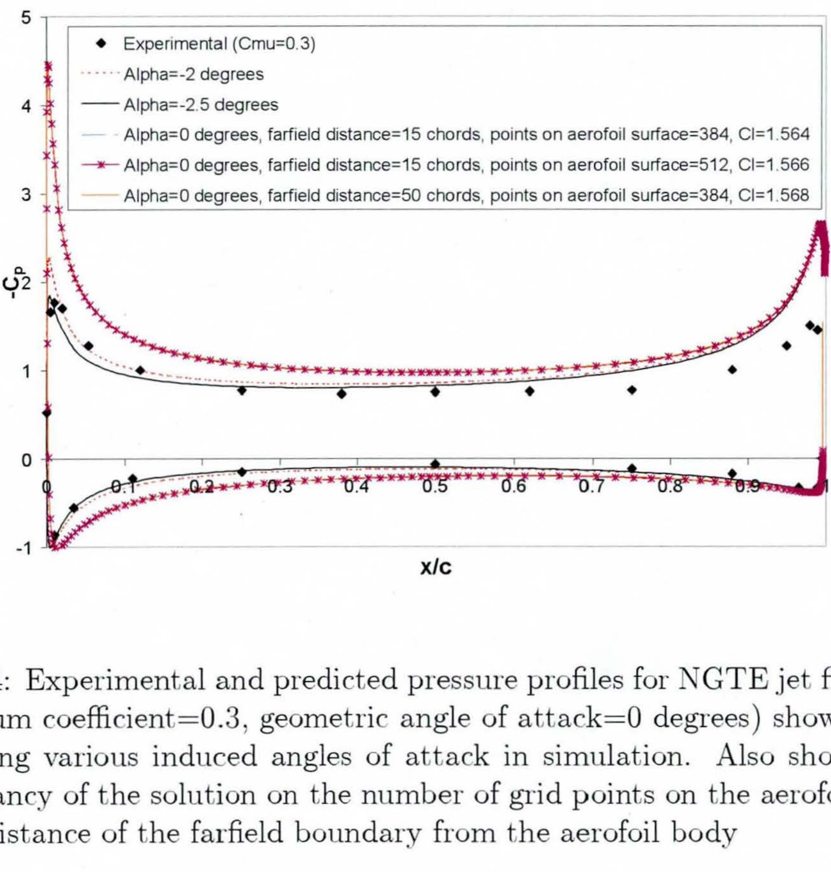

Figure 4.4: Experimental and predicted pressure profiles for NGTE jet flap ellipse (momentum coefficient=0.3, geometric angle of attack=0 degrees) showing effect of including various induced angles of attack in simulation. Also shown is the independancy of the solution on the number of grid points on the aerofoil surface and the distance of the farfield boundary from the aerofoil body

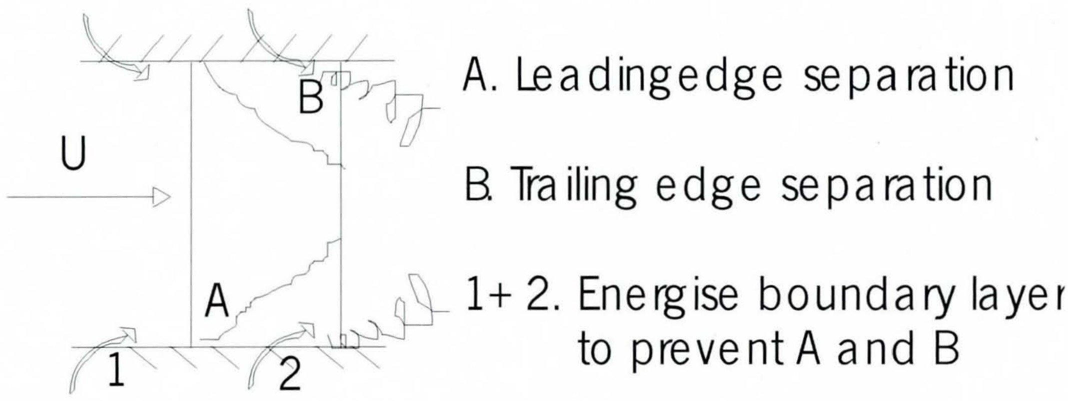

Figure 4.5: Schematic showing 2D aerofoil in wind tunnel with tunnel wall boundary layer energisation technique to prevent separation at leading and trailing edge adverse pressure gradients

upper surface, irrespective of the trip wire configuration used. A wall boundary separation mechanism particular to CCAs, by which a strong induced flow angle can be produced has been documented by Englar [112]. It occurs at the trailing edge by virtue of an interaction between the second adverse pressure gradient which exists on the profile and the tunnel wall boundary layer, and produces a shed vorticity and an induced flow angle in the much same way as a finite aspect ratio tip vortex does. This is shown in Figure 4.5 as the vorticity emanating from 'B'. Correcting for this with separate 'tip jets' where the trailing edge meets the tunnel wall has been shown to effect the lift by up to 15% [112].

For the C_μ=0.2 case, including an induced flow angle of 2 degrees gives a fairly good approximation of the conditions on the upper and lower surfaces over the first 50% of the chord, but as with all the results presented the upper surface pressure increasingly diverges from the experimental values over the rear 50% of the aerofoil. This pattern is common to the other two cases presented and it can also be seen that the induced angle tends to increase with C_μ as would be expected, although it is stressed that the angles presented (in solid lines) as being the closest to the experimental values are not intended to represent the exact induced angle to correct for experimental error. Unfortunately, due to the poor resolution provided by the small number pressure tappings it is impossible to attempt to define the induced angle by reference to the exact position of the stagnation point.

Of interest is the way in which, for each momentum coefficient, the simulated results converge at the suction peak at the trailing edge, at a value far removed from the experimentally derived one, independent of the induced angle used. The degree of error between the predicted and measured trailing edge suction peaks is 0.5, 0.8 and 1.1 respectively for Figures 4.2, 4.3 and 4.4, although proportional to the magnitude of the simulated suction peak, the error is 0.4 for all three momentum coefficients. This may be evidence of either a consistent over-prediction of the jet entrainment effect in the solver or the presence of another form of tunnel wall boundary layer separation described by Englar [112] and indicated in Figure 4.5. In this scenario, separation of the wall boundary layer occurs due to interaction with the leading edge adverse pressure gradient and then spreads across the span at an angle of 45° to the wall. When the small aspect ratio of the NGTE model is considered it is quite possible that this separation zone spreads across the entire span, reaching the centre-line pressure taps at around 75% chord - this is the region in which the experimental and simulated results are in greatest contradiction, after accounting for the presence of an induced flow angle.

4.4.2 Coanda CCA

Having established the lack of suitable data from jet flap experimental work, it was decided to look at more contemporary, Coanda CCA data. Fortunately, numerous two dimensional experimental studies have been carried out on Coanda CCAs, and these employ the greater understanding and improved testing methods developed [112] for wind tunnel testing of such devices. Also, partly due to the greater augmentation (as defined by Equation 2.4) displayed by this type of CCA, Coanda CCA data exists where more appropriate lower values of C_μ are employed. Despite the important difference in the designs, that is, the use of a jet expelled tangentially to the aerofoil surface rather than at some angle to it, it is felt that enough similarity exists between the two to make a case for its suitability as a means of code validation. Although the initial orientation of the Coanda jet is tangential to the aerofoil surface, it always interacts with the freestream at an angle after leaving the trailing edge, and the behaviour of the jet at this point should be fundamentally no different to one initially expelled at the same angle to the flow.

There are no data which allow for complete validation of the modelling presented in the next chapter, of jets aligned normal to the aerofoil surface at low and extremely low momentum coefficients and with jets expelled from the upper surface of a cambered aerofoil. However, the main experimental work presented in this section does include global lift results for aerofoils at negative angles of attack and since the sections tested were symmetrical about the chord line this does present a situation equivalent to negative jet deflection for a uncambered aerofoil. Also, as will be shown, Coanda CCAs exhibit an operational peculiarity, that is the reduction of the lift coefficient at extremely low momentum coefficients, for which one piece of data is known to exist [113]. This can be replicated by the code and as such is pertinent to the code validation, as well as the discussion on self pumping generated momentum coefficients and modelling of these extremely low momentum coefficients with jet flaps.

Experimental data set

The data used for validation here are from experimental work carried out by Englar in the course of a research program aimed at developing suitable sections for both sub-sonic and transonic applications for novel rotorcraft [34]. The quasi-two dimensional wind tunnel testing for the sub-sonic tests was conducted at a chord based Reynolds number between 5.2 and 5.5x10^5 and used two variants of the same 15% thick elliptic profile. Lift and pitching moments were defined with 53 mid-span static pressure taps and drag with a wake rake.

The first variant is a pure ellipse with a trailing edge radius to chord ratio (r/c) of 0.01125 and a tangential slot of height/chord ratio (h/c) equal to 0.00125 placed at 92.4% chord. The second variant uses the same basic profile, but with the elliptic trailing edge replaced by a blunter, rounded trailing edge ($r/c = 0.0403$); the slot height to chord ratio is reduced slightly due to the shortened chord ($h/c = 0.0013$) while the slot occurs at 96% chord.

Tunnel wall boundary layer control was provided by means of small tip jets fitted at the model trailing edge at either end of the aerofoil and regulated independently of the main CC slot, to prevent vortex shedding as previously described. The strength of the tip jets required to ensure two dimensional flow was adjusted for each operating condition, the correct strength being ascertained by trailing edge, spanwise pressure taps and visualisation at the wall/trailing edge interface with cotton tufts. Additionally, flow fences extending from 75% chord to 112.5% chord were placed between the tip jets and the main plenum to prevent inter-jet reaction. The experimental momentum coefficient was defined by measurement of the mass flow rate using an orifice plate in the main supply line, calculation of the jet velocity (assuming an isentropic expansion from the supply duct total pressure to freestream static pressure) and use of Equation 2.1.

Localised laminar separation bubble effects were detected under certain conditions, although the effect of Reynolds number variation was checked by preliminary runs in which the freestream velocity was increased to 2.75 times that used in the main testing program and found to be minor (a slight deviation was found

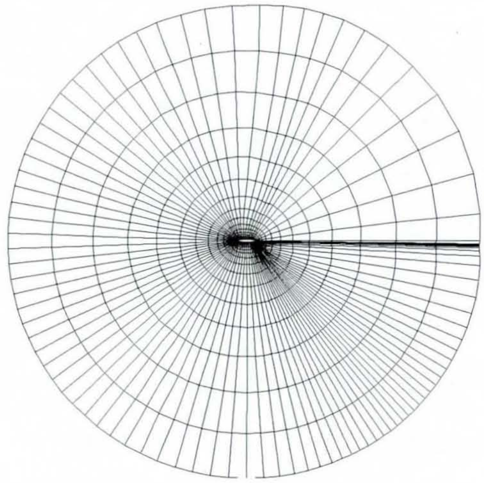

Figure 4.6: Mesh used for Coanda aerofoil simulations (cell density is reduced for clarity)

at the lowest momentum coefficients which diminished with increasing C_μ).

CFD model

The simulations of the two aerofoil variants were carried out on the O-meshes shown in Figures 4.6, 4.7 and 4.8, which show the entire mesh, a detail of the trailing edge for the ellipse and a detail of the slot region. It can be seen that for convenience in meshing the slot is placed on the lower surface. As the profile is symmetrical about the chordline (apart from the slot), it is straight forward to change the sign of the angle of attack and resulting forces. This should be remembered when viewing the subsequent plots.

Mesh independency was determined at a resolution of 384 cells around the aerofoil surface and 128 cells extending away from the body as shown in Figure 4.11. The farfield and outlet boundaries were placed at a distance of approximately 15 chord lengths from the aerofoil in all directions and the first cell height away

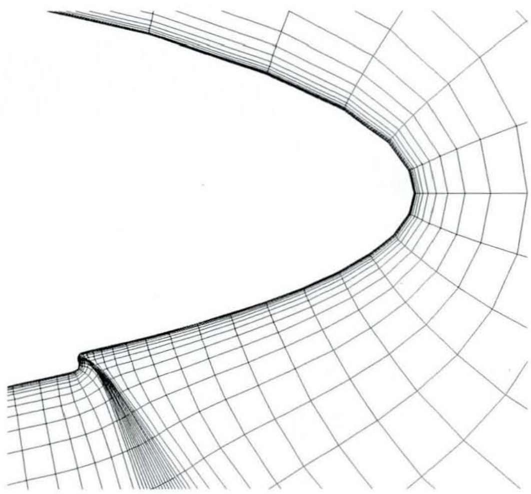

Figure 4.7: Detail of the trailing edge region of the mesh used for elliptic Coanda aerofoil simulations (cell density is reduced for clarity)

from the wall was defined as $1x10^{-5}c$. It can be seen in Figure 4.11 that the pressure coefficient values for a number of cells have been removed upstream and downstream of the slot because of the scatter or "wiggles" observed in the predictions at these points. The scatter is caused by a localised decoupling of the pressure and velocity fields; the magnitude of the scatter of the pressure values is most pronounced at the edges of the jet and is thought to occur as a result of using a central difference scheme in the interpolation of the pressure field [48]. Further grid refinement was tried in order to rid the solution of this phenomenon, as was defining a more realistic exit profile for the jet at the inlet boundary. However, neither approach produced a significant improvement and any variation in the magnitude of these "wiggles" did not appear to effect the solution elsewhere in the field.

The slot exit is represented by 32 cells and it can be seen that the region upstream of the slot and downstream of the jet both have a high mesh density. Also, it should

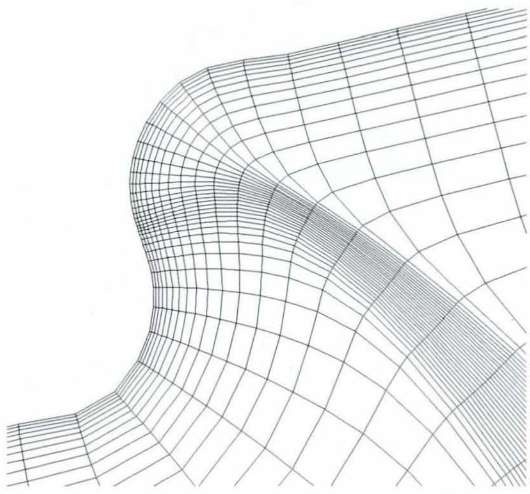

Figure 4.8: Detail of grid used for Coanda simulation showing slot (cell density is reduced for clarity)

be noted, there is some local rounding of the aerofoil surface above and below the slot in order to allow the smooth distribution of the cells on the aerofoil surface - this was minimised as far as possible and is not thought to have a significant effect on the flow around the aerofoil.

Results for the plain ellipse

The global lift coefficients determined experimentally and by simulation, for two momentum coefficients (0.015 and 0.073) are shown in Figure 4.9 and those for the drag at C_μ=0.073 in Figure 4.10. As before the direct component of the jet thrust has been added to the forces determined by the solver due to pressure and skin friction. For the lift coefficient this is as given in Equation 4.5 and for the drag coefficient this given by Equation 4.6

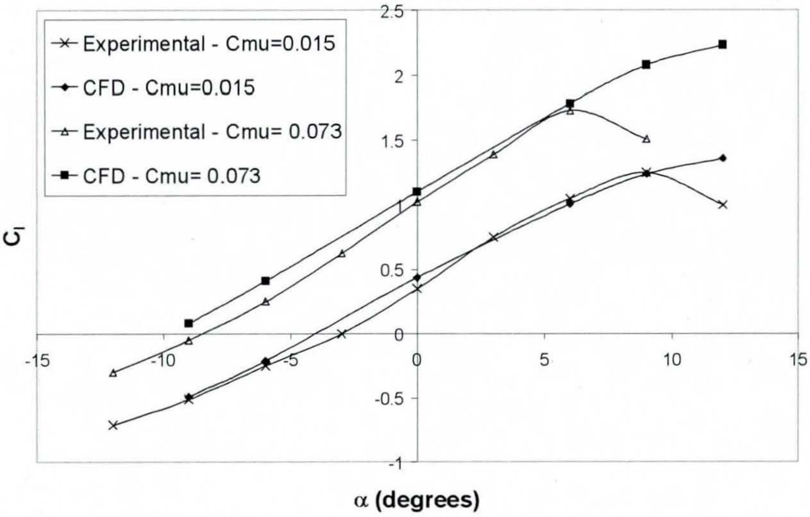

Figure 4.9: Predicted and experimental lift coefficients for plain Coanda ellipse (momentum coefficient=0.015 and 0.073)

$$C_{d_d} = C_\mu \cos(\tau + \alpha) \tag{4.6}$$

which for the tangentially expelled jet is clearly of greater significance.

There is generally excellent agreement between experimental and CFD results over the linear, attached flow region, although the CFD prediction produces lift coefficients slightly higher than that determined experimentally at negative incidences. However, the CFD code fails to predict the stall point and hence the upper limit to the lift enhancement caused by jet blowing for this geometry. It can be seen that at angles of attack higher than 6° and 9° for the respective momentum coefficients, the experimental lift falls away although not at a rate associated with complete leading edge separation. This is due to the formation of a leading edge laminar separation bubble occurring with increased C_μ or α, as indicated in Appendix 1, reproduced from [34], which would never be predicted when a fully turbulent boundary layer is assumed, as is the case here.

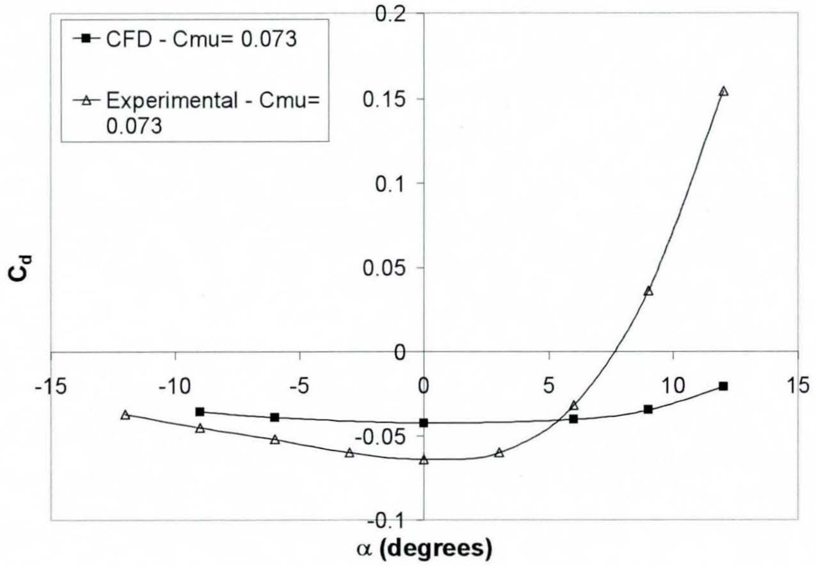

Figure 4.10: Predicted and experimental drag coefficients for plain Coanda ellipse (momentum coefficient = 0.073)

This is also seen in Figure 4.10 for the experimental drag coefficient which rises steeply after 6° as the flow starts to detach locally from the aerofoil surface. Note that the drag coefficient is generally negative; this is because of the direct thrust component from the jet rather than any significant alignment of the pressure field in the chordwise direction. There is also a notable over-prediction of the drag, not surprisingly caused by the lack of transition modelling and is consistent with previous results produced by the same solver for plain aerofoils [103], although the relative level of inaccuracy is less compared to an aerofoil with a sharp trailing edge due to the increased role of pressure drag compared to skin friction in the case of the ellipse.

The pressure profiles predicted by the solver at $C_\mu = 0.073$, $\alpha = 6°$ and $C_\mu = 0.071$, $\alpha = -6°$ are compared with those measured experimentally in Figures 4.11 and 4.12. Figure 4.11 also indicates the mesh independency determined at a resolution of 384×128 cells.

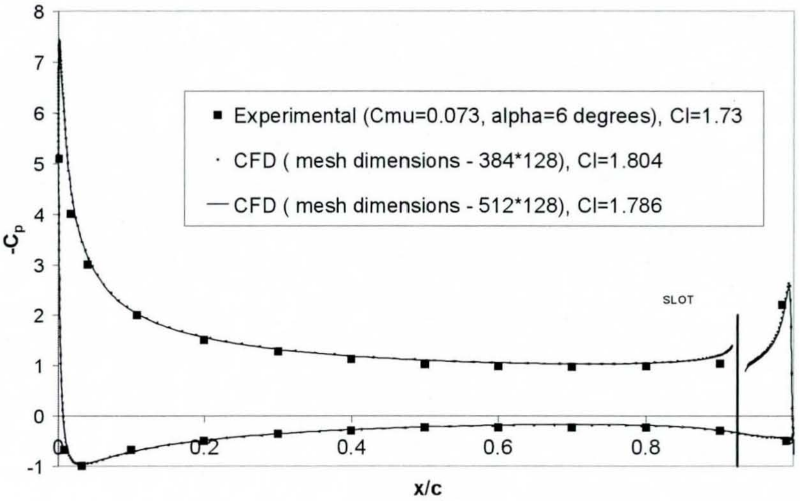

Figure 4.11: Predicted and experimental pressure profiles for plain Coanda ellipse (incidence = 6 degrees, momentum coefficient = 0.073). Also shown is mesh independancy.

The agreement for this detail of the solution is also seen to be extremely good, except for a slight under prediction of the suction pressure at the trailing edge and an over-prediction of the suction pressure at the leading edge. However, the disagreement should not be overstated and the results clearly show that the solver is correctly predicting not only the global lift coefficient, but also the detail of the flowfield around the aerofoil.

The accuracy of the CFD solution for the negative angle of attack is not as good as for the case with positive incidence, as is also seen in Figure 4.9 where the global values are shown. It would appear that the efficacy of the jet in producing lift in this situation is over-predicted and studying the surface pressure profiles it can be seen that this is predominantly due to the under-prediction of the pressure differential at the leading edge, indicating greater movement of the stagnation point from the upper to the lower surface than actually occurs. There is also an over-prediction of the suction on the upper surface on the rear portion of the aerofoil upstream of the slot as well as an under-estimation of the maximum

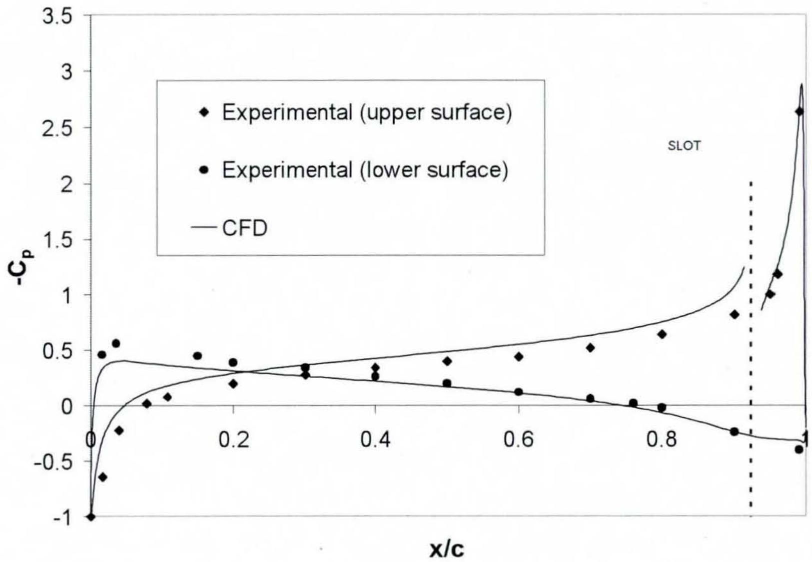

Figure 4.12: Predicted and experimental pressure profiles for plain Coanda ellipse (incidence = -6 degrees, momentum coefficient = 0.071).

suction over that portion of the aerofoil downstream of the jet as also occurs in the case of positive incidence.

Figures 4.13 and 4.14 show the streamlines at the trailing edge of the aerofoil for both the momentum coefficients presented in Figure 4.9. It can be seen that the point at which the jet leaves the trailing edge is almost independent of the momentum coefficient due to the small trailing edge radius and that the increase in lift is due to the degree of jet penetration into the freestream growing with C_{μ}.

Results for the rounded ellipse

The global lift coefficients determined experimentally and by simulation for the rounded ellipse at three momentum coefficients (0.01, 0.03 and 0.063) are shown in Figure 4.15.

The lift produced by this variant is greater than for the plain ellipse due to the larger trailing edge radius to chord ratio, allowing for greater jet deflection due to the Coanda effect. For the lower two momentum coefficients the solver consistently

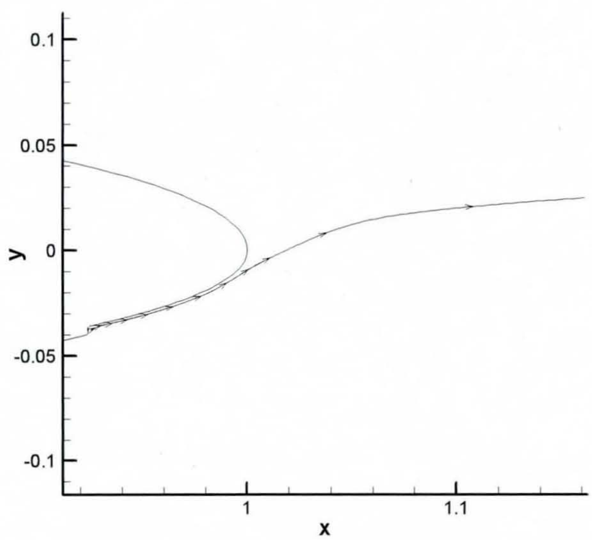

Figure 4.13: Streamlines at trailing edge of plain Coanda ellipse indicating jet path (momentum coefficient = 0.015)

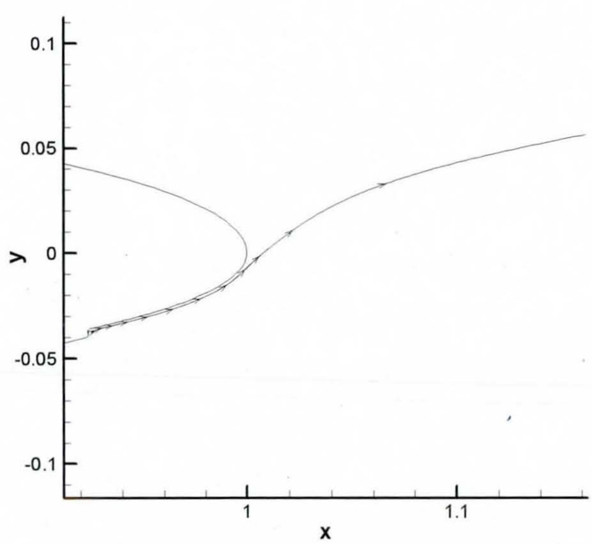

Figure 4.14: Streamlines at trailing edge of plain Coanda ellipse indicating jet path (momentum coefficient = 0.073)

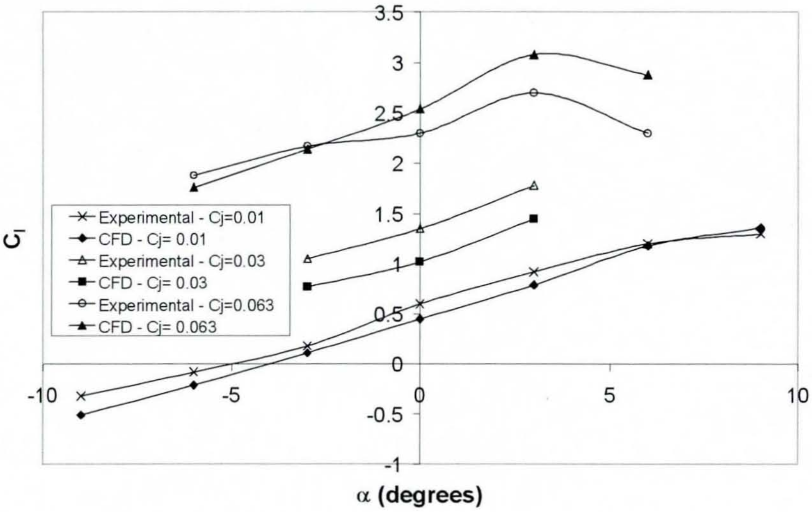

Figure 4.15: Predicted and experimental lift coefficients for rounded Coanda ellipse (momentum coefficient=0.01, 0.03 and 0.063)

under predicts the experimental lift coefficient and, presumably, the extent of jet attachment to the trailing edge. It is thought that the lowest C_μ shown probably represents a case rather like the plain ellipse where detachment is governed more by geometry rather than jet energy and, as such, the error is less than for the next higher value of C_μ considered. The increase in jet turning for the three momentum coefficients is shown in Figures 4.16, 4.17 and 4.18 (in all cases $\alpha = 0°$).

For the highest momentum coefficient presented for this case the lift is under-

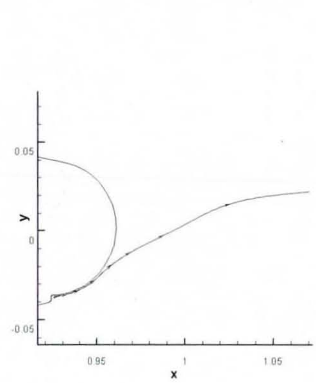

Figure 4.16: Streamlines at trailing edge of rounded Coanda ellipse indicating jet path (momentum coefficient = 0.01)

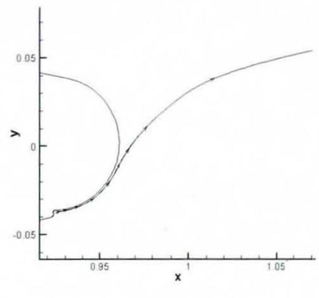

Figure 4.17: Streamlines at trailing edge of rounded Coanda ellipse indicating jet path (momentum coefficient = 0.03)

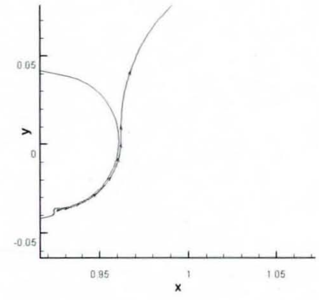

Figure 4.18: Streamlines at trailing edge of rounded Coanda ellipse indicating jet path (momentum coefficient = 0.063)

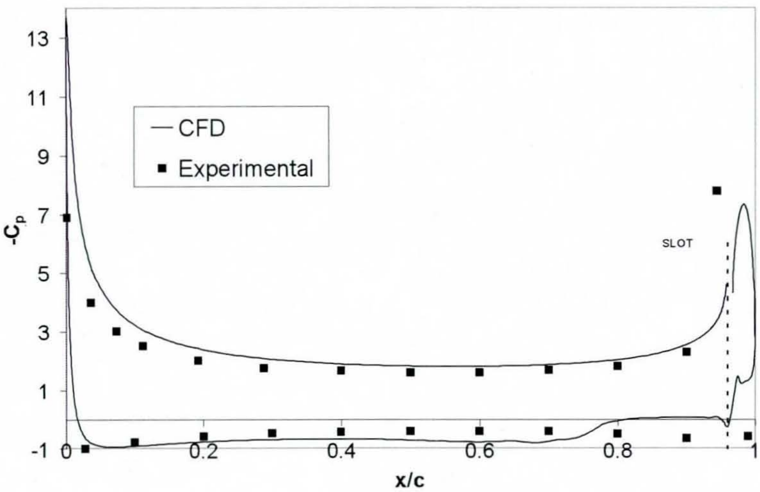

Figure 4.19: Predicted and experimental pressure profiles for rounded Coanda ellipse (incidence = 3 degrees, momentum coefficient = 0.063).

predicted at negative angles of attack and then highly over-predicted at zero incidence and at positive incidence. Only one relevant experimental pressure profile is given for this aerofoil in the original report; this is for the $C_\mu = 0.063$, $\alpha = 3^\circ$ case and is compared with the CFD result in Figure 4.19.

The leading edge suction peak is massively over-predicted, the peak value being nearly twice that determined experimentally, although this maybe at least in part due to the poor resolution of the experimental peak due to the density of the pressure taps. Other than that, the most striking feature is the low pressure region which appears along the lower surface from x/c=0.7. This is associated with a large separated region and an extremely high (and physically unrealistic for this momentum coefficient) degree of jet turning as can be seen in Figures 4.20 and 4.21 which depict the local boundary layer velocity profile, pressure field and streamlines.

The experimental and predicted drag coefficient is shown for the $C_\mu = 0.063$ case in Figure 4.22.

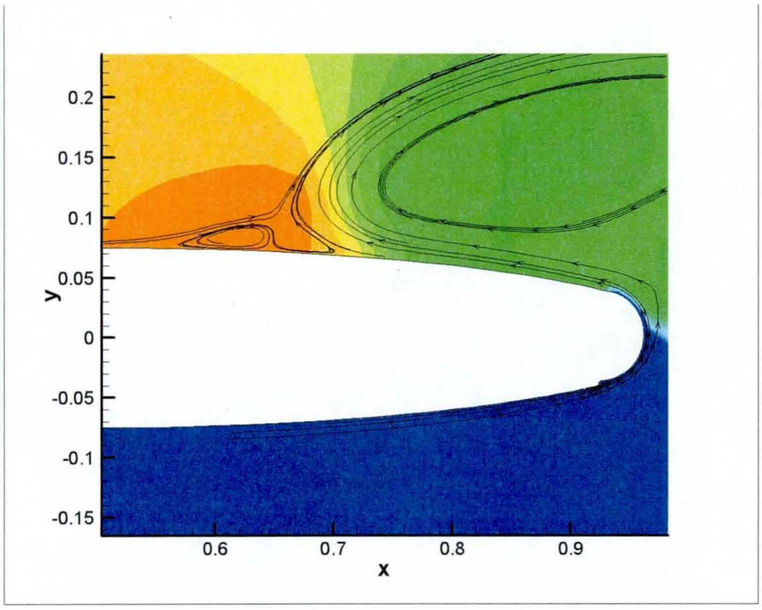

Figure 4.20: Pressure contours and streamlines of the predicted flowfield for the rounded Coanda ellipse (incidence = 3 degrees, momentum coefficient = 0.063

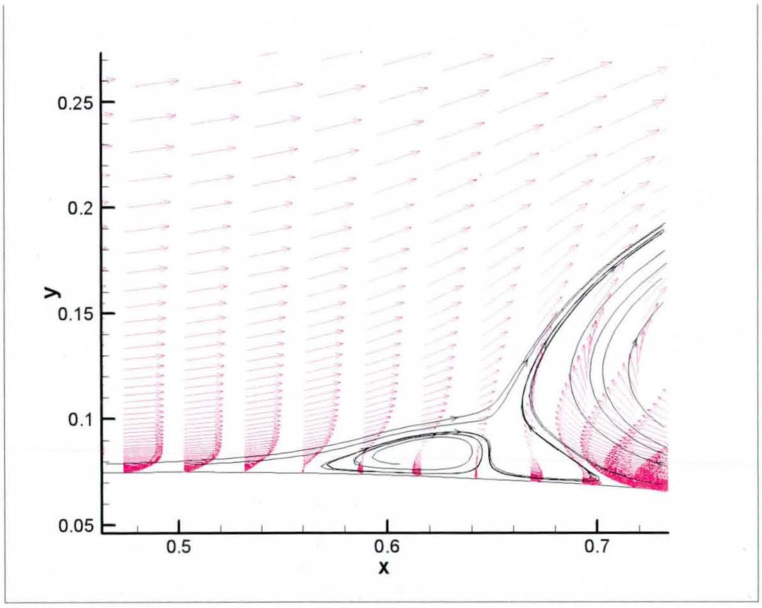

Figure 4.21: Detail of boundary layer and streamlines from the predicted flowfield for the rounded Coanda ellipse (incidence = 3 degrees, momentum coefficient = 0.063

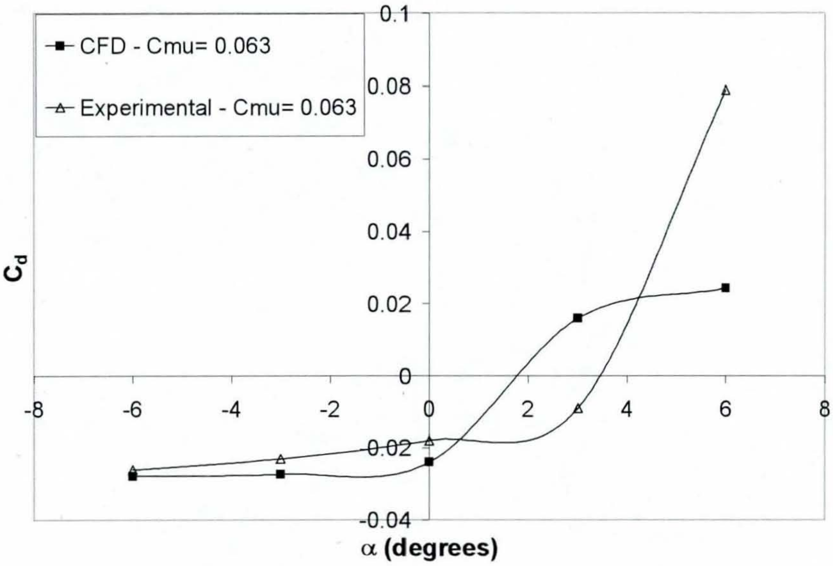

Figure 4.22: Predicted and experimental drag coefficients for rounded Coanda ellipse (momentum coefficient=0.063)

The drag produced by the rounded trailing edge is much higher than that of the ellipse and the agreement between the experimental and simulated results within the attached flow region is better than previously found. This is due to the increasing dominance of the pressure component of the drag and in this case the solver actually under-predicts the drag coefficient slightly.

Experimental data at extremely low momentum coefficients

Some time after the validation work was completed, an operational peculiarity of Coanda CCAs was brought to the author's attention [113] involving the reduction of the lift coefficient for such aerofoils at extremely low momentum coefficients. The only experimental evidence for the reduction known to the author is reproduced in Figure 4.23 and was obtained while testing a Coanda CCA with a height to chord ratio of 0.0021.

This particular experiment was set up within a wider testing program, specifically to try and detect any negative effects on lift enhancement which were suspected to

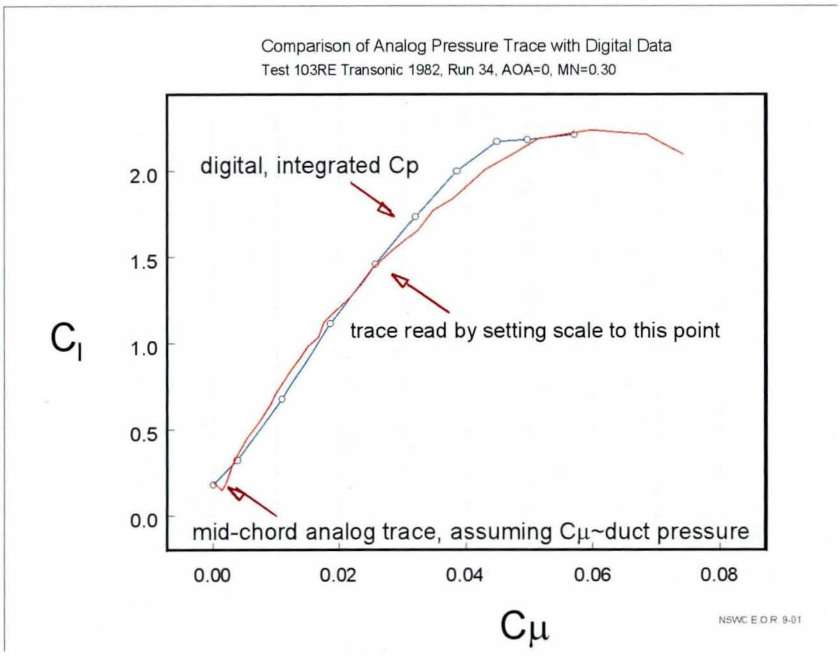

Figure 4.23: Experimental results showing reduction in lift coefficient for a Coanda CCA at extremely low momentum coefficients

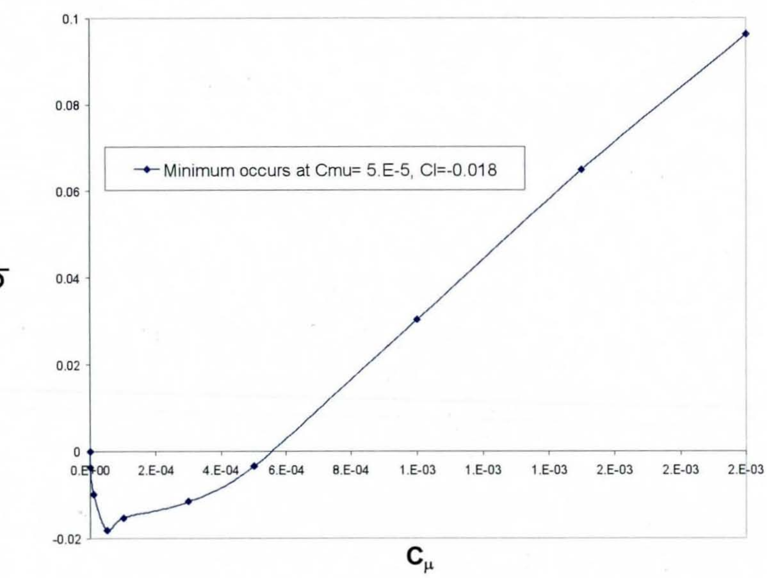

Figure 4.24: Predicted results showing reduction in lift coefficient for Coanda ellipse at extremely low momentum coefficients

exist at extremely low momentum coefficients, but had never been documented. As it had proved impossible to sustain low enough momentum coefficients over a time period adequate to acquire measurements reliably from the static pressure taps, the lift coefficients determined from integration of the static pressure taps were calibrated with respect to the mid-chord pressure differential at a higher C_μ. The time history of the mid-chord pressure differential was then recorded on an analogue plotter as the pressure in the aerofoil plenum chamber was increased from zero, allowing the effect of a continuous range of duct pressures to be measured and disclosing behaviour missed by the use of discrete point measurements.

The time-history revealed by the analogue plot of the rising momentum coefficient, clearly shows a drop in the lift coefficient as the duct is initially pressurised. This is of the order of 0.046 and occurred at an estimated momentum coefficient of 0.0014

As the exact geometry of the aerofoil used was not known, similarly low momentum coefficients were modelled with the elliptic profile previously used. The results of this are shown in Figure 4.24.

A similar trend is seen here as found experimentally, although they differ in quantitative detail. The reason for reduction in lift coefficient can be explained with reference to streamline plots of the flow at the trailing edge and in the slot vicinity. Figures 4.25-4.32 show the evolution of the flow as the momentum coefficient is increased from zero through C_μ=5x10^{-5}, 5x10^{-4} and 1x10^{-3}, representing the cases where ΔC_l=0, -0.018, -0.003 and +0.03 respectively.

Figures 4.25 and 4.26 show the region of separated flow that exists downstream of the slot, enclosed by the aerofoil surface and the bounding streamline in the external flow, and the recirculation caused by the blunt trailing edge when the aerofoil has no CC jet present. Figures 4.27 and 4.28 then show how the effective thickness of the aerofoil is increased as the low velocity jet (C_μ=5x10^{-5}) is expelled

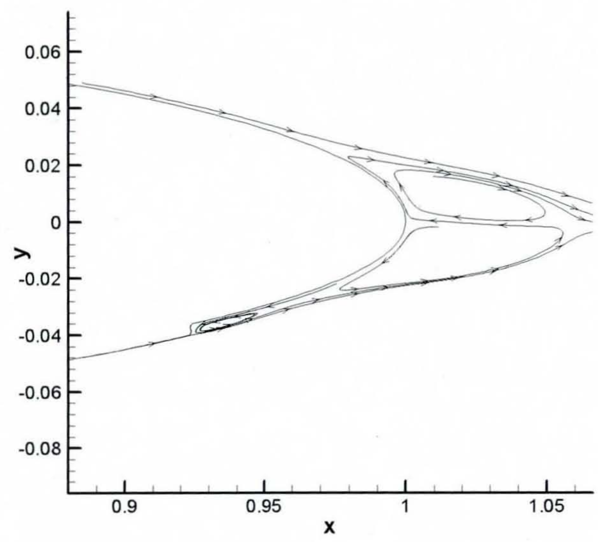

Figure 4.25: Streamlines at the trailing edge of Coanda ellipse (momentum coefficient = 0)

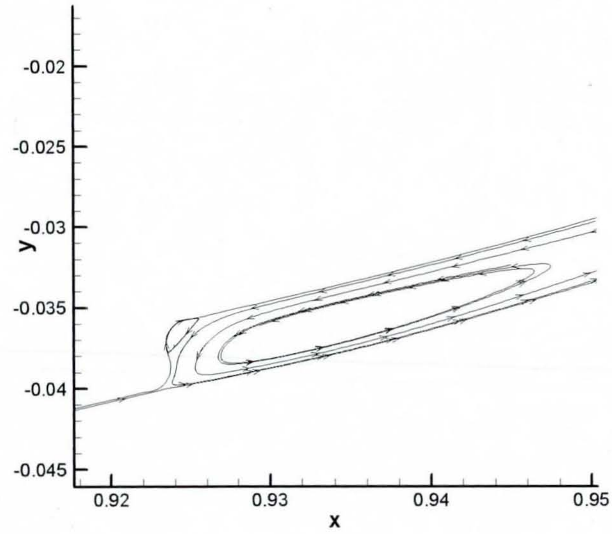

Figure 4.26: Streamlines in the slot region of Coanda ellipse (momentum coefficient = 0)

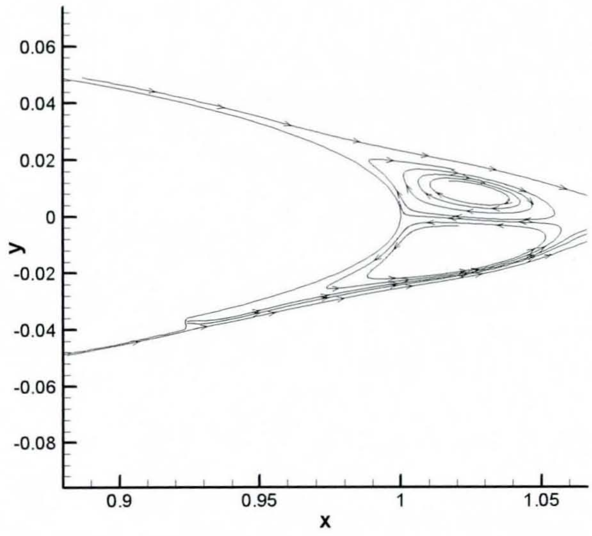

Figure 4.27: Streamlines at the trailing edge of Coanda ellipse (momentum coefficient = 5.E-5)

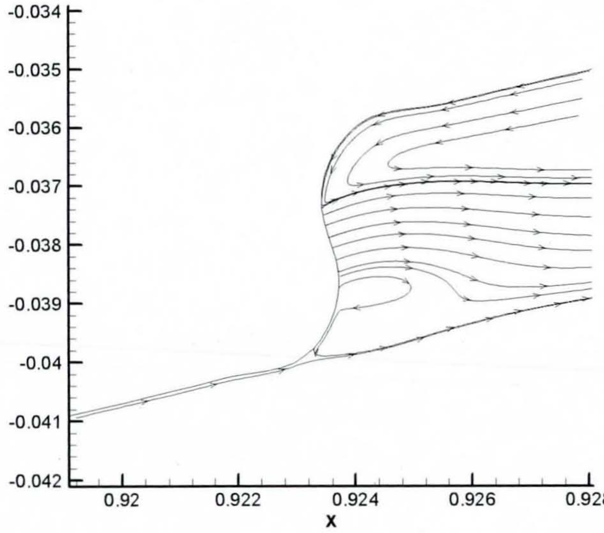

Figure 4.28: Streamlines in the slot region of Coanda ellipse (momentum coefficient = 5.E-5)

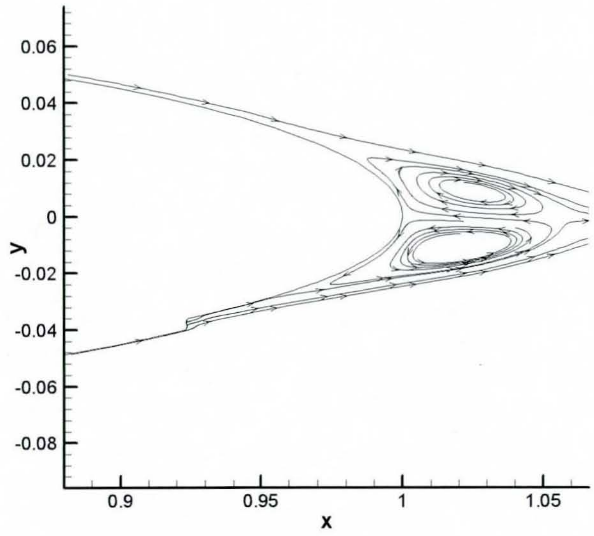

Figure 4.29: Streamlines at the trailing edge of Coanda ellipse (momentum coefficient = 5.E-4)

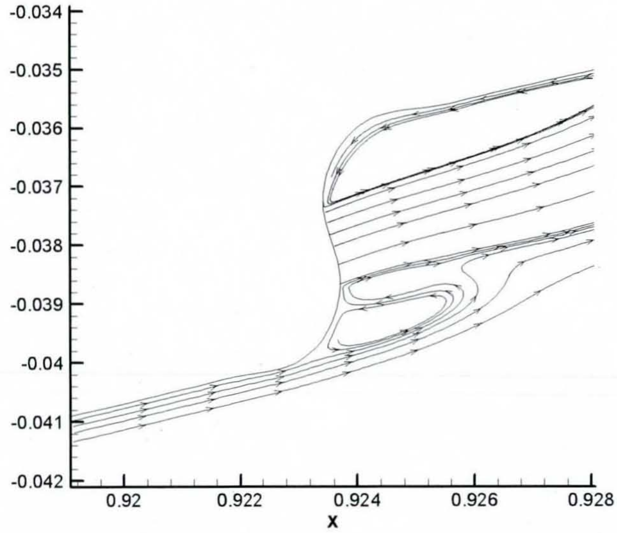

Figure 4.30: Streamlines in the slot region of Coanda ellipse (momentum coefficient = 5.E-4)

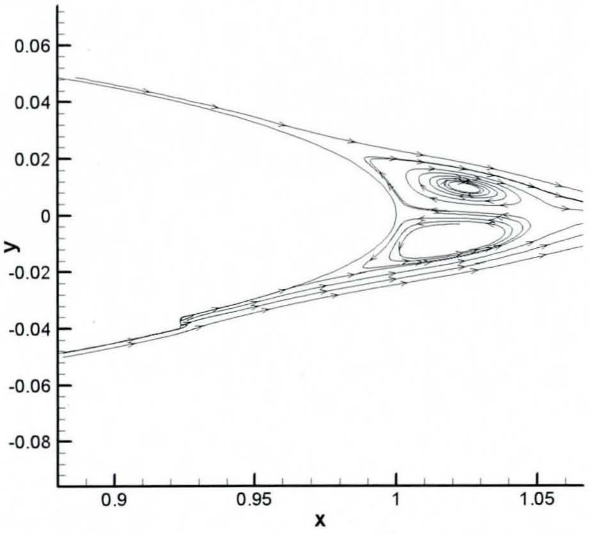

Figure 4.31: Streamlines at the trailing edge of Coanda ellipse (momentum coefficient = 1.E-3)

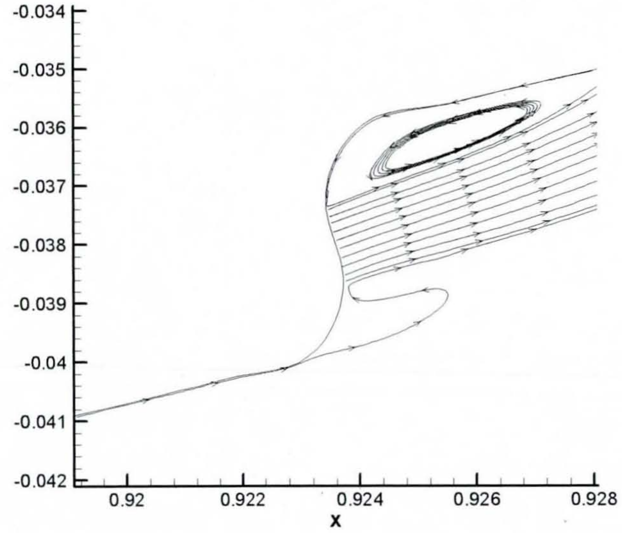

Figure 4.32: Streamlines in the slot region of Coanda ellipse (momentum coefficient = 1.E-3)

but is unable to maintain its initial orientation, becoming sandwiched between the recirculation close to the aerofoil and the external flow - this represents the case in which the negative lift is greatest. Finally, in Figures 4.29 and 4.30, and 4.31 and 4.32 we see how, with increasing velocity, the jet is able to leave the slot attached to the aerofoil wall, entrain the external flow, energising the boundary layer and start to have a positive effect on the lift coefficient. This affects the displacement of the boundary layer and can be most clearly seen at around the 97% chord point.

It is suggested here that the difference in the magnitude of the experimentally measured and CFD modelled negative lift coefficients is due to the increased h/c ratio of the aerofoil used in the experiment. Using a larger slot produces a jet with lower velocity and greater mass flux for a given C_μ thus injecting more low energy flow into the boundary layer at each given operating condition. It is also thought that the phenomenon is highly dependant on the precise slot and trailing edge geometry including both the unknown differences between the aerofoils used and the slightly approximate representation of the slot detail in the CFD model as described previously. Also, the experimental results are transient, while the simulated results are steady state.

4.5 Summary

- An introduction of the most relevant and important aspects of the CFD solver has been given.

- It has been argued in this chapter that two-dimensional modelling of CCAs is adequate for the purposes of this thesis, due to the intended use of the CCA sections on portions of a wind turbine blade least effected by rotational or wake effects.

- Experimental and simulated results have been presented for jet flap and Coanda circulation control aerofoils. It was found that there is serious disagreement between the experimental and modelled results in the case of the jet flap. However, it has been argued that this is due to the poor experimental quality of the data available. Further, it is concluded that, to the best of the author's knowledge, no reliable, high quality data exists for jet flap aerofoils suitable for CFD validation.

- However, such data does exist for Coanda CCAs and it has been shown that the solver is capable of predicting the effect of circulation control via blowing with jets in the case where the jet detachment point from the aerofoil is defined primarily by the geometry. It has been found that the solver predicts the correct trends for varying momentum coefficient and angle of attack, and that excellent quantitative agreement is found for results in the linear, attached flow region.

- It has also been found that the code is incapable of reliably predicting the detachment point of the wall jet under all the conditions simulated, in the case of a Coanda CCA with a trailing edge adequately round to make use of the Coanda effect. However, this does not present an impediment to the use of the code in the course of this thesis as, for reasons discussed in Chapter 3, it has been decided that jets expelled at an angle to the surface rather than tangential to it are more appropriate for wind turbine requirements.

- Finally, the code has been seen to be capable of predicting the occurrence of an operational peculiarity of Coanda CCAs, namely the production of negative lift at extremely low momentum coefficients, and insight has been gained into the mechanism by which this occurs. As well as being of general interest this is thought to be relevant to the modelling work which follows in the next Chapter.

Chapter 5

CFD Investigation of Aerofoil Suitability

5.1 Introduction

Three aerofoil types have been investigated with the CFD solver E2D for their suitability for use with circulation control jets. These are the FX77w153, the NACA 4415 and five members of the NACA 63xxx family, in particular the 63415. All three aerofoils have been used on large wind turbines at sometime, although none are considered state of the art HAWT aerofoils such as those developed at Risoe [114], although the FX77w153 was designed specifically for use on wind turbine blades. However, all three do have distinct characteristics, described later, which make them appropriate choices for this study.

The characteristics of all the aerofoils in their unmodified or 'plain' configuration, have been simulated under steady state conditions, over the attached flow and light stall regions. These results are compared with experimental data from various sources, before further modelling is carried out with circulation control jets added. The variation effected in the lift and drag coefficients, over an appropriate range of angle of attack and momentum coefficients, is presented for all three aerofoils, and the results of altering various jet parameters such as slot size, slot position and jet efflux angle are also explored. Results from simulations under similar conditions are presented for all the aerofoils in order to carry out a comparative study of their behaviour and the similarity to the physics of a Gurney flap is described. Finally, results are also provided for the FX77w153 under conditions representing low and extremely low (non-passive and passive) blowing conditions, using an extension to the mesh, which allows the region upstream of the jet exit slot on the profile surface to be included within the computational domain. Throughout, surface pressures and flowfield predictions from the simulations are used to determine a better understanding of how CCA jets produce changes in aerofoil circulation.

5.2 FX77w153

The FX77w153 was developed specifically for use with wind turbines, its primary feature in this respect being its high lift to drag ratio.(149 at 8.2° incidence). This is achieved by minimising skin friction drag by delaying boundary layer transition from laminar to turbulent at the leading edge - the gentle curvature of the leading edge and the (relatively) rearward position of the maximum thickness, keeps the location of the position of minimum pressure well aft. Having said this, it should be made clear that the appropriate Reynolds number of 4 million (with respect to the perceived end operating conditions - span position, chord, rotational speed) is high enough to avoid the serious margin of error for lift coefficient that can occur without transition modelling of such an aerofoil [103] [104]; drag, however, will be over-predicted. The pressure surface is almost completely flat and the trailing edge is almost symmetrical about the chordline, as can be seen in Figure 5.1. Although designed for use with wind turbines it should be said that it is

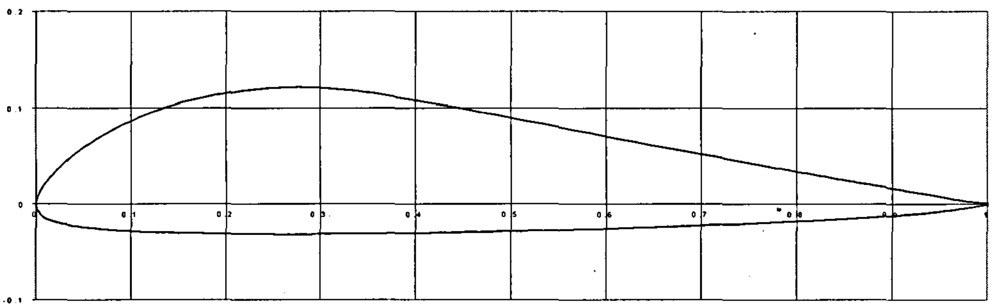

Figure 5.1: FX77w153 profile

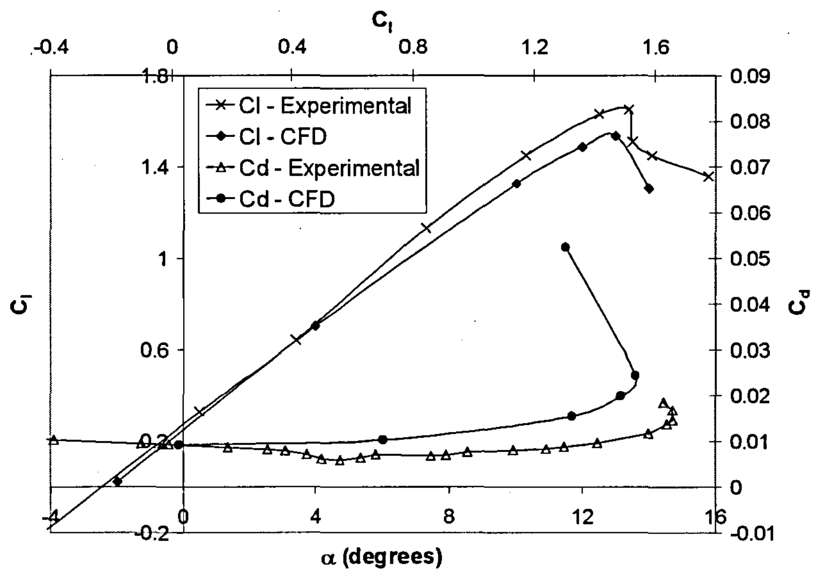

Figure 5.2: Predicted and experimental lift and drag coefficients for FX77w153

not representative of modern aerofoils used on pitch or stall controlled HAWTs, having a particularly sharp post stall lift reduction, as can be seen in Figure 5.2. The characteristics of the plain aerofoil as determined from wind tunnel testing [115] and simulation are shown in Figure 5.2. Note that the drag coefficient is plotted against the lift coefficient, rather than the angle of attack.

The agreement between simulated and experimental results is generally very good for the lift coefficient, although there is some disparity at higher angles of attack where the $C_l - \alpha$ slope changes; in this region the lift coefficient is very slightly under-predicted. The stall point is accurately predicted, even though the maximum C_l value is lower than measured and the modelled drop in lift at stall is less pronounced, probably due to the fact that the experimental curve indicates a sudden leading edge separation. Drag is over-predicted (as expected) due to the increased skin friction present with the turbulent boundary layer, although the trend of the drag evolution with incidence is well replicated. As discussed in the previous Chapter, this inaccuracy does not adversely effect the validity of the results with respect to changes made to the drag coefficient by the addition of circulation control jets.

The predicted characteristics were determined using an O-mesh, as will be used in the cases where upper or lower surface jets are present. Although the baseline (plain) aerofoil characteristics could have been solved on C-meshes (which have more suitable properties for this problem), this was not done. Rather, due to the relative nature of the study (i.e. the plain aerofoil lift and drag values act as a baseline value for the enhancements produced by the jets), it was thought that using grids of a similar type for all cases would help reduce the amount of variation in the numerical error present between different cases. The mesh at the aerofoil surface is shown in Figure 5.3 and this is representative of the grids used for the other aerofoils presented in this Chapter.

The mesh dimensions are 288x96 for the unblown simulations and 384x96 in the simulations with CC jets, mesh independency at this level having been determined for all the aerofoils modelled in this Chapter at these resolutions, as indicated by a representative selection of pressure profiles given in Appendix 2. The additional points in the CCA simulations are, of course, concentrated in the slot vicinity, typically resulting in the region around the slot (which will include the jet shear layers) having approximately 60 cells, the slot itself being represented by 12 cells for cases where $\delta/c = 0.0027$. The surface pressure plots showing mesh indepen-

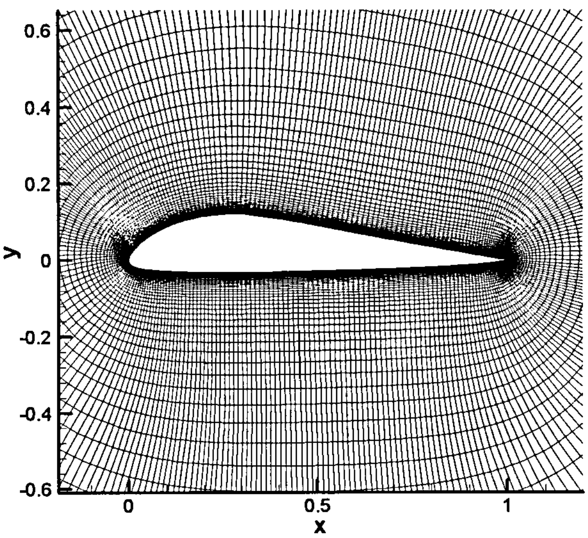

Figure 5.3: General mesh distribution for FX77w153

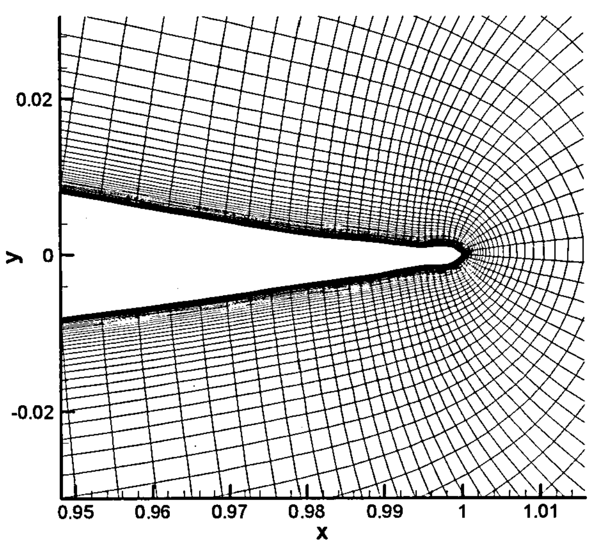

Figure 5.4: Trailing edge detail of mesh used for plain FX77w153

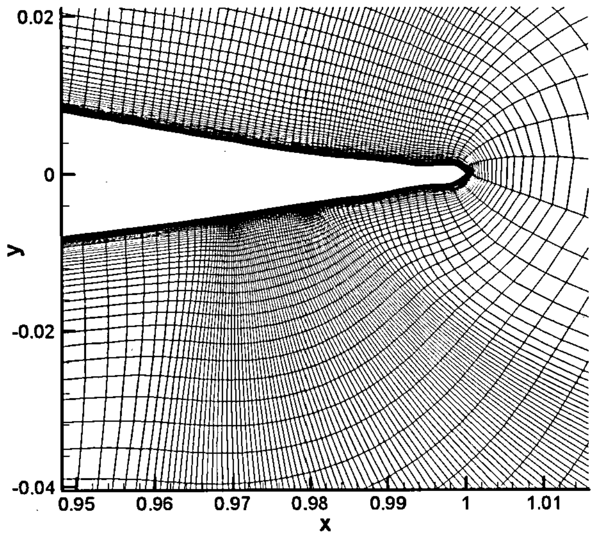

Figure 5.5: Trailing edge detail of mesh used for FX77w153CCA with positive jet

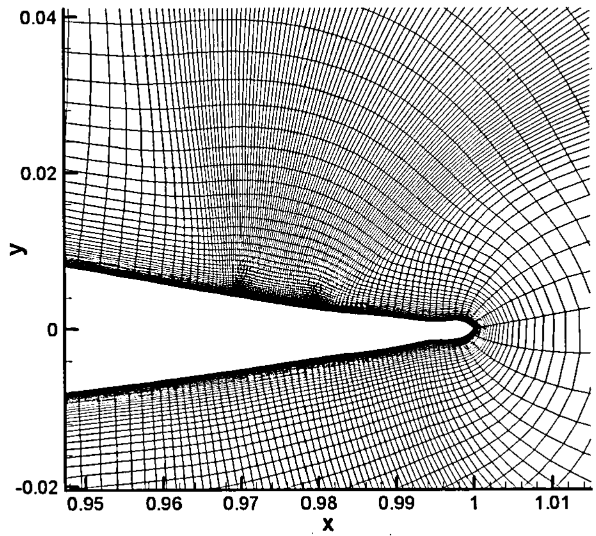

Figure 5.6: Trailing edge detail of mesh used for FX77w153 CCA with negative jet

dency in Appendix 2, include increasing the number of cells representing the slot to 16, indicating that 12 cells are enough to capture adequate detail of the jet for the purpose of this study. In all cases the first cell height is approximately 1×10^{-5}c, an appropriate dimension to ensure appropriate y^+ values (<2), over the entire aerofoil surface under all conditions. The distribution and number of cells at the trailing edge used for the plain aerofoil and CCA simulations can be seen in Figures 5.4, 5.5 and 5.6, showing the meshes used for this aerofoil without a jet, with a positive jet and with a negative jet, respectively. The areas of high mesh density at and around the jet inlet positions are clearly seen, in these cases the jet is located in the 97-98% chord region and, again, these are representative of the meshes used for the other aerofoils.

Defining circulation control jets at nominally 97% chord, independently on the upper and lower surfaces, of dimension $\delta/c = 0.0027$ and deflection angles normal to the aerofoil surface ($+82°$ and $-80°$ respectively), produces the incremental changes in lift and drag seen in Figures 5.7 and 5.8, when using $C_\mu = 0.01$. The ΔC_l and ΔC_d values are defined as the difference between the simulated results for the plain and CC aerofoils, due to changes in the surface pressure and skin friction (although the latter is negligible in all cases).

Substantial changes are made to the lift and drag coefficients by the presence of CC jets, even at the modest momentum coefficient shown here. The pressure-based nature of the change in the drag coefficient has been confirmed by the fact that no substantial change is made to the skin friction drag in any of the cases studied. It can be seen that a drag reduction (albeit of a lower magnitude than that produced with positive jet deflection at higher incidence) is also exhibited with a negative jet, at least below incidences of approximately 11°. The changes made to the pressure field and the movement of the stagnation point, relative to the flowfield depicted in Figure 5.9 for the plain aerofoil case, are clearly shown

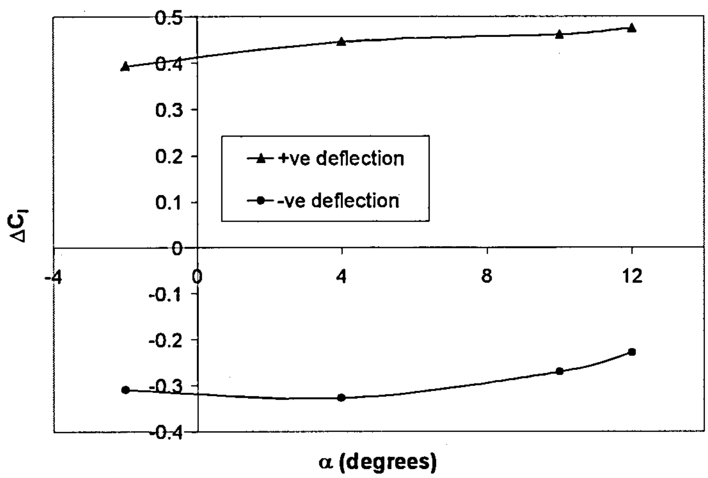

Figure 5.7: Change in lift coefficient for FX77w153 with positive and negative CC jets (momentum coefficient=0.01)

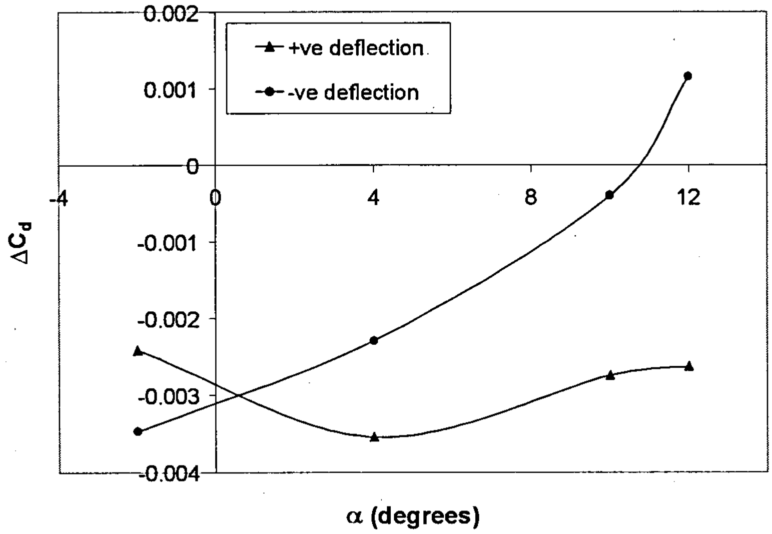

Figure 5.8: Change in drag coefficient for FX77w153 with positive and negative CC jets (momentum coefficient=0.01)

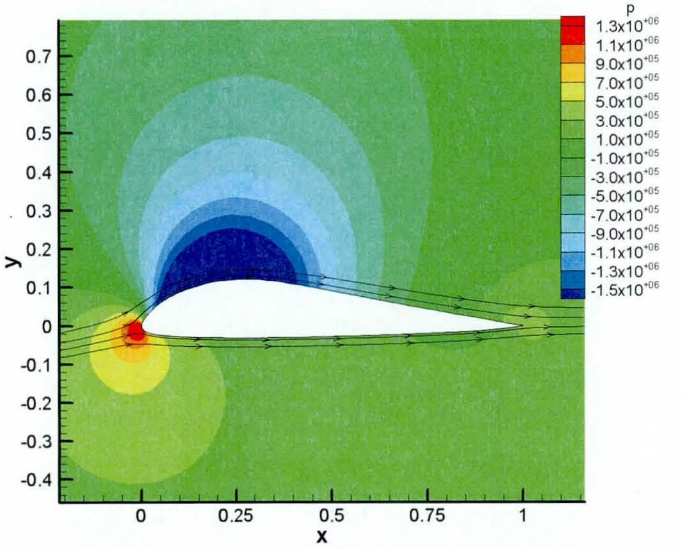

Figure 5.9: Pressure field and streamlines for the FX77w153 at an angle of attack of 4 degrees

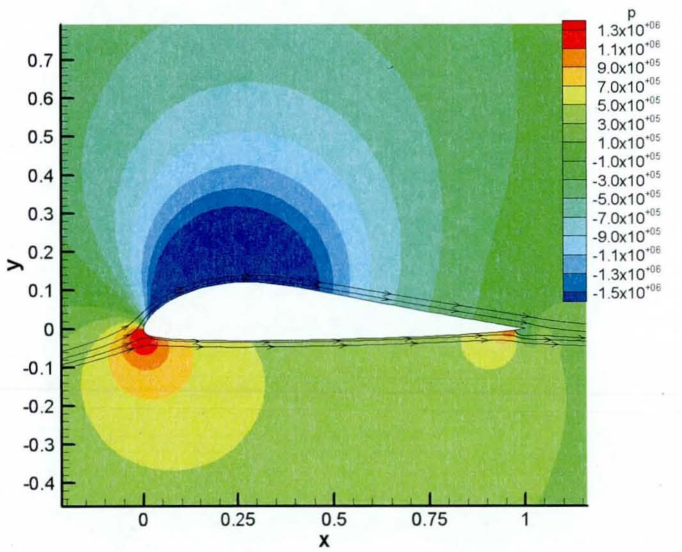

Figure 5.10: Pressure field and streamlines for the FX77w153 CCA with positive jet at a momentum coefficient of 0.01 and angle of attack of 4 degrees

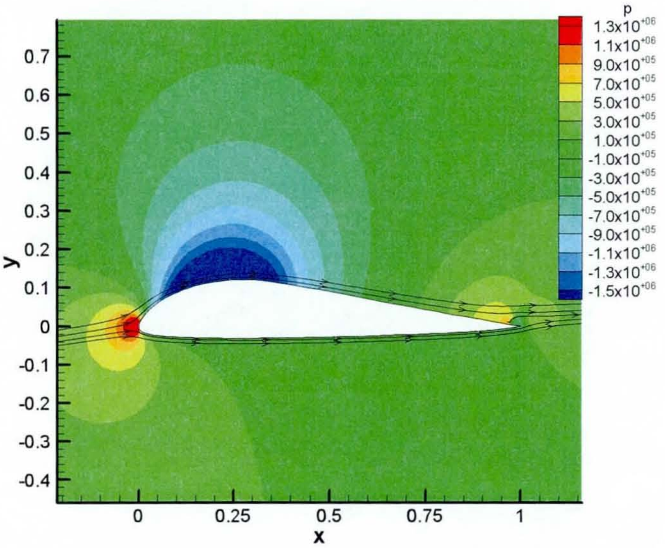

Figure 5.11: Pressure field and streamlines for the FX77w153 CCA with negative jet at a momentum coefficient of 0.01 and angle of attack of 4 degrees

in Figures 5.10 and 5.11 for the $C_\mu = 0.01$, $\alpha = 4°$ case.

5.2.1 Negative/Positive Jet Disparity

It can be seen that the lift enhancement gained with the presence of a positively deflected jet is greater than the lift reduction provided by the negative jet; at $\alpha = 4°$. The lower surface jet produces a 39% increase in lift coefficient compared to the plain aerofoil value, while that on the upper surface yields a decrease of 28% at $C_\mu = 0.01$, or in more appropriate terms, the respective gain values (as defined previously by Equation 2.3) are 46 and -34. This disparity extends across a wide range of momentum coefficients as indicated in Figure 5.12 which shows the ΔC_l values at $\alpha = 4°$ for $C_\mu = 0 - 0.03$. It is noted that the results for values of $C_\mu < 0.01$ come from the FX77w153 model with mesh extension presented in Section 6.5.

Plotting ΔC_l against $\sqrt{C_\mu}$ (not shown here) and providing linear curve fits to the

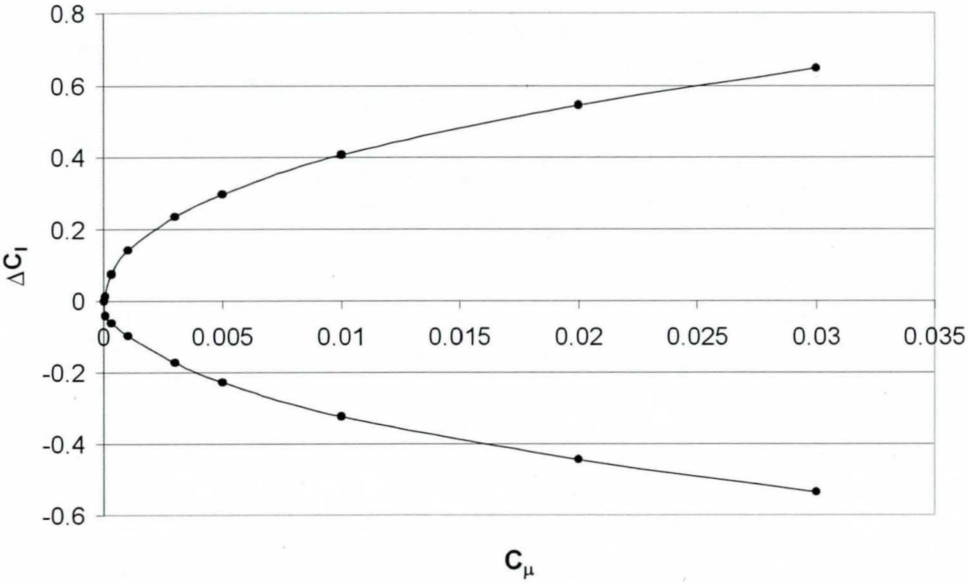

Figure 5.12: Positive and negative lift increment for FX77w153 CCA at an incidence of 4 degrees (momentum coefficient=0-0.03)

slopes of the negative and positive jet results independently, provides the following approximate relationships (Equations 5.1 and 5.2). For reasons explained in Section 5.5, values of $C_\mu < 5 \times 10^{-5}$ have been excluded.

$$\Delta C_{l\,\text{positive}\,jet} \approx 3.93\sqrt{C_\mu}.\sin\tau \tag{5.1}$$

$$\Delta C_{l\,\text{negative}\,jet} \approx -3.19\sqrt{C_\mu}.\sin\tau \tag{5.2}$$

As the jet acts primarily in the boundary layer at the low momentum coefficients where high augmentation values are possible and it is known *a priori* that the suction and pressure surface boundary layers on an aerofoil are significantly different in most instances, it is the interaction of the jet and boundary layers which

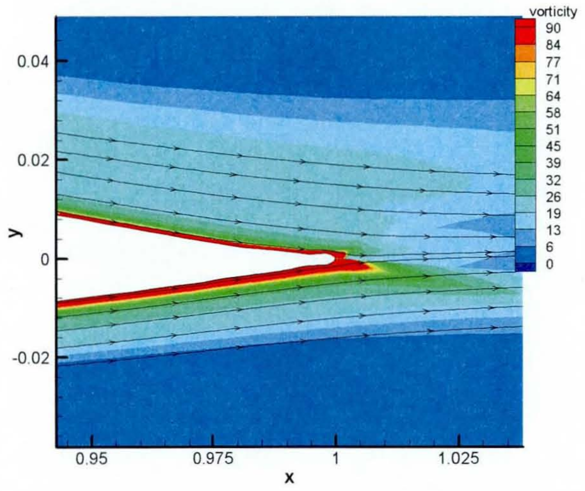

Figure 5.13: Vorticity at the trailing edge of plain FX77w153 (incidence=4 degrees)

is examined in the following Figures to explain this disparity. The extent of the boundary layers on the FX77w153 aerofoil at 4° angle of attack is visualised in Figure 5.13 by calculating the magnitude of the absolute vorticity in the flow field around the aerofoil. Although this means of visualisation is not exact (the precise location of the boundary layer edge can be 'shifted' slightly by altering the scale and range used), it is perfectly adequate for comparative purposes and the outer edge of the boundary layer can be said to occur when the vorticity equals zero. Note that the scale used is consistent in all three of the cases presented.

It is clear that the upper and lower surface boundary layers are quite different. The upper surface has a boundary layer more than twice the thickness of that on the lower surface, due to the adverse pressure gradient it has experienced. The effect that the positive and negative CC jets with $C_\mu = 0.01$ have on the boundary layer can be seen in Figures 5.14 and 5.15 respectively (in all cases the angle of attack is 4°).

In both cases the presence of the jet adds energy to the boundary layer into which

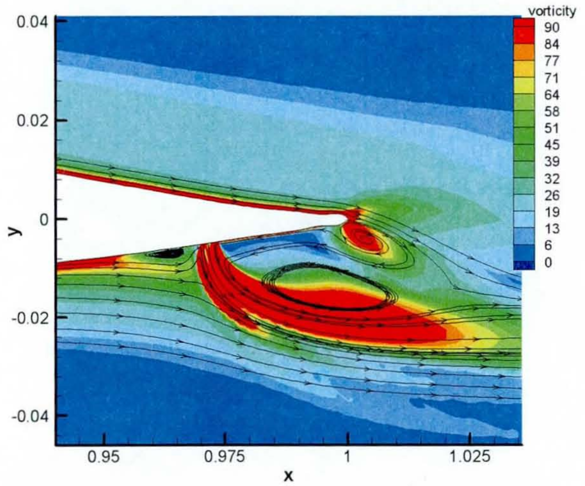

Figure 5.14: Vorticity and streamlines at the trailing edge of FX77w153 CCA with positive jet, momentum coefficient=0.01 (incidence=4 degrees)

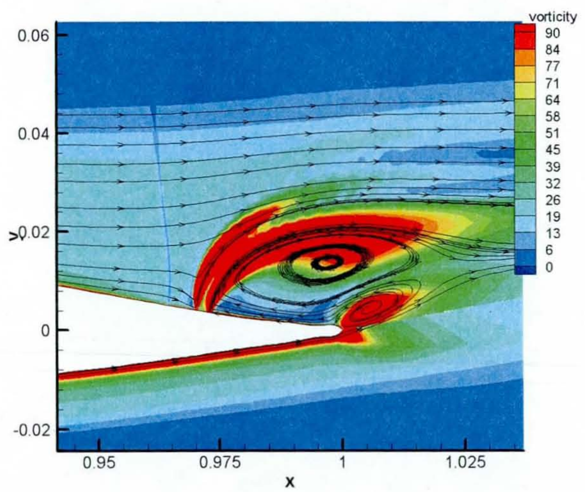

Figure 5.15: Vorticity and streamlines at the trailing edge of FX77w153 CCA with negative jet, momentum coefficient=0.01 (incidence=4 degrees)

it enters, as well as increasing its thickness. However, the displacement of the boundary layer on the side on which the jet is present is much greater in the case of the positively deflected jet and comparing Figures 5.13 and 5.14 closely, it can be seen that the positive jet also causes a slight thinning of the upper surface boundary layer. In the case of the negatively deflected jet, there is an almost imperceptible amount of thinning on the lower surface while the upper surface boundary layer clearly accommodates the jet with little change to itself, even though the jet penetration is greater in the case of the negatively deflected jet. As the displacement thickness of the boundary layer effectively defines the shape of the aerofoil seen by the external flow, it is clear from these plots why the lower surface jet is more effective than the upper surface jet.

It can also be seen from Figure 5.7 that the positive jet becomes progressively more effective as incidence increases, while the negative jet becomes less effective with increasing angle of attack. This is seen in an even more pronounced fashion with the next aerofoil presented, the NACA 4415, and as such, detailed investigation is presented in the following section.

5.3 NACA 4415

The NACA 44xx aerofoil family was used on the blades of the Tjaerborg 2MW wind turbine which has been the subject of extensive research [116] [117]). The well-documented nature of this turbine makes it suitable as a machine to be used as an example for investigating the effects of CCAs on a large, pitch-regulated wind turbine, although it is in no way suggested that it is necessarily representative of modern HAWTs of a comparable size. The 4415 section was used over the 60-85% (approximately) span of these blades with other thicknesses of the same series used over the entire blade. Hence, determining the behaviour of this aerofoil in

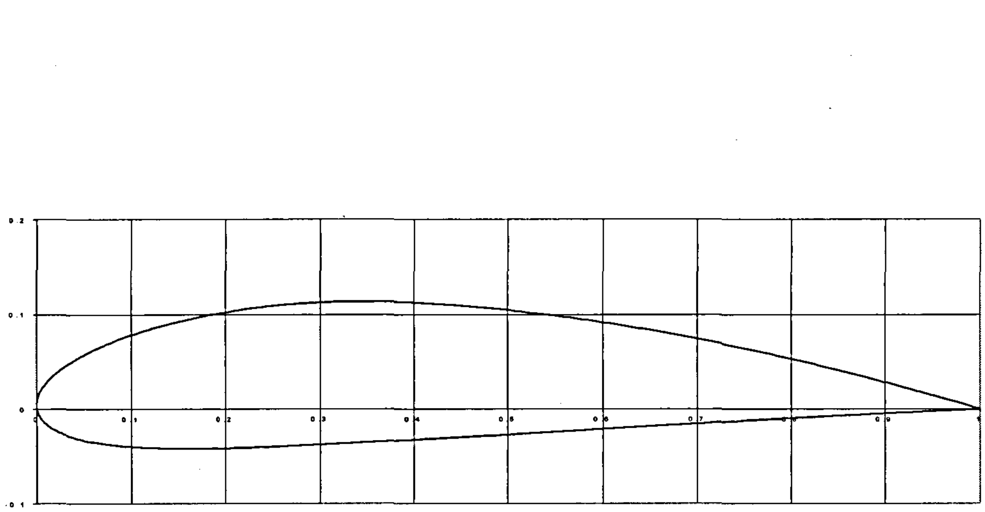

Figure 5.16: NACA 4415 profile

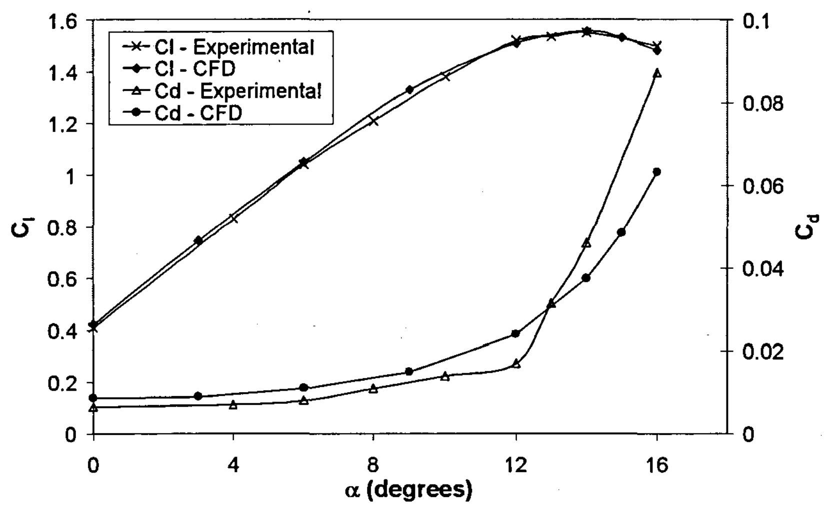

Figure 5.17: Predicted and experimental lift and drag coefficients for NACA 4415

connection with circulation control jets facilitates analysis of the likely behaviour of the machine with CCAs.

As well as the need for data on this section for the purposes of the BEM simulations in the following Chapters, it also has a particular characteristic, which makes it of interest here. This is its highly pronounced progressive trailing edge stall; this characteristic can be used to study the effect localised aft separation has on CCA efficacy, useful as HAWT aerofoils are generally designed to stall progressively from the trailing edge. The section is shown in Figure 5.16.

The characteristics of the plain aerofoil as determined from wind tunnel testing

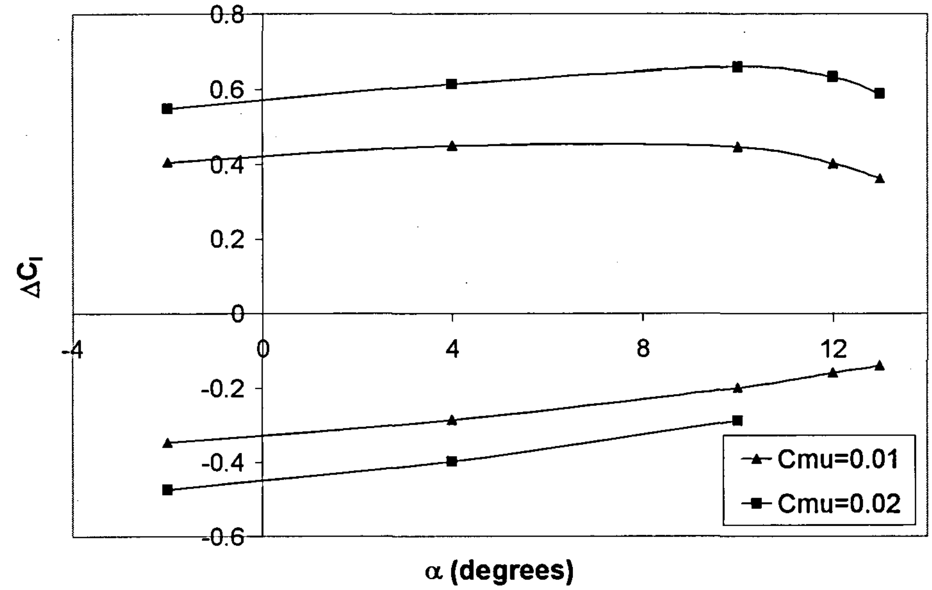

Figure 5.18: Change in lift coefficient for NACA 4415 with positive and negative CC jets

[116] and simulation, at a Reynolds number of $6x10^6$are shown in Figure 5.17. Excellent agreement is found in the case of the lift coefficient, including the onset of stall, while the over-prediction of the drag coefficient is as expected due to the fully turbulent boundary layer assumption in the solver. The lift is so well predicted due to the high Reynolds number and the nature of the stall of the NACA 4415.

The position of the jets were set at 97% chord for both lower and upper surface slots, the jet deflection angles were defined normal to the aerofoil surface ($+90°$ and $-74°$ respectively in this case) and the slot dimension was, $\delta/c = 0.0028$. The incremental changes in lift and drag are seen in Figures 5.18 and 5.19, when using $C_\mu = 0.01$ and 0.02.

A similar behaviour is seen in the slope of the ΔC_l curves as commented on in the previous section. In this case the positive jet becomes slightly more efficient as the incidence increases from $-2°$, ΔC_l rising until to $4°$ and $10°$ at $C_\mu = 0.01$ and 0.02

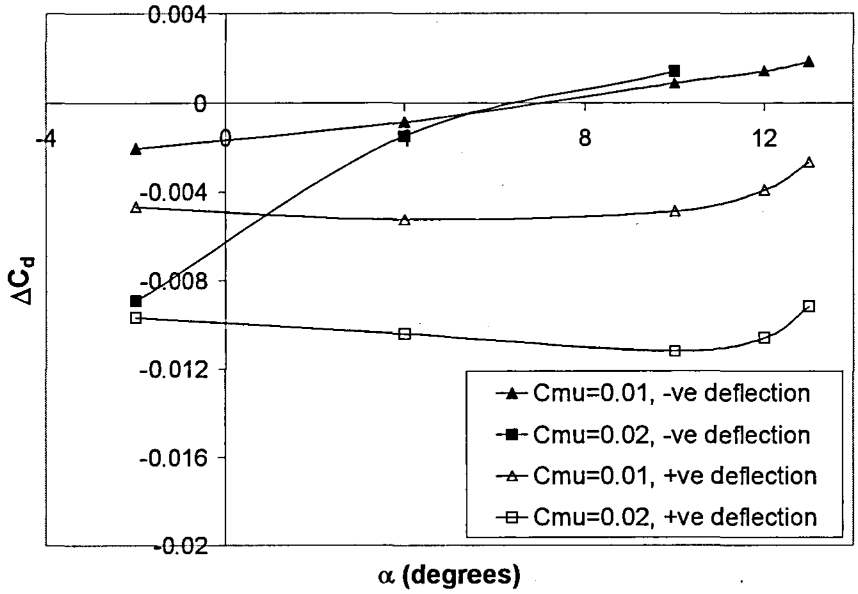

Figure 5.19: Change in drag coefficient for NACA 4415 with positive and negative CC jets

respectively, from which point it decreases. In the case of the negative deflection the jet efficacy declines at an increasingly faster rate as the angle of attack rises. In both the negative and positive jet cases, the effect is seen to be magnified with increasing momentum coefficient, as witnessed by the change in slope gradients. The reason for these changes in ΔC_l with increasing angle of attack can be readily explained with reference to the local conditions at the trailing edge upper surface as seen in the following Figures.

Figure 5.20 shows the fully attached condition of the upper surface boundary layer for the plain aerofoil at $\alpha = 4°$, and Figures 5.21 and 5.22 depict the increasing trailing edge separation which occurs at $\alpha = 10°$ and $12°$.

Figure 5.23 shows how, even at $\alpha = 4°$, when the boundary layer is fully attached to the suction surface, the presence of the negative jet causes a pronounced region of separation upstream of itself. At $\alpha = 10°$ the separated region upstream of the jet extends as far as 0.9c as shown in Figure 5.24, and this trend continues as the

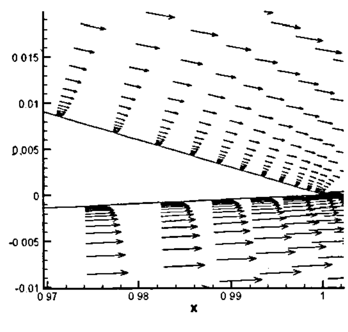

Figure 5.20: Boundary layer profiles at the trailing edge of NACA 4415 at an incidence of 4 degrees

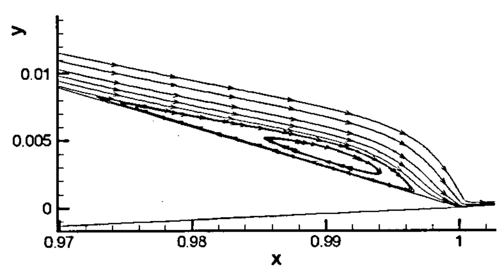

Figure 5.21: Streamlines at the trailing edge of NACA 4415 at an incidence of 10 degrees

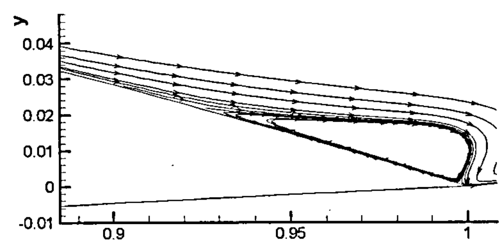

Figure 5.22: Streamlines at the trailing edge of NACA 4415 at an incidence of 12 degrees

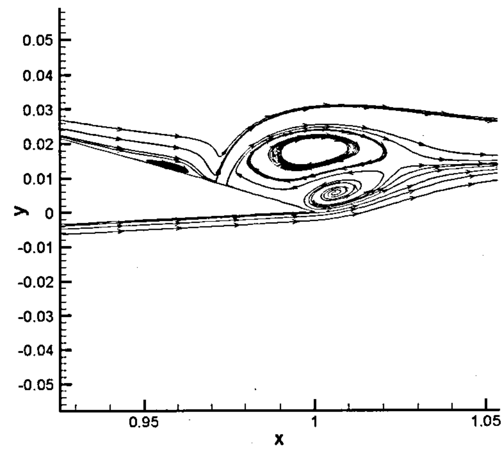

Figure 5.23: Streamlines at trailing edge of NACA 4415 CCA with negative jet (momentum coefficient=0.01) at an incidence of 4 degrees

incidence is increased.

On the other hand, with the positive jet (C_μ=0.01) the flow is encouraged to remain fully attached on the upper surface up to $\alpha = 10°$, separation only starting to occur at $\alpha = 12°$, as seen in Figures 5.25 and 5.26. Increasing the momentum coefficient to 0.02 prevents upper surface, trailing edge separation occurring until 12° incidence, as shown in Figure 5.27. Note that in all cases the positive jet also forces a separation upstream of itself, but that, due the stronger boundary layer on the pressure surface, this separation is confined to a smaller region than in the case of the negatively deflected jet.

In conclusion, it can be said that as well as the difference in negative/positive jet performance explained in the previous section in terms of the boundary layer thickness, there are additional (and associated) effects which alter both the negative and the positive jet performance with changing incidence. This is the loss of negative ΔC_l efficiency due to inducement of upstream separation (which effectively increases the thickness of the boundary layer into which the jet enters) and the increase of positive ΔC_l due to the suppression of trailing edge separation

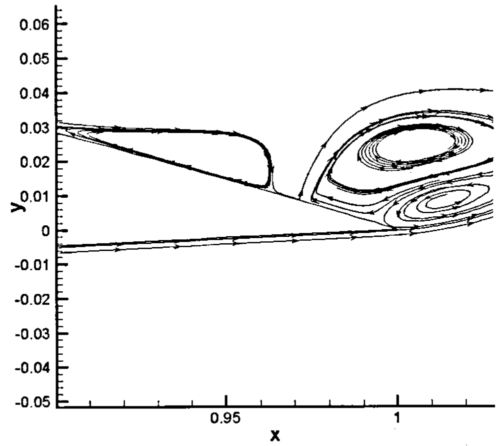

Figure 5.24: Streamlines at trailing edge of NACA 4415 CCA with negative jet (momentum coefficient=0.01) at an incidence of 10 degrees

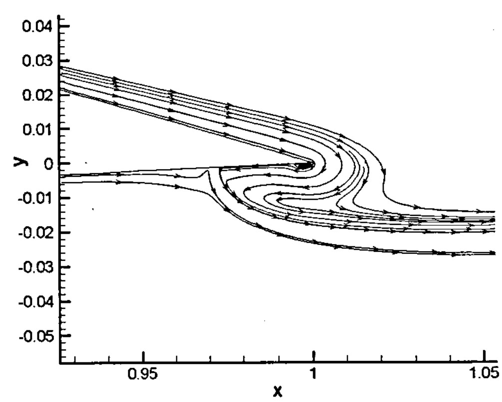

Figure 5.25: Streamlines at trailing edge of NACA 4415 CCA with positive jet (momentum coefficient=0.01) at an incidence of 10 degrees

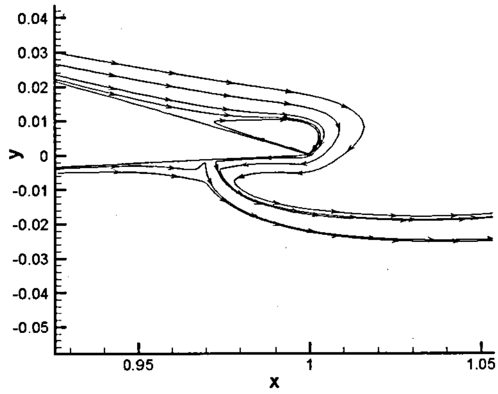

Figure 5.26: Streamlines at trailing edge of NACA 4415 CCA with positive jet (momentum coefficient=0.01) at an incidence of 12 degrees

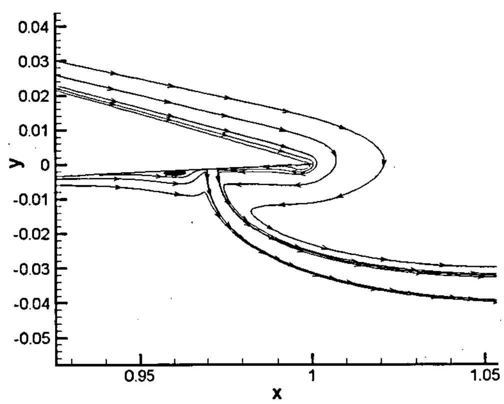

Figure 5.27: Streamlines at trailing edge of NACA 4415 CCA with positive jet (momentum coefficient=0.02) at an incidence of 12 degrees

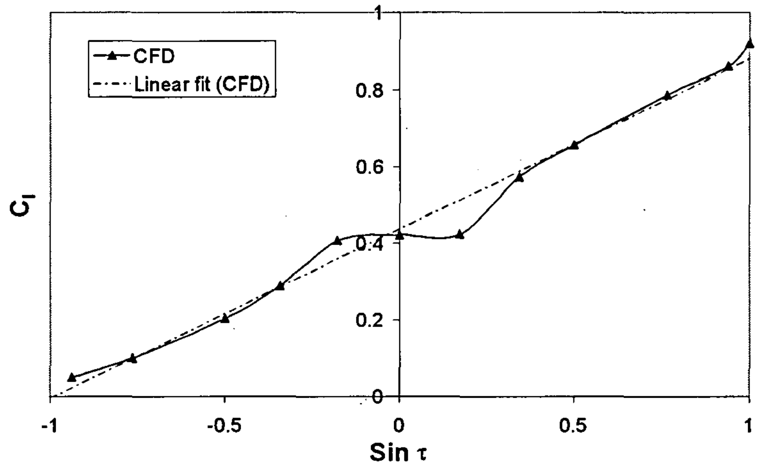

Figure 5.28: Effect of varying jet deflection angle between +90 and -90 degrees on lift increment for NACA 4415 CCA using a momentum coefficient of 0.01

which occurs in the case of the plain aerofoil, at higher incidences.

5.3.1 Jet Deflection Angle

Additional simulations were carried out with the NACA 4415 profile at $\alpha = 0°$ to assess the effect of using different deflection angles. This was considered a useful exercise for two different reasons. Firstly, although it had previously been decided to use as great a deflection angle as possible (i.e. normal to the local surface) in conjunction with a variable momentum coefficient operating strategy, it is quite possible that such a steep deflection may be undesirable or unobtainable due to turning losses/nozzle efficiency or fabrication constraints. Therefore, by quantifying the effect of reducing the deflection angle, any future performance losses encountered due to this can be accounted for. Secondly, previous experiments, most notably those carried out at ONERA [6], determined a linear relationship between ΔC_l and $\sin \tau$ and if this is predicted by the solver it adds an additional validation check on the code.

It can be seen in Figure 5.28 that there is a clear linear variation of C_l with $\sin \tau$, which is only violated at very low deflection angles, further validating the code. Figure 5.28 also indicates that for positive jet deflection only a very small loss of lifting efficiency would be experienced (approximately 12% in ΔC_l) in changing the deflection angle from 90° to 70°. Further, it is worth pointing out that should a variable deflection angle technique be considered in any future work, it should be one that uses a device which can achieve deflection angles of at least 50° to ensure that it can introduce a useful range of ΔC_l.

5.3.2 Reynolds Number Effects

The effect that changes in Reynolds number (assuming a fully turbulent boundary layer) may have upon performance (in terms of ΔC_l and ΔC_d) was also checked with the NACA 4415 profile. It was found that the absolute lift values increased slightly (particularly at higher angles of attack) with increasing Reynolds number for both the plain (as reported from experiment [118]) and CCA configurations, but that the variation in the ΔC_l and ΔC_d values was minimal; at $\alpha = 4°$, $C_\mu = 0.01$, increasing Re from $3x10^6$ to $6x10^6$ only decreased ΔC_l from 0.449 to 0.444 and ΔC_d from -0.0053 to -0.0054. It can be concluded that changing Reynolds number within the above range does not effect the CCA performance to a significant degree.

5.4 NACA 63xxx Family

NACA 63xxx aerofoils have been widely used on wind turbine blades since the commercial development of electricity generating HAWTs began in the 1970s. The reason for their widespread application is their high lift to drag ratio, although they have been somewhat superceded by purpose-built aerofoils that do not have their less desirable characteristic of high roughness sensitivity, which can produce

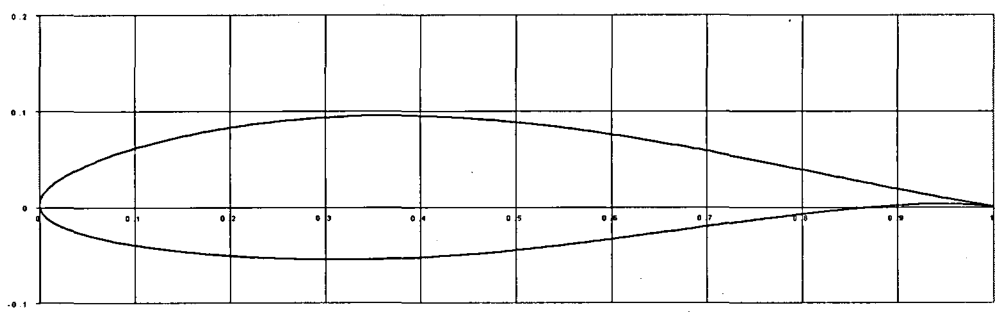

Figure 5.29: NACA 63415 profile

a severe loss in performance as well as a tendency to 'double stall'. The main feature of interest on this aerofoil family, with regard to this work, is the presence of significant aft camber and a cusped trailing edge region, as shown in Figure 5.29 which depicts the NACA 63415. This feature is common on purpose-designed wind turbine aerofoil sections (it is present on three of the four families which the author is familiar with - the Risoe, SERI and TUDelft aerofoils [114], but not all of the NTUA designed sections [119]) and so the interaction of this feature with circulation control jets placed in its vicinity is of particular interest. Further, the fact that the 63xxx family is an extended one (there are 5 standard thicknesses and 3 standard camber lines) means that it can be used as part of a parametric study of the effect of these geometric variables.

The characteristics of the plain aerofoil as determined from wind tunnel testing [118] and simulation at $Re = 3x10^6$ are shown in Figure 5.30. Mesh specifications are generally as previously detailed for the FX77w153.

Agreement between predicted and experimental values for lift are good, although not as well predicted as for the NACA 4415 section; the lift coefficient is slightly over-predicted in the attached flow region and the rate at which stall develops with increasing incidence is under-predicted, hence both the value of maximum lift, as well as the incidence at which it occurs, are over-predicted. This discrepancy may

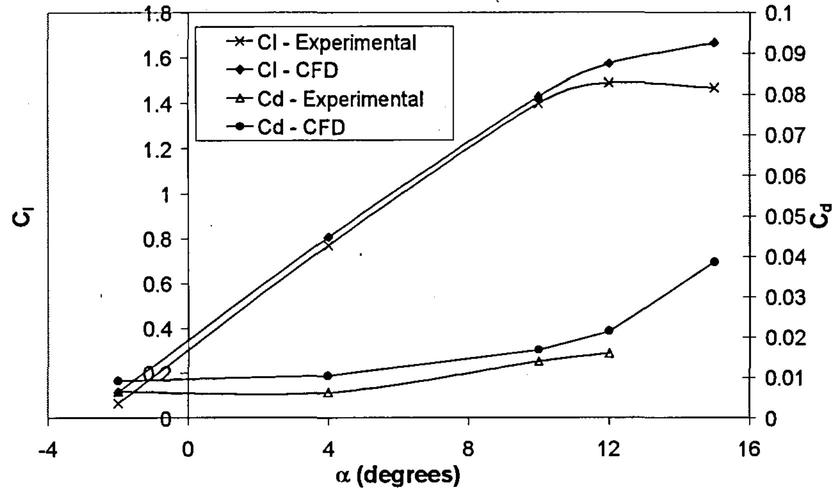

Figure 5.30: Lift and drag coefficients for NACA 63415

be associated with the use of an O-mesh, as simulations conducted at Risoe [114] with a C-mesh (which gives a better resolution of the flow in the aerofoil wake region) show a better correlation, particularly in the attached flow region. The drag is also over-predicted to a slightly greater degree than with the 4415 section. Due to the reduced trailing edge thickness of the 63415 compared to the FX77w153 and NACA 4415, the position of the jets were set at 97% chord for the lower surface and 95% chord for the upper surface for the CCA simulations, which provides adequate space for the duct/plenum system required to supply the slots with air. Again, the jet deflection angles were defined as normal to the aerofoil surface ($+90°$ and $-70°$ respectively in this case) and the slot dimension was much the same as the previous cases, being $\delta/c = 0.0029$. The incremental changes in lift and drag for $C_\mu = 0.01$ are seen in Figures 5.31 and 5.32.

It is clear that the 63415 section does not achieve the same negative or positive lift increment from the addition of CC jets as the FX77w153 or the NACA 4415, the deficit being greatest for the positive jet. This is seen more clearly in Figures 5.33 and 5.34 where the incremental changes made to the force coefficients normal and

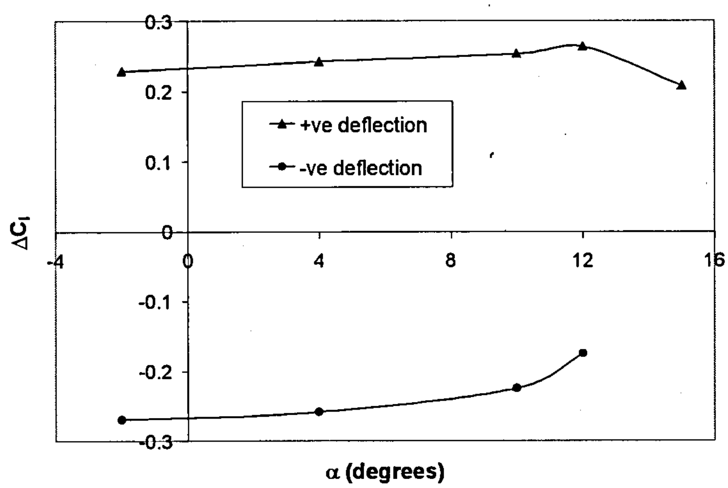

Figure 5.31: Change in lift coefficient for NACA 63415 with positive and negative CC jets (momentum coefficient=0.01)

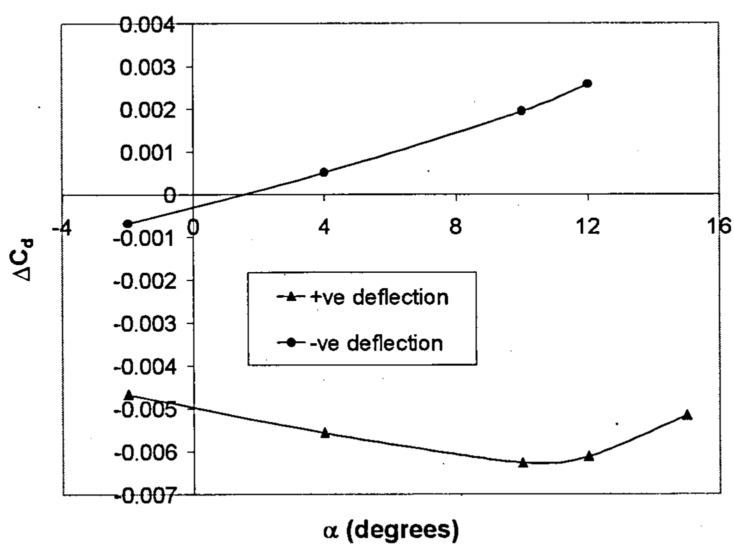

Figure 5.32: Change in drag coefficient for NACA 63415 with positive and negative CC jets (momentum coefficient=0.01)

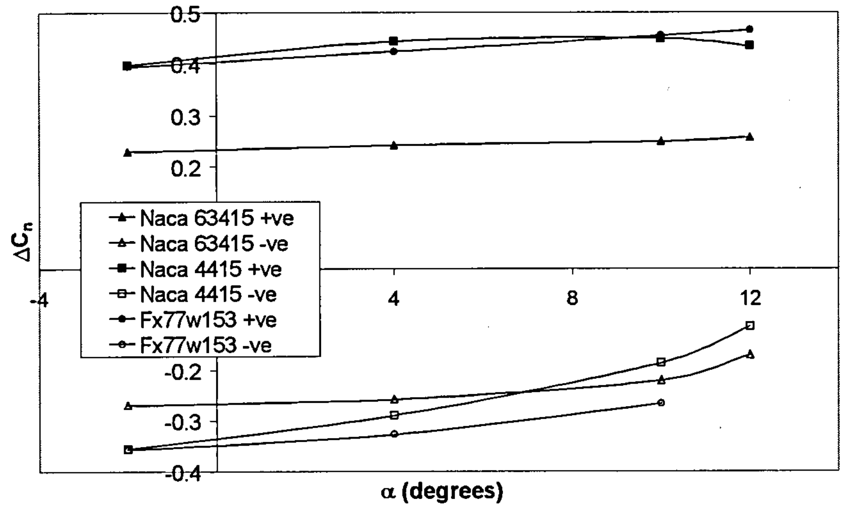

Figure 5.33: Incremental change made to normal force coefficient for NACA 4415, NACA 63415 and FX77w153 with negative and positive jets (momentum coefficient=0.01 in all cases)

tangential to the chordline, ΔC_n and ΔC_t, are presented for all three aerofoils with positive and negative CC jets at C_μ=0.01. C_n and C_t, are used as they give a clearer indication of the changes which will be present in a wind turbine rotor's in-plane and out-of-plane loading due to the CCAs. They are defined by Equations 5.3 and 5.4.

$$C_n = C_l \cos\alpha + C_d \sin\alpha \tag{5.3}$$

$$C_t = C_l \sin\alpha - C_d \cos\alpha \tag{5.4}$$

In order understand why the NACA 63415 has poorer performance coefficients (ΔC_n and ΔC_t) when compared with the FX77w153 and NACA 4415, it is first

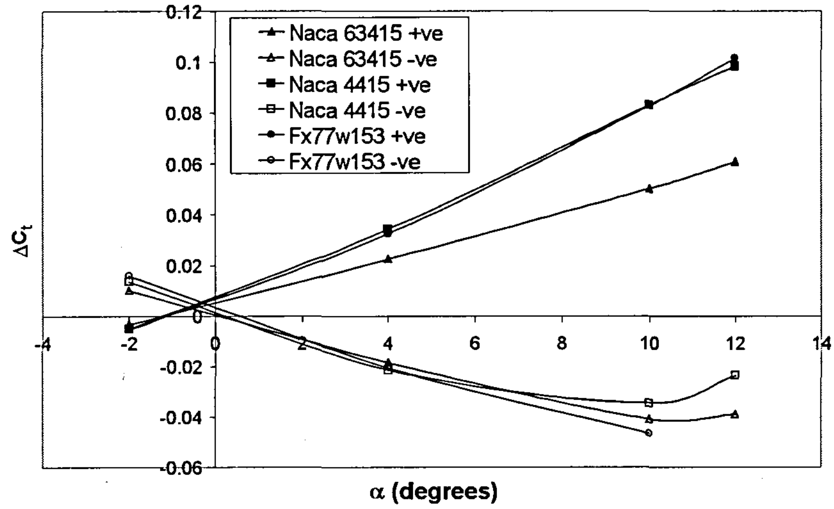

Figure 5.34: Incremental change made to tangential force coefficient for NACA 4415, NACA 63415 and FX77w153 with negative and positive jets (momentum coefficient=0.01 in all cases)

instructive to explore the similarities between the behaviour of the CCA micro-jet flaps (in positive deflection) studied here and that of aerofoils fitted with Gurney flaps and Divergent Trailing Edges (DTEs), as described in Chapter 2.

5.4.1 Gurney Flaps and Aerofoil suitability

The fact that both Gurney Flaps and CCAs produce the same changes in the pressure profile (decreased pressure on the suction surface, most pronounced at the leading and trailing edges, and slightly increased pressure on the lower surface, particularly at the trailing edge just upstream of the device) indicates that there may be a fundamentally similar mechanism at work in both cases. They also share other characteristics such as the disproportionately greater effect produced with smaller flap to chord heights or momentum coefficients, and the fact that neither device significantly changes the gradient of the lift curve. The lowering of the stall incidence caused by the Gurney flap is hard to determine with a CFD model, but is a well documented effect for both Coanda and jet flap CCAs

There is one respect in which the behavior of the two devices is distinctly different - that is the sign of the change made to the drag coefficient. Apart from work conducted by Liebeck [66] and Kentfield [120] all the published data for aerofoils fitted with Gurney flaps show a highly significant (70 - 190%) increase in drag at low to mid range angles of attack. This is not seen to occur for CCAs in the simulations presented here. Rather, at the momentum coefficients which cause comparable changes in lift, a definite decrease is seen in the drag coefficient. There is a simple explanation for this, however, as the Gurney flap presents a surface, aligned normal to the freestream and connected to the main body of the aerofoil, on which a pressure differential can exist from front to back. This has been confirmed in an experiment by Jeffrey et al. [121] who showed that the drag increment is negative (i.e. there is decreased drag) when the forces are determined by integration of surface pressures on the aerofoil alone and positive (i.e. increased drag) when they are determined by a force balance, or when the integration includes the surface pressures on the faces of the Gurney flap. This cannot, of course, occur in the case of the micro-jet flap where no such connected surface exists. This, incidentally, is also likely to explain why DTEs, wedges and flaps aligned at angles significantly less than 90° show a reduced drag penalty for a given lift increment [70] [122] [123] [71]. It should be mentioned here that with the presence of CC jet(s) very little change is seen in the viscous friction force values, so any decrease in drag must be attributable to changes in the pressure field and as such the ΔC_d values should be superposable on the correct experimental values. The only caveat to this is that the change in pressure distribution may, in some instances (e.g. at higher incidences), make a difference to the transition point which in turn may effect the drag adversely. However, this cannot be determined without a transition model in the CFD code and the effect is anyway likely to be small in comparison to the changes made to the drag coefficient by the CC related pressure forces.

Liebeck [66] first suggested the presence of a separation bubble upstream of the Gurney flap and a pair of counter rotating vortices behind the flap as the dominant features of the flowfield in the locale of a Gurney flap. This was later predicted by Jang et al [124] using CFD (RANS) simulations of an aerofoil with Gurney flap and time averaged results from Laser Doppler Anemometry experiments carried out by Jeffrey et al [121] on an aerofoil fitted with a 4% Gurney flap confirm this, showing precisely this flow structure upstream and downstream of the flap. Figure 5.35 shows the streamlines at the trailing edge of the NACA 4415 profile with CC jet ($C_\mu = 0.01$) and indicates that a similar flow structure exists upstream and downstream of the CC jet; it is felt that this favourable comparison with Gurney flap behaviour provides a useful analogy and further validation of the code's ability to be used as a tool for simulation of CCAs. It is also thought that the similarity is great enough to suggest that the primary mechanism by which such micro-jet flaps operate, lies in the 'blocking' effect they have on the local flow and subsequent change to the effective aerofoil profile just as they do when greater momentum coefficients are used and the jet penetrates the freestream significantly, rather than in an addition of energy to the local boundary layer.

Quantitatively, it is seen from the results presented here that a momentum coefficient of 0.01 produces the same ΔC_l (≈ 0.44) on the NACA 4415, as a Gurney flap of between 1% chord ($\Delta C_l \approx 0.4$) and 1.5% chord ($\Delta C_l \approx 0.5$) does on the same aerofoil, as measured by Storms and Jang [72]. Figure 5.35 also has a superimposed line (marked in bold) which indicates the approximate length of a Gurney flap (1.3% chord) required to produce the same change in the lift coefficient. It can be seen that by the time the jet has penetrated this far into the boundary layer it has been forced to turn through around 45° already and probably produced the majority of the effect it will have on the aerofoil circulation.

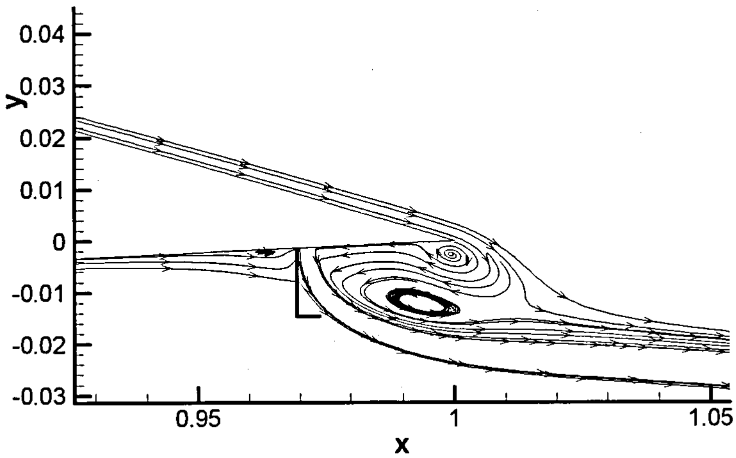

Figure 5.35: Streamlines at the trailing edge of NACA 4415 CCA with positive jet present (momentum coefficient=0.01)

A survey of the results from various experimental investigations into Gurney flaps with different aerofoils [72] [70] [125] [126] [121] [71] indicates that different profiles do interact more or less effectively with Gurney flaps; most interestingly in the light of the modelling carried out here are the results of Bloy [70] who reports a $\Delta C_l \approx 0.27$ for a 1% chord flap on a NACA 63215 which is slightly greater than the values reported here for the NACA 63415, if the same scaling of flap height to momentum coefficient is used as in the case of the NACA 4415. Approximately the same value is reported by Timmer and van Rooy [71] in the case of the DU93-W-210 which is an aerofoil section designed specifically for use on wind turbines, and which has a similarly cusped trailing edge.

It has been shown by Jeffrey et al [121] that the effect a Gurney flap has on the pressure profile can be successfully replicated by introducing a finite pressure difference at the trailing edge, rather than applying a true Kutta condition, in an aerofoil panel method code, and hence that it is the creation of this pressure difference at the trailing edge which is the mechanism by which the Gurney flap works. Turning to Figures 5.36, 5.37and 5.38, which depict the pressure profiles

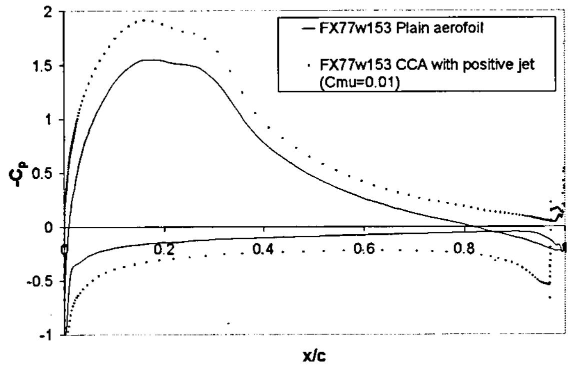

Figure 5.36: Pressure profiles for FX77w153 as plain aerofoil and with positive CC jet, momentum coefficient=0.01 (incidence =4 degrees both cases)

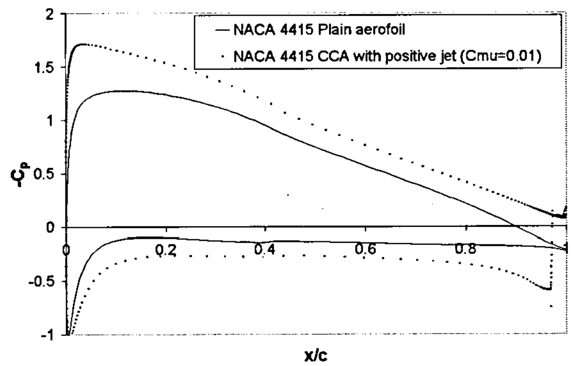

Figure 5.37: Pressure profiles for NACA 4415 as plain aerofoil and with positive CC jet, momentum coefficient=0.01 (incidence =4 degrees both cases)

for all three aerofoils with and without a positively deflected CC jet ($C_\mu = 0.01$), it can be seen that the micro-jet flap produces an almost identical pressure difference ($\Delta C_p \approx 0.6$) at the trailing edge on all three profiles.

What is different between the three, however, is the pressure difference that exists just upstream of the trailing edge on the plain aerofoil sections, the NACA 63415 having a markedly larger differential than the other two, and it is suggested that it is this which has the largest influence on how effective the presence of a CC jet or Gurney flap will be. The high trailing edge pressure difference is in turn attributable to the aft camber of the aerofoil, and it would appear that this

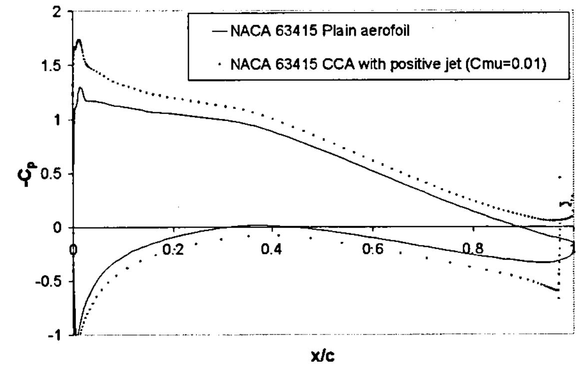

Figure 5.38: Pressure profiles for NACA 63415 as plain aerofoil and with positive CC jet, momentum coefficient=0.01 (incidence =4 degrees both cases)

geometrical feature is highly detrimental to the effective operation of both positive and negative CCA jets. In the case of the positive jet, the aft camber has already produced some of the aerofoil's lift by the same means which the jet creates additional lift. In much the same way, the negative jet performance suffers as it has to overcome the pressure differential created at the trailing edge by the aft camber (this is analogous to the interaction of simultaneously active positive and negative jets, considered in the next section). As already mentioned, in wind tunnel tests the DU93-W-210 was recorded as having approximately equal values of ΔC_l for given a given Gurney flap height [71] as the NACA 63215 [70] which has a similarly designed rear section and subsequent aft loading. Indeed, this is a design feature common to several HAWT aerofoil designs [114], although not all [119], as previously mentioned. This raises the question of whether CC jets can usefully be considered as an 'add-on' to conventional HAWT aerofoil sections, or whether the design criteria for HAWT CCAs should be reconsidered with CC jet efficacy traded off against other (otherwise desirable) characteristics.

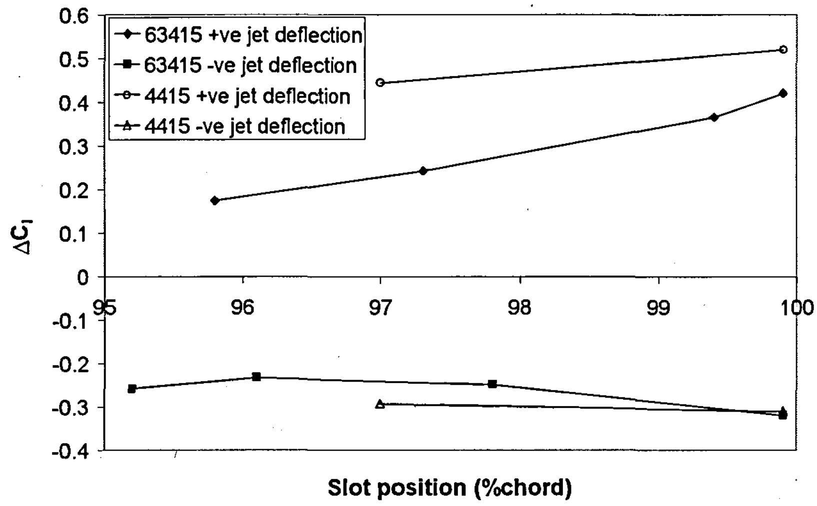

Figure 5.39: Effect of moving slot forward from trailing edge on NACA 63415 and NACA 4415 CCAs

5.4.2 Slot Position

The sensitivity of CCA performance to slot position was tested with the NACA 63415 section at a momentum coefficient of 0.01. Figure 5.39 shows the variation in lift coefficient at $\alpha = 4°$, $C_\mu = 0.01$, with the upper and lower surface slots placed at 4 positions between the very end of the trailing edge (a physically unrealistic situation although of use here), and approximately 95% chord, with 2 intermittent values.

The effectiveness of both upper and lower surfaces jets diminishes as the slot is moved from the trailing edge to physically realisable positions. However, the upper surface jet performance appears almost independent of its position as it is moved forward from 98% chord, while the lower surface jet continues to decrease steadily in performance.

Additionally, a check was made on these values with the NACA 4415 section, using the slot positions described in the previous section and another set of the (unrealisable) slots at the trailing edge - these results are also shown in Figure 5.39.

Two things are of note: firstly, the value of the lift increment is always greater for the NACA 4415 (as previously noted and commented on) and secondly, the gradient of the slope is shallower, that is the jet loses less of its effectiveness as it is moved forward. In the case of both aerofoils it can be said that the trailing edge region behind the jet 'shields' the flow on the non-blown surface from the effect of the jet and it is suggested that the small cusp at the trailing edge of the NACA 63415 (which provides some of the aft camber) does this more effectively than the nominally flat trailing edge surfaces of the NACA 4415. As such, the local trailing edge geometry of a CCA is also a variable which effects how sensitive the aerofoil will be to the position of the slot with respect to the chord.

5.4.3 Thickness and Camber

Firstly, it should be noted that the results presented for the study of different thickness and camber values in the NACA 63XXX family were conducted with the slot defined at the very trailing edge which (as previously mentioned) is physically impossible to realise. It is for this reason that the ΔC_l values are higher than previously presented.

Figure 5.40 shows how the positive jet interacts slightly more favourably with the thicker sections; no discernable change is seen with the negative jet. This finding is in agreement with observations made in Coanda CCA design [113] and with the behaviour of conventional aerofoil flaps [118].

Figure 5.41 presents the corresponding values for the 3 camber lines (camber is greatest with the 63615 section). In this case the picture is less clear, and no obvious conclusions can be drawn, except that, generally speaking, the less cambered sections perform better.

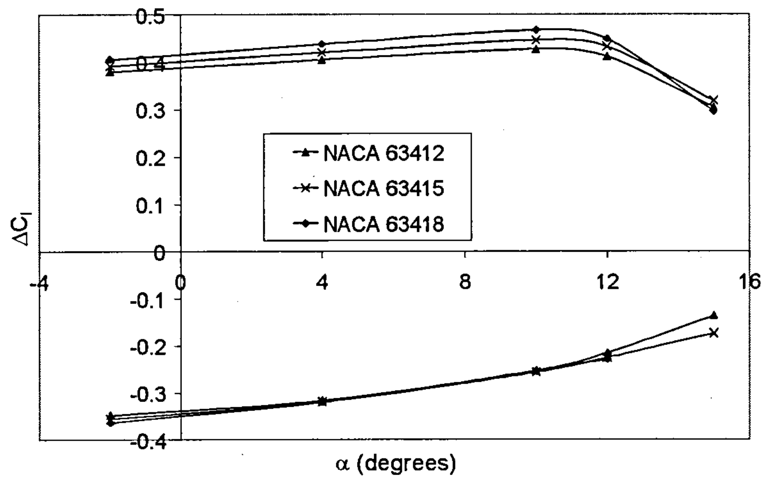

Figure 5.40: Effect of varying thickness on negative and positive lift increment due to presence of CC jets on NACA 63xxx aerofoils

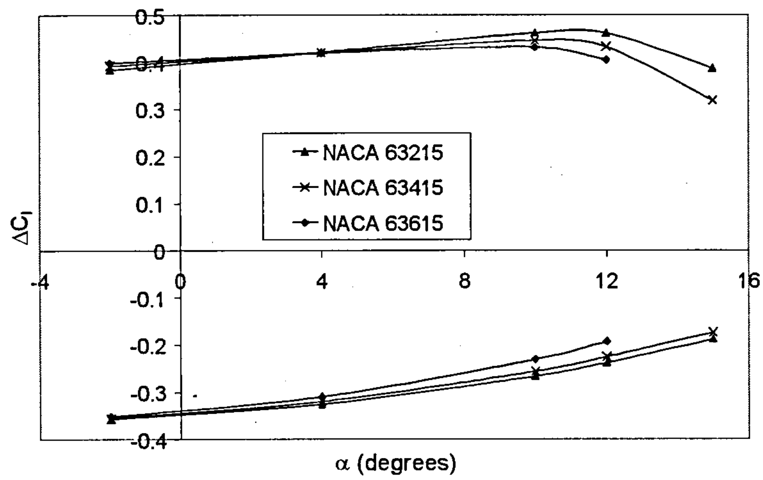

Figure 5.41: Effect of varying camber on negative and positive lift increment due to presence of CC jets on NACA 63xxx aerofoils

5.5 Extended Mesh for FX77153 including Slot Channel

It was reasoned that simulations with lower momentum coefficients or larger slots and hence lower jet velocities could possibly tend toward an increasing inaccuracy due to increased deflection of the jet in the direction of the freestream, 'upstream' of the slot exit. As such, an addition to the model for the FX77w153 CCA was introduced in the form of an extension of the mesh which penetrates into the aerofoil profile. This enabled the slot inlet conditions to be defined from within the aerofoil profile and, as such, enables the interaction of the jet and local freestream, and the resulting jet velocity profile at the slot exit, to be represented more accurately. In a CFD code which allows for total pressure to be specified as a boundary condition this would have had much the same effect, but this is not an option with E2D. The channel leading to the slot was defined after the main mesh had been built, using a simple program which adds additional cells by marching, normal to the aerofoil surface, away from the user defined slot at a constant stretching factor. Due to the multi-block nature of the B2D/E2D programs these additional cells could then be included in the mesh file as extra blocks (their actual position in the file being unimportant) and their physical/computational position within the mesh deduced by the pre-processor. A close-up of the mesh with the slot channel included can be seen in Figure 5.42; this is from a model with $\delta/c = 0.0027$ and in this instance the length of the channel is approximately 4mm (relative to a chord of 1m).

Mesh detail at trailing edge of FX77w153 showing channel upstream of slot exit

The difference between the results for ΔC_l for the positive jet, produced with and without channels is reasonably small (6.6%) at the momentum coefficient for which results have generally been presented for up to this point (i.e. $C_\mu = 0.01$).

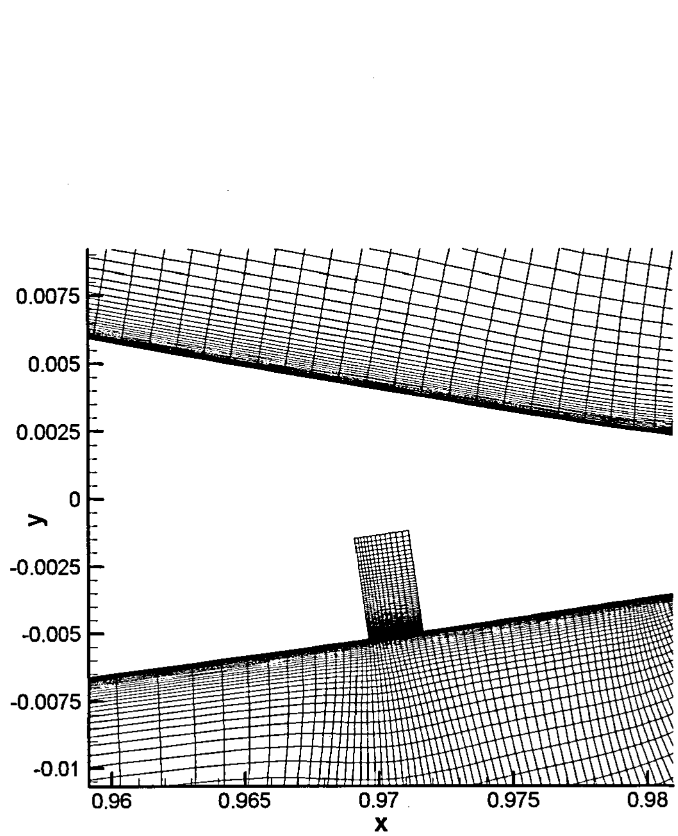

Figure 5.42: Mesh detail at trailing edge of FX77w153 showing channel upstream of slot exit

However, over the range of $C_\mu = 0.0001 - 0.01$, the decrease in ΔC_l relative to that predicted without the channel being modelled increases to 51.8%, hence, the need for this additional mesh detail is clear. As expected, the jet is deflected to its leeward side to a greater extent and made to contract upstream of the slot exit by the localised high pressure region which exists just outside the slot exit by virtue of the interaction of the jet and external flow. This can be seen in Figures 5.43, 5.44 and 5.45 which depict the streamlines in the slot locality with and without the channel modelled at $C_\mu = 0.0001$.

Although the length of the channel depicted in Figure 5.42 is fairly realistic, considering the local skin thickness of the aerofoil, a check was made for the dependency of the upstream jet deflection on the length of the channel. It was found that lengthening the channel to twice that shown in Figure 5.42 had a negligible effect ($< 1.5\%$ change in ΔC_l) even at the lowest momentum coefficients

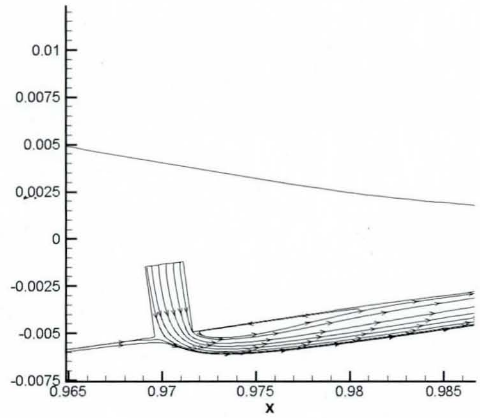

Figure 5.43: Streamlines in slot locality with upstream channel modelled (momentum coefficient=0.0001)

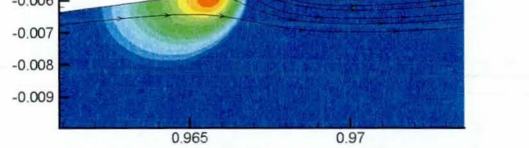

Figure 5.44: Detail of pressure contours and streamlines in slot locality with upstream channel modelled (momentum coefficient=0.0001)

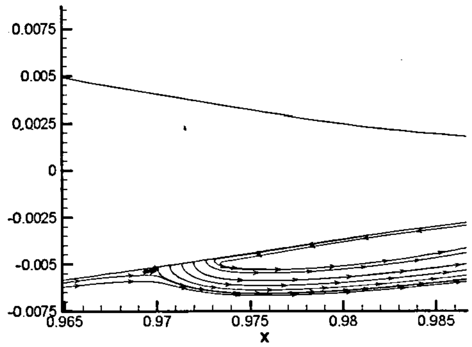

Figure 5.45: Streamlines in slot locality without upstream channel modelled (momentum coefficient=0.0001)

and largest slot sizes investigated here.

5.5.1 Extremely Low Momentum Coefficients

All the results presented in this section have been derived with a model which has two slots of $\delta/c = 0.0025$ simultaneously defined (including channels of approximately 4mm in length) positioned at 96.5% chord.

If some means of sealing the upper and lower surface slot exits individually is utilised, then the only scenario that need be considered with respect to passive pumping, is the effect of a passively supplied low momentum jet from the positive slot, below rated power. Since in its passively blown state (that is, when air is expelled from the slot or slots due to the effect of centripetal pumping), a HAWT CCA will have the same role as a plain aerofoil it is preferable to view the characteristics under these conditions in terms of the force coefficients normal and tangential to the chordline, C_n and C_t, defined previously by Equations 5.3 and 5.4. Of greatest significance under the conditions considered here is the tangential force coefficient as below rated power one is concerned with the effect the jets will have on the power capture of the HAWT. The effect a passively aspirated positive jet will have in isolation on the tangential force coefficient is seen in Figure 5.46;

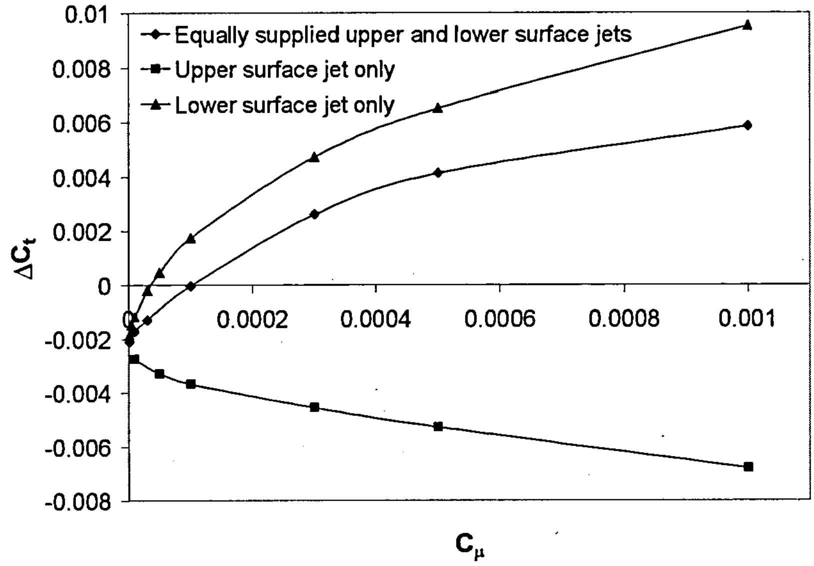

Figure 5.46: Incremental change made to tangential force coefficient with upper and lower surface jets for FX77w153 CCA

a fairly wide range of C_μ has been shown due to the uncertainties in predicting the passively produced momentum coefficient (discussed in Chapter 6).

It can be seen that even at extremely low momentum coefficients which can occur without an active energy input, an isolated positive jet can make a useful contribution to the aerofoil performance. However, a lower threshold exists, below which the presence of the positive, extremely low momentum coefficient, jet produces a negative lift increment, as was shown to occur for the Coanda type CCA in Chapter 4. The threshold appears to be around $C_\mu = 4x10^{-5}$ and by $C_\mu = 1x10^{-6}$, $\Delta C_t = -0.00186$.

If a permanently open slot arrangement is used a subsequent centripetally derived pressure gradient in the blade duct exists (discussed in Chapter 6) and there is likely to always be a small amount of efflux from both the upper and lower surface slots simultaneously. Two things need to be taken into consideration at this point. Firstly, the effect of low C_μ jets present at both slots when the CC facility is not being used (e.g. below rated power) and secondly, the effect that the low C_μ jet issuing from one slot will have on the performance of the other which is being actively supplied with air.

Under the assumptions that the small static pressure difference on the upper and lower surfaces of the trailing edge will not cause a significant difference in C_μ on the suction and pressure surface jets, and that each slot has identical upstream conditions within the blade duct/plenum, the effect of equal and extremely low C_μ at both upper and lower surface slots is seen in Figure 5.46. Also shown for comparison are the predicted force coefficients produced for isolated upper and lower surface jets at the same momentum coefficients.

As with higher momentum coefficients the positive jet is seen to be generally the most effective of the two, and when both jets are present it dominates the net effect in ΔC_t, as can be seen most clearly at the lowest momentum coefficients. There is a fairly consistent offset between the two towards positive ΔC_t, and the net effect, although relatively small, will be beneficial to turbine performance below rated power with respect to power capture. As with the isolated positive jet, the combination of upper and lower surface jets produces a negative tangential force increment until $C_\mu = 1x10^{-4}$.

Due to the dominance of the lower surface jet it is necessary to define the momentum coefficient difference between the jets for which the upper surface jet is effectively inoperative as is shown in Figure 5.47 for ΔC_n (ΔC_t is not shown as it is very similar and in this instance we are interested in the efficacy of the negative jet when in use above rated power). It can be seen that only a very small increase in the strength of the jet on the upper surface over that on the lower surface is required to obtain a negative ΔC_n, but that the presence of a lower value momentum coefficient jet on the lower surface causes a considerable reduction in the ΔC_n value produced by the upper surface jet (approximately 50% at $C_\mu = 0.0005$). It

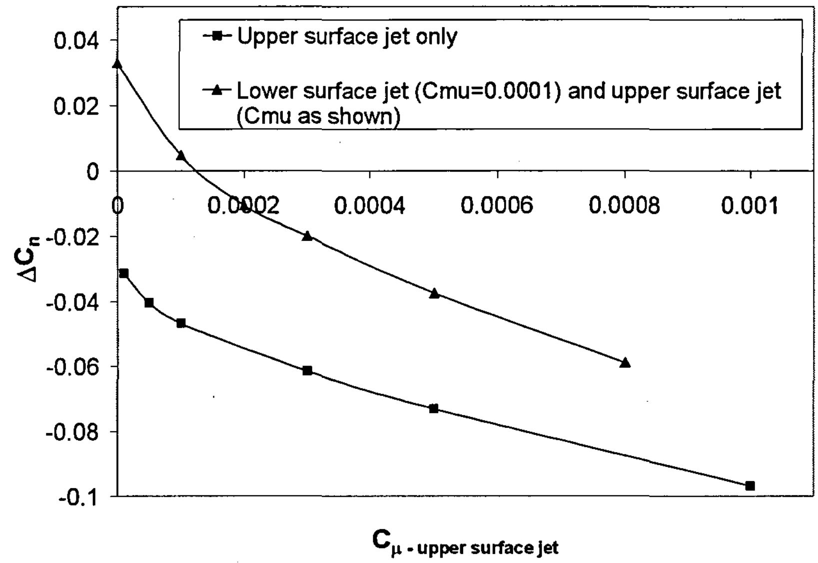

Figure 5.47: Effect presence of positive jet has on incremental normal force coefficient performance of negatively deflected jet

can also be seen that the reduction due to the lower surface jet falls as the upper surface momentum coefficient is increased.

The results presented in 5.47 are extended in Figure 5.48 which shows the effect the passively aspirated slot will have on the other, actively supplied slot for two momentum coefficients, $C_\mu = 0.005$ and 0.01. Again, only ΔC_n is shown as it is representative of both ΔC_n and ΔC_t. The detrimental effect of the passive, secondary jet is greatest with negative jet; at the lower momentum coefficient value shown ($C_\mu = 0.005$) the negative jet shows a maximum reduction of approximately 34% over the range of $C_{\mu-passive}$ shown, while for the same scenario the positive jet ΔC_n value is only reduced by approximately 6%. The changes are 13% and 2% respectively for $C_\mu = 0.01$.

It can be seen that all of the above findings lend weight to the argument for including a means of sealing the upper and lower surface slots independently. Most importantly such an option may prove necessary in order to ensure that

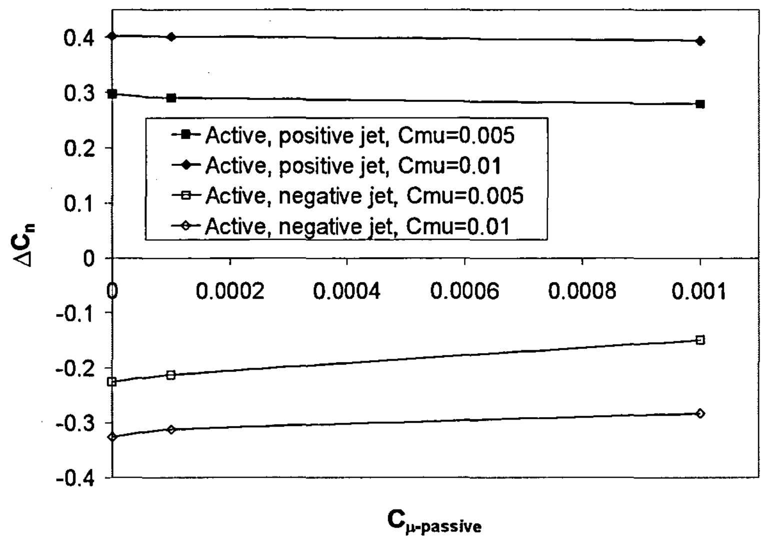

Figure 5.48: Incremental normal force coefficient for simultaneously passively aspirated and actively supplied slots

turbine performance with respect to power capture is not lost below rated power and in order to ensure reasonable performance of the negative jet.

5.5.2 Increased slot size

The effect that slot size has on the performance is of particular interest to the application of CCAs to wind turbines for the reasons outlined in Chapter 3. Simulations have been conducted with 3 different size slots, $\delta/c = 0.0027$, 0.0044 and 0.007 and the results for the positively deflected jet are shown in Figure 5.49. It is seen that increasing the slot size produces an increase in ΔC_l over a range of C_μ and although the effect is not particularly large (an increase of approximately 8% is seen between the largest and smallest slot at C_μ=0.005) it is consistent - a similar behaviour is seen with the negatively deflected jet. This is in agreement with the experimental findings at ONERA [5] [6], when the slot size was varied to confirm the momentum coefficient as the primary variable in jet flap research.

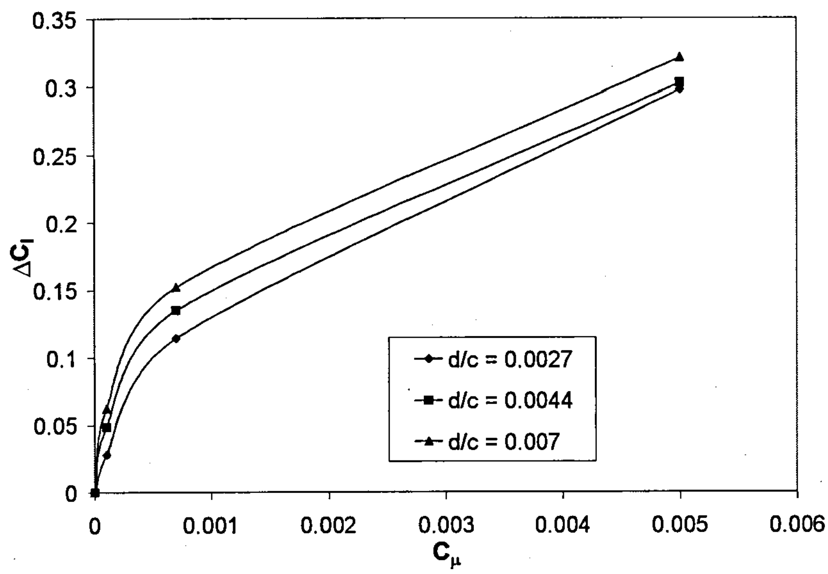

Figure 5.49: Effect of increasing slot size on lift increment for FX77w153 CCA with positive jet

5.6 Summary

- CFD simulations conducted on O-meshes have been used to predict the performance of three aerofoils in their plain and enhanced CCA configurations. Good agreement has been found with experimental data for the lift coefficient of the plain aerofoils in the attached flow region, although the drag is over-predicted due to the fully turbulent boundary layer assumption in the modelling. Nothing unrealistic has been found in the physics of the solutions to suggest that the simulations with CCA jets are erroneous and a useful correlation between the behaviour of Gurney flaps and CCA jets has been established.

- The different thicknesses of the boundary layer on the suction and pressure surfaces at the trailing edge, and the ensuing difference in displacement of them by the jets, is thought to be responsible for the reduced effectiveness of the negatively deflected jet compared to that of the positively deflected one. Also, upper surface trailing edge separation is seen to impose a heavy penalty on the effectiveness of negatively deflected jets as the angle of attack increases.

- It has been found that aerofoils with significant aft camber and cusped trailing edges do not interact particularly favourably with jet flap circulation control due to the aft pressure distribution produced by these features. This is unfortunate as this detail appears on many aerofoils used on wind turbines and would suggest that some purpose-built CCA design is required in order to meet the lift, drag and roughness insensitivity requirements of aerofoils designed for HAWTs, while avoiding or minimising use of aft camber.

- Slot position with respect to aerofoil chord, is found to effect to the incremental lift coefficient produced to a greater degree when a cusped trailing edge is present on the aerofoil. Other than this, movement of the slot within the range of realisable positions investigated does not effect the incremental force coefficients significantly.

- The proportionality of ΔC_l with $\sqrt{C_\mu}$is seen to extend to extremely low momentum coefficients ($< 1x10^{-4}$) for both negatively and positively deflected jets. However, below values of $C_\mu = 2x10^{-4}$ the positively deflected jet is seen to induce negative force coefficients which has implications for the performance of a HAWT blade fitted with permanently open slots. An extension was made to the mesh to represent the throat leading to the slot for use in instances like these when modelling where jet velocity was low. This was which was found to provide a more accurate representation of the flow field in the locality of the jet/freestream, including the upstream jet deflection (by the external flow) within the aerofoil body.

- The use of larger slots is seen to enhance the performance of the CCA for a given momentum coefficient. This is of particular interest as using larger slots also reduces the energy input required to sustain the jets and reduces the chance of fouling.

- C_l is seen to vary linearly with the jet deflection angle, $\sin\tau$, for both negative and positive jet deflections angles except at very low ($< 20^\circ$) angles where the variation is less than that suggested by the linear relationship.
- Marginally better performance is seen as aerofoil thickness is increased from 12-18% as is also found with conventional flaps and Coanda CCAs.
- A Reynolds number variation between $3 - 6x10^6$ is not found to have any significant effect on the behaviour of CCAs.

Chapter 6

CCA SYSTEM APPLICATION TO WIND TURBINES

6.1 Introduction

This Chapter deals with what are perceived as the more important overall system issues involved in applying circulation control aerofoils to large wind turbines. First, the general implementation strategy (when in use etc.) of the proposed system is outlined. The second section then proceeds to examine the likely efficiencies and head losses incurred in such a system and the power input required to achieve the necessary momentum coefficients, with particular attention paid to the optimisation of the slot dimensions and spanwise position with respect to the power input. Key areas are identified and then expanded on in the following sub-sections which deal with the choice of an appropriate prime mover (fan, blower or compressor), the air inlet, filtration and valve requirements, and finally duct and slot layout (with their possible manufacturing implications). The third section deals with the effects of 'self pumping' due to centrifugal pressure rise in the blade ducts and the resulting power extraction from the rotor.

6.2 Initial CCA Rotor Specification

For the application of circulation control aerofoils to wind turbine blades it is thought that any electrical devices (i.e. valves and their motors) outboard on the blade will be prone to damage due to lightning, as well as the usual wear and reliability issues. Although such devices are not excluded as a possibility and a potential form of 'out-blade' valving is considered, the focus of this thesis will be on a permanently open or passively sealed slot with valves located in the hub. If a system utilising both upper and lower surface jets is used, as suggested here, and valving is located at the hub, it will be necessary to supply the two slots independently of each other, indicating that two separate supply ducts are required. A single duct will suffice if valves are situated at the slots themselves. In either case the degree of circulation control at any point in time is applied by variation of the momentum coefficient, C_μ, through the slots and the systems proposed here will be geared towards simplicity and durability.

Further, due to the energy intensive nature of CCAs, which although clearly an issue, has not proved such a powerful constraint in aviation applications pursued elsewhere, the focus will also be on creating a design which minimises energy input. These requirements alone are fairly onerous, but are deemed essential for any HAWT control system.

It will become apparent in this Chapter and those that follow that even after strenuous efforts are made to reduce the energy input, the level of power consumed by CCAs requires that their operation be restricted to periods when the HAWT is running at, or above, rated power. This is not as limiting as it may first seem, as it is within this part of the operational envelope that HAWTs experience their highest load cases and in which power regulation is needed. As such all assessments are restricted to operation between 15 and 25 m/s.

6.3 Energy Input Assessment and System Design

As indicated by Equations 3.4-3.7 in Chapter 3, energy input requirements to the CCAs may be reduced by use of larger slots, and this has already defined the choice of CCA as being of the jet flap type. As well as the primary energy requirements, the prime mover will also have to overcome pressure losses incurred in delivering air to the slots and these losses should also be reduced as much as possible. The principal losses are pipe friction and pressure drops across fittings such as bends, contractions and the valves required to throttle the air flow. In addition there will be a pressure rise from centrifugal pumping along the blade and the possibility of placing the air intake at the front of the hub, thereby utilising the dynamic pressure present in the wind incident to the turbine.

6.3.1 Primary Ducts

Due to the length (>30m) of the blades on large (>1MW) HAWTs, a significant head loss can be experienced in the blade ducts feeding the slots. For this reason it is desirable to maximise the cross sectional area of the ducts. Fortuitously, the design of modern wind turbine blades includes a substantial amount of void space and it is reasoned that this can be directly utilised for the ducts without adding significant complexity to either the design or manufacture of the blade. Almost all large HAWT blades are manufactured from glass fibre reinforced plastic (GRP) and the construction technique utilised is to make the blade shell in two halves, one half being the upper (or downwind) surface of the blade and the other being the lower (or windward) surface. The two shell halves are then brought together around a box-beam section (also made from GRP) that provides the structural strength of the blade. This structural member is positioned around the 30% chord region, where the profile thickness of the aerofoil is greatest.

In the case where valving is housed in the hub, two independent ducts can be formed by placing a dividing sheet of GRP, running from the structural beam to the trailing edge, between the two blade halves before they are brought together. In order to produce a duct surface with extremely low surface roughness the interior of the blades can be gel-coated (requiring the use of an additional male mold) and polished as is the case with for the exterior surfaces or lined with a material such as PTFE sheet. It is now possible to make an initial energy assessment and optimisation of slot height before considering other sources of pressure loss.

6.3.2 Initial Energy Assessment and Optimisation of Slot Height

For the purpose of the energy assessment the Tjaerborg turbine used in Chapter 7 will be used, due to its well documented nature and appropriate size. The physical details of the Tjaerborg turbine can be found in Appendix 3. As discussed in Chapter 3, if CCA sections are to be effective across a wide operating range, including periods where a significant yaw error is present, they must be positioned outboard of the 50% blade span. Additionally, prior knowledge of tip loss effects suggests that they will not be as effective further outboard than 90-95% of the blade span. As such, energy assessments will be limited to CCAs within this 50-95% span region.

The ideal fan power required per blade, for a range of slot width to chord ratios and momentum coefficient is shown in Figure 6.1 for a slot covering 50-75% of the blade radius. The duct cross sectional area and hydraulic diameter have been defined with relation to a triangular approximation of the aft 70% of the NACA 44XX aerofoil, into which two equally sized ducts have been fitted. The pressure loss in the pipe has been calculated for instances where the entire flow rate required for $C_{\mu\,\max}$ is passing through one of the two ducts. The pressure drop due to friction is a function of the duct characteristics (length, hydraulic diameter, internal surface roughness) and is calculated here using a formula due to Swamee and Jain which is applicable for Reynolds numbers in the range $5 \times 10^3 - 1 \times 10^8$, based on diameter, and specific roughness (k/D) values of $1 \times 10^{-6} - 1 \times 10^{-2}$. It is cited in [127] as,

$$f = \frac{0.25}{\left[\log\left(\left(\frac{k}{3.7 \times d'}\right) + \left(\frac{5.74}{\mathrm{Re}^{0.9}}\right)\right)\right]^2} \tag{6.1}$$

where k is the pipe roughness factor and d' is the hydraulic diameter (defined as, 4 x Cross-sectional area/Wetted perimeter) upon which the Reynold's number is based.

The pipe roughness factor has been defined as $k = 0.00001$m and the Coefficient of Velocity for the slot, $C_v = 0.95$. The blade has been resolved into 0.5m elements for the analysis and the ideal fan power is defined as the product of total volume flow rate and the static pressure rise required.

It can be seen from Figure 6.1 that the relationship (Equation 3.6) indicating that larger slot heights relate to lower power requirements holds to a certain point. However, as the slot size is increased beyond $\delta/c = 0.005$ the increased pipe friction losses due to increased volume flow rate and hence velocity in the duct begin to outweigh energy savings at the slot. Hence for this configuration and others similar to it, the optimum value of slot to chord ratio is found to be 0.005.

Using this slot to chord ratio of 0.005, two further figures are given as Figure 6.2 and Figure 6.3 which show the variation in required ideal fan power for different

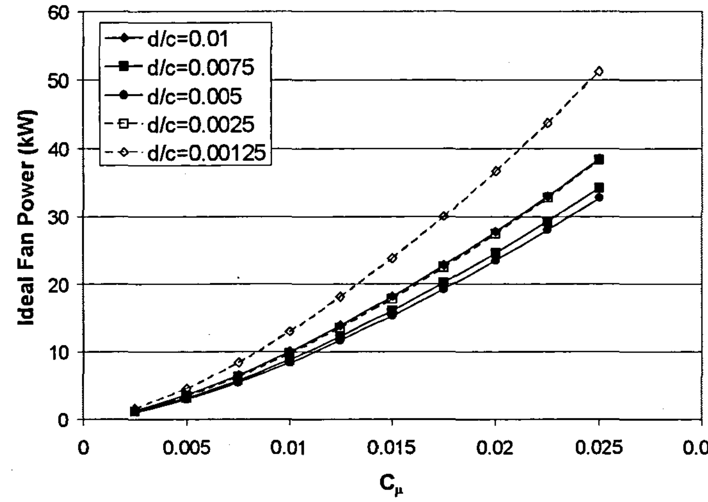

Figure 6.1: Variation of Ideal Fan Power with Slot to Chord Ratio for Range of Momentum Coefficient at a Wind Speed of 25m/s

spanwise locations and percentages of span covered.

Realising that further losses have yet to be taken into account the maximum C_μ feasible would appear to be in the region of 0.01 - 0.02 dependent on the location and length of the slot, if the power consumption of the CCA sections is not to exceed 4-5% of rated power. This level of power consumption is in line with the power absorbed in electrical converter (AC-DC) technologies which enable variable rotor speeds to be achieved. A more accurate figure for the acceptable power consumption can only be determined when the benefits of such a system are quantified.

In the analysis till now it has been assumed that a constant momentum coefficient can be achieved over the length of the slot. The radial variation of relative velocity along the blade span has been taken into account and a constant value of δ/c has been defined. However, this results in a varying jet velocity distribution along the slot which is physically unrealistic as the static pressure distribution that defines the jet velocity will be (at least nominally) constant. There is potential to rectify

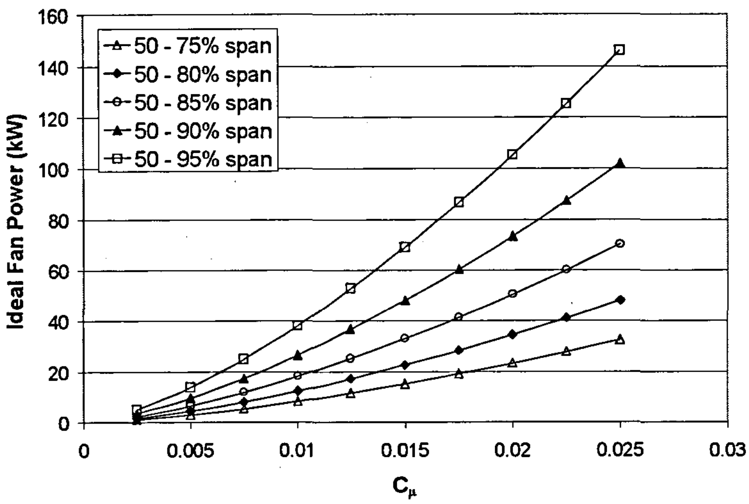

Figure 6.2: Variation of Ideal Fan Power with Increasing Spanwise Coverage of CCAs for a Range of Momentum Coefficient at a Wind Speed of 25m/s

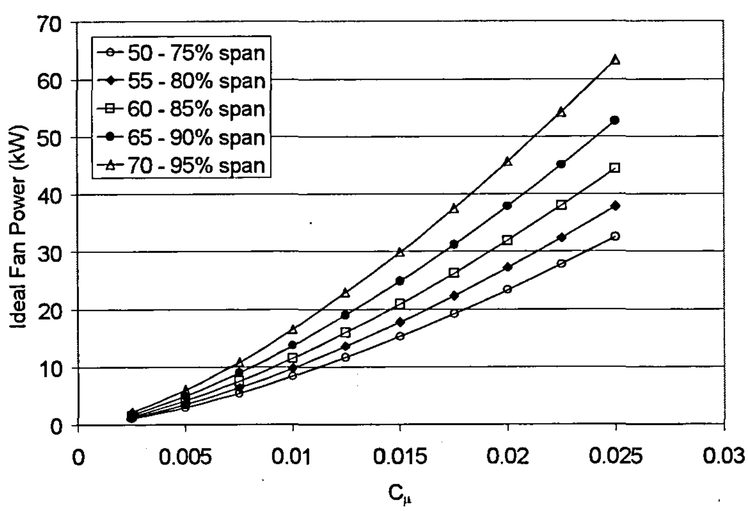

Figure 6.3: Variation of Ideal Fan Power with Different 25% Spanwise Coverage Positions of CCAs for a Range of Momentum Coefficient at a Wind Speed of 25m/s

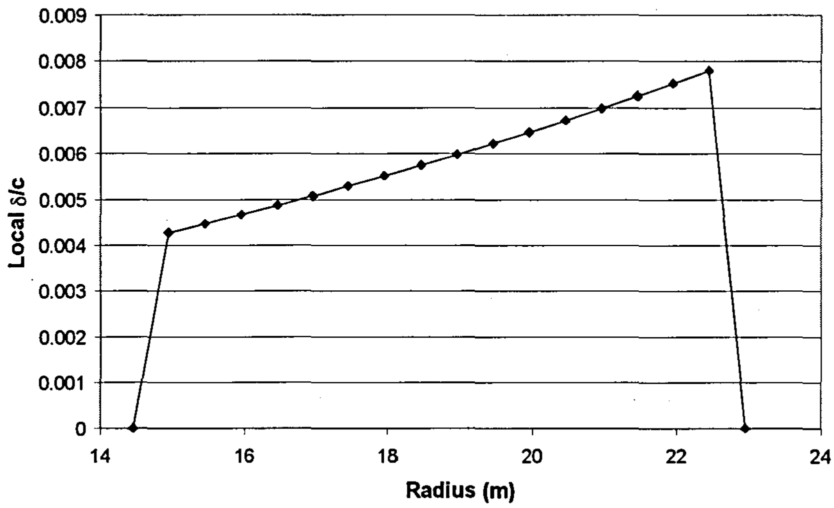

Figure 6.4: Distribution of slot width to chord ratio required to achieve a constant momentum coefficient along slot length of 50-75% span

the problem by varying the δ/c ratio along the slot length, which will have the effect of altering the volume flow rate through each slot element for a given static pressure in the duct. The δ/c distribution required to attain a constant C_μ along the slot is shown in Figure 6.4 for the 50-75% spanwise configuration.

The variation in volume flow rate through each element of the slot for $C_\mu = 0.0025$ is shown in Figure 6.5 along with the physical dimension of the slot width. It should be noted that these values do not account for a capacity coefficient for the slot, but this can be accommodated for when the slot characteristics are known through prototyping.

It is thought that the unequal distribution of two-dimensional momentum coefficient (which is more pronounced in rotorcraft applications where the slot typically extends the length of the blade), along with tip and root effects, explains the reduced gain coefficients documented in helicopter literature [56] when compared with two-dimensional data. Both of these observations are supported by lift and momentum coefficient distributions calculated and measured by Dunham [32].

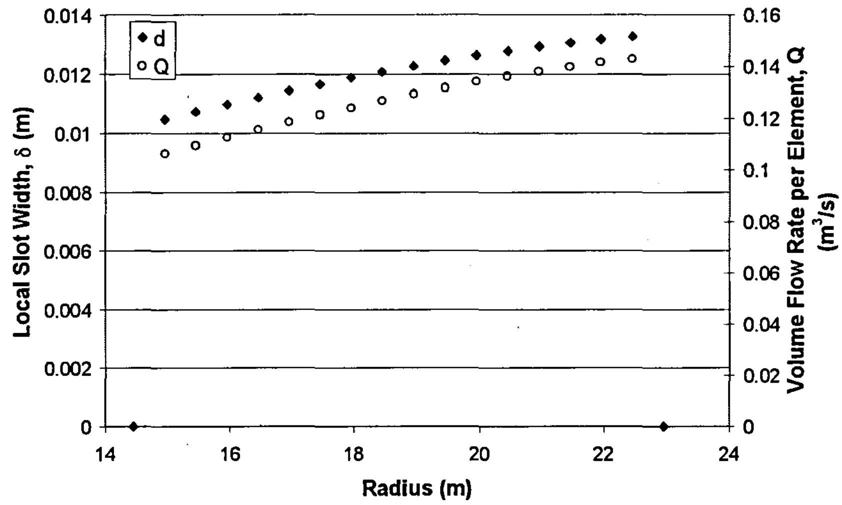

Figure 6.5: Radial Variation of Local Slot Width and Volume Flow Rate per Element for Constant Momentum Coefficient=0.0025 (50-75% span slot)

6.3.3 Other Sources of Pressure Loss and Prime Mover Selection

The number of sources of pressure loss encountered will depend on the type of system layout proposed. However, two sources are unavoidable; they are the pressure drop across the filter required to prevent duct and slot fouling over time and the pressure drop across the valving required to vary the momentum coefficient. The system complexity and further associated pressure losses can be vastly reduced if the prime mover (fan, blower or compressor) can be mounted in the rotating hub, rather than the stationary nacelle. Discussions with pneumatic component suppliers indicate that this rules out the use of a compressor and the use of larger slot heights to reduce power input is also incompatible with compressors, which are designed for high pressure/low volume flow rate applications. Further, housing the air supply unit in the nacelle then necessitates the use of rotating seals and the only route for the supply pipe is along the centre-line of the (hollow) main shaft.

A centrifugal blower or blowers can be mounted in the rotating hub and would be capable of supplying the volume flow rates required at appropriate pressure for any of the slot lengths or spanwise positions presented in Figures 6.2 and 6.3. Details of suitable sizes are given in Appendix 4. Some additional head loss will be experienced with such an arrangement due to the ducting required to link the blower with the three blades, although this may be minimised by using a triple outlet volute casing.

If the pressure and volume flow rates do not exceed $5.5kPa$ and $6.5m^3/s$ respectively, individual Centraxial blowers can be mounted in the root section of each blade. Again details of suitable sizes are given in Appendix 4.

Axial fans may also be considered as an option for mounting in the blade root, although this is limited to slot configurations which use high volume flow rates at pressures less than $3kPa$.

Whichever of the above three options is used, the prime mover(s) will be required to run at full capacity, while the turbine is operating above rated power. It will not be possible to cut them in and out around rated power cut-in ($15m/s$), due to the run up time of the prime mover(s) (typically around 6 seconds). The time scale of mean windspeed changes may make it feasible to run the prime mover(s) over a limited range of Q and P with inverter driven motors in order to produce a constant C_μ over the operating range, but this extra complexity is not considered here. Rather the prime mover is run at its design point and the momentum coefficient is allowed to vary (by approximately 0.0025) between $U_\infty = 15m/s - 25m/s$.

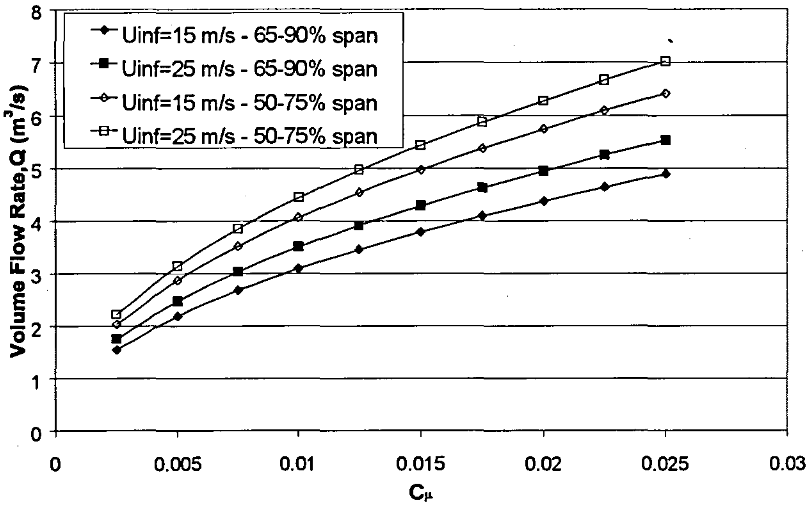

Figure 6.6: Required Volume Flow Rate over a Range of Momentum Coefficients for Two Spanwise Configurations at Rated and Cut-out Wind Speeds

6.3.4 Fan and Blower Sizing

Using appropriate head loss coefficient values of k =0.5 and k =0.2 for the two essential components (a medium gauze filter of approximate solidity=0.3, and an open butterfly valve respectively) and the optimised slot detailed in Figures 6.4 and 6.5, the required static pressure rise and volume flow rates per blade at wind speeds of 15m/s and 25m/s are given in Figures 6.6 and 6.7. Also shown are P and Q requirements for a slot of equal length with a similarly optimised slot, but running spanwise from 65-90% radius.

Considering the 50-75% span case, the static pressure rise required for momentum coefficients above 0.01 is rather high for an axial fan, although the volume flow rates present no problem. However, it is possible to use a contra-rotating axial fan unit, which is basically two axial fans in series. Such units are commercially available off the shelf and the specifications for one such range of fan units is given in Appendix 4. It can be seen that such units can provide static pressure rises up to $3kPa$ at a volume flow rate of $5m^3/s$. Using Figures 6.6 and 6.7 it can be

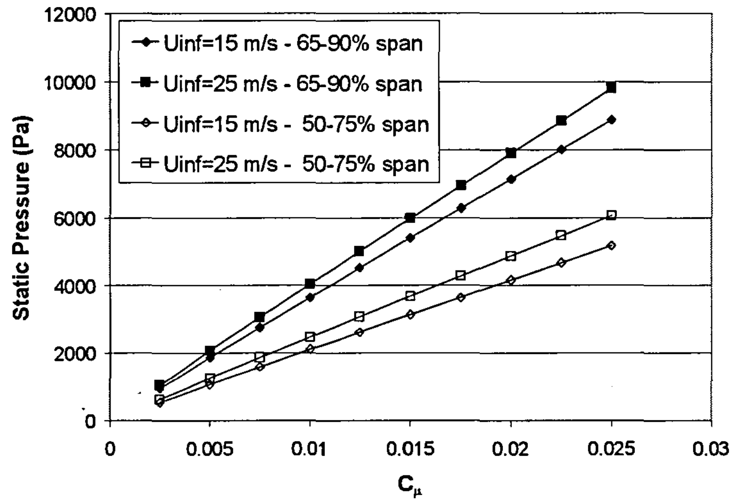

Figure 6.7: Required Static Pressure Rise over a Range of Momentum Coefficients for Two Spanwise Configurations at Rated and Cut-out Wind Speeds

seen that this allows momentum coefficients of 0.015 and 0.0125 to be achieved at wind speeds of 15 and 25m/s respectively. However, the rated power for the two motors combined is 30kW (due to the inefficiencies encountered in combining two axial fans in series), although the physical dimensions are such that it will fit comfortably in the blade root section.

For the 65-90% span case the pressures demanded rise considerably (although the volume flow rates fall). Using one of the Centraxial blowers in each blade, momentum coefficients of 1.5 and 1.25 can be achieved comfortably for wind speeds of 15 and 25m/s. These are rated at approximately 33kW per unit. Alternatively, momentum coefficients of 0.01 and 0.0075 can be achieved comfortably for wind speeds of 15 and 25m/s using units rated at approximately 18kW per unit.

Details of a larger single centrifugal blowers to deliver the two previously specified duties for all three blades are also given in Appendix 4. Their absorbed power levels are 110kW and 55kW respectively

There will also be a centrifugal pressure rise on the order of $650 - 2530Pa$ dependent on the spanwise location along the slot for the examples shown here that will conservatively raise the momentum coefficients at rated and cut-out wind speeds by 0.0025.

Placing the primary air inlet on the front of the HAWT spinner will provide additional total head from the freestream although this will varying with gusting and yaw angle. Again, being conservative, this will not be relied upon to increase the momentum coefficient at the slots, but will be assumed to be adequate to overcome losses due to pipe friction and bends in the primary air intake leading to the filter.

A further resource that should be considered as a means of reducing the pressure demand placed on the fans or blowers is to install a series of curved baffles in the ducts where the slot is present, in order to reclaim a proportion of the dynamic head as a static pressure rise.

6.3.5 Valves and valve drives

In order to vary the momentum coefficient on the upper and lower surface slots it will be necessary to install a valve in each of the two ducts, or at the slots in the case of a single duct layout, as direct variation of the pressure and flow rate levels by altering impeller, guide vane settings or fan speed will not produce changes rapid enough to keep up with 1P variations. Swing-clear, elliptic butterfly valves with electric motor drives are considered suitable for this in the former case. As the blower(s) must be kept running at full power above the turbine's rated power windspeed, an additional valve may be required to allow excess pressure and mass flow to be vented to atmosphere when not required.

As discussed in Chapter 3, water or particle ingress may make open slots unattractive. In this case a series of sliding or rotating valves may be fitted along each slot and these would then be capable of throttling the flow through each duct.

This type of arrangement may be preferable with respect to the duct flow dynamics. Experiment or simulation of each arrangement is suggested, although not undertaken here, in order to assess these options.

A synthesis of the previous options is also proposed whereby the slots are sealed with a flexible membrane that will open under pressure from the air in the duct. This should be fixed at the duct lip closest to the trailing edge, and open from the forward duct lip. When open, such a flap would also further reinforce the action of the expelled air (in the manner of a Gurney flap, although it would consequently incur a drag penalty) and due to its potential simplicity is considered the favoured option.

It should also be borne in mind that the motors required to drive the valves will consume some energy, although this will be of a magnitude considerably lower than the energy demanded by the fans or blowers.

6.3.6 Final Layout and Components

The system layout for the individual, blade root-mounted fans or blowers is shown in the schematic given as Figure 6.8.

It can be seen that the components have been reduced to the minimum in this example, providing a simple and potentially robust system.

6.3.7 Structural implications

In terms of a blade's structural integrity, the formation of slot(s) along a considerable portion of the blade length, presents the greatest challenge. Although the trailing edge region is not in itself of particular load bearing significance the fact that it is part of a shell structure means that any disruption to the contour, must be replaced by some equivalent supports. On previous Coanda CCA helicopter blade prototypes [128] this has been achieved by peg inserts and this maybe ap-

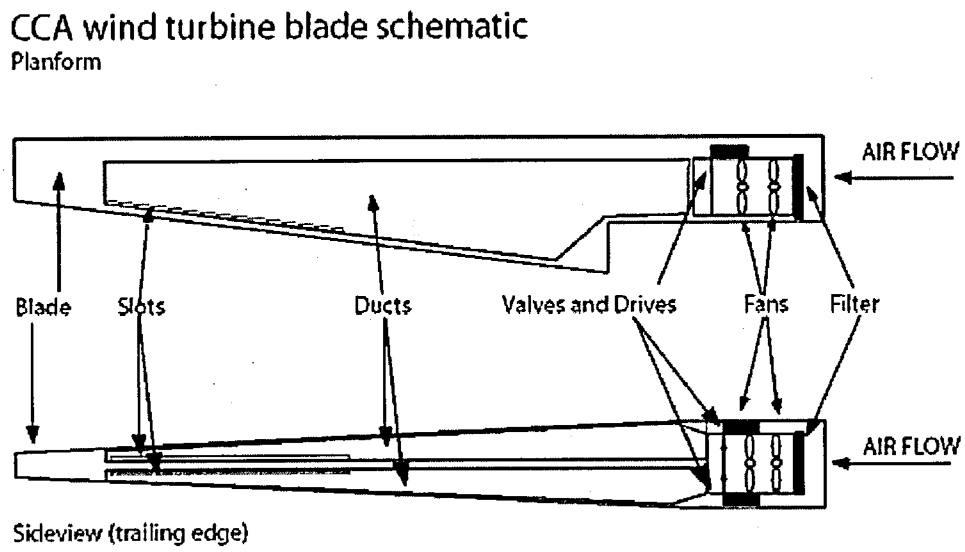

Figure 6.8: Schematic of Suggested CCA Blade Layout for a Horizontal Axis Wind Turbine

propriate for wind turbine blades as well. As mentioned in Chapter 3 the use of jet-flap CCAs rather than those of the Coanda type means that the gap will be flush to the aerofoil surface and not normal to it. The jet-flap CCA slot is therefore nominally aligned in the rotor plane and edgewise loads and deflections of the blade are of an order of magnitude less than those in the flapwise sense. As such the structural implications of a HAWT CCA blade are lessened when a jet-flap rather than Coanda CCA section is used. The detailed design of the blade trailing edge region is beyond the scope of this work.

6.4 Self pumping

A fixed and permanently open slot arrangement, although simpler, brings with it other issues that must be addressed. Firstly, if the slots at the trailing edge of the blade cannot be closed centrifugal pumping of the air within the blade ducts will occur with a related consumption of power (expressed as work done against the Coriolis force) from the wind turbine itself.

Secondly, when the circulation control facility is not required and no pressure is actively created in the blade ducts, there will still be airflow from the slots. This cannot be prevented by sealing the ducts at the root as this still leads to a pressure gradient being created within the ducts along the slots length. This pressure gradient has been found experimentally to be negative at the inboard end of the ducts, rising to a positive pressure at the outboard end [113]. This in turn will result in suction of the external airflow into an (undefined) length of the slots inboard on the blade and a corresponding expulsion of air from the slots outboard. It is thought that, although suction of the external flow (at least on the upper surface) can have a positive effect on aerofoil performance, it should be avoided due to the increased risk of slot fouling.

6.4.1 Quantification of the momentum coefficient resulting from self pumping

The total pressure rise along the blade duct due to the centrifugal action can be calculated, in the first instance, as the pressure rise that would occur in a sealed pipe of the same radius and rotational speed as the blade duct, given as

$$P_{centrif} = \frac{1}{2}\rho\omega^2 r^2 \tag{6.2}$$

Theoretically, assuming no losses across the slot exit (i.e. all the static pressure at each element of the slot is converted to dynamic pressure) and ignoring frictional losses in the duct, the jet velocity is related to the centrifugal pressure rise by

$$P_{centrif} = \frac{1}{2}\rho\omega^2 r^2 = \frac{1}{2}\rho V_j^2 \tag{6.3}$$

That is the jet velocity at each element along the slot is equal to the product of the rotational speed, ω, and the radius of each element.

The theoretical momentum coefficient for a wind turbine where the freestream velocity is the relative velocity seen at the blade is then given as

$$C_\mu = \frac{\rho V_j^2 \delta}{\frac{1}{2}\rho U_{rel}^2 c} = \frac{2(\omega r)^2 \delta}{U_{rel}^2 c} \tag{6.4}$$

The square of the ratio between the jet velocity and the relative windspeed at 50% and 95% radius (the most inboard and outboard sections on the blade span where a slot has been considered here) then defines the maximum and minimum theoretical momentum coefficients along the blade for a given slot to chord ratio. For the Tjaerborg turbine operating at $25m/s$ these are given by Equations 6.5 and 6.6

$$C_{\mu\,\mathrm{min}} = 1.32\frac{\delta}{c} \tag{6.5}$$

$$C_{\mu\,\mathrm{max}} = 1.78\frac{\delta}{c} \tag{6.6}$$

As already noted, the work required to produce the momentum coefficient experienced at the slot in this manner comes from work done against the Coriolis force. The Coriolis force is given by Equation 6.7

$$Force_{Coriolis} = 2mv\omega \tag{6.7}$$

where m is the mass of the fluid travelling along the duct at velocity, v, which is rotating at a rotational speed, ω

The mass of the fluid can be expressed as the density of the fluid and the volume of the duct like

$$m = \rho A r \tag{6.8}$$

where A is the duct cross sectional area and r is its length

and the velocity along the duct can be expressed as the volume flow rate, Q, divided by the cross sectional area, A

$$v = \frac{Q}{A} \tag{6.9}$$

Substituting Equations 6.8 and 6.9 into 6.7 and knowing that the mass flow rate, $\dot{m}$, is the product of the volume flow rate, Q, and the fluid density, ρ, the Coriolis force can then be expressed as

$$Force_{Coriolis} = 2\,\dot{m}\,r\omega \tag{6.10}$$

The power extraction per blade from the rotor is therefore given by the relationship

$$Power_{Coriolis} = 2\omega^2 \int^{R} \dot{m}\,r \quad dr \tag{6.11}$$

As noted by Nichols [129], the efficiency of this self-pump action is always 50% i.e. the power extraction due to Coriolis is twice the centrifugal power input (defined as the product of the pressure rise and subsequent volume flow rate). This can be clearly seen if the mass flow rate is assumed constant along the duct i.e. not dependent on r (which is the case if the duct is of constant cross-section and vented at the far end) and Equation 6.11 is integrated. The efficiency thus defined is given as

$$Self\ Pump\ Efficiency = \frac{Power_{Centrif}}{Power_{Coriolis}} = \frac{\frac{1}{2}\omega^2 r^2 \rho Q}{\omega^2 r^2\ \dot{m}} = 50\% \qquad (6.12)$$

For a slot having a constant $\delta/c = 0.005$ and a spanwise extent of 50-75%, the self pump momentum coefficient varies between 0.0066 and 0.0084. For such a frictionless, lossless CCA blade the power extraction due to the Coriolis force is approximately 6kW per slot.

A better approximation of the momentum coefficient produced and power extracted from the rotor due to the Coriolis force in the case where there is no active pumping, may be achieved by reasoning that the volume flow rate of air which will flow in the duct is determined by the balance between the pressure drop due to frictional losses in the pipe and the pressure rise due to centrifugal compression. Again the friction factor, f, is calculated using Equation 6.1 and the pipe roughness factor, k, is as defined previously. A further approximation (and without empirical evidence to support or refute the assumption) is that the volume flow rate created by the centrifugal pumping is said to exit the slot in an evenly distributed manner and the slot velocity is equal to the volume flow rate divided by the slot width. Calculating in this manner an average passive, self-pump momentum coefficient of 0.0032 is found for a 50-75% span CCA with $\delta/c = 0.005$. The power extraction in this case is calculated as 3.2kW per blade per slot. The volume flow rates along the duct and through the slot along with

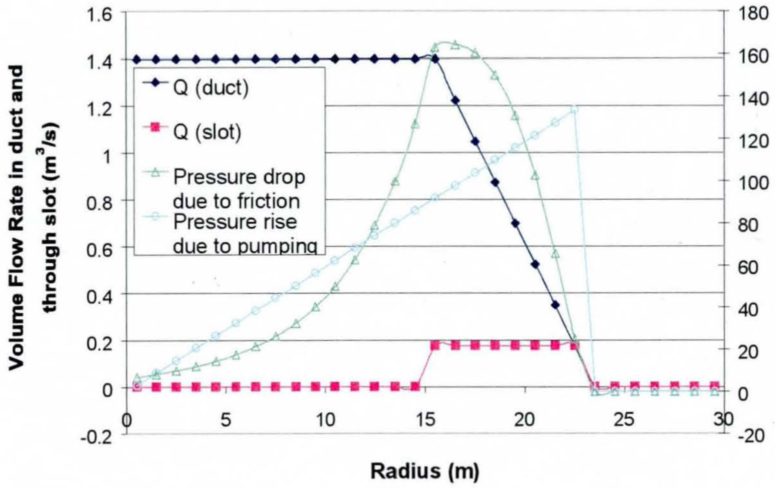

Figure 6.9: Pressure and Volume Flow Rate Characteristics for Self Pump Scenario

the associated pressure drop and pressure rise are shown in Figure 6.9. It can be seen that the pressure balance is conducted on a global level, rather than on an element by element basis.

It should be remembered that the momentum coefficient will be experienced by both upper and lower surface slots when not supplied with air from the fan and, based on the findings in the previous Chapter for actively and passively supplied jets, will result in significantly reduced performance of the actively supplied jet. This then provides a further argument for the use of either passively sealed slots or positioning the valves at the slots themselves.

6.5 Summary

- The energy requirements to produce significant levels of blowing over a sensible portion of the blade span have been quantified. These are substantial and the amount of power that can be acceptable is set at 4-5% of rated power. This limit will provide a hard cap on the affect that CCA sections can have on the regulation of blade forces.

- A detailed system layout and associated set of component specifications have been proposed for the application of CCAs to large HAWTs, which has focused on reducing the complexity and reliability of the system. This has resulted in a system which employs permanently open slots to which the flow is throttled by the use of valves in the blade root as a means of varying the momentum coefficient at the blade.

- The delivery of air to the slots can be achieved using the void space present in a large HAWT blade, thus maximising cross-sectional area and reducing frictional losses.

- The optimum slot width (defined as that which results in the greatest momentum coefficient for the smallest energy input) has been identified and a spanwise slot distribution which results in a constant momentum coefficient along the slot length has been defined.

- The pressure losses due to pipe friction, filtration and valves have been quantified and different, suitable prime movers to supply the air to the slots have been suggested for various $C_{\mu\,\max}$ and spanwise positions/extents of the slots. These include a contra-rotating axial fan unit and a Centraxial blower that has suitable pressure rise and volume flow rate characteristics and can be mounted in the blade root, as well as a single centrifugal blower that can be mounted in the nacelle.

- The power extraction from the rotor due to centrifugal pumping and the associated Coriolis power consumption has been quantified along with the resulting momentum coefficient for a theoretical, lossless system. A second, less simplified approach at analysis has also been conducted, although significant assumptions are still made. Neither analysis is considered sophisticated enough to provide an adequate estimate of the self pumping effects, however, significant effects are predicted and further work is required in this area in order to make a thorough assessment of the need for sealing at the slots.

Chapter 7

Application to Wind Turbines

7.1 Introduction

This Chapter presents results obtained using the previously derived two dimensional CCA data in conjunction with the BEM code, Fast_AD.v4 (FAD4) [130] in order to assess likely areas in which CCAs may be usefully applied in wind turbine design.

Firstly, a resume of the important elements of the FAD4 code is presented, including descriptions of the dynamic inflow and dynamic stall models used by the code. Secondly, details of the Tjaerborg turbine and its representation for simulation are given and results validating the model against several well documented test cases are shown.

The data derived in Chapters 4 and 5 is then extended to cover the stall region with reference to experimental Gurney flap data. The 360° range of angle of attack and dynamic stall data required by FAD4 are then generated using the program FoilCheck [131]. The model is then adapted, using this data, to represent blades fitted with NACA44XX CCAs.

As this thesis has dealt predominantly with the development of a variant of circulation control aerofoil suitable for use with wind turbines, the author is content here to examine potential applications for such devices on large wind turbines.

7.2 Background to BEM code, Fast_AD

As previously discussed in Chapter 4, engineering simulation tools for HAWTs are currently based on the classical BEM theory, although many adaptations and improvements have been developed in the last ten years to allow improved prediction of aerodynamic loads. These improvements have generally been in the manner in which time dependant effects are represented (classical BEM assumes equilibrium conditions) and are discussed in the following section.

As BEM based simulation codes rely on 2D aerofoil data as a primary input, much work has also been dedicated to developing methods by which readily available wind tunnel data for aerofoil sections can be extended to account for dynamic stall and rotational effects. FAD4 offers the ability to use a dynamic stall model due to Beddoes and Leishman [132], although no rotational separated flow effects have been modelled in, for example, the manner of Snel [133]. This is not thought be significant, as on a pitch regulated turbine, at the mid to outboard blade sections that are of interest with regard to the use of CCA sections, rotational effects are minimal compared to the inboard section on a stall regulated turbine.

7.2.1 Code Description

FAD4 is written in Fortran90 by staff at NREL and the Oregon State University and is available as freeware in its source code format. For a three-bladed HAWT, it has the capability of modelling up to 16 degrees-of-freedom, using a modal representation of the blade and tower deflections in order to introduce structural flexibility to these major model elements. The code has been widely used for wind turbine design, as well as being validated (for accuracy in both aerodynamic and structural modelling) against experimental data and the ADAMS WT code [134] [130].

The aerodynamic sub-routines used in FAD4, collectively known as AeroDyn.v12.46 (AD12) [131], are also common to YawDyn (a simpler NREL code that represents the HAWT blades with a simple spring-hinge model) and AdamsWT (a HAWT sub-set of the generalised dynamics modelling package, Adams), which are capable of structural modelling of lesser and greater complexity, respectively. AD12 allows use of a classical BEM approach or a more advanced method using dynamic inflow theory for predicting the aerodynamic loads on a wind turbine's blades and hence overall structure. The latter has been used in the simulations presented here. Details of some of the more important elements of the code are given below. The turbulent windfields used in the simulations have been generated with the NREL code SNWind [135].

Dynamic Inflow Model

The dynamic inflow phenomenon occurs in wind turbine operation when the rotor experiences a rapid change of pitch angle, yaw angle or windspeed. Under these conditions the equilibrium wake reached by iteration in classical BEM theory will not replicate the transient loads which are known to occur. Essentially, dynamic inflow introduces a time lag to the induced velocities experienced in the rotor plane, in response to the (near) step change in wind speed or blade pitch angle. The appropriate time scale for dynamic inflow events is given by D_{rotor}/U_{∞}, which for modern, utility scale wind turbines is of the order of 1-10 seconds.

The dynamic inflow model used in AeroDyn12 (and hence, the FAST_AD code) is an adaptation, due to Suzuki [136], of the Generalised Dynamic Wake model [137] developed for rotorcraft from the theory of Pitt and Peters [138]. All these models use a finite set of superimposed velocity fields to represent the induced velocities created by a rotor. In the case of the Pitt and Peter's model, 3 velocity distributions are used (a mean distribution uniform across the rotor plane and two terms which vary respectively with the sine and cosine of the azimuth angle). In the GDW model the number of distributions are theoretically infinite, but are restricted to 6 in Suzuki's implementation. The velocity distributions are determined by polynomials of a particular sort, known as Legendre functions. Representation of tip loss effects are inherent in the GDW model.

Yawed Flow Model

Yawed rotor conditions are said to occur when the wind incident on the rotor plane is no longer normal to it. The resulting flow conditions are complex and not yet fully understood, although the resulting blades loads are known to be the result of a combination of the advancing/retreating blade effect, and the non-uniform induced velocities caused by the axially asymmetrical wake behind the rotor and each blade's azimuthal position relative to it. Classical BEM uses a skewed wake correction factor to try and account for the asymmetry of the induced velocities (and hence loading) in the rotor plane, which occurs during yawed operation. The dynamic inflow model described previously has an inherent ability to account for such asymmetric flow conditions due to its multi-component treatment of the induced velocity field.

Dynamic Stall Model

Dynamic stall (or stall hysteresis) occurs when the angle of attack of an aerofoil section changes rapidly in time and the aerofoil is close to or beyond α_{stall}, although milder hysteresis loops are also evidenced when α varies in time in the fully attached flow region. In wind turbine operation this is the norm rather than the exception:- due to turbulence the wind incident at the rotor is time varying;

yawed operation creates a variation of α over each revolution; structural flexibility allows a blade motion dominated by flapping (motion in and out of the rotor plane); as well as the changes introduced by pitch regulated or variable speed operation. This time varying motion means that the static lift and drag data available for most aerofoils is generally inadequate for wind turbine modelling. However, it can be used as the basis for determining more appropriate lift and drag data in conjunction with knowledge of the reduced frequency, k, of the relative motion of the aerofoil and incident wind (the reduced frequency, k, is usually related to the pitching oscillation frequency and this is assumed to be valid for cases where the aerofoil is describing a plunging motion, which is more often the case for torsionally stiff wind turbine blades).

The appropriate time scale for dynamic stall events is given by $c/\Omega R$, which for wind turbines is of the order of 0.01-0.1 seconds. The dynamic stall model implemented in AeroDyn12 is that due to Beddoes and Leishmann [132], which unlike other models [139] does not require any calibration or empirical information other than the steady state lift and drag data for the aerofoil.

7.3 Tjaerborg Turbine Model Description

7.3.1 Specification of Tjaerborg 2MW HAWT

The Tjaerborg 2MW turbine is a three-bladed, upwind turbine with power control achieved by a single, hydraulically driven blade pitch mechanism. The rotor diameter is 61.1m and its speed is nominally constant around 22 rpm, having an induction generator with 2% slip driven through an epicyclic gearbox. Further details can be found in [116] and in Appendix 3, which also shows the input files used to specify the turbine in FAD4. The blades are each represented by 33 elements of equal length, with appropriate values of chord, twist, blade mass and edgewise and flapwise stiffness specified at each mid-element position. The edgewise and flapwise natural frequencies are matched to the measured values and the modal shapes of the blade are determined using the FAD4 ancillary program, Modes.v222 [140]. Similar details are provided and determined for the tower. Again the exact specifications used can be found in the input files shown in Appendix 3.

7.3.2 Aerofoil Data

The aerofoil data used for the plain NACA 44XX sections is that presented in various ECN reports [116]. For the CCA sections appropriate increments were added to this lift and drag data as determined by the CFD simulations of this aerofoil reported in Chapter 5. Additional adjustments were made to this data in accordance with the findings made for the FX77w153 aerofoil at extremely low momentum coefficients and subsequent checks were made on this data using an extended mesh for the NACA 4415.

As no time dependant CFD simulations were conducted and steady state data is only possible to achieve into the light stall regime, post-stall data has been determined based on experimental observations in the literature. Using the similarity previously established between the behaviour of jet-flap CCAs at low momentum coefficients and aerofoils with Gurney flaps in the attached and lightly separated flow regimes, experimentally derived data for aerofoils fitted with Gurney flaps in deeper stall conditions [72] [67] has been used as a guide in extrapolating the lift and drag curves for the NACA 4415 CCA from 12° to 24°. Using [72] it can be seen that the Gurney flap, post-stall behaviour follows the pattern of a very slightly decreased stall angle (albeit at a higher lift coefficient), a steeper initial post-stall curve and a higher deep stall lift value compared to the plain aerofoil. As Gurney flaps increase the lift value in deep stall, it is assumed here that the jet

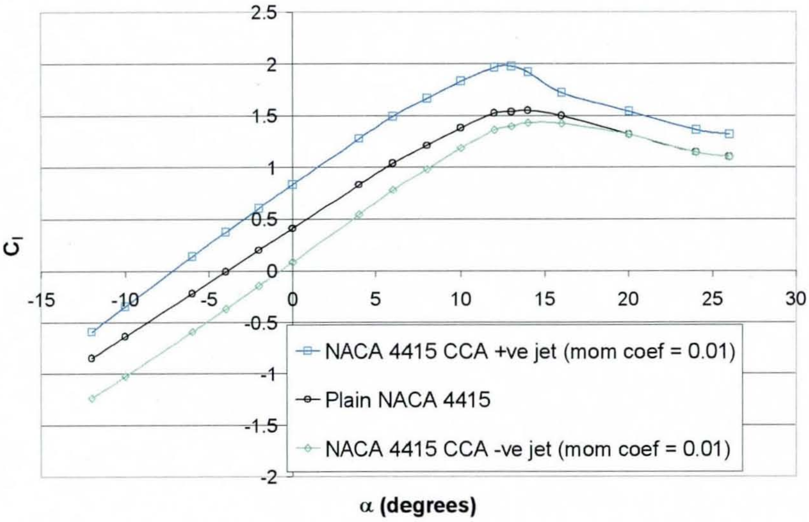

Figure 7.1: Lift Data for NACA 4415 CCAs Derived from Gurney Flap Relationship

flap CCA will exhibit similar characteristics. For the negative jet deflections for which no similar experimental data exists, the stall is reasoned to be gradual and the blown lift coefficient is allowed to merge with the plain aerofoil value at 20°. The data produced in this manner can be seen in Figure 7.1 for the $C_\mu = 0.01$ case with negative and positive jets and is compared with the NACA 4415 section in its plain configuration.

The data for $\alpha = -2° - 24°$ was then used in conjunction with the FoilCheck program [131] provided with the AD12 code, in order to determine appropriate data for the aerofoil sections over the range $\alpha = -180° - +180°$. It should be noted that the primary reason for defining aerofoil data over such a wide range is to satisfy the software requirements and prevent run-time crashes. During the simulations conducted the angle of attack for the CCA sections so defined rarely exceeds $-7°/+14°$. At the same time the author considers the arguments used to derive the $\alpha = -2° - 24°$ CCA data to be sufficiently robust. AD12 allows the specification of any number of aerofoil data sets, which can be used to represent the variation of any appropriate variable, such as Reynold's number. Each set of lift and drag data is identified with a given operating point in the input file (in this case the magnitude of the momentum coefficient), and AD12 interpolates between the tables at each time step in accordance with the state of the variable, in order to provide appropriate lift and drag data for that point in time. Tables for $C_\mu = \pm 0.001, 0.003, 0.005, 0.01, 0.02$ were used in the input file, as well as the lift and drag table for the plain aerofoil, all of which can be seen in Appendix 3. No adjustments have been made to CCA sections at either end of the slot where interaction between blown and non-blown span sections will occur [56]. No time dependant CFD simulations were carried out for any of the aerofoils and changes in aerofoil circulation due to changes in momentum coefficient are assumed to be instantaneous from the point in time at which the momentum coefficient changes at the slot exit. Work by Ghee and Leishman [65] justifies using static lift values as a *conservative* estimate, as long as reduced jet frequencies (defined as $\omega_j c/2V_\infty$ where ω_j is the jet frequency) do not exceed 0.2. This is generally adhered to in the simulations presented.

7.3.3 Controller logic

In order to provide an appropriately detailed assessment of the performance of the Tjaerborg turbine with and without CCAs, it is essential to be able to model the turbine's performance in a realistic time-varying wind field. In order to achieve this the simulations must include a representation of the controller logic used to maximise the energy capture below rated power and limit the energy capture above the rated windspeed. This has been achieved using Equation 7.1 to represent the dominant proportional-integral action of the PID controller for the demanded pitch rate in degrees/second, as suggested by Oye [116].

$$\dot{\theta}_p = \frac{0.02(P_{ELEC} - 2000)}{(1 + \theta_p/4.6)} \tag{7.1}$$

Anti-wind up has also been implemented in the sub-routine controlling the pitch action. The coding takes the form of a saturation function and can be seen in Appendix 3.

A first order time lag with a time constant 0.25s has also been included to represent the response of the hydraulic pitch actuators, also after Oye [116].

7.3.4 Test and validation cases

The ECN report, Joint Investigation of Dynamic Inflow Effects and Implementation of an Engineering Method [116] details several suitable test cases from the Tjaerborg turbine. The comparison between the model used here and the experimental results for yawed flow conditions is shown in Figure 7.2 for test case VII.1 [116]. Comparison of the measured and predicted results for three other yawed test cases are given in Appendix 5. In all cases a steady wind condition is used with the wind shear exponent varying between 0.17 and 0.31 and the flatwise blade moments are measured at r=2.75m.

It can be seen that (in common with the other results presented in Appendix 5) the agreement is generally good, indicating that the FAD4 code and the model of the Tjaerborg turbine specified here are appropriate for modelling structural and aerodynamic response in yawed and un-yawed flow conditions.

7.4 CCA Position on Blade

Following the energy input assessments made in Chapter 6 of the variation of energy demand that occurs for different CCA lengths and spanwise positions, the

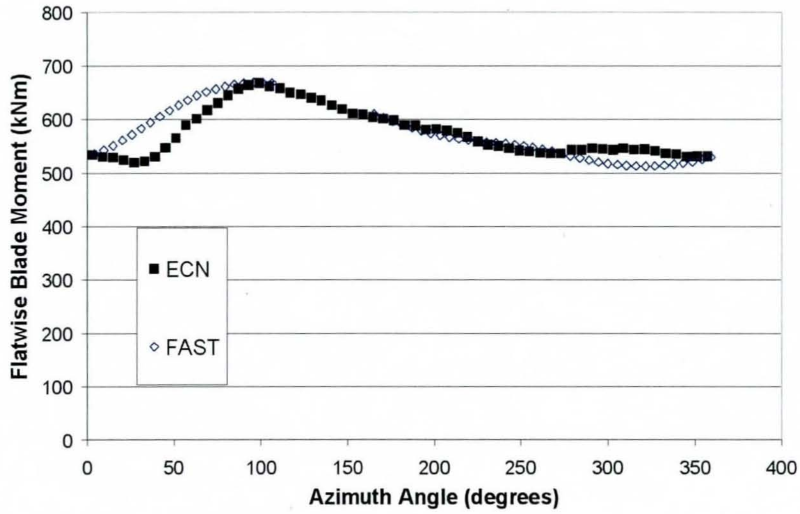

Figure 7.2: Measured and Predicted Flatwise Blade Moments at r=2.75m (Yaw Error = 32 degrees, Uinf = 8.5m/s, wind shear exponent = 0.31)

effectiveness of the CCA sections in these different configurations is simulated here. The wind conditions are artificial (steady wind with no shear), but are appropriate to this brief assessment. The results are presented as the change made to the generator power. In all cases the wind speed is 20m/s and the pitch angle of the blades is kept constant at 15° (in this rotor state no limitations are placed upon the additional force generated by the CCAs due to axial induction factors exceeding 1/3). Figure 7.3 shows ΔP_{gen} for 25% blown sections at different spanwise positions, using $C_\mu = 0.01$.

Firstly, it can be seen that moving the CCA sections beyond the 90% span region initially provides a diminishing return (68-94% span) and then an actual reduction in the change to power output (74-100% span). This is due to the tip losses experienced by the blades. At the same time reference to Figure 6.3 shows that the input power required increases as the CCA sections are moved outboard. Clearly placing the CCA sections beyond the 90% span point is an inefficient use of the input power.

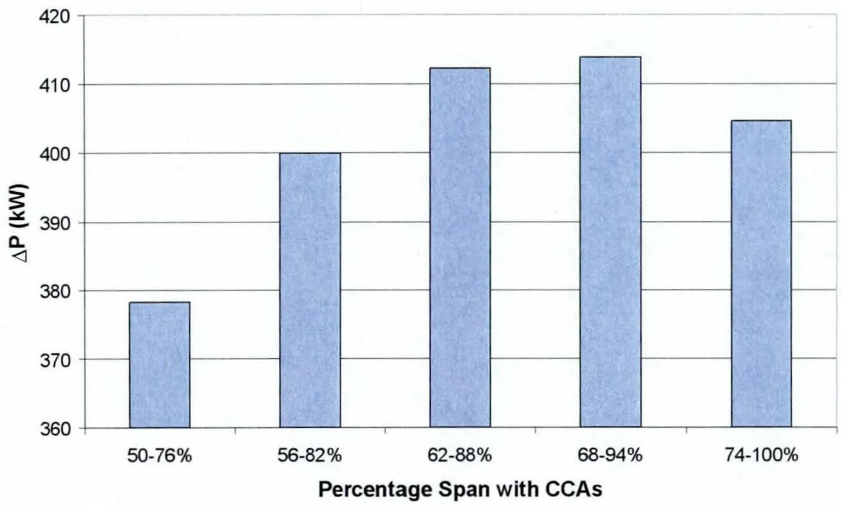

Figure 7.3: Change in Power Output Caused by Presence of +ve jet CCAs (momentum coefficient = 0.01)

The length of the CCA section is next considered. Figure 7.4 presents the change in power output non-dimensionalised by the corresponding ideal fan power for three different spanwise lengths of CCA section.

All three cases use $C_\mu = 0.01$ and it can be seen that in this case the most effective use of the input power is achieved by restricting the CCA sections to 26% of the span, positioned from 62% span outward. It is also recognised that specifying a lower maximum momentum coefficient and extending the spanwise extent of the CCAs is another viable alternative, due to the non-linear variation of ΔC_l with C_μ.

7.5 Power Control

In order to give an initial feel for the degree of power control that maybe achievable with CCA equipped HAWT blades results from simulations with steady windfields are given in Table 7.1. In all cases the CCA slots extend from 62-88% of the blade radius as determined previously and $C_\mu = 0.01$.

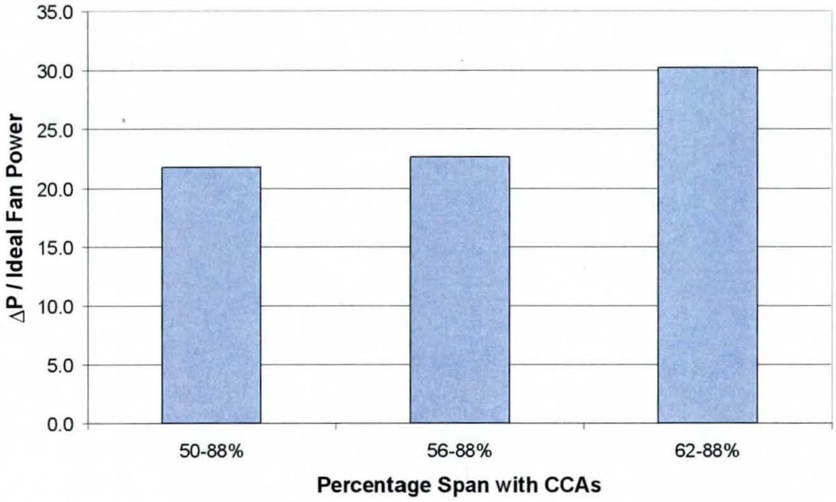

Figure 7.4: Specific Change in Power Output Caused by Presence of +ve jet CCAs over Three Different Span Lengths (momentum coefficient = 0.01)

U_∞	CCA +ve jet	Plain aerofoils	CCA -ve jet
16m/s	2253kW	1979kW	1819kW
20m/s	2454kW	2048kW	1767kW
25m/s	2488kW	1952kW	1469kW

Table 7.1: Variation of Changes to Rated Power with Positive and Negative Jets for 2MW HAWT with 62-88% span CCAs ($C_\mu = 0.01$)

The increasing effect experienced with rising wind speed occurs primarily because the energy present in the wind is increased (due to the higher wind speed and lower induction factor at the rotor), so for a given change in C_l (i.e. ΔC_μ), a greater increase (or decrease) of blade forces is experienced. This is exactly the same effect that occurs with blade pitch and is the reason why the gain used in a pitch controller falls off with increasing wind speed. In practice, this effect will be reduced, as for a fan or blower running at constant duty the energy that produces $C_\mu = 0.01$ at 16m/s will produce a lower momentum coefficient at 25m/s, as can be seen from Figures 6.6 and 6.7. However, there is a secondary effect that occurs, particularly with respect to the negative jet. This is due to the variation of ΔC_l with angle of attack; referring to Figure 5.18 it can be seen that the efficacy of the negative jet is greatest at lower angles of attack for reasons discussed in Chapter 5. At 16m/s the mean angle of attack at 70% radius is 4°, while at 25m/s it is $-3°$.

Blades fitted with CCAs should be capable of responding faster to both turbulent gusting and coherent gusts in the windfield than pitch control mechanisms, due to the physical limitations placed upon actuator size and the adverse structural loads that can be imposed by excessive blade pitch action. The results presented below in Figures 7.5-7.10 compare the power output and blade pitch variation of the Tjaerborg turbine with and without CCAs present, as well as showing the demanded CCA variation with time.

The control used to drive the CCA variation is of the same proportional, integral control used for the blade pitching, as given in 7.1, although the proportional constant used is 2×10^{-5} rather than 0.02 and no gain scheduling (represented by the denominator of Equation 7.1) has been used. It is accepted that this is a rather simplistic approach, arrived at by varying the proportional constant in order to achieve a fast, but reasonably stable response. However, the development of suitable control techniques are beyond the scope of this thesis and are considered a suitable area for further work.

No representation of the time lag which will be introduced by the pressure wave propagation and transient fluid dynamics within the duct or ducts, or by the valve dynamics have been implemented as these require experimental investigation to define. As such the results can be viewed as a best case scenario for a CCA system layout where valving is located in the hub (the pressure wave propagation time is approximately 0.08 seconds for a blade of these dimensions) or as a fair approximation for a system where valving is located at the trailing edge. This should be remembered when viewing all the results presented in this Chapter.

The variation of $C_{\mu\,\max}$ (i.e. the momentum coefficient for a given blower specification (Q and P) at the slot when the valve for that duct is fully open and the valve for the other duct is fully closed) with wind speed changes between rated power (15m/s) and cut-out (25m/s) is approximately 0.0025. The variation is linear and is specified in the simulation as 7.2

$$C_{\mu\,\max} = C_{\mu\,\max\,rated} - ((U_{HH} - 15) \times 0.0025) \tag{7.2}$$

where U_{HH} is the instantaneous hub height wind speed and $C_{\mu\,\max\,rated}$ is the maximum momentum coefficient attainable by the blower at a wind speed of 15m/s (which is specified in the CCA input file, see Appendix 3). This maximum is negative in the case of the upper surface jet and Equation 7.2 is adjusted to reflect this.

For all the simulations presented in this Chapter, CCAs are specified over 62-88% of the blade span and $C_{\mu\,\max\,rated}$ is set at 0.01. This configuration requires an absorbed power level of approximately 55kW for all 3 blades, excluding the power required to drive the control valves. All the simulations use the pitch controller previously specified.

Figure 7.5 shows the hub-height wind speed and resulting pitch action of the blades with and without CCAs in a 10 minute windfield with a mean hub height windspeed of 20m/s and a turbulence intensity of 8%.

Figures 7.6 and 7.7 show the subsequent power output and the required response of the CCA sections.

It can be seen that as well as generally improving the power quality, the pitch duty is also significantly reduced. In fact the main effect of using the CCAs with this

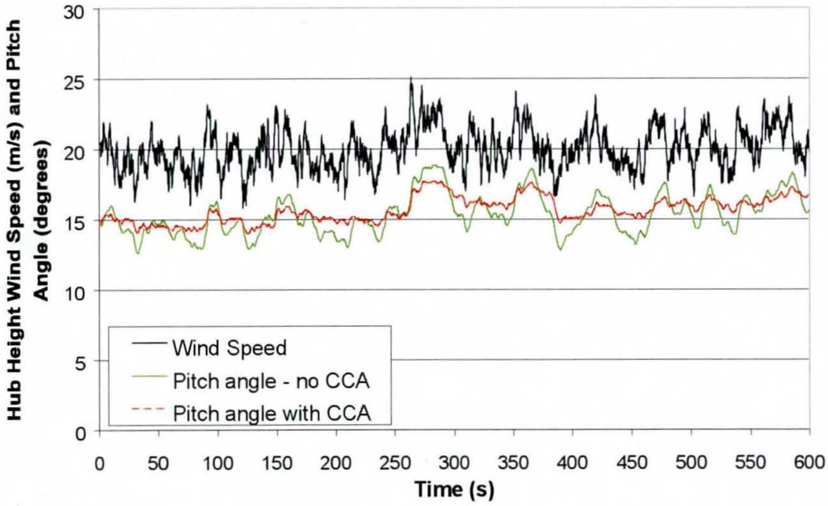

Figure 7.5: Hub Height Windspeed and Pitch Action with and without CCAs at a Mean Windspeed of 20m/s with Turbulence Intensity of 8%

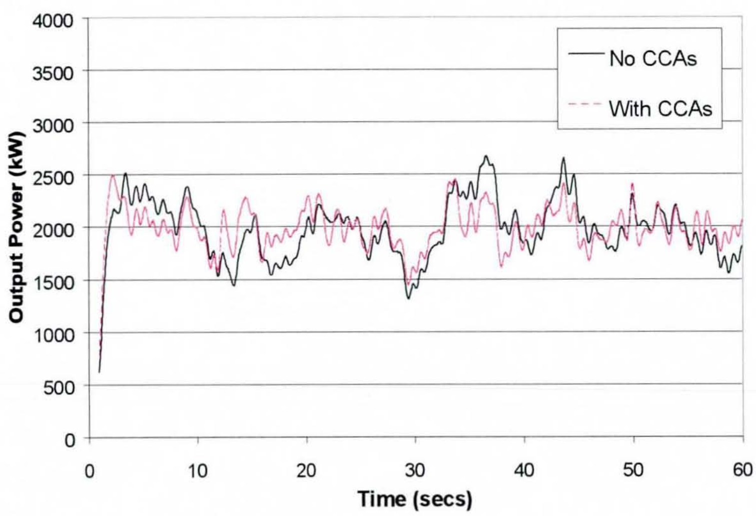

Figure 7.6: Resulting Power Output with and without CCA sections over a Representative 1 minute period (U=20m/s, TI=8%)

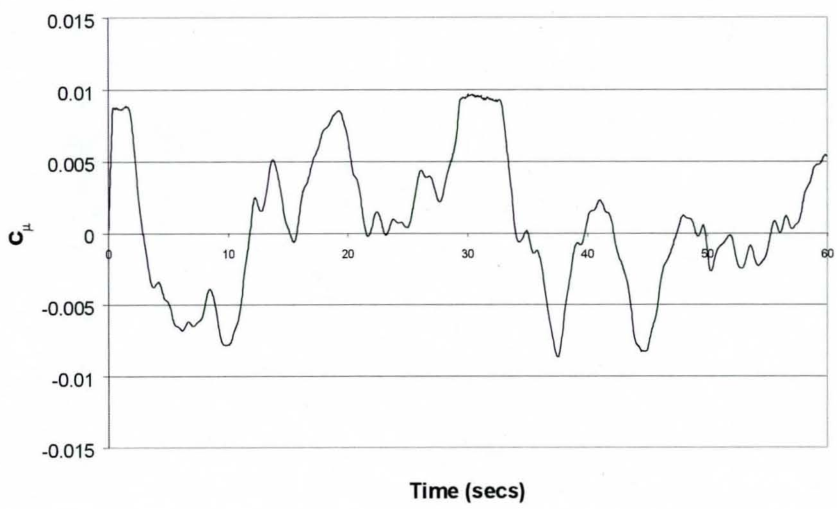

Figure 7.7: CCA Action over a Representative 1 minute period (U=20m/s, TI=8%)

type of control is to reduce the pitch duty (rather than significantly improving the power quality). This may have potential in itself, but it is clear that if the pitch actuation were maintained at the same level which exists in the case without CCAs that the improvement in power quality would be greater. However, the control implementation of CCAs used here is also capable of degrading the power quality as witnessed by the increased power excursions above and below rated power around $t = 15s$ and $t = 37s$.

It is also seen in Figure 7.7 that the demand placed on the CCA sections is quite modest and it is thought that more appropriate control should be able to further exploit the potential rapid response time that CCAs offer. The variation of the maximum momentum coefficient with windspeed (for conditions of constant Q and P from the blower(s)) can be seen to have been effectively implemented in the simulation.

Increasing the turbulence intensity in the windfield to an IEC class B windfield produces the results shown in Figures 7.8-7.10.

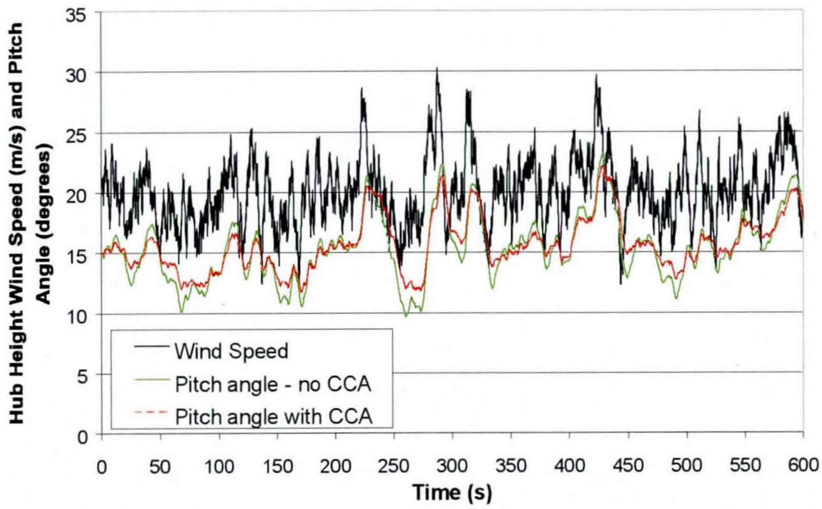

Figure 7.8: Hub Height Windspeed and Pitch Action with and without CCAs at a Mean Windspeed of 20m/s with IEC Turbulence Intensity Class B

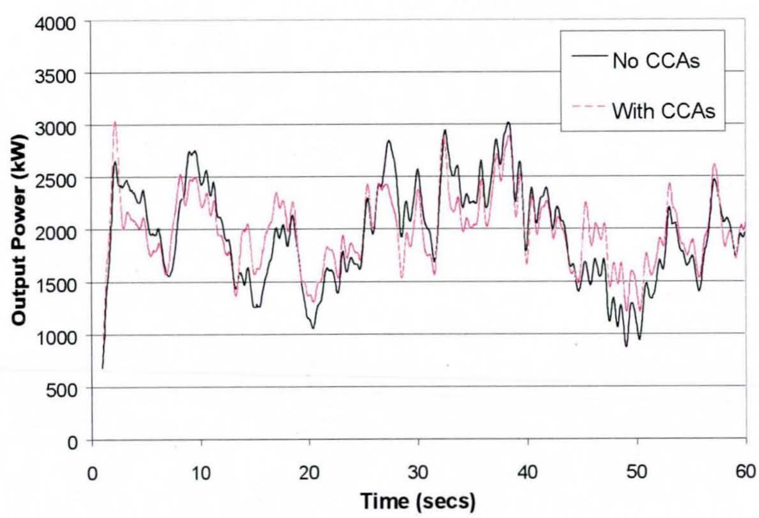

Figure 7.9: Resulting Power Output with and without CCA sections over a Representative 1 minute period (U=20m/s, IEC Turbulence Class B)

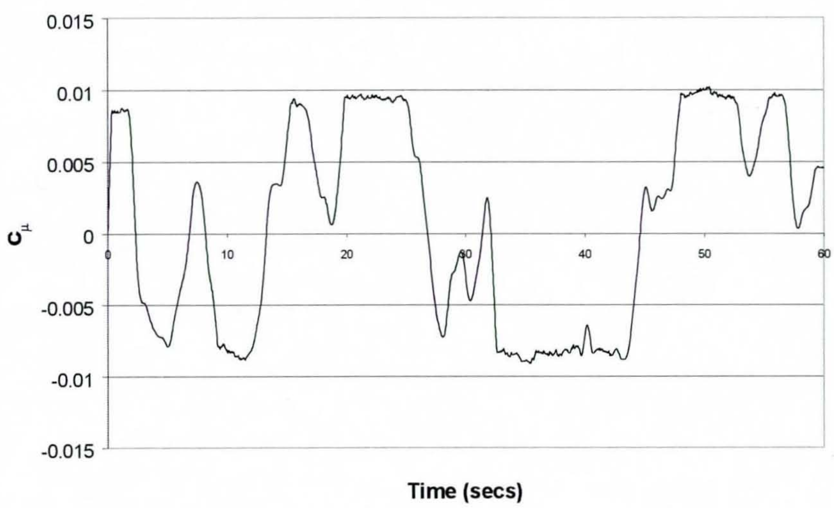

Figure 7.10: CCA Action over a Representative 1 minute period (U=20m/s, IEC Turbulence Class B)

As would be expected, the level of turbulence in the approaching windfield has a significant effect on the power output and both the pitch control and CCA control have to work harder, while power excursions about rated still increase. It can be seen that the effectiveness of the CCA sections in smoothing the power output is reduced, although some improvement is still seen in both the power quality and in reducing the pitch duty.

Any control action has the potential to affect the loadings on the various turbine components. The effect on the flapwise loading is shown in the form of a Power Spectral Density plot in Figure 7.11. These have been generated with the NREL post-processing tool GPP [141].

The PSDs with and without CCAs are very similar (the prominent 1P spike seen in the blade root flap moment is present to the same degree without CCAs) and no significant additional loading is placed on the blade.

Figure 7.12 shows the PSD for the High Speed Shaft. It can be seen that some additional loading is placed on the High Speed Shaft, around the 3P frequency.

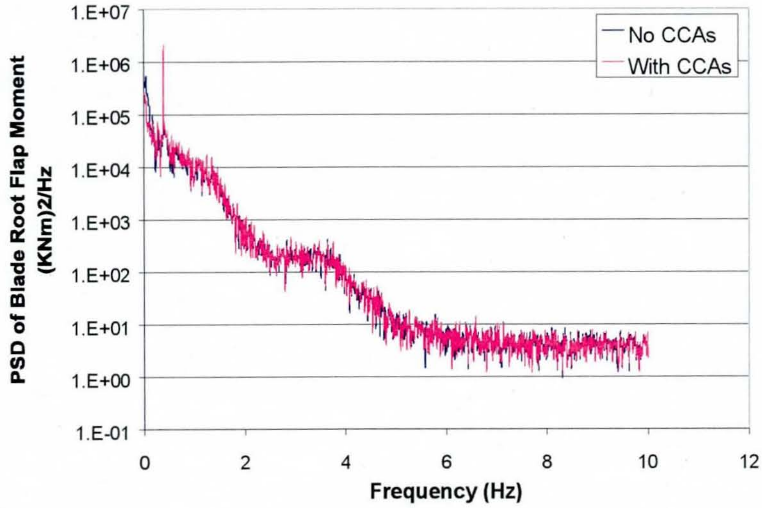

Figure 7.11: PSD for Flapwise Blade Root Moment with and without CCA sections (U=20m/s, IEC Turbulence Class B)

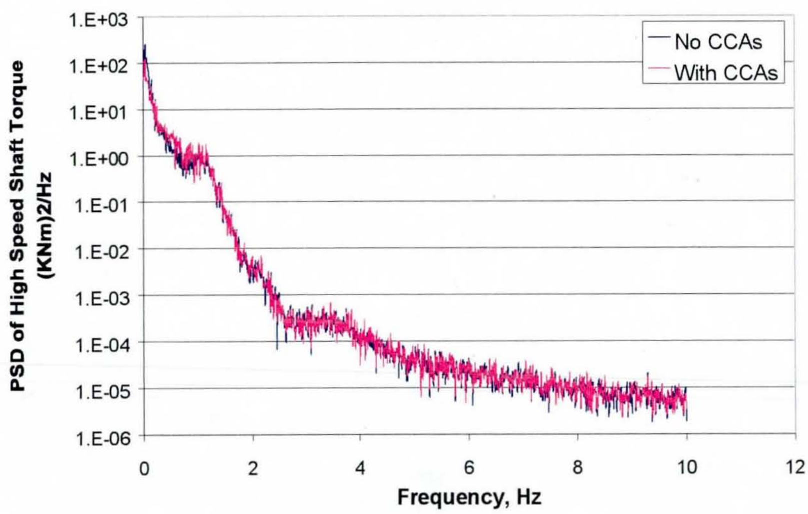

Figure 7.12: PSD for High Speed Shaft Torque with and without CCA sections (U=20m/s, IEC Turbulence Class B)

7.6 Wind Shear and Yawed Flow Conditions

HAWTs commonly operate for periods of minutes in heavily yawed conditions as the wind vane readings which control the yaw motors are averaged over several minutes. Additionally the windfield approaching a HAWT varies from the bottom of the swept area to the top due to wind shear. Both of these phenomenon, along with tower shadow, produce a cyclically varying load history on the blades and, consequently, other turbine components. The rapid speed at which CCAs are able to operate should make it potentially possible to respond to and attenuate the magnitude of these cyclic loads, if used in conjunction with appropriate sensors such as the Sarcos load sensors or Lidar nacelle anemometry equipment, as identified in Chapter 2.

This section is dedicated to exploring this possibility using a quite different control technique to that used for the power control. Over each revolution each blade's flap moments are individually sampled, summed and a mean blade load calculated. This is then used over the next rotor revolution, along with the maximum blade flap moment recorded in the previous cycle, to schedule the CCA response according to Equation 7.3.

$$C_{\mu} = C_{\mu\max}\frac{M_{flap(t)} - M_{flap(average)}}{M_{flap(\max)} - M_{flap(average)}} \tag{7.3}$$

Figures 7.13-7.16 show the attenuation of the blade flap moment in a steady windfield of 23m/s with a wind shear exponent of 0.31, in yaw conditions of 0, 15°, -30° and -45°. In each case the CCAs are activated after approximately 10 seconds.

The CCA variation corresponding to Figure 7.16 can be seen in Figure 7.17. This is representative of the previous three cases.

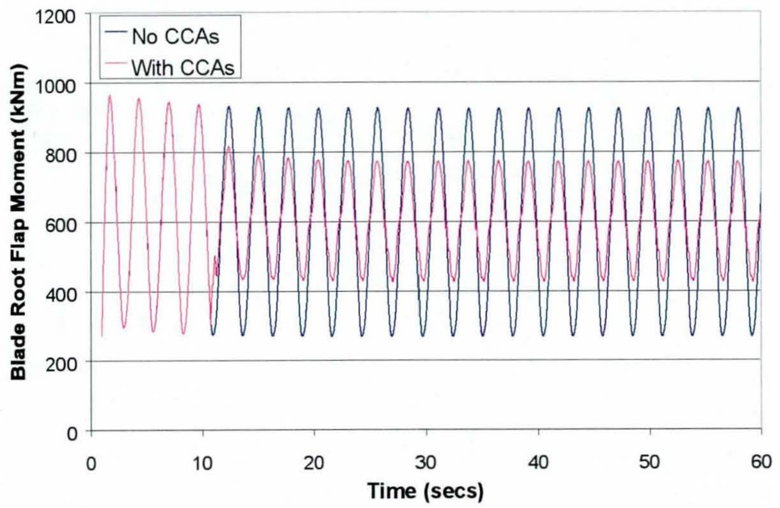

Figure 7.13: Blade Root Flapwise Bending Moment with and without CCAs. Wind Shear Exponent=0.31, Yaw Error=0 degrees, Steady Windfield, 23m/s

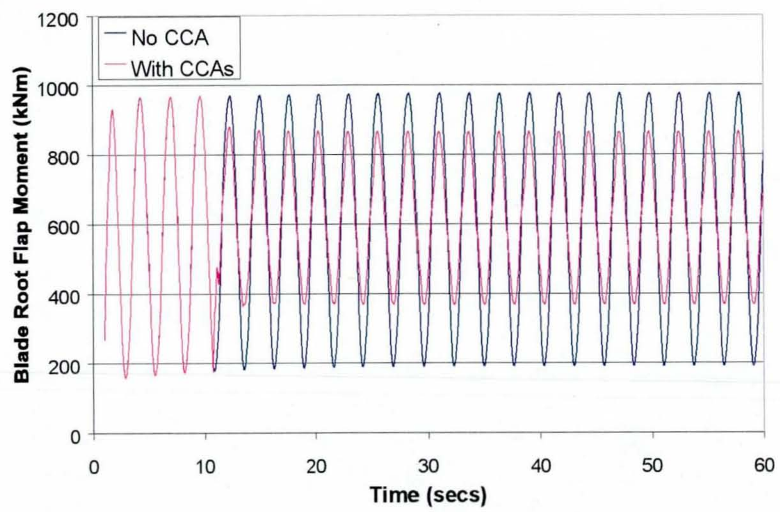

Figure 7.14: Blade Root Flapwise Bending Moment with and without CCAs. Wind Shear Exponent=0.31, Yaw Error=15 degrees, Steady Windfield, 23m/s

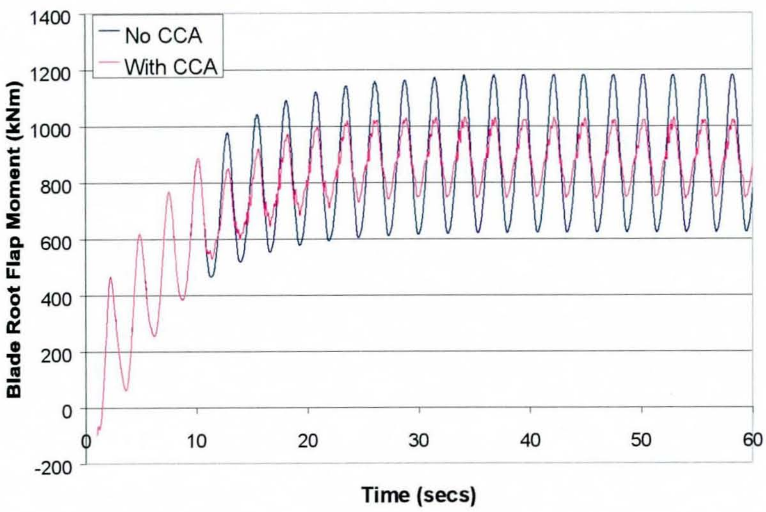

Figure 7.15: Blade Root Flapwise Bending Moment with and without CCAs. Wind Shear Exponent=0.31, Yaw Error=-30 degrees, Steady Windfield, 23m/s

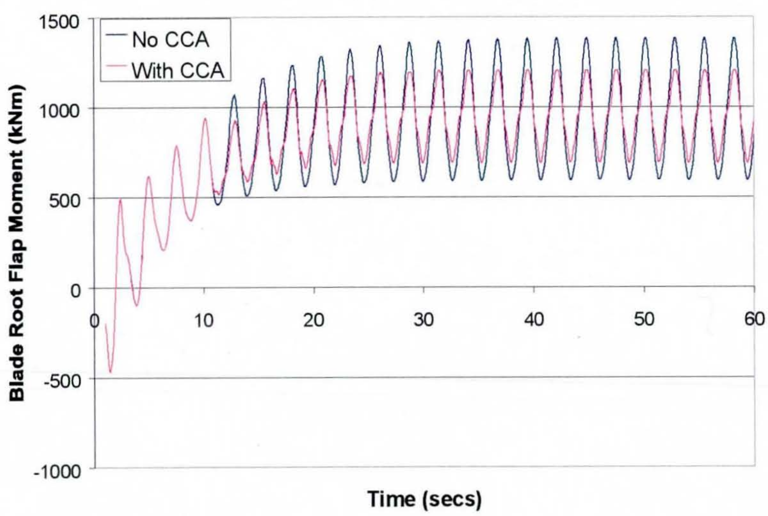

Figure 7.16: Blade Root Flapwise Bending Moment with and without CCAs. Wind Shear Exponent=0.31, Yaw Error=-45 degrees, Steady Windfield, 23m/s

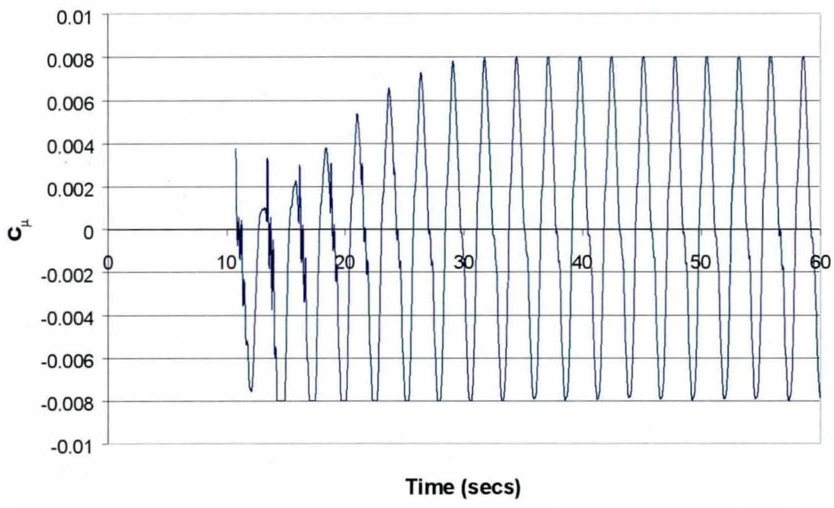

Figure 7.17: Variation of Momentum Coefficient Demanded to Reduce Cyclic Variation of Blade Root Flap Moment for -45 degree Yaw Case

The transient behaviour seen in Figures 7.15 and 7.16 is due to an initial pitching action to achieve rated power. It can be seen that the CCAs can be effective in reducing the magnitude of the load cycles by up to 50% in these steady windfields, although the reduction is as low as 25% in the -45° case. The CCA action in all these cases is regular and cyclic, although the action is not maximised until after 20 seconds of operation in the cases where a pitching transient is present. This gives an indication of the problems that may occur with such a simplified control algorithm in an unsteady windfield.

Results are presented in Figures 7.18 7.23 for cases of 0°, -15° and 30° yaw error using a time-varying, turbulent windfield and the same control algorithm. The windfields have mean speeds of 20, 16 and 23 m/s respectively, with an IEC turbulence Class A intensity in the -15° case and of 8% in the others.

It can be seen that in the time varying windfields a cyclic variation of the blade root flapwise moment still occurs due to the yaw error and/or wind shear present, although the amplitude is no longer constant due to the turbulence in the wind.

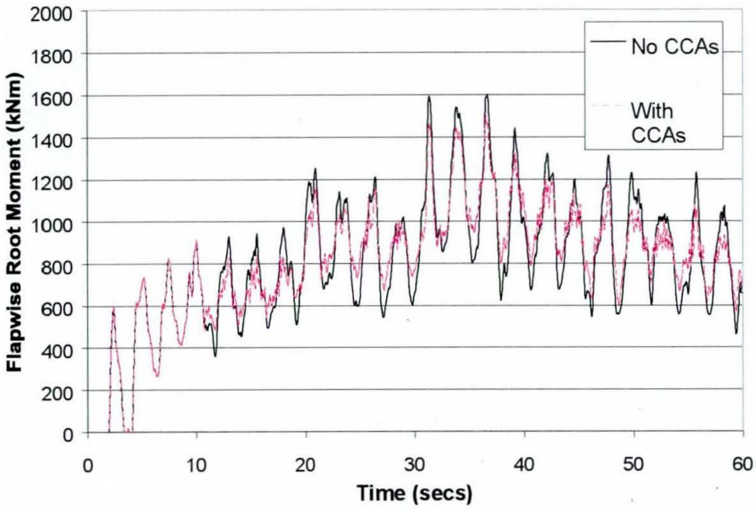

Figure 7.18: Blade Root Flap Bending Moment with and without CCA sections over a Representative 1 minute period in a Time Varying Windfield (U=20m/s, TI=8%) and 0 Yaw Error

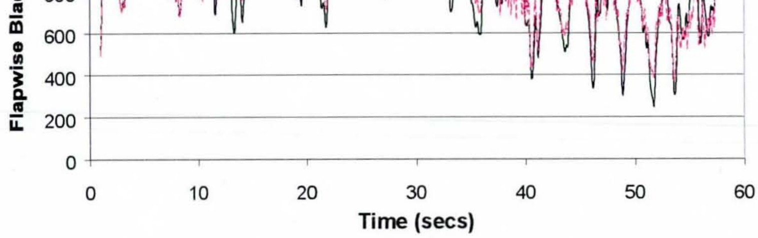

Figure 7.19: Blade Root Flap Bending Moment with and without CCA sections over a Representative 1 minute period in a Time Varying Windfield (U=16m/s, IEC Turbulence Class A) and a Yaw Error of -15 Degrees

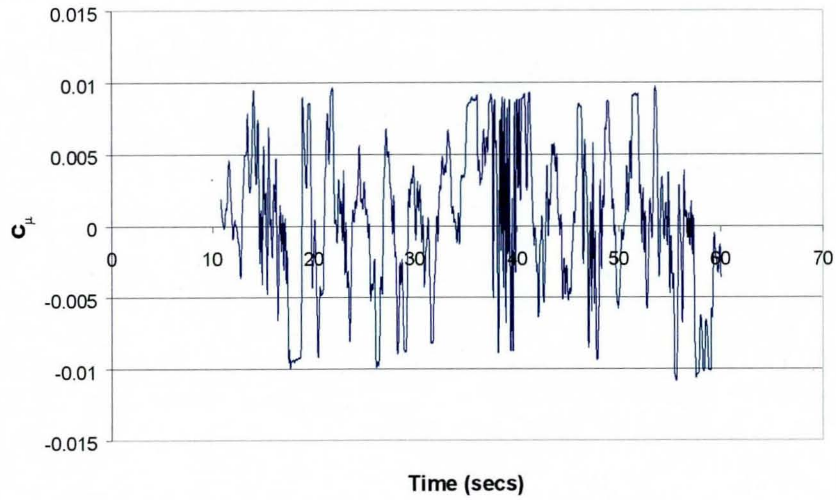

Figure 7.20: Variation of Momentum Coefficient Demanded to Reduce Cyclic Variation of Blade Root Flap Moment for -15 Degree Yaw Case in Unsteady WindField

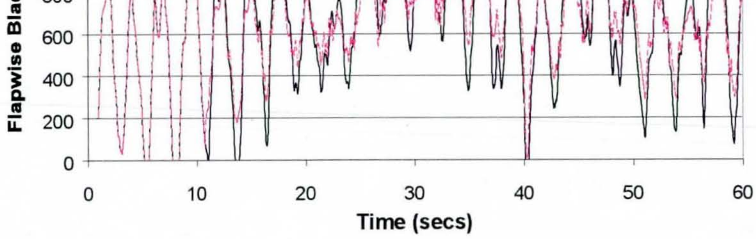

Figure 7.21: Blade Root Flap Bending Moment with and without CCA sections over a Representative 1 minute period in a Time Varying Windfield (U=23m/s, TI=8%) and a Yaw Error of 30 Degrees

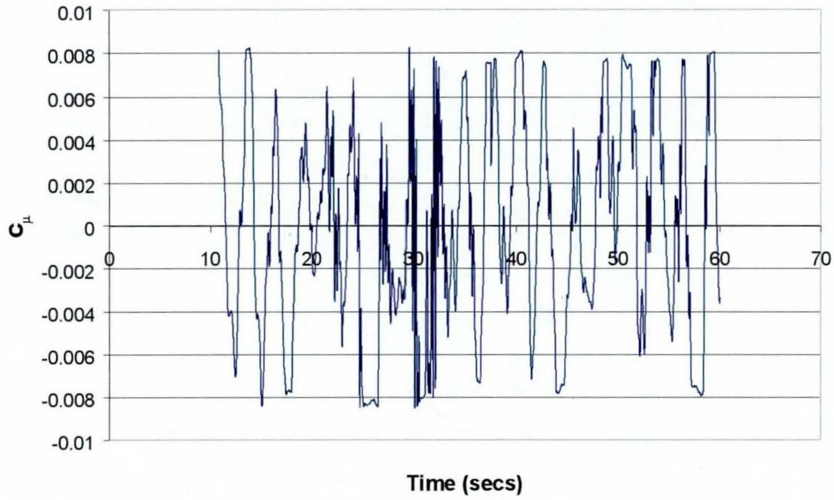

Figure 7.22: Variation of Momentum Coefficient Demanded to Reduce Cyclic Variation of Blade Root Flap Moment for 30 Degree Yaw Case in Unsteady WindField

As already indicated this presents a problem for the controller used here as it relies upon the flap moments generated in the previous rotation to define its behaviour in the next and the success of the approach is minimal at best. The case where only wind shear is present produces the best results. Where yaw is present the improvement is negligible and in all cases it can be seen that higher frequency fluctuations are introduced. This is most clearly seen in the -15° case where the turbulence levels are higher and the CCA action is greatest.

The ensemble averaged blade root flap moment also clearly shows the higher frequency excitation introduced, although, more positively, a noticeable improvement is seen between the 1P and 6P frequencies.

7.7 Summary

- An introduction to the most relevant aspects of the BEM code FAD4 and its aerodynamic sub-routines, AD12, as well ancillary programs has been presented.

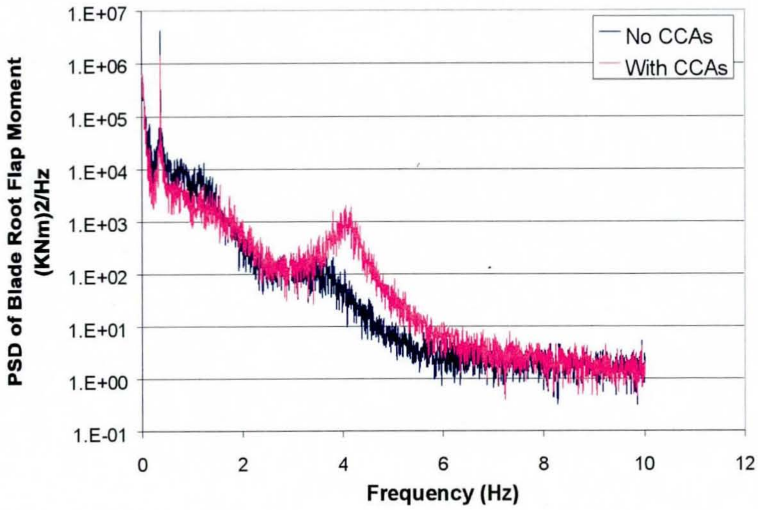

Figure 7.23: Ensemble Averaged PSD for Flapwise Blade Root Moment with and without CCA sections

- An appropriate model of the Tjaerborg 2MW wind turbine has been developed and validated against experimental data.
- An argument for the validity of using post-stall Gurney flap data to extend the steady state CFD results for the NACA4415 CCA (for predominantly attached flow) to the post-stall region has been presented, and aerofoil data tables have been correspondingly derived.
- The optimum position and length of CCAs on the blade (being 62-88% of the rotor radius) have been calculated with respect to the effect on potential power regulation and the absorbed power required to provide the pressure and mass flow rate in the ducts.
- The steady state performance of the Tjaerborg turbine using blades with CCA sections has been modelled and results presented for the ability to regulate power and reduce blade root flapwise moments in wind fields with appreciable wind shear and yaw error. The potential to achieve these two roles is appreciable, but clearly limited by the absorbed power constraints.

- The behaviour of the Tjaerborg turbine with and without blades fitted with CCA sections has been modelled in turbulent windfields. The simple control algorithms used to define the CCA action have been found inadequate and need improvement for a satisfactory exploration of the possibilities.

Chapter 8

Conclusions and Suggestions for Further Work

This Chapter presents conclusions and suggestions for further work.

8.1 Conclusions

It has been established from the wind turbine literature and background knowledge of the subject that there is a need to find ways of providing greater control over the dynamic loads experienced by modern wind turbines in order to reduce the future cost of wind generated electricity. The role of this thesis has been to determine the suitability of circulation control aerofoils to wind turbines and to begin to assess their potential in respect to active load and power control.

The large body of literature on the subject of circulation control aerofoils has been thoroughly reviewed and a clear understanding of the behaviour of CCAs has been established. Two variants of CCAs have been identified, being the jet flap and Coanda CCA, and the information available on their characteristics has been used to determine the preferred type for use with wind turbines. This has been found to be the jet flap CCA, due to it's potential for use with aerofoils with a sharp trailing edge, its ability to utilise larger slot width to chord ratios in order to reduce absorbed power consumption and its preferable slot alignment (nominally parallel to the chordline rather than normal to it). Additionally, the use of a variable momentum coefficient rather than a variable jet deflection angle has been adopted, primarily due to the difficulty of assuring satisfactory aerofoil behaviour (i.e. lift to drag ratio) when the jet stream is not present and the additional system complexity required to vary the jet angle over any sensible range.

The amount of power absorbed by the equipment used to raise the required pressure and mass flow rates at the CCA slot is clearly the strongest limitation on the capability of the CCAs to produce changes in the blade forces. As such it has been recommended that a dual slot blade is utilised; that is a blade with slots on the upper and lower surfaces of the aerofoil. This allows for the CCA sections to reduce, as well as increase, the sectional C_l values of the aerofoil, thereby increasing the range of C_l for a given momentum coefficient.

The effect positively and negatively deflected jets located at the trailing edge of an aerofoil have on the aerofoil's sectional characteristics at low momentum coefficients ($C_\mu \leq 0.02$) have been investigated with the two-dimensional, incompressible, RANS CFD code, EllipSys2D. The code has been satisfactorily validated for the modelling of jet flap CCAs against experimental data for a Coanda CCA. Although the code has been found to produce excellent results for the cases where sectional force coefficients are modified by the presence of a jet entering the aerofoils boundary layer and the surrounding freestream, deficiencies were found in its ability to correctly predict the point at which the jet separates from the aerofoil surface. However, this has no impact on the applicability of the code to model jet flap CCAs. Somewhat incidentally, the code has also been found capable of replicating an operational peculiarity of CCAs, being the ability of a positive jet to reduce the lift coefficient at extremely low momentum coefficients ($C_\mu \leq 5\times10^{-4}$). The CFD modelling of jet flap CCAs conducted in the course of this work is, to the best of the author's knowledge, the only such satisfactory study of its kind. Interestingly, the results suggest that some previous experimental work, which many jet flap theories have been validated against, has been substantially in error.

In relation to the CFD study, the most significant findings are that:

- negatively deflected jets affect a smaller change in the sectional coefficients compared to positively deflected jets for any cambered aerofoil, due to the relative thicknesses of the upper and lower surface boundary layers
- the degree of variation in C_l for a given C_μ is highly dependent on the type of aerofoil used, with the presence of a cusped trailing edge strongly reducing the effect of the jet in both positive and negative deflections
- the performance of negative jets are compromised by any significant degree of trailing edge separation, while positive jets act to suppress trailing edge separation
- for both negative and positive jets the change made to the lift coefficient is proportional to the square root of the momentum coefficient
- both negative and positive jets reduce the sectional drag coefficient of the plain aerofoil due to changes made to the surface pressure distribution

Other findings which have a bearing on the application of CCAs to wind turbines are that increasing the slot to chord ratio has a positive effect on the change in lift coefficient for a given momentum coefficient, and that CFD modelling of momentum coefficients less than 0.01 must take account of the jet/freestream interaction in the channel leading to the slot mouth for accurate results to be achieved.

The power extraction from the rotor due to centrifugal pumping and the associated Coriolis power consumption has been quantified along with the resulting momentum coefficient for a theoretical, lossless system and a second, less simplified, analysis which balances the pressure rise due to centrifugal compression with the pressure drop due to friction in the duct. The mean momentum coefficient raised for each case has been calculated at 0.0077 and 0.0032 respectively with associated power extractions due to the Coriolis force of approximately 6kW and 3.2kW per blade per slot. However, the assumptions made in each analysis are significant and the figures quoted should be treated with caution.

A CCA system layout suitable for use with wind turbines has been proposed which comprises fans or centrifugal blowers, filters and butterfly valves mounted in the blade root section (alternatively, a single centrifugal blower can be mounted in the nacelle and used to supply all three blades). This equipment supplies and throttles clean air at suitable pressure and mass flow rate to the slots on the upper and lower aerofoil surfaces via the void space in the blade, which is divided such that independent ducts supply the positively and negatively deflected jets. The slots may be left permanently open or passively sealed by flaps that open under pressure. Alternatively, a single blade duct with valving at the slots themselves is proposed, should the dynamic behaviour of the fluid in the ducts prove problematic. The energy requirements of such a system, using slots extending from 62-88% of the blade radius with a maximum momentum coefficient of 0.01 at a windspeed of 15m/s, is calculated to be in the region of 2.75% of rated power (i.e. 55kW for the 2MW wind turbine considered). For the blades considered an optimum slot width to chord ratio of 0.005 has been determined.

The effect such a CCA equipped wind turbine rotor can have on the power output and blade root flapwise bending moment has been assessed in steady state wind conditions with recourse to a validated BEM/modal analysis model of the Tjaerborg 2MW wind turbine. This has shown that power variations of $-160kW$ to $+270kW$ can be achieved, although due to the non-linear behaviour of the CCA sections with angle of attack this can vary considerably, especially with regard to the negatively deflected jet. The magnitude of the cyclic variation of the blade flapwise bending moment can be reduced by as much as 50% in yawed and sheared wind fields.

Simulations of the same turbine with and without CCA sections have also been conducted in turbulent windfields. For power control, the main effect seen is a reduction of pitch actuator duty and a small improvement in power quality. For reduction of the variation of the flapwise blade load the benefits shown here are limited due to the simple control algorithms used to define the CCA action. In both cases the control algorithms have been found inadequate and need improvement for a satisfactory exploration of the potential of CCA rotors in realistic windfields.

8.2 Suggestions for Further Work

1. Experimental confirmation of negative blowing effects. Although no physical anomalies were apparent in the CFD modelling of negative or positive jets, no accurate validation of the predicted effects can be made without further wind tunnel tests of aerofoils with negatively deflected jets.

2. Dynamic simulations of varying angle of attack at constant C_μ and varying C_μ at constant angle of attack (particularly in changing from positive to negative blowing). Also time dependent simulations of the CCA behaviour beyond stall should be conducted to assess the accuracy of the data derived

here by comparison with known Gurney flap behaviour. Further to this, modelling or experiment to predict the dynamic stall behaviour of jet flap CCAs is desirable for input to wind turbine analysis codes.

3. Design and optimisation of a type of aerofoil most suitable for use with HAWT CCAs. This should take into consideration the general requirements for aerofoils used with HAWTs, as well as the dynamic behaviour of jet flap CCAs.

4. An improved analysis or experiment to determine the momentum coefficients produced by centrifugal pumping and the subsequent power extraction by the Coriolis force. It would then be possible to assess the possibility of using passive, self-pump positive jets to produce an aerofoil with extremely good lift to drag ratio, for use on HAWTs, as well as being better able to assess the performance losses due to passive pumping from the unblown slot.

5. Experiment to determine the dynamic behavior of jet flap CCAs of the type developed here with respect to the fluid dynamic behaviour in the blade ducts, produced by the use of valves located in the blade root. This would then allow accurate inclusion of the time lags and any possible hystereses caused by the valve mechanism in further BEM modelling.

6. The development of appropriate and effective control algorithm's in order to thoroughly assess the capability of jet flap CCAs on wind turbines in time varying windfields.

7. Further exploration of potential applications of CCAs to wind turbines. This should involve modelling other wind turbines, which are more representative of contemporary machines than the Tjaerborg 2MW turbine. Model elements may most importantly include a range of structural flexibility (par-

ticularly with regard to the blades) and an inclusion of variable speed operation. Possible areas for study, additional to those already touched upon here, include:

- the potential for damping instabilities and vibrations which may occur on a specific machine under particular conditions
- an assessment of the fatigue life benefits with regard to active blade load control
- reducing tower motions and oscillations in the light of rotor/tower interaction
- a comparative assessment of the benefits of using CCAs as opposed to full span pitch control to achieve the same load control objective
- use of negative jet CCAs to produce active stall control of stall regulated machines
- the potential for the use of CCAs with other pneumatic devices, such as air jet vortex generators.

8. Rotor testing (either in a wind tunnel or full scale) of a wind turbine using CCA sections. Alternatively, in the future three–dimensional CFD rotor simulation may be available as a design tool as may be used for a similar full scale assessment.

Bibliography

[1] Lachmann, G. V. *Boundary Layer and Flow Control : Its Priciples and Application;* Pergamon: 1961.

[2] Dimmock, N. "An Experimental Introduction To the Jet-Flap", Current Paper 344, Aeronautical Research Council, 1957.

[3] Dimmock, N. "Some Further Jet-Flap Experiments", Current Paper 345, Aeronautical Research Council, 1957.

[4] Dimmock, N. *Aeronautical Quarterly* **1957,** *8,* 331-345.

[5] Malavard, L.; PoissonQuinton, P.; Jousserandot, P. *Aero Digest* **1956,** 21-27, 46-59, 34-46.

[6] Malavard, L.; PoissonQuinton, P.; Jousserandot, P. "Theoretical and Experimental Investigations of Circulation Control", Report (translation) 358, Princetown University, 1956.

[7] Foley, W.; Reid, E. *Journal of the Aerospace Sciences* **1959,** *26,* 385-387.

[8] Bevilaqua, P. *Journal of Fluid Mechanics* **1984,** *141,* 347-364.

[9] Bevilaqua, P.M.;, C. P. S. E. "Progress Towards a Theory of Jet-Flap Thrust Recovery (Final Report May 78 -Sep 80)", Technical Report AFOSR-TR-81-0900, Rockwell International, Columbus, Ohio, 1980.

[10] Yuan, S. *Journal of Aircraft* **1970,** *7*, 417-423.

[11] Spence, D. *Journal of the Aeronautical Sciences* **1956,** 92-94.

[12] Spence, D. *Royal Society of London Proceedings Series A* **1957,** *238*, 42-68.

[13] Helmbold, H. B. *Journal of the Aeronautical Sciences* **1955,** 341-342.

[14] Spence, D. *Royal Society of London Proceedings Series A* **1961,** *261*, 94-118.

[15] Spence, D. *Aeronautical Quarterly* **1958,** *9*, 395-406.

[16] Kuchemann, D. "A Method for Calculating the Pressure Distribution over Jet-Flapped Wings", Reports and Memoranda 3036, Royal Aeronautical Establishment, 1956.

[17] Lissaman, P. *AIAA Journal* **1968,** *6*, 1356-1362.

[18] Kida, T.; Takanori, T. *Bulletin of the JSME* **1970,** *13*, 987-995.

[19] Leamon, R.; Plotkin, A. *Journal of Aircraft* **1972,** *9*, 631-635.

[20] Halsey, N. *Journal of Aircraft* **1974,** *11*, 540-546.

[21] Sato, J. *AIAA Journal* **1973,** *11*, 968-973.

[22] O'Mahoney, R.; Smith, F. *Aeronautical Quarterly* **1978,** 44-59.

[23] Tang, V.; Tinkler, J. *Canadian Aeronautics and Space Journal* **1979,** *25*, 260-270.

[24] Mateescu, D.; Newmann, B. *Journal of Aircraft* **1991,** *28*, 789-795.

[25] Chen, G.-R.; Shaw, H.-J. *Transactions of the Japan Society for Aeronautical and Space Sciences* **1996,** *39*, 126-141.

[26] Davidson, I. "Aerofoil Boundary Layer Control Systems", British Patent No. 913754, 1960.

[27] Kind, R.; Maul, D. *Aeronautical Quarterly* **1968,** *19,* 170-182.

[28] Kind, R. *Aeronautical Quarterly* **1968,** *19,* 205-223.

[29] Cheeseman, I.; Seed, A. *Journal of the Royal Aeronautical Society* **1967,** *71,* 451-463.

[30] Cheeseman, I. *Aircraft Engineering* **1969,** .

[31] Dunham, J. *The Aeronautical Journal* **1970,** *74,* 91-103.

[32] Dunham, J. *The Aeronautical Journal* **1970,** *74,* 175-186.

[33] Marwood, R. "An Experimental Investigatioin of the Coanda Effect", Master's thesis, Purdue University, 1948.

[34] Englar, R. "Two-Dimensional Subsonic Wind Tunnel Tests of Two 15-Percent Thick Circulation Control Airfoils", Technical Report AL-211, David Taylor Naval Ship Research and Development Center, Aviation and Surface Effects Dept., Bethesda, Maryland 20084, 1971.

[35] Englar, R. "Low Speed Aerodynamic Characteristics of a Small Fixed-Trailing-Edge Circulation Control Wing Configuration Fitted to a Supercritical Airfoil", Technical Report DTNSRDC/ASED/-81/08, David Taylor Naval Ship Research and Development Center, Aviation and Surface Effects Dept., Bethesda, Maryland 20084, 1981.

[36] Englar, R. J.; Huston, G. G. *Journal of Aircraft* **1984,** *21,* 476-483.

[37] Englar, R. J. *Journal of Aircraft* **1975,** *12,* 457-463.

[38] Englar, R. *Journal of Aircraft* **1981,** *18,* 51-58.

[39] Englar, R. *Journal of Aircraft* **1994,** *31*, 1160-1177.

[40] Wood, N. *Journal of Aircraft* **1987,** *24*, 38-44.

[41] Harvell, J.; Franke, M. *Journal of Aircraft* **1985,** *22*, 737-742.

[42] Dunham, J. *Journal of Fluid Mechanics* **1968,** *33*, 495-514.

[43] Gibbs, E.; Nathan, N. *Journal of Aircraft* **1976,** *13*, 158-160.

[44] Dvorak, F.; Kind, R. *Journal of Aircraft* **1979,** *16*, 23-28.

[45] Tai, C.; Kidwell, G.; Vanderplaats, G. *Journal of Aircraft* **1982,** *19*, 145-150.

[46] Soliman, M.; Smith, R.; Cheeseman, I. "Modelling of Circulation Control by Blowing", Technical Report CP 365, AGARD, 1984.

[47] Shrewsbury, G. *Journal of Aircraft* **1989,** *26*, 29-34.

[48] Shrewsbury, G. *Dynamic Stall of Circulation Control Airfoils,* Thesis, Georgia Institute of Technology, Atlanta, 1990.

[49] Richards, E.; Jones, J. *Journal of the Helicopter Society of Great Britain* **1956,** 414-423.

[50] Crimi, P.; White, R. *Journal of the American Helicopter Society* **1965,** *7*, 22-31.

[51] Kretz, M. *Vertica* **1976,** *1*, 95-105.

[52] Potthast, A. X-Wing Stability and Control Development and Wind Tunnel Demonstration Tests - Helicopter, Conversion and Fixed Wing Flight. In *36th Annual Forum of the American Helicopter Society*; Washington, D.C., 1980.

[53] Abramson, J.; Rogers, E. Optimization Theory Applied to Higher Harmonic Control of Circulation Controlled Rotors. In *37th Annual Forum of the American Helicopter Society*; New Orleans, Louisiana, 1981.

[54] Reader, K.; Dixon, W. Evaluation of a 10-Foot Diameter X-Wing Rotor. In *40th Annual Forum of the American Helicopter Society*; Arlington, Virginia, 1984.

[55] Watkins, C.; Reader, K.; Dutta, S. *Journal of the American Helicopter Society* **1985,** 23-31.

[56] Schwartz, A.; Rogers, E. *AIAA Paper* **1992,** .

[57] Spence, D. *Journal of Fluid Mechanics* **1961,** *10*, 237-258.

[58] Spence, D. *Philisophical Transactions of the Royal Society Series A* **1965,** *257*, 445-477.

[59] Simmons, J.; Platzer, M. *Journal of Aircraft* **1971,** *8*, 587-592.

[60] Simmons, J. *AIAA Journal* **1976,** *14*, 1297-1302.

[61] Theodorsen, T. "General Theory of Aerodynamic Instability and the Mechanism of Flutter", Technical Report 496, NACA, 1935.

[62] Simmons, J. *AIAA Journal* **1978,** *16*, 237-241.

[63] Simmons, J.; Platzer, M.; Smith, T. *Journal of Fluid Mechanics* **1978,** *84*, 33-53.

[64] Simmons, J.M.; Pullin, D. *AIAA Journal* **1984,** *23*, 1118-1120.

[65] Ghee, T.; Leishman, J. *AIAA Journal* **1992,** *30*, 289-299.

[66] Liebeck, R. *Journal of Aircraft* **1978,** *15*, 547-561.

[67] Zerihan, J.; Zhang, X. *AIAA Journal* **2001,** *39,* 772-780.

[68] Kentfield, J. *Wind Engineering* **1994,** *18,* 63-74.

[69] Bao, N. *Wind Engineering* **2000,** *24,* 25-34.

[70] Bloy, A.; Durrant, M. *Wind Engineering* **1995,** *19,* 167-172.

[71] Timmer, W.; Van Rooy, R. The Effect of Stall Strips, Guerney Flaps and Vortex Generators on the Performance of a Stall Controlled Wind Turbine. In *Proceedings of the European Community Wind Energy Conference*; 1995.

[72] Storms, B.; Jang, C. *Journal of Aircraft* **1994,** *31,* 542-547.

[73] Oliver, A. Use of Air Jet Vortex Generators Leading to Improved Energy Capture and Power Regulation of a Wind Turbine. In *Proceedings of the British Wind Energy Association*; 1996.

[74] Oliver, A. Wind Turbine Blades Equipped with Air-Jet Vortex Generators: Full Scale Verification of Blade Optimised for Increased Performance. In *Proceedings of the European Wind Energy Conference*; 1997.

[75] Oliver, A. *Air Jet Vortex Generators for Wind Turbines,* Thesis, City University, London, 1997.

[76] Rao, H.; Pelera, G. Application of Tangential Wall Jets for High Lift Generation. In *Proceedings of the British Wind Energy Association*; 1986.

[77] Rao, H.; Perera, G. The Aerodynamics of Wall Jet Action on Octoganol Cylinders for Application to a VAWTG. In *Proceedings of the British Wind Energy Association*; 1987.

[78] Bannister, W. An Investigation Into the Use of Boundary Layer Control as a Method of Overspeed Prevention for Vertical Axis Wind Turbines. In *Proceedings of the British Wind Energy Association*; 1985.

[79] Bannister, W.; Fawkes, J. A Pneumatic Method of Rotational Speed Control of Horizontal Axis Wind Turbines. In *Proceedings of the European Wind Energy Conference*; 1989.

[80] Bannister, W.; Fawkes, J.; Sinclair, I. Rotational Speed Control of the Rutland 1800. In *Proceedings of the British Wind Energy Association*; 1990.

[81] Leithead, W.; de la Salle, S.; Reardon, R. *International Journal of Control* **1992,** 845-876.

[82] Knudsen, T.; Anderson, P.; Toffner-Clausen, S. *Proceedings of the European Wind Energy Conference* **1997,** 546-550.

[83] Bossanyi, *Wind Energy* **2000,** *3*, 149-163.

[84] Caselitz, *European Wind Energy Conference* **1996,** 821-824.

[85] Caselitz, *Proceedings of the European Wind Energy Conference* **1997,** 555-558.

[86] Wettergren, E. "Overview of Embedded Strain Measurement Methods for Composite Materials", Technical Report 91122-98-03, Industrial Research Limited, Auckland, 1999.

[87] Maclean, B. *Proceedings of Material Research Society Symposium* **1997,** .

[88] QuinetiQ, *Promotional Literature* **2002,** .

[89] Causebrook, A. *Proceedings of the British Wind Energy Conference, 24* **2002,** .

[90] Heier, S.; Arnold, G. Grid Control with Wind Energy Converters. In *Proceedings of the Second Internetional Workshop on Tramsmission Networks*

for Offshore Wind Farms; Ackermann, T., Ed.; Royal Institute of Technology, Stockholm, Sweden, 2001.

[91] Timmer, W.; Van Rooy, R. The Performance of New Wind Turbine Blade Tip and Root Airfoils Up to High Angles-of-Attack. In *Proceedings of the European Community Wind Energy Conference*; Dublin Castle, Ireland, 1997.

[92] Fugslag, P. Course on Advanced Topics in Wind Turbine Aerodynamics. In ; DCAMM, Danish Technical University, Lyngby., 2000.

[93] Sorenson, N. "General Purpose Flow Solver Applied to Flow over Hills", Technical Report Riso-R-827(EN), Risoe National Laboratory, Roskilde, Denmark, 1995.

[94] Sorenson, N. "HypGrid2D: A Hyperbolic Mesh Generator", Technical Report Riso, Risoe National Laboratory, Roskilde, Denmark, 1998.

[95] Michelsen, J. A. "Basis3D - a Platform for Development of Multiblock PDE Solvers", Technical Report AFM 92-05, Technical University of Denmark, 1992.

[96] Jens, N. S. "VISCWIND - Viscous Effects on Wind Turbine Blades", Technical Report ET-AFM-9902, Department of Energy Engineering, Technical University of Denmark, 1999.

[97] Michelsen, J. A. "Solution of the Navier-Stokes Equations on General Non-Orthoganol Meshes", Technical Report AFM 89-08, Technical University of Denmark, 1989.

[98] Rhie, C.; Chow, W. *Journal of the AIAA* **1983,** *21,* 1525-1532.

[99] Pantankar, S.; Spalding, D. *Internatinal Journal of Heat and Mass Transfer* **1972,** *15,* 1787.

[100] Menter, F. *AIAA Journal* **1994,** *32,* 1598-1605.

[101] Wilcox, D. C. *Turbulence Modeling for CFD;* La Canada, CA: 1994.

[102] Sorenson, N. "K-Omega Turbulence Models - Implementation and Testing", Technical Report Riso-R-864(EN), Risoe National Laboratory, Roskilde, Denmark, 1995.

[103] Johansen, J. "Prediction of Laminar/Turbulent Transition in Airfoil Flows", Technical Report R-987(EN), Risoe, Roskilde, Denmark, 1997.

[104] Michelsen, J. A.; Sorensen, N. N. Current Developments in Navier-Stokes Modelling of Wind Turbine Rotor Flow. In *Proceedings of the European Wind Energy Conference, Copenhagen*; 2001.

[105] Sorensen, N. N.; Michelsen, J. A.; Schreck, S. Detailed Aerodynamic Prediction of the NREL/NASA AMES Wind Tunnel Tests Using CFD. In *Proceedings of the European Wind Energy Conference, Copenhagen*; 2001.

[106] Ronsten, G. Static Measurements on a Rotating and a Non-Rotating 2.375m Wind Turbine Blade - Comparison with 2D Calculations. In *Proceedings of the European Community Wind Energy Conference*; Van Hulle, F., Ed.; Elsevier Science: Nice, France, 1991.

[107] Bjorck, A. "Dynamic and 3D Effects. Final Report EC DGXII (Joule 2 Project)", Technical Report JOU2-CT93-0345, FFA, Sweden, 1993.

[108] Savory, E. An Experimental and Numerical Study of the Velocity Field Associated with a Jet in a Crossflow. In *Engineering Turbulence Modelling and Experiments*; Rodi,; Ganic,, Eds.; Elsevier Science: 1990.

[109] Abromovich, G. *The Theory of Turbulent Jets;* MIT: 1963.

[110] Andreopoulos, J.; Rodi, W. *Journal of Fluid Mechanics* **1984,** *138,* 93-127.

[111] Versteeg, H.; Malalasekera, W. *An Introduction to Computational Fluid Dynamics;* Longman scientific and technical: 1995.

[112] Englar, R.; Williams, R. *Canadian Aeronautics and Space Journal* **1973,** *19,* 93-108.

[113] Rogers, E. Private Communications.

[114] Bertagnolio, F. "Wind Turbine Aerofoil Catalogue", Technical Report Riso-R-1280(EN), Risoe National Laboratory, Roskilde, Denmark, 2001.

[115] Althaus, D. *Niedriggechwinddigkeitsprofile;* Vieweg: 1996.

[116] Snel, H.; Scheppers, J. "Joint Investigation of Dynamic Inflow Effects and Implementation of an Engineerring Method", Technical Report ECN-C-94-107, Netherlands Energy Research Foundation, ECN, 1995.

[117] Van Grol, H. "Reference Procedure to Establish Fatigue Stresses for Large Wind Turbines", Technical Report ECN-C–94-013, ECN, 1994.

[118] Abbot, I.; Von Donehoff, A. *Theory of Wing Sections;* Dover Publications Inc.: 1959.

[119] Alafouzos, V. V. "Assessment of a New Family of Low-Drag Airfoils Designed for Wind Turbines", Technical Report, 1998.

[120] Kentfield, J. The Potential of the Gurney Flap for Improving the Performance of Wind Turbine Blading. In *Proceedings, Windpower '91, American Wind Energy Association, Washington D.C.*, Vol. 18; 1991.

[121] Jeffrey, D. *Journal of Aircraft* **2000,** *37,* 295-301.

[122] Bloy, A.; Tsioumanis, N. *Wind Engineering* **1997,** *21,* 39-44.

[123] Bloy, A.; Harrison, D. *Wind Engineering* **1998,** *22,* 149-158.

[124] Jang, C. **1992,** .

[125] Kentfield, J. *Wind Engineering* **1996,** *20*, 93-106.

[126] Myose, R. *Journal of Aircraft* **1998,** *35*, 206-211.

[127] Shames, I. H. *Mechanics of Fluids;* McGraw-Hill: 1992.

[128] McCoubrey, G. Design and Development of a Hybrid Composite Rotor Blade for the Circulation Control System. In *35th Annual Forum of the American Helicopter Society*; Washington, D.C., 1979.

[129] Nichols, J. *Aeronautical Journal* **1972,** 552-565.

[130] Buhl, M. "FastAD User's Manual", Technical Report, 2002.

[131] Laino, D; Hansen, A. "User Guide to the Wind Turbine Aerodynamics Computer Software AeroDyn", Windward Engineering, 2001.

[132] Leishman, J.G.;Beddoes, T. *42nd Annual Forum of the American Helicopter Society* **1986,** 243-265.

[133] Snel, H. Sectional Prediction of 3-D Effects for Stalled Flow on Rotating Blades and Comparison with Measurements. In *Proceedings of the European Wind Energy Conference*; 1993.

[134] Buhl, Jr. M.L.; Wright; A.D.; Pierce, K. FastAD Code Verification: A Comparison to ADAMS. In *The 20th ASME Wind Energy Symposium, Reno, Nevada*; 2001.

[135] Buhl, M. "SNWind User's Guide", National Renewable Energy Laboratory, 2001.

[136] Suzuki, A. *Generalised Dynamic Wake Theory for Wind Turbines,* Thesis, University of Utah, 2000.

[137] He, C. J. *Development and Application of a Generalised Dynamic Wake Theory for Lifting Rotors*, Thesis, School of Aerospace Engineering, Georgia Institue of Technology, 1989.

[138] Pitt, D.M.; Peters, D. *Vertica* **1981,** *5*, 21-34.

[139] Gormont, R. "A Mathematical Model of Unsteady Aerodynamics and Radial Flow for Application to Helicopter Rotors", Technical Report 72-67, USAAMRD, 1973.

[140] Buhl Jr., M. "A Simple Mode-Shape Generator for Both Towers and Rotating Blades", NWTC Design Codes (Modes), http://wind.nrel.gov/designcodes/modes/, 2002.

[141] Buhl, M.L.; Weaver, N. "GPP Version 6 User's Manual", National Renewable Energy Laboratory, 1999.

Appendix 1

Reproduction of Experimental Results

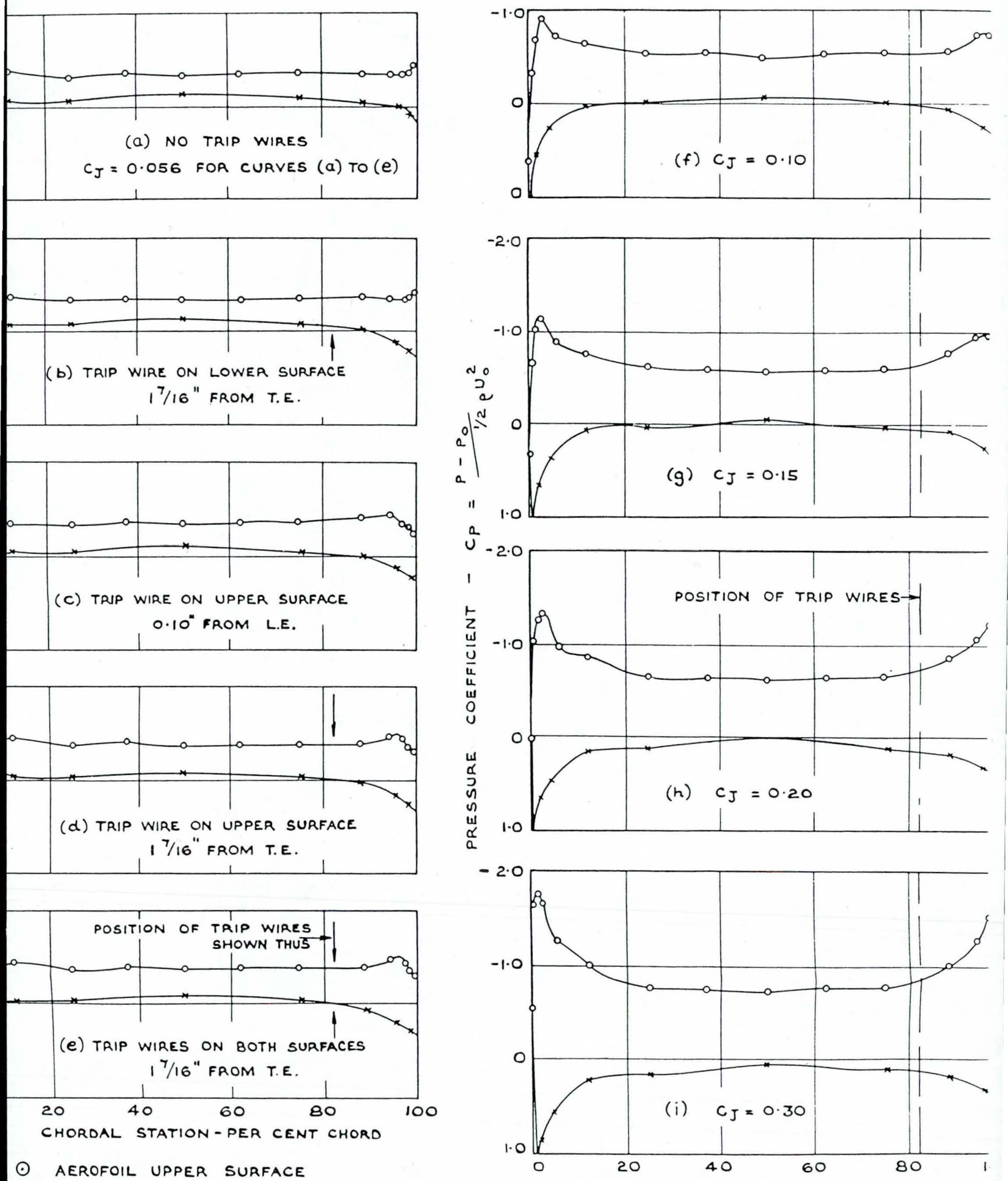

ESSURE DISTRIBUTIONS AT ZERO INCIDENCE — 30° MODEL.

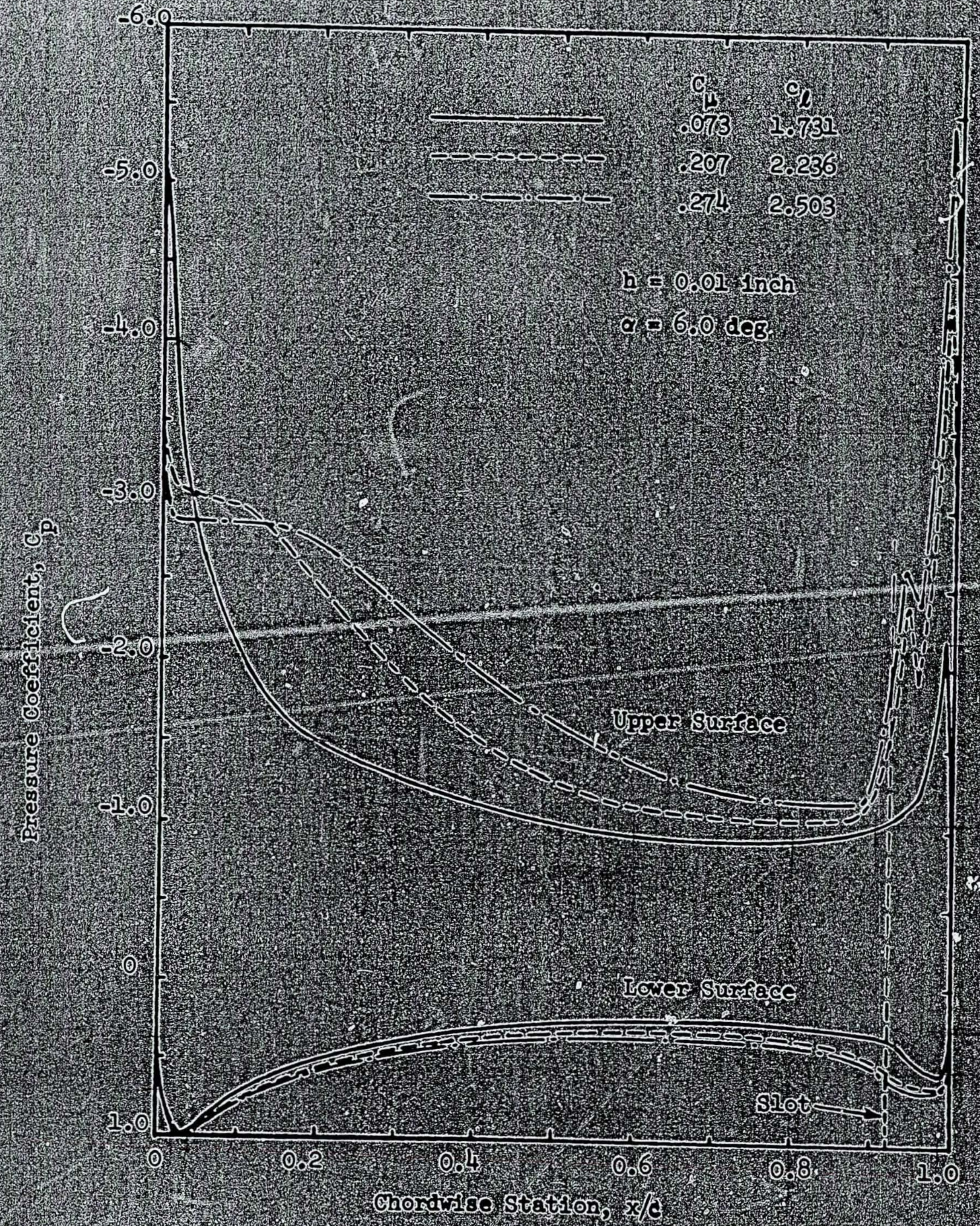

Figure 8 - Experimental Pressure Distributions for the Pure Ellipse Showing Leading Edge Bubble Formation

Appendix 2

Representative Mesh Independency Plots

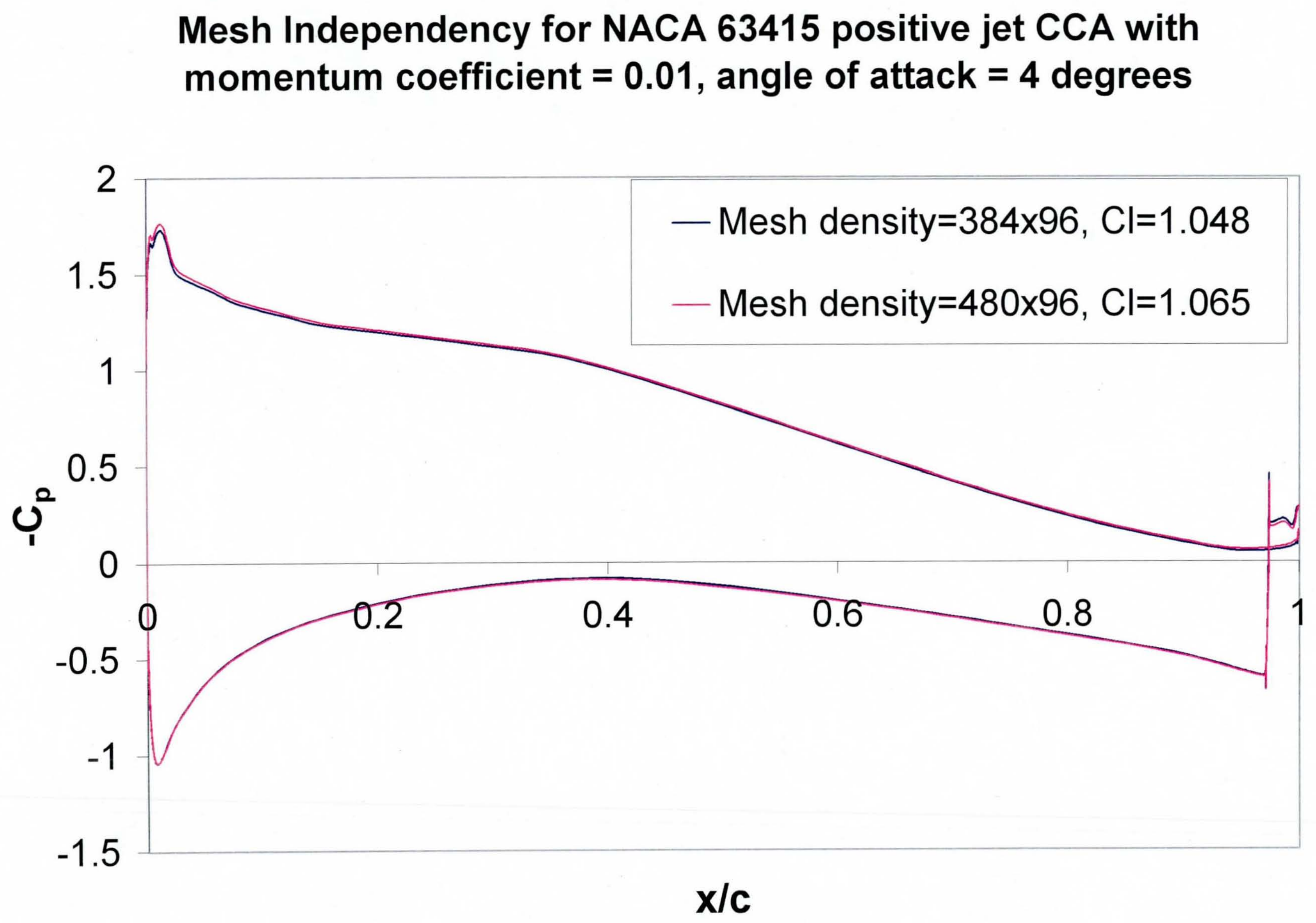
Mesh Independency for NACA 63415 positive jet CCA with momentum coefficient = 0.01, angle of attack = 4 degrees
Mesh density=384x96, Cl=1.048
Mesh density=480x96, Cl=1.065
2
1.5
1
0.5
0
-0.5
-1
-1.5
-C_p
0
0.2
0.4
0.6
0.8
1
x/c

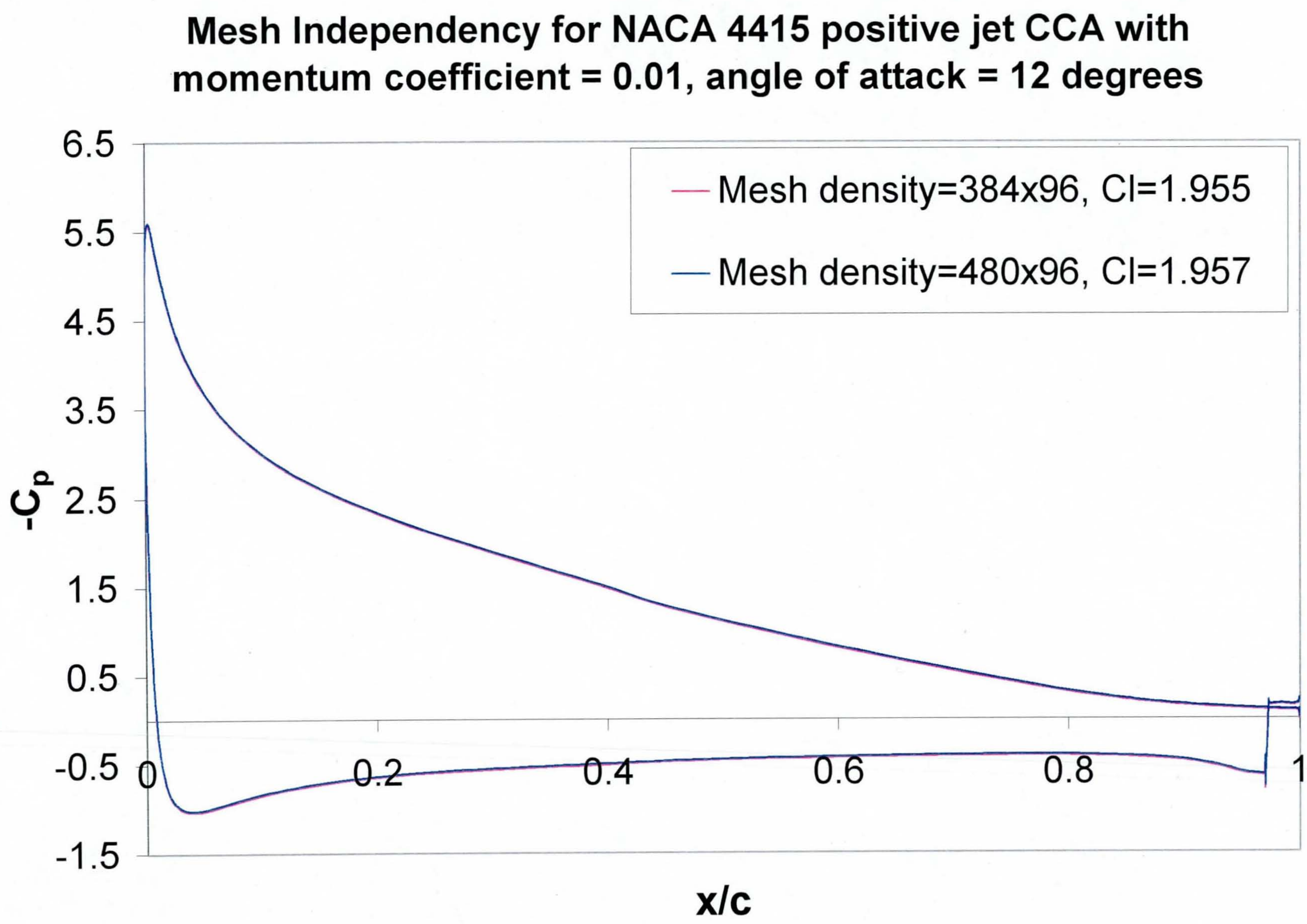
Mesh Independency for NACA 4415 positive jet CCA with momentum coefficient = 0.01, angle of attack = 12 degrees
Mesh density=384x96, Cl=1.955
Mesh density=480x96, Cl=1.957
6.5
5.5
4.5
3.5
2.5
1.5
0.5
-0.5
-1.5
$-C_p$
0
0.2
0.4
0.6
0.8
1
x/c

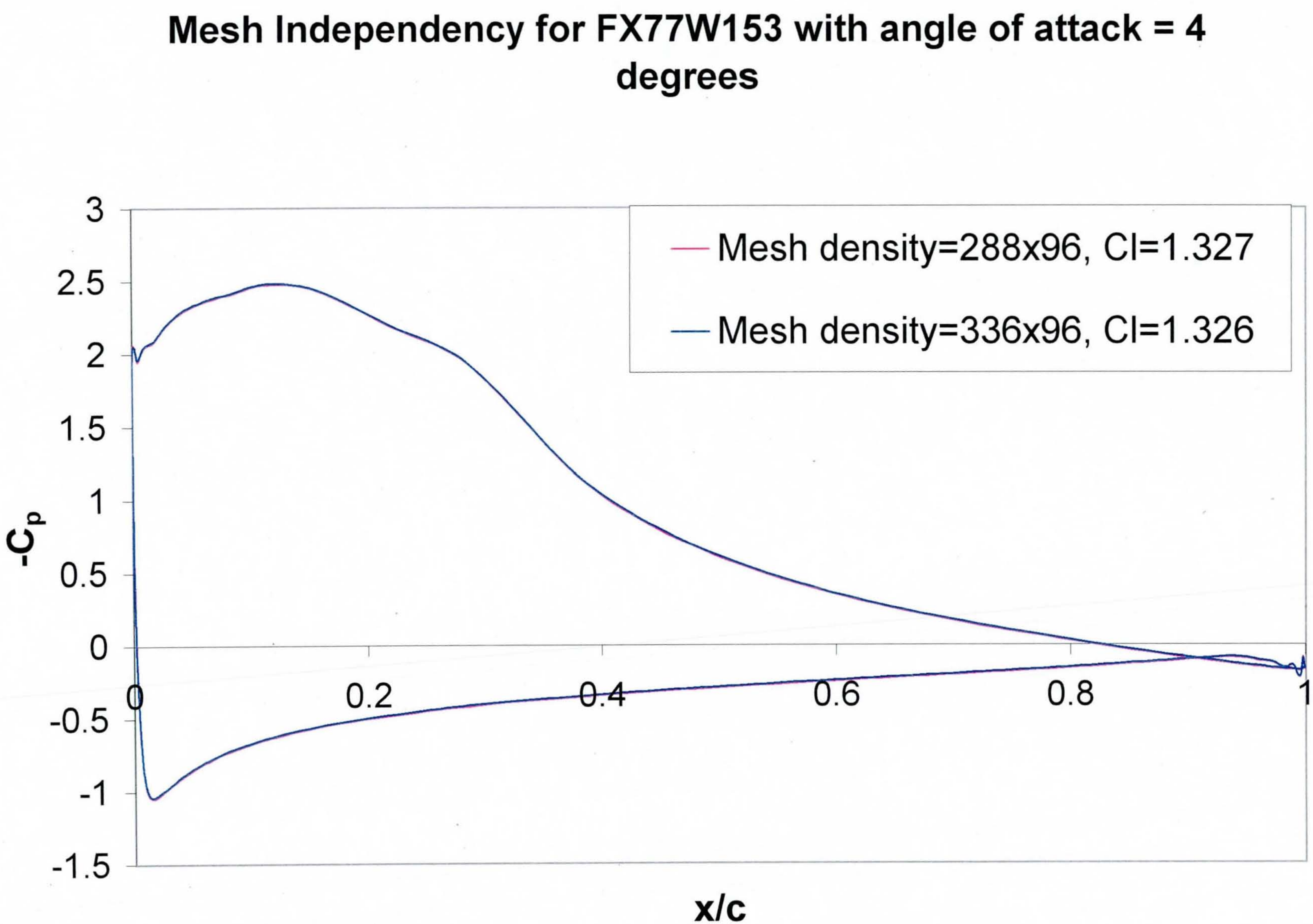
Mesh Independency for FX77W153 with angle of attack = 4 degrees
Mesh density=288x96, Cl=1.327
Mesh density=336x96, Cl=1.326
-Cp
x/c
3
2.5
2
1.5
1
0.5
0
-0.5
-1
-1.5
0
0.2
0.4
0.6
0.8
1

Appendix 3

Details of Tjaerborg Turbine and Fast_AD Input Files

APPENDIX T. GLOBAL AND AERODYNAMIC DATA OF TJÆREBORG TURBINE

Rotor data:

- Number of blades: 3
- Diameter: 61.1 m
- Orientation: upwind
- Tilt angle: 3 deg
- Cone angle: 0 deg
- Hub height: 61 m
- Rotor overhang: 6.76 m
- Rated electrical power: 2MW
- Rated shaft power: 2.2MW
- Synchronous rotor speed: 21.93 rpm
- Rotor speed at rated power: 22.36 rpm
- Power control: full span pitch
- Operational pitch angle: 0-35 deg
- Idling pitch angle: 55 deg
- Stop pitch angle: 90 deg

Blade geometry

- Length incl. 0.1 m tip cap: 29.1 m
- Flange distance from rotor axis: 1.46 m
- Planform: see figure T.1
- Tip chord: 0.90 m
- Taper (linear): 0.1 m/m
- Thickness: see table T.1
- Twist (linear): 0.333 deg/m
- Airfoil family: NACA 44xx
- Airfoil data: see table T.2 to T.6

Tower geometry

- Height: 56 m
- Shape upper half: conical
- Diameter at h = 56 m: 4.25 m
- Diameter at h = 28 m: 4.75 m
- Diameter at base: 7.25 m

Example AeroDyn.ipt file for Tborg CCA power control without timelag.

```
SI                         SysUnits - System of units for used for input and
output [must be SI for FAST] (unquoted string)
BEDDOES                    StallMod - Dynamic stall included [BEDDOES or
STEADY] (unquoted string)      STEADY
NO_CM                      UseCm    - Use aerodynamic pitching moment model?
[USE_CM or NO_CM] (unquoted string)
DYNIN                      InfModel - Inflow model [DYNIN or EQUIL] (unquoted
string)
SWIRL                      IndModel - Induction-factor model [NONE or WAKE or
SWIRL] (unquoted string)
 0.005                     AToler   - Induction-factor tolerance (convergence
criteria) (-)
PRANDTL                    TLModel  - Tip-loss model (EQUIL only) [PRANDtl,
GTECH, or NONE] (unquoted string)
"Wind\16ms.wnd"            WindFile - Name of file containing wind data
(quoted string)   \Tborgtrial
61.356                     HH       - Wind reference (hub) height [TowerHt+
Twr2Shft+OverHang*SIN(NacTilt)] (m)
 0.3                       TwrShad  - Tower-shadow velocity deficit (-)    !
check what this should be for an upwind TB - 0 means no shadow
 2.30                      ShadHWid - Tower-shadow half width (m)    !half of
tower width at approximately 42 metres!
 6.81                      T_Shad_Refpt - Tower-shadow reference point (m)
 1.225                     Rho      - Air density (kg/m^3)
 1.4639e-5                 KinVisc  - Kinematic air viscosity [CURRENTLY
IGNORED] (m^2/sec)
 0.004                     DTAero   - Time interval for aerodynamic
calculations (sec)
 5                         NumFoil  - Number of airfoil files (-)
"aerodata\naca4424.dat" FoilNm   - Names of the airfoil files [NumFoil
lines] (quoted strings)
"aerodata\naca4421.dat"
"aerodata\naca4418.dat"
"aerodata\naca4415range_cm02.dat"
"aerodata\naca4412.dat"
33                         BldNodes - Number of blade nodes used for analysis
(-)
RNodes   AeroTwst DRNodes    Chord NFoil PrnElm
1.89  0.00  0.88  3.757 1    NOPRINT
2.77  0.00  0.88  3.669 1    NOPRINT
3.65  8.94  0.88  3.581 1    NOPRINT
4.53  8.64  0.88  3.493 1    NOPRINT
5.41  8.35  0.88  3.405 1    NOPRINT
6.29  8.06  0.88  3.317 1    NOPRINT
7.17  7.76  0.88  3.229 1    NOPRINT
8.05  7.47  0.88  3.141 1    NOPRINT
8.93  7.18  0.88  3.053 1    NOPRINT
9.81  6.88  0.88  2.965 1    NOPRINT
10.69 6.59  0.88  2.877 2    NOPRINT
11.57 6.30  0.88  2.789 2    NOPRINT
12.45 6.00  0.88  2.701 2    NOPRINT
13.33 5.71  0.88  2.613 2    NOPRINT
14.21 5.42  0.88  2.525 3    NOPRINT
15.09 5.12  0.88  2.437 3    PRINT
15.97 4.83  0.88  2.349 3    PRINT
16.85 4.54  0.88  2.261 3    PRINT
17.73 4.24  0.88  2.173 3    PRINT
18.61 3.95  0.88  2.085 3    PRINT
19.49 3.66  0.88  1.997 4    PRINT
20.37 3.36  0.88  1.909 4    PRINT
21.25 3.07  0.88  1.821 4    PRINT
22.13 2.78  0.88  1.733 4    PRINT
23.01 2.48  0.88  1.645 4    PRINT
```

```
23.89 2.19  0.88  1.557 4     PRINT
24.77 1.90  0.88  1.469 4     PRINT
25.65 1.60  0.88  1.381 4     PRINT
26.53 1.31  0.88  1.293 4     PRINT
27.41 1.02  0.88  1.205 5     PRINT
28.29 0.72  0.88  1.117 5     PRINT
29.17 0.43  0.88  1.029 5     PRINT
30.08 0.13  0.94  0.938 5     PRINT
SINGLE
SINGLE
SINGLE
USER
SINGLE
```

Example CCA.ipt file for Tborg CCA power control without timelag.

```
Simple CCA blade flap control trial
8            !Number of constants used in controls
-0.01        !Minimum momentum coefficient permissable at 15m/s (dimless)
CNST(1)
0.01         !Maximum momentum coefficient permissable at 15m/s (dimless)
CNST(2)
2000         !Power output set point (electrical - kW)           CNST(3)
4.6          !Gain numerator                                     CNST(4)
NOT USED
0.005        !Signaling time interval for pitch control (sec)    CNST(5)
NOT USED
10           !Decimation factor for output file                  CNST(6)
0.25         !Actuator time contant for first order lag          CNST(7)
NOT USED
0.00002      !Proportional constant for control model            CNST(8)
```

Example PITCH.ipt file for Tborg CCA power control without timelag.

```
Simple pitch control scheme using details from ECN report
7           !Number of constants used in controls
0           !Minimum pitch angle permissable (degs)               CNST(1)
35          !Minimum pitch angle permissable (degs)               CNST(2)
2000        !Power output set point (electrical - kW)             CNST(3)
4.6         !Gain numerator                                       CNST(4)
0.05        !Signaling time interval for pitch control (sec)      CNST(5)
10          !Decimation factor for output file                    CNST(6)
0.25        !Actuator time contant for first order lag            CNST(7)
```

Example PRIMARY.FAD file for Tborg CCA power control without timelag.

```
--------------------------------------------------------------------------------
-----
------- FAST INPUT FILE --------------------------------------------------------
-----
Tborg simulation of power control with CCAs.
Compatible with FAST v3.6.
---------------------- SIMULATION CONTROL --------------------------------------
-----
False        Echo        - Echo input data to "echo.out" (switch)
   3         NumBl       - Number of blades (-)
   600.0      TMax        - Total run time (s)
   0.004     DT          - Integration time step (s)
---------------------- TURBINE CONTROL -----------------------------------------
-----
   1         PCMode      - Pitch control mode {0: none, 1: power control, 2:
speed control} (switch)
   1         TPCOn       - Time to enable active pitch control (s)
   0         VSContrl    - Variable-speed control {0: none, 1: simple VS, 2:
user-defined VS}  (switch)
   0.0       RatGenSp    - Rated generator speed for simple variable-speed
generator control (HSS side) (rpm) [used only when VSContrl=1]
   0.0       Reg2TCon    - Torque constant for simple variable-speed
generator control in Region 2 (HSS side) (N-m/rpm^2) [used only when
VSContrl=1]
   1         GenModel    - Generator model {1: Simple, 2: Thevenin, 3: User
Defined} (-)
True         GenTiStr    - Method to start the generator {T: timed using
TimGenOn, F: generator speed using SpdGenOn} (switch)
True         GenTiStp    - Method to stop the generator {T: timed using
TimGenOf, F: when generator power = 0} (switch)
1500.0       SpdGenOn    - Generator speed to turn on the generator for a
startup (HSS speed) (rpm)
   0.0       TimGenOn    - Time to turn on the generator for a startup (s)
9999.9       TimGenOf    - Time to turn off the generator (s)
9999.9       THSSBrDp    - Time to initiate deployment of the HSS brake (s)
9999.9       TiDynBrk    - Time to initiate deployment of the dynamic
generator brake [CURRENTLY IGNORED] (s)
9999.9       TTpBrDp(1)  - Time to initiate deployment of tip brake 1 (s)
9999.9       TTpBrDp(2)  - Time to initiate deployment of tip brake 2 (s)
9999.9       TTpBrDp(3)  - Time to initiate deployment of tip brake 3 (s)
[unused for 2 blades]
9999.9       TBDepISp(1) - Deployment-initiation speed for the tip brake on
blade 1 (rpm)
9999.9       TBDepISp(2) - Deployment-initiation speed for the tip brake on
blade 2 (rpm)
9999.9       TBDepISp(3) - Deployment-initiation speed for the tip brake on
blade 3 (rpm) [unused for 2 blades]
9999.9       TPitManS(1) - Time to start override pitch maneuver for blade
1 and end standard pitch control (s)
9999.9       TPitManS(2) - Time to start override pitch maneuver for blade
2 and end standard pitch control (s)
9999.9       TPitManS(3) - Time to start override pitch maneuver for blade
3 and end standard pitch control (s) [unused for 2 blades]
9999.9       TPitManE(1) - Time at which override pitch maneuver for blade
1 reaches final pitch (s)
9999.9       TPitManE(2) - Time at which override pitch maneuver for blade
2 reaches final pitch (s)
9999.9       TPitManE(3) - Time at which override pitch maneuver for blade
3 reaches final pitch (s) [unused for 2 blades]
7.0       B1Pitch(1)  - Blade 1 initial pitch (degrees)
7.0       B1Pitch(2)  - Blade 2 initial pitch (degrees)
7.0       B1Pitch(3)  - Blade 3 initial pitch (degrees) [unused for 2
blades]
0.5       B1PitchF(1) - Blade 1 final pitch for pitch maneuvers (degrees)
```

```
0.5      BlPitchF(2) - Blade 2 final pitch for pitch maneuvers (degrees)
0.5      BlPitchF(3) - Blade 3 final pitch for pitch maneuvers (degrees)
[unused for 2 blades]
---------------------- ENVIRONMENTAL CONDITIONS ---------------------------
-----
   9.80665  Gravity     - Gravitational acceleration (m/s^2)
---------------------- FEATURE SWITCHES -----------------------------------
-----
 True        FlapDOF1    - First flapwise blade mode DOF (switch)
 True        FlapDOF2    - Second flapwise blade mode DOF (switch)
 True        EdgeDOF     - First edgewise blade mode DOF (switch)
 False       TeetDOF     - Rotor-teeter DOF (switch) [unused for 3 blades]
 True        DrTrDOF     - Drivetrain rotational-flexibility DOF (switch)
!must be turned on in order to correctly calculate generator power!
 True        GenDOF      - Generator DOF (switch)
 False       TiltDOF     - Nacelle-tilt DOF (switch)
 False       YawDOF      - Yaw DOF (switch)
 True        TwFADOF1    - First fore-aft tower bending-mode DOF (switch)
 True        TwFADOF2    - Second fore-aft tower bending-mode DOF (switch)
 True        TwSSDOF1    - First side-to-side tower bending-mode DOF
(switch)
 True        TwSSDOF2    - Second side-to-side tower bending-mode DOF
(switch)
 True        CompAero    - Compute aerodynamic forces (switch)
---------------------- INITIAL CONDITIONS ---------------------------------
-----
   0.0      OoPDefl     - Initial out-of-plane blade-tip displacement,
(meters)
   0.0      IPDefl      - Initial in-plane blade-tip deflection, (meters)
   0.0      TeetDefl    - Initial or fixed teeter angle (degrees) [unused
for 3 blades]
   0.0      Azimuth     - Initial azimuth angle for blade 1 (degrees)
  22.36     RotSpeed    - Initial or fixed rotor speed (rpm)
  -3.0      NacTilt     - Initial or fixed nacelle-tilt angle (degrees)
  00.0      NacYaw      - Initial or fixed nacelle-yaw angle (degrees) !
Uses same convention as ECN report
   0.0      TTDspFA     - Initial fore-aft tower-top displacement (meters)
   0.0      TTDspSS     - Initial side-to-side tower-top displacement
(meters)
---------------------- TURBINE CONFIGURATION ------------------------------
-----
  30.55     TipRad      - The distance from the rotor apex to the blade
tip (meters)      !from ECN!
   1.45     HubRad      - The distance from the rotor apex to the blade
root (meters)     !from ECN!
   1        PSpnElN     - Number of the innermost blade element which is
still part of the pitchable portion of the blade for partial-span pitch
control [1 to BldNodes] [CURRENTLY IGNORED] (-)
   0.0      UndSling    - Undersling length [distance from teeter pin to
the rotor apex] (meters) [unused for 3 blades]
  -0.54     HubCM       - Distance from rotor apex to hub mass [positive
downwind] (meters)      !from ECN!
  -6.81     OverHang    - Distance from yaw axis to rotor apex [3 blades]
or teeter pin [2 blades] (meters)   !from ECN!
   0.58     ParaDNM     - Distance parallel to shaft from yaw axis to
nacelle CM (meters)     !from ECN!
   0.0      PerpDNM     - Perpendicular distance from shaft to nacelle CM
(meters)
  56.0      TowerHt     - Height of tower above ground level (meters)    !
from ECN!
   5.0      Twr2Shft    - Vertical distance from the tower top to the yaw/
shaft intersection (meters)   !from ECN!
   0.0      TwrRBHt     - Tower rigid base height (meters)
   0.0      Delta3      - Delta-3 angle for teetering rotors (degrees)
[unused for 3 blades]
   0.0      PreCone(1)  - Blade 1 cone angle (degrees)
```

```
   0.0      PreCone(2)   - Blade 2 cone angle (degrees)
   0.0      PreCone(3)   - Blade 3 cone angle (degrees) [unused for 2
blades]
 180.0      AzimB1Up     - Azimuth value to use for I/O when blade 1 points
up (degrees)
--------------------- MASS AND INERTIA ----------------------------------
-----
154.0e3     NacMass      - Nacelle mass (kg)      !from ECN!
425.0e2     HubMass      - Hub mass (kg)          !from ECN!
   0.0      TipMass(1)   - Tip-brake mass, blade 1 (kg)
   0.0      TipMass(2)   - Tip-brake mass, blade 2 (kg)
   0.0      TipMass(3)   - Tip-brake mass, blade 3 (kg) [unused for 2
blades]
312.0e3     NacYIner     - Nacelle inertia about yaw axis (kg m^2)
312.0e3     NacTIner     - Nacelle inertia about tilt axis (kg m^2)
171.0e0     GenIner      - Generator inertia about HSS (kg m^2)
!inertia about LSS (from ECN)/(GB^2)
   0.0      HubIner      - Hub inertia about teeter axis (kg m^2) [unused
for 3 blades]
--------------------- DRIVETRAIN ----------------------------------------
-----
 100.0      GBoxEff      - Gearbox efficiency (%)       !from ECN!!!gearbox
and generator efficiencies are lumped below!!
  90.0      GenEff       - Generator efficiency [ignored by the Thevenin
and user-defined generator models] (%) !!lumped value for gearbox and
generator efficiencies!!
  68.4      GBRatio      - Gearbox ratio (-)      !calculated from ECN!
False       GBRevers     - Gearbox reversal {T: if rotor and generator
rotate in opposite directions} (switch)
9999.9      HSSBrTqF     - Fully deployed HSS-brake torque (N-m)
   0.5      HSSBrDt      - Time for HSS-brake to reach full deployment once
initiated (sec)
"DynBrk.dat"DynBrkFi     - File containing a mech-gen-torque vs HSS-speed
curve for a dynamic brake [CURRENTLY IGNORED] (quoted string)
   1.1e8    DTTorSpr     - Drivetrain torsional spring (N-m/rad)    !from
ECN!
   2.2e6    DTTorDmp     - Drivetrain torsional damper (N-m/s) !calculated
as 2% of the drive train torsional spring!
--------------------- SIMPLE INDUCTION GENERATOR ------------------------
-----
   1.9333   SIG_SlPc     - Rated generator slip percentage [>0] (%)
Now HSS side!     !from ECN -refstress!
1500.0      SIG_SySp     - Synchronous (zero-torque) generator speed [>0]
(rpm)  Now HSS side!    !from ECN -refstress!
12393.0     SIG_RtTq     - Rated torque [>0] (N-m)
Now HSS side!     !calculated from previous figures from ECN!
   2.0      SIG_PORt     - Pull-out ratio (Tpullout/Trated) [>1] (-)
!reasonable figue!
--------------------- THEVENIN-EQUIVALENT INDUCTION GENERATOR -----------
-----
   0.0      TEC_Freq     - Line frequency [50 or 60] (Hz)
   0        TEC_NPol     - Number of poles [even integer > 0] (-)
   0.0      TEC_SRes     - Stator resistance [>0] (ohms)
   0.0      TEC_RRes     - Rotor resistance [>0] (ohms)
   0.0      TEC_VLL      - Line-to-line RMS voltage (volts)
   0.0      TEC_SLR      - Stator leakage reactance (ohms)
   0.0      TEC_RLR      - Rotor leakage reactance (ohms)
   0.0      TEC_MR       - Magnetizing reactance (ohms)
--------------------- TOWER ---------------------------------------------
-----
  21        TwrNodes     - Number of tower nodes used for analysis (-)
"tborg_tower.dat" TwrFile - Name of file containing tower properties
(quoted string)
--------------------- NACELLE-YAW ---------------------------------------
-----
   0.0      YawSpr       - Nacelle-yaw spring constant (N-m/rad)
```

```
   0.0      YawDamp     - Nacelle-yaw constant (N-m/rad/s)
   0.0      YawNeut     - Neutral yaw position--yaw spring force is zero
at this yaw (degrees)
--------------------- NACELLE-TILT -------------------------------------
-----
   0.0      TiltSpr     - Nacelle-tilt linear-spring constant (N-m/rad)
   0.0      TiltDamp    - Nacelle-tilt damping constant (N-m/rad/s)
   0.0      TiltSStP    - Nacelle-tilt soft-stop position (degrees)
   0.0      TiltHStP    - Nacelle-tilt hard-stop position (degrees)
   0.0      TiltSSSp    - Nacelle-tilt soft-stop linear-spring constant (N-
m/rad)
   0.0      TiltHSSp    - Nacelle-tilt hard-stop linear-spring constant (N-
m/rad)
--------------------- ROTOR-TEETER -------------------------------------
-----
   0        TeetDMod    - Rotor-teeter damper model (0: none, 1: linear, 2:
user-defined) (switch) [unused for 3 blades]
   0.0      TeetDmpP    - Rotor-teeter damper position (degrees) [unused
for 3 blades]
   0.0e4    TeetDmp     - Rotor-teeter damping constant (N-m/rad/s)
[unused for 3 blades]
   0.0      TeetCDmp    - Rotor-teeter rate-independent Coulomb-damping
moment (N-m) [unused for 3 blades]
   0.0      TeetSStP    - Rotor-teeter soft-stop position (degrees)
[unused for 3 blades]
   0.0      TeetHStP    - Rotor-teeter hard-stop position (degrees)
[unused for 3 blades]
   0.0      TeetSSSp    - Rotor-teeter soft-stop linear-spring constant (N-
m/rad) [unused for 3 blades]
   0.0e6    TeetHSSp    - Rotor-teeter hard-stop linear-spring constant (N-
m/rad) [unused for 3 blades]
--------------------- TIP-BRAKE ----------------------------------------
-----
   0.0      TBDrConN    - Tip-brake drag constant during normal operation,
Cd*Area (m^2)
   0.0      TBDrConD    - Tip-brake drag constant during fully-deployed
operation, Cd*Area (m^2)
   0.0      TpBrDT      - Time for tip-brake to reach full deployment once
released (sec)
--------------------- BLADE --------------------------------------------
-----
"Tborg_blades.dat" BldFile(1) - Name of file containing properties for
blade 1 (quoted string)
"Tborg_blades.dat" BldFile(2) - Name of file containing properties for
blade 2 (quoted string)
"Tborg_blades.dat" BldFile(3) - Name of file containing properties for
blade 3 (quoted string) [unused for 2 blades]
--------------------- AERODYN ------------------------------------------
-----
"AeroDyn.ipt" ADFile  - Name of file containing AeroDyn input parameters
(quoted string)
--------------------- OUTPUT -------------------------------------------
-----
True        SumPrint    - Print summary data to "<RootName>.fsm" (switch)
True        TabDelim    - Generate a tab-delimited tabular output file.
(switch)
"ES10.3E2"  OutFmt      - Format used for tabular output except time.
Resulting field should be 10 characters. (quoted string)  [not checked for
validity!]
   1.0      TStart      - Time to begin tabular output (s)
  10        DecFact     - Decimation factor for tabular output [1: output
every time step] (-)
   1.0      SttsTime    - Amount of time between screen status messages
(sec)
   0.0      ShftGagL    - Distance from rotor apex [3 blades] or teeter
pin [2 blades] to shaft strain gages [positive for upwind rotors] (meters)
```

```
   1         NBlGages     - Number of blade nodes that have strain gages for
output [0 to 5] (-)
2            BldGagNd     - List of blade nodes that have strain gages [1 to
BldNodes] (-) 2
             OutList      - The next line(s) contains a list of output
parameters.  See OutList.txt for a listing of available output channels, (-
)
"uWind"
"Azimuth"                 - Rotor azimuth
"PtchPMzc1"               - Blade 1 pitch angle (position)
"GenPwr"                  - High Speed Shaft Power, Generator power
"RootMyb1, RootMyb2, RootMyb3"    - Blade 1-3 root flapwise bending moments
"LSShftFxa"               - Low-speed shaft thrust force (this is constant
along the shaft and is equivalent to the rotor thrust force)
"HSShftTq"                - High-speed shaft torque (this is constant along
the shaft)
"YawBrMzn"                - Tower-top / yaw bearing yaw moment
"TTDspFA, TTDspSS"        - Fore-aft and (minus) side-to-side tower-top
displacements
"TwrBsMxt"                - Tower base roll (or side-to-side) moment (i.e.,
the moment caused by side-to-side forces)                              |
|
"TwrBsMyt"                - Tower base pitching (or fore-aft) moment (i.e.,
the moment caused by fore-aft forces
END of FAST input file (the word "END" must appear in the first 3 columns
of this last line).
--------------------------------------------------------------------------
-----
```

Example TBORG_BLADES.dat file for Tborg CCA power control without timelag.

```
------------------------------------------------------------------------------
-----
---------------------- FAST INDIVIDUAL BLADE FILE ----------------------------
-----
Tjaerborg 2MW blades.
---------------------- BLADE PARAMETERS --------------------------------------
-----
  21        NBlInpSt     - Number of blade input stations (-)
False       CalcBMode    - Calculate blade mode shapes internally {T:
ignore mode shapes from below, F: use mode shapes from below} [CURRENTLY
IGNORED] (switch)
   3.9      BldFlDmp(1) - Blade flap mode #1 structural damping in percent
of critical (%)
  12.0      BldFlDmp(2) - Blade flap mode #2 structural damping in percent
of critical (%)
  11.4      BldEdDmp(1) - Blade edge mode #1 structural damping in percent
of critical (%)
---------------------- BLADE ADJUSTMENT FACTORS ------------------------------
-----
   1.00     FlStTunr(1) - Blade flapwise modal stiffness tuner, 1st mode (-
)
   1.00     FlStTunr(2) - Blade flapwise modal stiffness tuner, 2nd mode (-
)
   1.0      AdjBlMs      - Factor to adjust blade mass density (-)
   1.0      AdjFlSt      - Factor to adjust blade flap stiffness (-)
   1.0      AdjEdSt      - Factor to adjust blade edge stiffness (-)
---------------------- DISTRIBUTED BLADE PROPERTIES --------------------------
-----
BlFract  AeroCent  StrcTwst  BMassDen    FlpStff     EdgStff
  (-)      (-)       (deg)     (kg/m)     (Nm^2)      (Nm^2)
0      0.25  00.00 2100  15000000000 15000000000
11.34
0.05  0.25  00.00 492   2200000000  2200000000
10.77
0.1   0.25  10.20 453   1549788571  1877714286
0.15  0.25  9.63  415   878825714   1545142857
0.2   0.25  9.06  380   491426667   1249940000
0.25  0.25  8.49  346   323616667   983675000
0.3   0.25  7.92  313   211043333   771430000
0.35  0.25  7.35  283   153328333   612835000
0.4   0.25  6.78  254   108178667   482186667
0.45  0.25  6.21  226   79030167    387126667
0.5   0.25  5.64  201   55326667    306000000
0.55  0.25  5.07  177   40582667    247800000
0.6   0.25  4.50  154   28016000    194966667
0.65  0.25  3.93  134   20159000    153741667
0.7   0.25  3.36  115   13236867    115452000
0.75  0.25  2.79  98    9056167     85770000
0.8   0.25  2.22  82    5309467     58496000
0.85  0.25  1.65  68    3384017     41327000
0.9   0.25  1.08  56    1620700     25293567
0.95  0.25  0.51  45    936850      16820617
1     0.25  -0.06 37    8350000     9350000
--------------------- BLADE MODE SHAPES --------------------------------------
-----
0.0061
0.5424
-0.2188
2.0709
-1.4006
-0.1971
1.8132
-20.4122
34.9782
```

-15.1821
0.0713
2.5561
-3.6783
3.4415
-1.3906

Example TBORG_TOWER.dat file for Tborg CCA power control without timelag.

```
--------------------------------------------------------------------------------
-----
--------------------- FAST TOWER FILE -----------------------------------------
-----
Tborg tower file - based on data in ECN report and values provided by Stig
Oye.
--------------------- TOWER PARAMETERS ----------------------------------------
-----
   17          NTwInpSt     - Number of input stations to specify tower
geometry
False        CalcTMode     - Calculate tower mode shapes internally {T:
ignore mode shapes from below, F: use mode shapes from below} [CURRENTLY
IGNORED] (switch)
   5.0       TwrFADmp(1)  - Tower 1st fore-aft mode structural damping ratio
(%)
   5.0       TwrFADmp(2)  - Tower 2nd fore-aft mode structural damping ratio
(%)
   5.0       TwrSSDmp(1)  - Tower 1st side-to-side mode structural damping
ratio (%)
   5.0       TwrSSDmp(2)  - Tower 2nd side-to-side mode structural damping
ratio (%)
--------------------- TOWER ADJUSTMUNT FACTORS --------------------------------
-----
   1.0       FAStTunr(1)  - Tower fore-aft modal stiffness tuner, 1st mode (-
)
   1.0       FAStTunr(2)  - Tower fore-aft modal stiffness tuner, 2nd mode (-
)
   1.0       SSStTunr(1)  - Tower side-to-side stiffness tuner, 1st mode (-)
   1.0       SSStTunr(2)  - Tower side-to-side stiffness tuner, 2nd mode (-)
   1.0       AdjTwMa      - Factor to adjust tower mass density (-)
   0.8       AdjFASt      - Factor to adjust tower fore-aft stiffness (-)
   0.8       AdjSSSt      - Factor to adjust tower side-to-side stiffness (-)
--------------------- DISTRIBUTED TOWER PROPERTIES ----------------------------
-----
  HtFract  TMassDen     TwFAStif     TwSSStif
    (-)     (kg/m)       (Nm^2)       (Nm^2)
0.00  14621 1.44E+12    1.44E+12
0.08  13212 1.07E+12    1.07E+12
0.14  12252 8.50E+11    8.50E+11
0.20  11415 6.87E+11    6.87E+11
0.26  10721 5.70E+11    5.70E+11
0.32  10149 4.83E+11    4.83E+11
0.39  9700  4.22E+11    4.22E+11
0.45  9373  3.81E+11    3.81E+11
0.51  9189  3.59E+11    3.59E+11
0.57  9067  3.45E+11    3.45E+11
0.63  8944  3.31E+11    3.31E+11
0.69  8801  3.15E+11    3.15E+11
0.75  8679  3.03E+11    3.03E+11
0.82  8556  2.90E+11    2.90E+11
0.88  8434  2.78E+11    2.78E+11
0.94  8291  2.64E+11    2.64E+11
1.00  8168  2.52E+11    2.52E+11
--------------------- TOWER FORE-AFT MODE SHAPES ------------------------------
-----
 0.625        TwFAM1Sh(2) - Mode 1, coefficient of x^2 term
 0.858        TwFAM1Sh(3) -       , coefficient of x^3 term
 0.171        TwFAM1Sh(4) -       , coefficient of x^4 term
-1.133        TwFAM1Sh(5) -       , coefficient of x^5 term
 0.479        TwFAM1Sh(6) -       , coefficient of x^6 term
-12.025       TwFAM2Sh(2) - Mode 2, coefficient of x^2 term
-29.519       TwFAM2Sh(3) -       , coefficient of x^3 term
 99.275       TwFAM2Sh(4) -       , coefficient of x^4 term
-70.653       TwFAM2Sh(5) -       , coefficient of x^5 term
```

```
 13.921      TwFAM2Sh(6) -       , coefficient of x^6 term
---------------------- TOWER SIDE-TO-SIDE MODE SHAPES ---------------------
-----
 0.625       TwSSM1Sh(2) - Mode 1, coefficient of x^2 term
 0.858       TwSSM1Sh(3) -       , coefficient of x^3 term
 0.171       TwSSM1Sh(4) -       , coefficient of x^4 term
-1.133       TwSSM1Sh(5) -       , coefficient of x^5 term
 0.479       TwSSM1Sh(6) -       , coefficient of x^6 term
-12.025      TwSSM2Sh(2) - Mode 2, coefficient of x^2 term
-29.519      TwSSM2Sh(3) -       , coefficient of x^3 term
 99.275      TwSSM2Sh(4) -       , coefficient of x^4 term
-70.653      TwSSM2Sh(5) -       , coefficient of x^5 term
 13.921      TwSSM2Sh(6) -       , coefficient of x^6 term
```

```
!
!     ************************************************
!     SUBROUTINE CCACNTRL
!     Reads a data file containing minimum and maximum momentum
coefficients,
!     electrical power set point or any other variable to be controlled
!     TFOUTPUT = desired momntum coefficient returned by this subroutine
(dimless)
!     TFINPUT  = Input to the CCA control
!     ************************************************

      SUBROUTINE CCACntrl (TFOutput, TFInput, TwrAccel, Curr_CMU)

!New variables and calls etc for arguements passed from main rotine
      USE   SimCont
      USE TurbCont      USE Output

      IMPLICIT NONE

      INTEGER ::  IER
      INTEGER ::  IERR
      INTEGER ::  IDADAMS
      INTEGER ::  NCNST
      INTEGER ::  I
      INTEGER ::  OUT_INC
      INTEGER ::  OUT_SKP
      INTEGER ::  N
      INTEGER ::  DTC_INC
      INTEGER ::  DTC_SKP     INTEGER ::  MyNumOuts   INTEGER ::
K

      INTEGER, PARAMETER :: CON=12

      REAL(4)       :: TFInput (3)
      REAL(4)       :: TFOutput(3)
      REAL(4)       :: TwrAccel
      REAL(4)       :: CURR_CMU(3)                 REAL(4)      :: MyOutData
(CON)       REAL(4)      :: PROP_CON                    REAL(4)      ::
HHWndVect  (3)
      REAL ::       STRTPCH
      REAL ::       CNST (CON)
      REAL ::       CMUMIN
      REAL ::       CMUMAX      REAL ::      CMUMINin    REAL ::      CMUMAXin
      REAL ::       ELEC_SET
      REAL ::       GAIN_NUM
      REAL ::       DTCNTRL
      REAL ::       CMU(3)
      REAL ::       CMU_DOT(3)
!     REAL ::       CMU2(3)
      REAL ::       PHI_LAST
      REAL ::       PHI_ACT
      REAL ::       A
      REAL ::       B
      REAL ::       ATL

      REAL, EXTERNAL :: SAT2

      LOGICAL ::  INITFLAG = .TRUE. !Initialization flag

      CHARACTER*80       :: DESCRIP  CHARACTER(37)      :: Frmt
CHARACTER(28)      :: HeadFrmt

      SAVE              INITFLAG

!           Start initialisation of CCA parameters
      IF ( INITFLAG ) THEN
```

```
!        Read control parameters from cca.ipt

            CALL OpenInFile ( 43, 'cca.ipt' )

            READ(43,1000) DESCRIP

            WRITE(*,*) ' '
            WRITE(*,*) '**********************************************'
            WRITE(*,*) 'Running with control option using data from:'
            WRITE(*,*)  DESCRIP
            WRITE(*,*) '**********************************************'
            WRITE(*,*) ' '

            READ(43,*) NCNST

            DO I = 1, NCNST
                 READ(43,*) CNST(I)
            END DO

            CLOSE(43)


!Initialise time and counters

            OUT_SKP = 0               DTC_SKP = 0

!        Assign variable values from the cca.ipt file

            CMUMINin            = CNST(1)   !Minimum Cmu (dimless)
            CMUMAXin            = CNST(2)   !Maximum Cmu (dimless)
            ELEC_SET            = CNST(3)   !Power output set point
(electrical - kW)
            GAIN_NUM            = CNST(4)   !Gain numerator in ECN pitch eq.
(deg)
            DTCNTRL                    = CNST(5)  !Time interval for pitch
control (sec)
            OUT_INC                    = CNST(6)  !Decimation factor for
output file
            ATL                        = CNST(7)  !Actuator time lag
PROP_CON            = CNST(8)  !Proportional constant for control model


!        Open file to receive control variable output for debug (if
desired)

            OPEN(UNIT = 44, FILE = 'cca.out', STATUS = 'UNKNOWN',
     &                 IOSTAT = IER )

            IF(IER .NE. 0)  THEN
                 WRITE(*,*) 'ERROR OPENING FILE cca.out'
                 WRITE(*,*) 'IOSTAT=',IER, ' FILE INDEX= 44'
                 WRITE(*,*) ' '
                 CALL USRMES (.TRUE., 'Aborting in CCA', 44, 'STOP')
            ENDIF  !       Header output to pitch control.out file
              WRITE(44, *) ' '
            WRITE(44, *) 'Output of CCA control subroutine
     & using input file', DESCRIP
            WRITE(44, FMT='(A50,F6.3)') 'Time at which CCA control
     & actually commences', ZTIME          WRITE(44, *) ' '
            WRITE(44, 1001)      &  'Time             ',      &
'Signal1        ',      &       'Signal2        ',      &       'Signal3
',
     &       'Output1        ',      &       'Output2        ',      &
'Output3        '              WRITE(44, *) ' '

!     Initialisation of CCA values to zero
```

225

```
      DO K=1, 3
            TFOutput(K)=0
      ENDDO           !    Calculation of Cmu max and min wrt HH wind speed
CALL GetHubWind( HHWndVect )           CMUMAX = CMUMAXin - ((HHWndVect(1) -
15) *0.00025)      CMUMIN = CMUMINin + ((HHWndVect(1) - 15) *0.00025)

!     and save the output value for phi2 for the next time

!!    PHI_LAST = PHI2

!     Initial time step output to cca.out file

      MyNumOuts=6        MyOutData(1)= TFINPUT(1)       MyOutData(2)=
TFINPUT(2)  MyOutData(3)= TFINPUT(3)       MyOutData(4)= TFOUTPUT(1)
MyOutData(5)= TFOUTPUT(2)      MyOutData(6)= TFOUTPUT(3)        Frmt =
'(F8.3,200(:,A ,'//TRIM( OutFmt )//'))'   WRITE(44,Frmt)  ZTime, ( TAB,
MyOutData(I), I=1,MyNumOuts )

      INITFLAG = .FALSE.

      RETURN

      END IF

!     End of initialisation and return to main program on first call
!     Start counter for use of DTCNTRL to ensure that pitch signal time is
used

      DTC_INC = DTCNTRL/DT
      DTC_SKP=DTC_SKP+1

      IF (DTC_SKP.GE.DTC_INC) THEN
      DTC_SKP = 0

!     Variation of Cmu in response to power signal
      DO K=1, 3            CMU_DOT(K) = PROP_CON *(ELEC_SET - TFINPUT(K))   !
integrate cmu rate of change to give new cmu demanded
CMU(K) = CURR_CMU(K) + (CMU_DOT(K) * DTCNTRL)

!     Actuator first order time lag

!     A = DTCNTRL/(ATL+(DTCNTRL/2))
!     B = (DTCNTRL/2)/(ATL+(DTCNTRL/2))
!     PHI_ACT = CURR_PITCH_DEG +
!     &          A * (PHI_LAST - CURR_PITCH_DEG)
!     &         + B * (PHI - PHI_LAST)

!     and save the output value for phi for the next time
!     note that this is not necessarily the actual pitch angle due to
saturation function

!     PHI_LAST = PHI   ! Calculation of Cmu max and min wrt HH wind speed
CALL GetHubWind( HHWndVect )          CMUMAX = CMUMAXin - ((HHWndVect(1) -
15 ) *0.00025)      CMUMIN = CMUMINin + ((HHWndVect(1) - 15 ) *0.00025)
 !    Check that new Cmu is within limits of CMUmin and CMUmax
TFOutput(K) = SAT2(CMU(K), CMUMIN, CMUMAX) !Cmu returned to FAST for use
as CCA       ENDDO

!     End of ECN pitch control

      END IF

!     Counter and output for pitchcnrl.out file

      OUT_SKP=OUT_SKP+1
```

```
!     Write to controller output file when desired
      IF (OUT_SKP.GE.OUT_INC) THEN
            OUT_SKP = 0         MyNumOuts=6        MyOutData(1)= TFINPUT(1)
MyOutData(2)= TFINPUT(2)        MyOutData(3)= TFINPUT(3)        MyOutData(4)=
TFOUTPUT(1)        MyOutData(5)= TFOUTPUT(2)        MyOutData(6)= TFOUTPUT(3)
WRITE(44,Frmt)  ZTime, ( TAB, MyOutData(I), I=1,MyNumOuts )
      ENDIF

      RETURN

 1000 FORMAT(A)  1001 FORMAT(20(:A13))
      END
```

Appendix 4

Suitable Fan and Centrifugal Blower Specifications nuaire

FAN DATA SHEET

ire Limited, Western Industrial Estate, Caerphilly, CF83 1XH, United Kingdom. email:info@nuaire.co.uk
Technical Enquiries Tel:029 2085 8200 Fax:029 2085 8300 International Enquiries Tel:+44 29 2085 8335 Fax:+44 29 2085 8278

n Data

C - Axus Circular Contra Rotating, 2 Pole, GRP Blades

ular Contra Rotating Axial Fan

Code:	**AXC63AD-223**
ign Duty:	5 m³/s @ 3000 Pa
ual Duty:	5.207 m³/s @ 3253 Pa
ual at Design Flow:	5 m³/s @ 3333 Pa
de Angle:	30 / 25 °
Speed:	2,935 / 2,935 RPM
or Pole:	2 / 2
or Phase:	3
or Power:	15 / 15 kW
or Current:	fc: 28.2 / 28.2 A
or Current:	sc: 235 A (DOL) 78.333 A (SD)

rting currents are nominal.

x. Operating Temp.: 55°C

to our policy of ongoing product development and continuous improvement, eserve the right to make technical changes without prior notice.

ound Data

se Breakout 86 dBA @ 3m

akout level is hemi-spherical. For spherical deduct 3 dBA.

und Power Levels re 1 pWatts (Hz):

	125	250	500	1k	2k	4k	8k
uct Inlet	109	113	115	108	101	98	104
uct Outlet	112	114	117	109	102	98	105
en Inlet	105	111	115	108	101	98	104
en Outlet	107	112	116	109	102	98	105
eakout	105	107	109	97	90	82	83

se calculated at Actual Duty of fan with selected ancillaries.

Viring Information

s is a guide only. Please refer to the installation manual.

hase For Star / Delta Starting W and above)

e:
all DOL (Direct On Line) ration or inverter type speed trol wire in Delta.

otor overheat protection is cified, terminals T1 & T2 must connected to the fan control uit. Failure to do this will alidate the warranty.

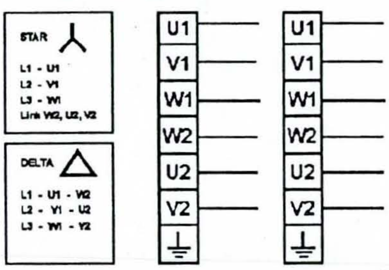

400V 3 phase 50Hz supply

Selected Ancillaries

2 x NAV5	Anti-vibration mounting kit
2 x CMB63	Mounting bracket (pair)
2 x CMF63	Matching flange
2 x CFC63	Flexible connector

Specification

Axus contra-rotating circular inline axial flow fan manufactured from galvanised steel. Fan incorporates inlet and outlet flanges with pre-drilled bolt holes, and an external terminal box to IP55. The motor is totally enclosed and protected to IP55, foot mounted class 'F' insulated and has sealed for life ball bearings. Blades manufactured from injection moulded GRP mounted in a die cast aluminum alloy hub as standard.

Fan Dimensions

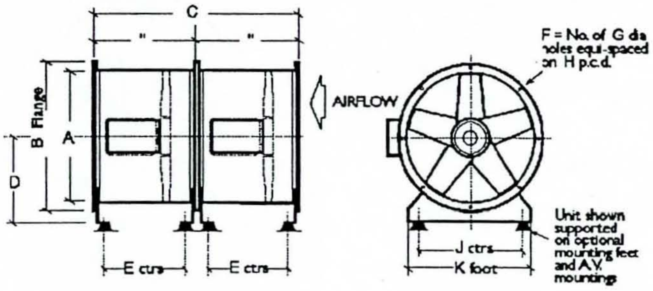

	A	B	C	D	E	F	G	H	J	K	kg
mm:	630	740	880	430	360	12	12	690	500	550	242

Performance Curve

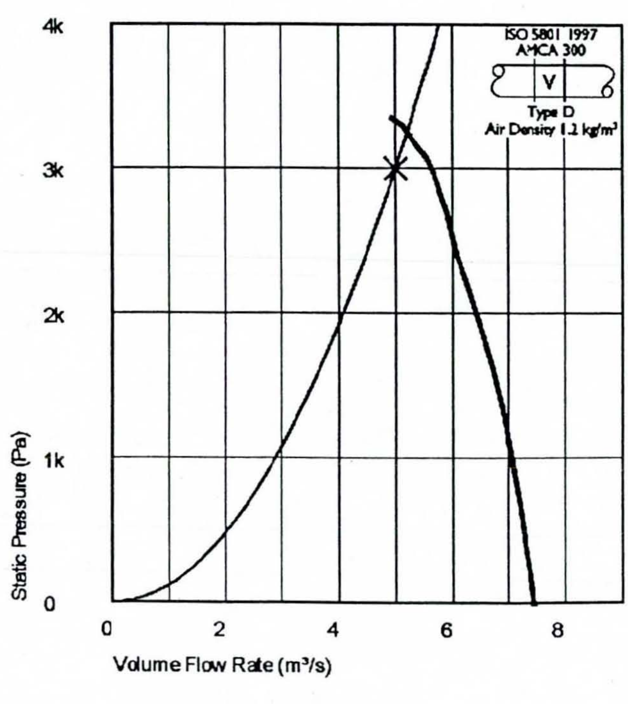

NUAIRE AXUS - Contra-rotating Axial Flow Fans for Smoke Control
300°C for 1 Hour

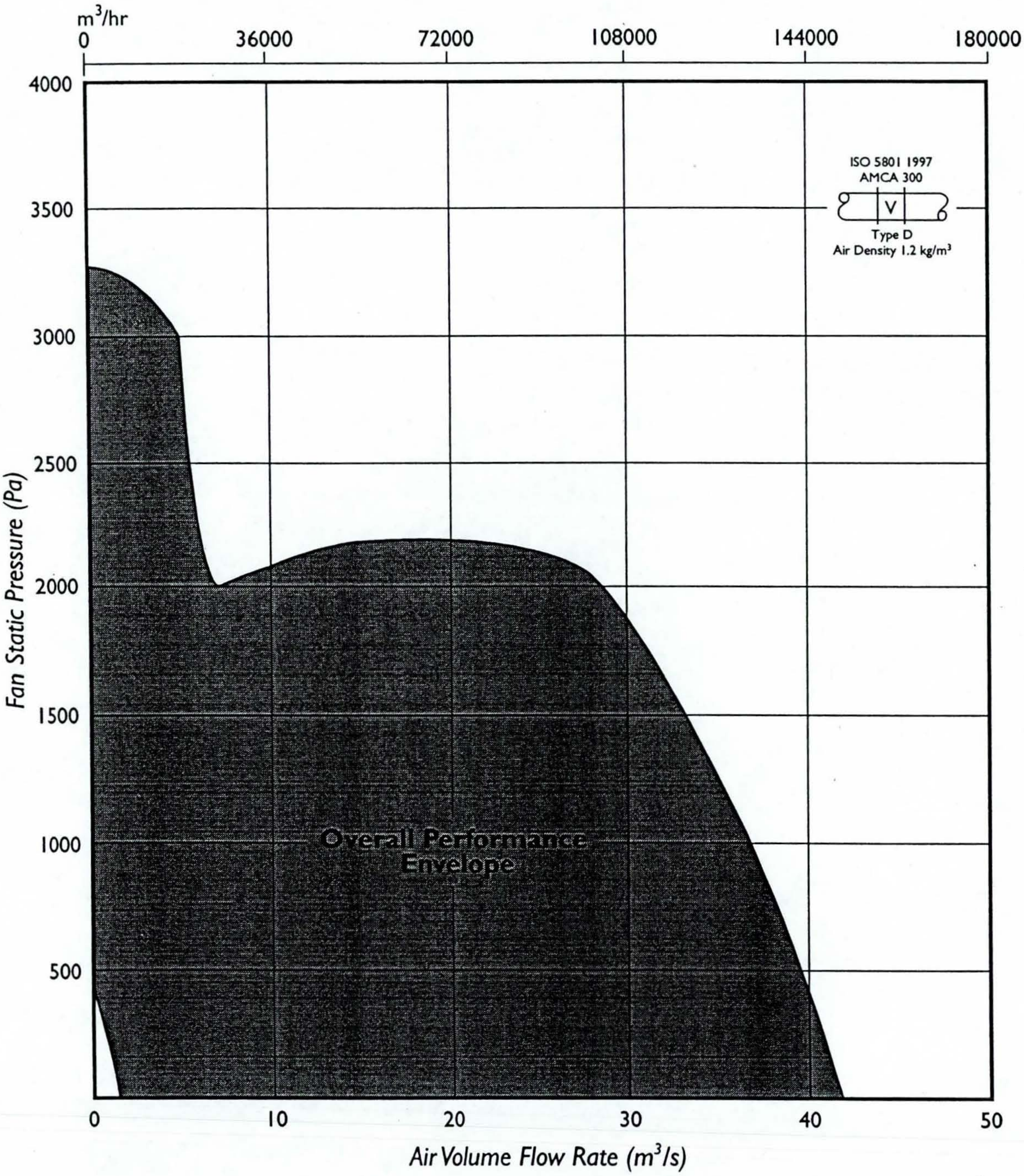

How to select

1. Use this page to identify the possible fan speed options for your duty requirement.

2. Use the individual envelopes opposite to select the appropriate fan size.

3. For full selection and technical information please do one of the following:-

- Contact Fans Direct on 08705 121 500.

Customer		*Page* 7 / ...
		WinEole V3.2d
Contract reference		Fläkt
Reference **Dulas - Centraxial 3**	*Qty of equipment* **1**	
Quotation No **Q70704A00**	*Position No* **3** / *Variant No* **01**	*Study* **1398**
Contact **Richard Bannister**	*Phone* **0121-717-4686**	*26/11/2002*
Product	**CENTRAXIAL MP 560 ED ADX STD**	

Requested characteristics

Type of fluid	**Air clean**			
Temperature of fluid at inlet	**20**	*°C*		
Site altitude	**0**	*m*		
Density	**1.2**	*kg/m3*	*at* **20** *°C*	
Design temperature	**20**	*°C*		
Starting temperature	**20**	*°C*		
Intake flowrate	**3.1**	*m3/s*		
Intake pressure	**- 0**	*Pa*	*at* **20**	*°C*
Discharge pressure	**+ 3600**	*Pa*	*at* **20**	*°C*
Static pressure differential	**3600**	*Pa*	*at* **20**	*°C*
Inlet ducted			*Outlet ducted*	

Aeraulic characteristics

Flowrate	**3.04**	*m3/s*		
Static pressure differential	**3532**	*Pa*		
Total pressure differential	**4000**	*Pa*		
Power consumption	**17.08**	*kW*	*at* **20**	*°C*
Minimum driving power	**17.94**	*kW*		
Efficiency	**82.14**	*%*		
Rotation speed	**2933**	*rpm*		
Max. rotation speed	**3395**	*rpm*		
Impeller diameter	**560**	*mm*		
Impeller inertia	**0.92**	*kg.m2*		
Start-up time	**3**	*s*		

Acoustic

Acoustic power level in free field conditions *(Intake free - Outlet ducted)*

Overall level **104** *dB* *According to standard BS848 Part 2*

Acoustic power spectrum in free field conditions

Octave bands	*63*	*125*	*250*	*500*	*1000*	*2000*	*4000*	*8000*	*Hz*
Lw spectrum	**69**	**82**	**85**	**95**	**91**	**88**	**85**	**79**	*dB(A)*

Overall mean acoustic pressure **90** *dB(A)* *at 1 m in free field conditions*

Acoustic power level in free field conditions *(Inlet ducted - Outlet ducted)*

Overall level **99** *dB* *Casing breakout noise*

Overall mean acoustic pressure **84** *dB(A)* *at 1 m in free field conditions*

Comment: *The values for acoustic pressure (or power) levels do not take account of the noise radiation from other sources (motor noise, resonance of walls...)*

Tolerances: *on overall levels: ± 3 dB*
per octave band: ± 5 dB

Customer				*Page* **8 / ...**
				WinEole V3.2d
Contract reference				Fläkt
Reference **Dulas - Centraxial 3**			*Qty of equipment* **1**	
Quotation No **Q70704A00**	*Position No* **3**	*Variant No* **01**		*Study* **1398**
Contact **Richard Bannister**		*Phone* **0121-717-4686**		*26/11/2002*
Product	**CENTRAXIAL MP 560 ED ADX STD**			

Impeller diameter	**560**	*mm*	*Peripheral speed*	**86**	*m/s*
Rotation speed	**2933**	*rpm*	*Max. rotation speed*	**3395**	*rpm*
Intake flowrate	**3.19**	*m3/s*	*Total pressure*	**4000**	*Pa*
Density	**1.2**	*kg/m3*	*at temperature*	**20**	*°C*
and Absolute pressure reference	**101325**	*Pa*	*and Altitude*	**0**	*m*
Curve plotted according to intake conditions			*Density*	**1.2**	*kg/m3*

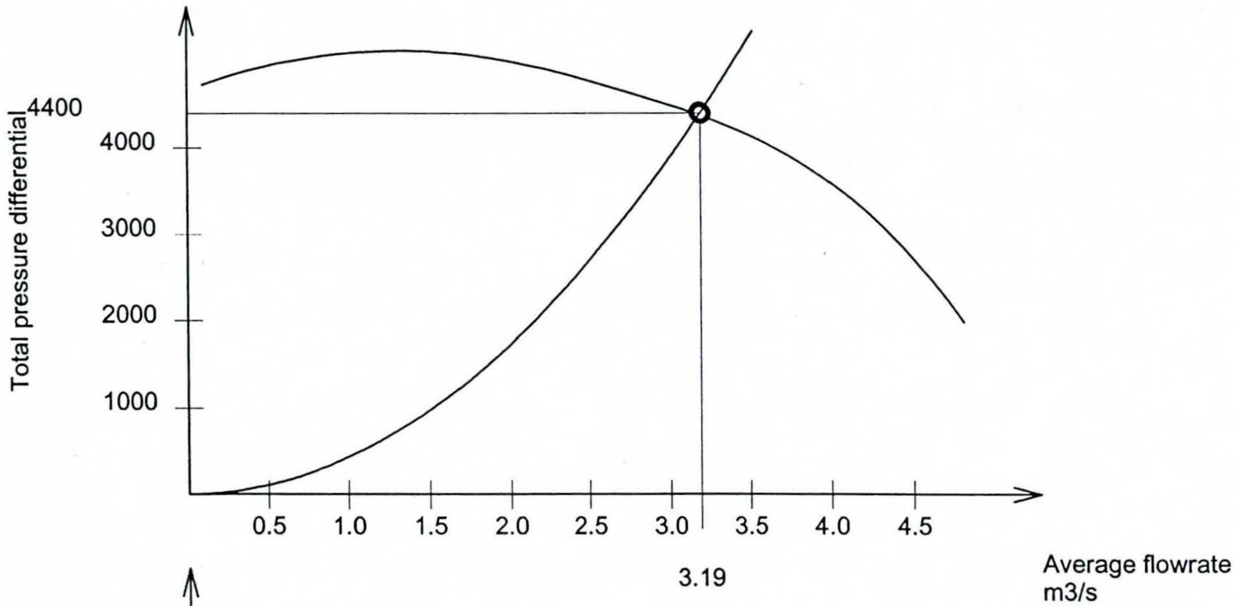

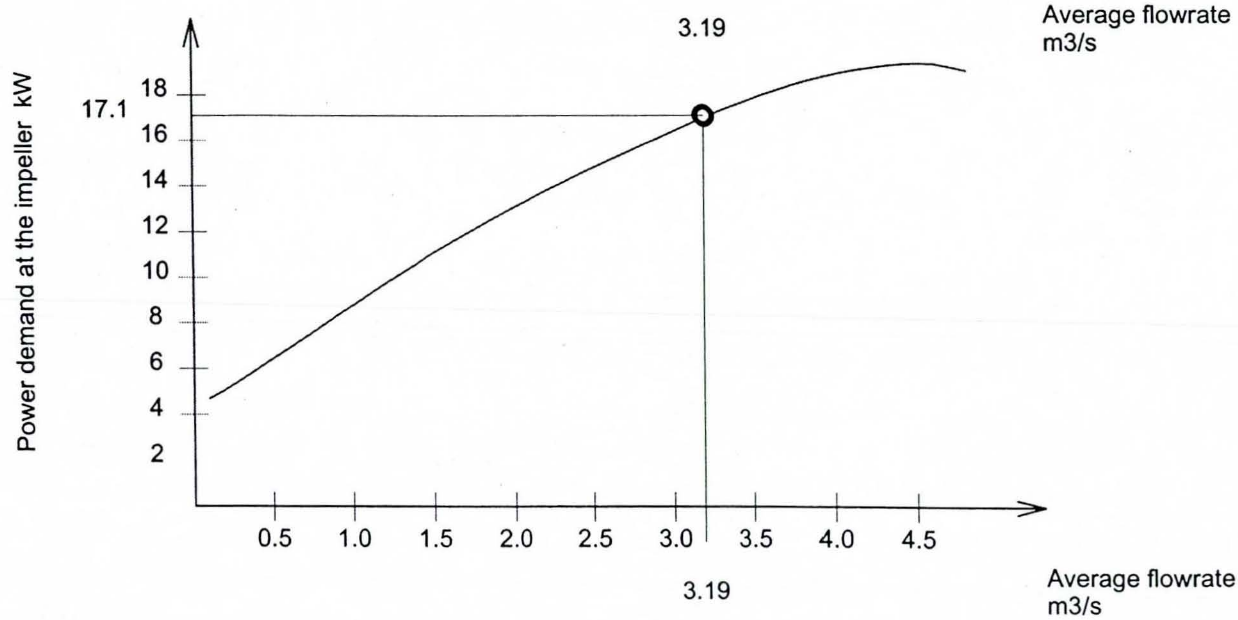

Customer		Page 1 / ...
		WinEole V3.2d
Contract reference		Fläkt
Reference Dulas - Centraxial 1	Qty of equipment 1	
Quotation No Q70704A00 · Position No 1	Variant No 01	Study 1395
Contact Richard Bannister	Phone 0121-717-4686	26/11/2002
Product	**CENTRAXIAL MP 630 ED ADX STD**	

Requested characteristics

Type of fluid	Air clean				
Temperature of fluid at inlet	20	°C			
Site altitude	0	m			
Density	1.2	kg/m3	at 20 °C		
Design temperature	20	°C			
Starting temperature	20	°C			
Intake flowrate	4.2	m3/s			
Intake pressure	- 0	Pa	at	20	°C
Discharge pressure	+ 5000	Pa	at	20	°C
Static pressure differential	5000	Pa	at	20	°C
Inlet ducted			Outlet ducted		

Aeraulic characteristics

Flowrate	4.03	m3/s			
Static pressure differential	4769	Pa			
Total pressure differential	5280	Pa			
Power consumption	29.86	kW	at	20	°C
Minimum driving power	32.85	kW			
Efficiency	82.33	%			
Rotation speed	2943	rpm			
Max. rotation speed	3040	rpm			
Impeller diameter	630	mm			
Impeller inertia	1.42	kg.m2			
Start-up time	2	s			

Acoustic

Acoustic power level in free field conditions *(Intake free - Outlet ducted)*

Overall level **108** dB According to standard BS848 Part 2

Acoustic power spectrum in free field conditions

Octave bands	63	125	250	500	1000	2000	4000	8000	Hz
Lw spectrum	73	86	89	99	95	92	89	83	dB(A)

Overall mean acoustic pressure **94** dB(A) at 1 m in free field conditions

Acoustic power level in free field conditions *(Inlet ducted - Outlet ducted)*

Overall level **103** dB Casing breakout noise

Overall mean acoustic pressure **87** dB(A) at 1 m in free field conditions

Comment: *The values for acoustic pressure (or power) levels do not take account of the noise radiation from other sources (motor noise, resonance of walls...)*

Tolerances: *on overall levels: ± 3 dB*
per octave band: ± 5 dB

Customer		Page 2 / ...
		WinEole V3.2d
Contract reference		Fläkt
Reference **Dulas - Centraxial 1**	Qty of equipment **1**	
Quotation No **Q70704A00**	Position No **1** / Variant No **01**	Study **1395**
Contact **Richard Bannister**	Phone **0121-717-4686**	26/11/2002
Product	**CENTRAXIAL MP 630 ED ADX STD**	

Impeller diameter	**630**	*mm*	*Peripheral speed*	**97.1**	*m/s*
Rotation speed	**2943**	*rpm*	*Max. rotation speed*	**3040**	*rpm*
Intake flowrate	**4.23**	*m3/s*	*Total pressure*	**5280**	*Pa*
Density	**1.2**	*kg/m3*	*at temperature*	**20**	*°C*
and Absolute pressure reference	**101325**	*Pa*	*and Altitude*	**0**	*m*
Curve plotted according to intake conditions			*Density*	**1.2**	*kg/m3*

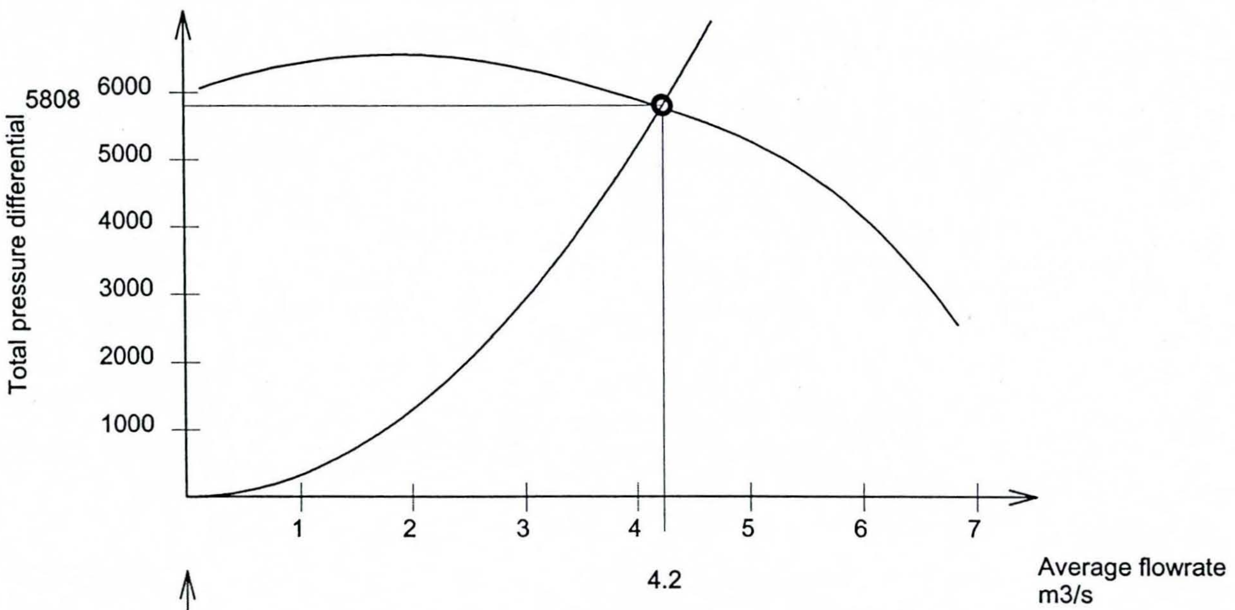

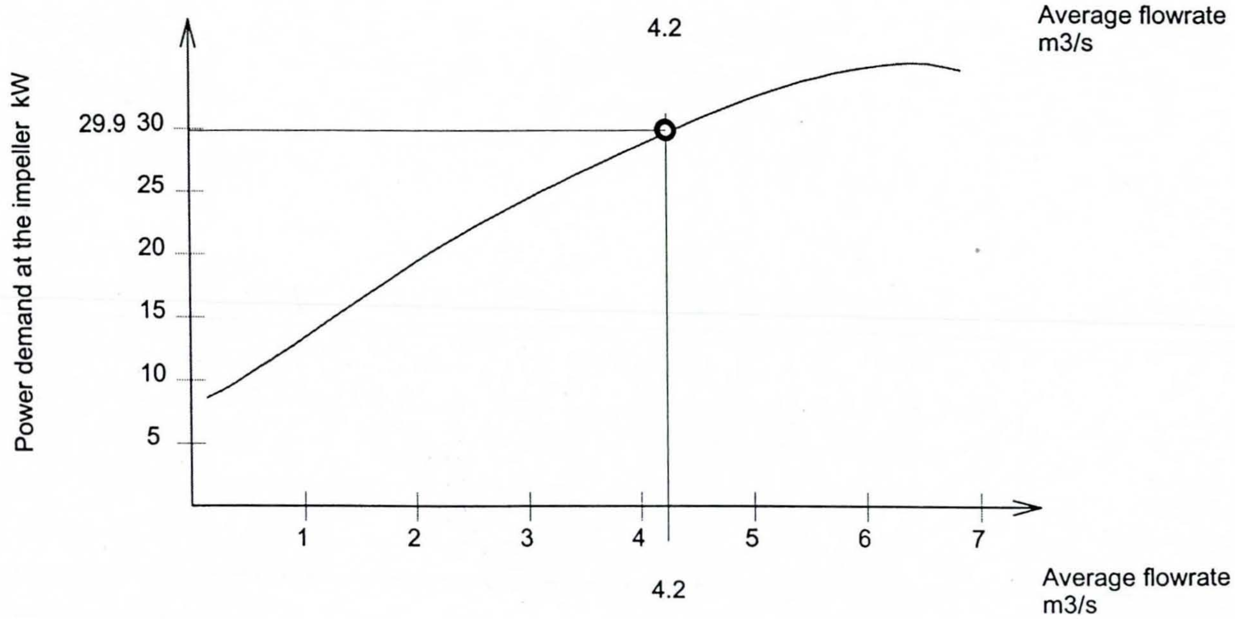

FläktWoods

Fläkt

Date: 25/11/02 DATA SHEET FOR CENTRIFUGAL FAN

Yorkshire HX48HB, Tel.: +44 (14 22) 378 131 Fax: +44 (14 22) 378 672

CUSTOMER: dulas ltd, Unit 1 Dyfi Eco Park, Powys, SY20 8RX	ENQUIRY: from 25/11/02	Item: 2	TENDER No.: 25110201BMA
YOUR REF.: Conrad Trevelyan	PROJECT: ?? Y/DESC.:	Units: 1	Handled by: B.Horrocks (+44) 1892 852520

Type : A-LRZ9/800/1250/1

TECHNICAL DATA

Volume flow rate		V m³/h	45,360
Static pressure at ρ=1.2	kg/m³	Δp_{st} Pa	6,059
Total pressure at ρ=1.2	kg/m³	Δp_t Pa	6,436
Static pressure at ρ=	kg/m³	Δp_{st} Pa	
Total pressure at ρ=	kg/m³	Δp_t Pa	
Speed		n 1/min	1,483
Impeller power at ρ= 1.2	kg/m³	P_W kW	91.96
Impeller power at ρ=	kg/m³	P_W kW	
Sound pressure,free field		L_p dB(A)	86-1m
for installation type D (ISO) calculated acc. to VDI 3731			
Sound power level		L_W dB(A)	111
Fan weight (without motor) approx.		kg	1,394
Operating temperature		°C	20
maximum temperature		°C	40

Flow medium ■ fresh air ■ dust free ☐

Ex-protection ☐ zone 0 ☐ zone 1 ☐ zone 2 ☐ shipbuilding rules

☐ for speed control : block resonance frequencies

INSTALLATION TYPE according to ISO 13349

- ☐ A -Free inlet, free outlet
- ☐ B -Free inlet, ducted outlet
- ☐ C -Ducted inlet, free outlet
- ■ D -Ducted inlet and outlet

Exhaust position according to EUROVENT **RD90**

MOTOR

Make		**Standard IEC Motor**
Type/Size		**/ 315S**
Rated voltage U/Frequency f	V/Hz	**3x400V / 50**
Rated speed n approx.	1/min	**1485**
Rated power P	kW	**110**
Design/protection class		**B3 / IP55**
Motor weight approx.	kg	**795**
Classification		**IEC**
Insulation class/utilised		**F/B**
Rated current I/ Starting current I approx.	A	**197 / 6.5-times**

- ☐ Ex-protection
- ☐ Multi speed
- ■ Direct-Connection
- ■ Thermistor protection 3-times
- ☐ Space heater
- ☐ without motor terminal box, with cable
- ☐ Drain in flange

OTHER REQUIREMENTS

Documentation
Legal basis :2
Tolerance according to B. S. 848
Fan Systems Terms and Conditions
Payment terms conditional on positive credit rating

CENTRIFUGAL FAN

- ■ Single inlet
- ■ Direct drive, impeller mounted on motor shaft
- ☐ Belt drive
- ☐ Drive through elastic coupling
- ☐ Blocklager Bearing Unit
- ■ Indoor installation
- ☐ Shaft seal
- ■ 1 x Split casing
- ■ 1 x Flanged Inlet spigot size 800 mild steel
- ■ 1 x Drain plug 1/2"
- ■ 1 x Inspection opening
- ■ 1 x Strengthened pedestal for large motor

MATERIAL

Impeller	S355J2G3=St52-3
Casing	S235JRG2=RSt37-2
Base frame/support	S235JRG2=RSt37-2
Inlet cone	S235JRG2=RSt37-2

SURFACE TREATMENT

Impeller	no paint
Casing outside	Standard grey hammer
Casing inside	primer
Base frame/support	Standard grey hammer

PRICE PER UNIT EXCL. VAT

	£
■ Centrifugal fan base price	4,760.00
■ Motor	incl.
☐ Cooling disc	
☐ Protection grill inlet	
☐ Protection grill outlet	
☐ Anti-spark lining (brass)	
■ 1 x RSC Base	incl.

SEPARATE PARTS

- ☐ Vibration attenuators
- ☐ Counter flange inlet
- ☐ Counter flange outlet
- ☐ Flex.connect. inlet
- ☐ Guide duct inlet
- ☐ Flex.connect. outlet
- ☐ Guide duct outlet

Total price/unit excl. VAT	**£**	**4,760.00**
Total price excl. VAT	**£**	**4,760.00**

Delivery time (EXW): To be agreed

Delivery conditions:
EXW (Incoterms'00), Hollybank Works

Payment conditions:
30 days net

Guarantee
12 months after delivery, wear and tear parts 6 months

Tender valid: 25/01/03

235

FAN SYSTEMS

TECHNICAL DATA FOR CENTRIFUGAL FAN

Date: 25/11/02ified

CUSTOMER: dulas ltd Unit 1 Dyfi Eco Park Powys SY20 8RX	ENQUIRY: from 25/11/02	Item: 2	TENDER No.: 25110201BMA
YOUR REF.: Conrad Trevelyan	PROJECT: ?? Y/DESC.:	Units: 1	Handled by: B.Horrocks (+44) 1892 852520

Fan type : A-LRZ9/800/1250/1 **Fan type: Centrifugal fans**

Input data :

Input data	:	2 - T1 - P1
Medium	:	Air
Airflow-input	V [m3/s]:	12.60
Static pressure	ps = pt-pd2 [Pa]:	6000.00
Gas constant	R [J/(kgK)]:	288.20
Isentropic exponent	kappa [-]:	1.40
Pressure addition	% of pd2 [%]:	0.00
Tolerances acc. to DIN 24 166 class	:	2

Selection data :

Flow rate	V [m3/h]	45360.00
Static pressure	ps = pt-pd2 [Pa]	6059.84
Total pressure	pt [Pa]	6436.85
Inlet density	Rho [kg/m3]	1.20
Inlet pressure	p1 [kPa]	101.32
Inlet temperature	T1 [°C]	20.00
Fan speed	N [1/min]	1483.00
Impeller power	Pw [kW]	91.97
Rated motor power	PM [kW]	110.00
Efficiency	Eta [%]	86.25
Impeller power (Rho1.2)	Pw [kW]	91.97
St.pressure (Rho1.2) pst=pt-pd2 [	Pa] [ ]	6060.00
Total pressure (Rho1.2)	pt [Pa]	6437.00
Sound pressure 1m (ISO-D)	Lp [dB(A)]	86.00
Sound power	Lw [dB(A)]	111.00
Blade frequency	f [Hz]	222.00
Tip speed	u2 [m/s]	97.06
Inlet speed	c1 [m/s]	25.06
Temperature increase	dT [°C]	6.03
Impeller power (Vol=0)	Pw [kW]	
Compressibility coeff.	k [-]	0.98
Fan flow-rate coeff.	phi [-]	0.11
Pressure coeff.	psi [-]	1.09
Rough approximation of starting time :		
Appx. impeller weight	[kg]	192.00
Appx. mass moment of inertia [	kg m²] [ ]	48.75
Appx. starting time	ta [s]	12
ca. Standard Rundown time	td [s]	72

FANCURVE FOR CENTRIFUGAL FAN

Date: 25/11/02

CUSTOMER: dulas ltd Unit 1 Dyfi Eco Park Powys SY20 8RX	ENQUIRY: from 25/11/02	Item: 2	TENDER No.: 25110201BMA
YOUR REF.: Conrad Trevelyan	PROJECT: ?? Y/DESC.:	Units: 1	Handled by: B.Horrocks (+44) 1892 852520

V.2

Fan type : A-LRZ9/800/1250/1 **Fan type: Centrifugal fans**

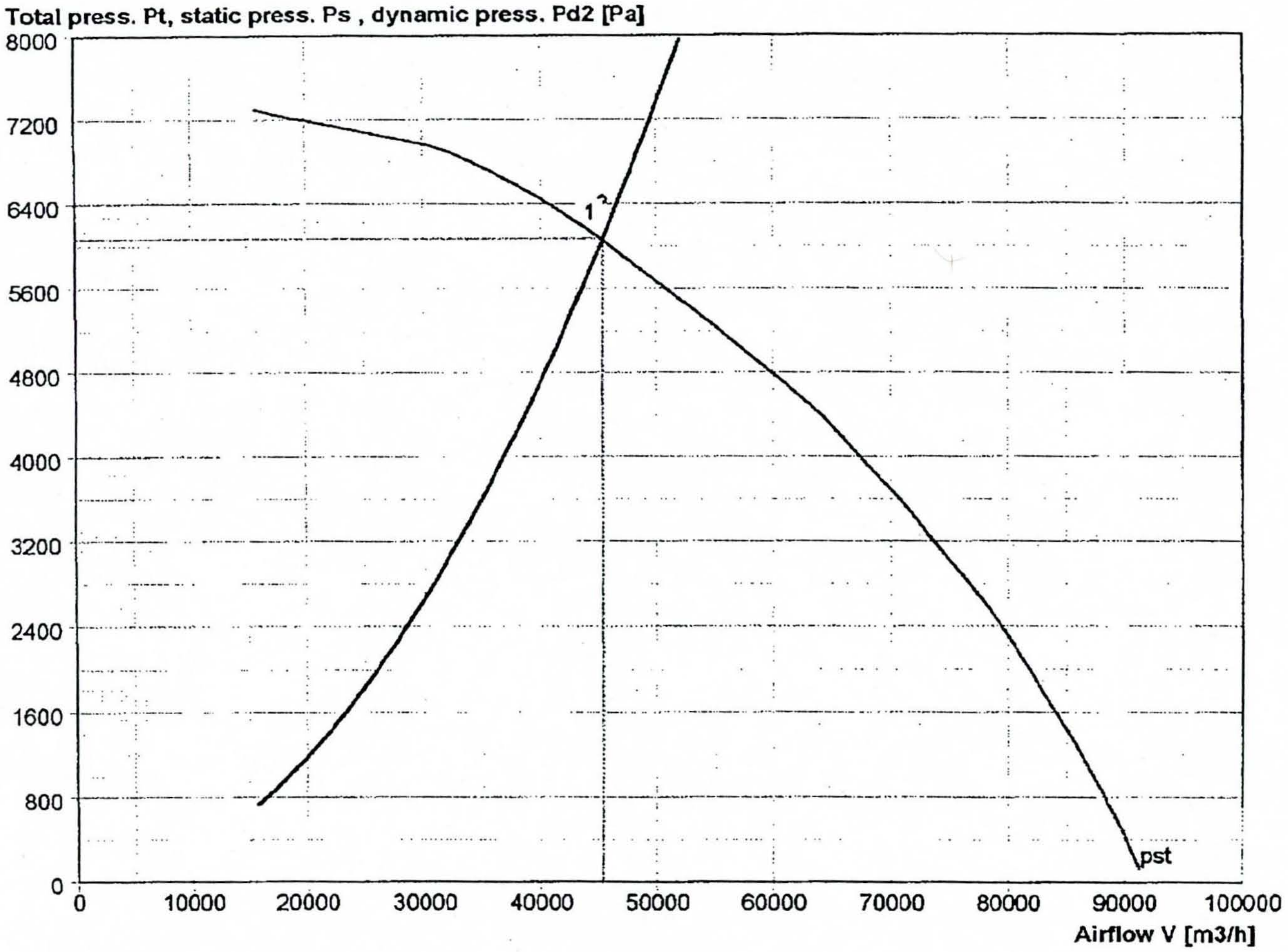

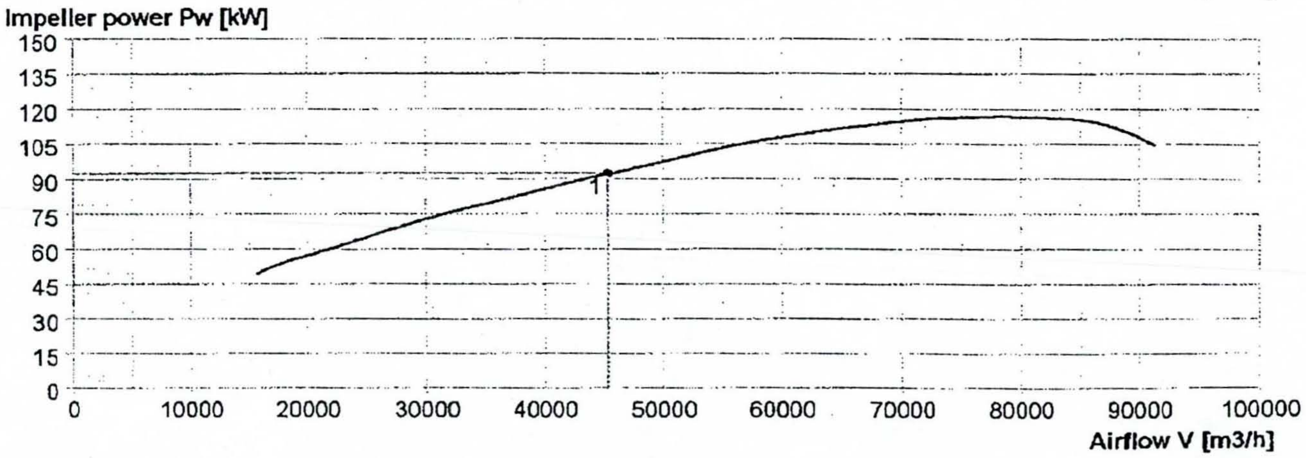

		1				
Air volume	V [m3/h]	45360.00				
Inlet density	Rho [kg/m3]	1.20				
Fan speed	N [1/min]	1483.00				

STARTUP-/RUNDOWN CURVE

Date: 25/11/02tified

CUSTOMER: dulas ltd Unit 1 Dyfi Eco Park Powys SY20 8RX	ENQUIRY: from 25/11/02	Item: 2	TENDER No.: 25110201BMA
YOUR REF.: Conrad Trevelyan	PROJECT: ?? Y/DESC.:	Units: 1	Handled by: B.Horrocks (+44) 1892 852520

Fan type : A-LRZ9/800/1250/1 **Fan type: Centrifugal fans**

Flow rate	V [m3/h]:	45360.00
Inlet density	Rho [kg/m3]:	1.20
Fan speed	N [1/min]:	1483.00
Impeller power	Pw [kW]:	91.97
Rated motor power	PM [kW]:	110.00
Rough approximation of starting time :		
Appx. impeller weight	[kg]:	192.00
Appx. mass moment of inertia [kg m²]	[ ]:	48.75
Appx. starting time	ta [s]:	12
ca. Standard Rundown time	td [s]:	72

Run up time

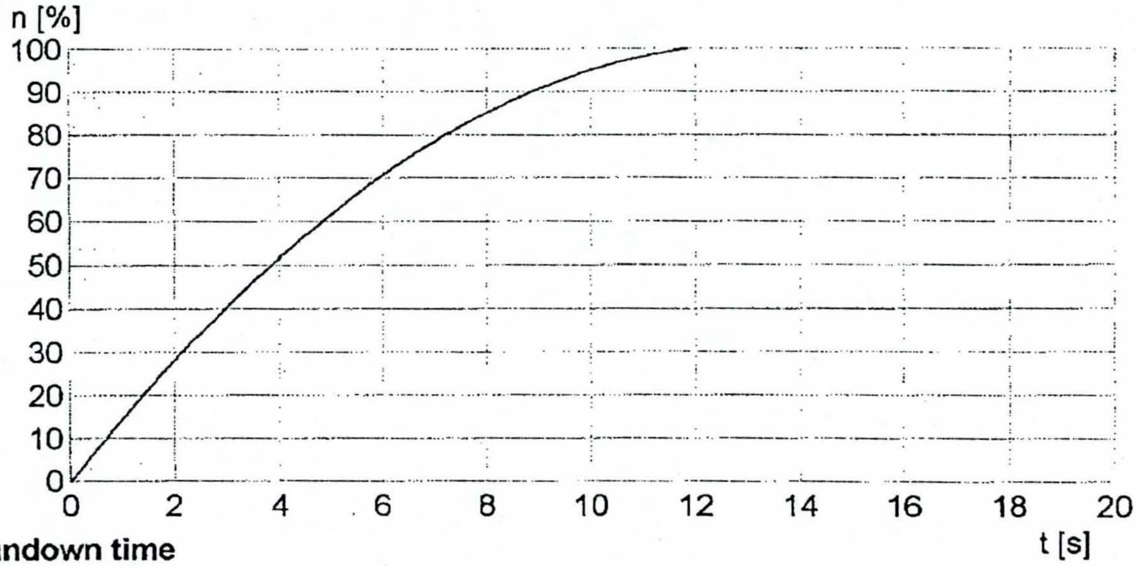

Rundown time

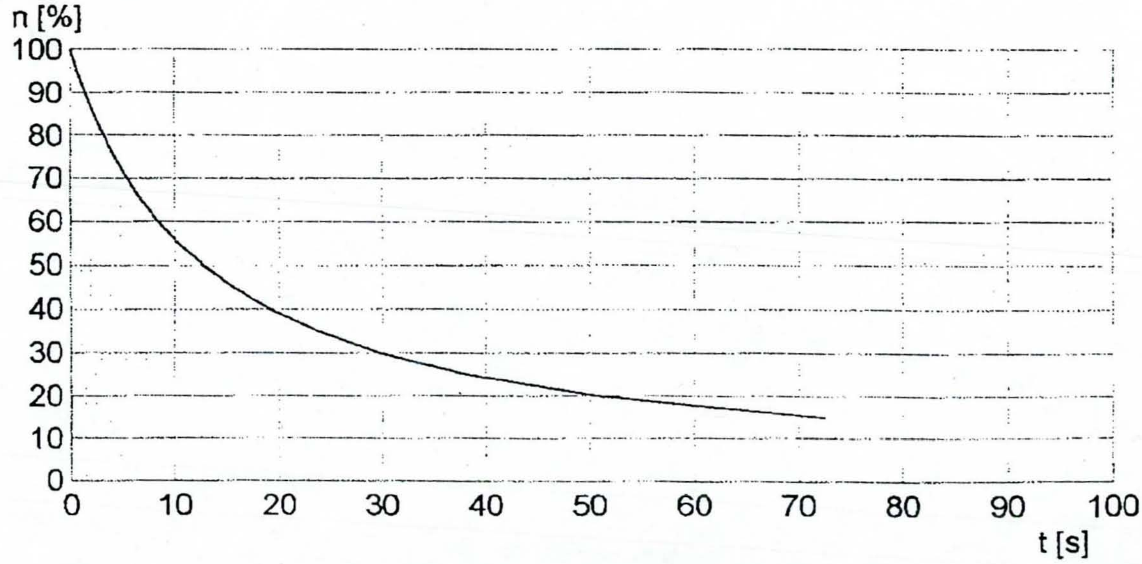

The stated times are a first approximation only. Significant variance for different motor suppliers due to differ motor-torque are to be expected. At start-up against closed damper 10 - 20 % faster times can be achieved. The values only apply for direct on line start/ the given density, for star/delta start the switching time is releva

STATE	DATE	REVISION

OUTLET POSITIONS

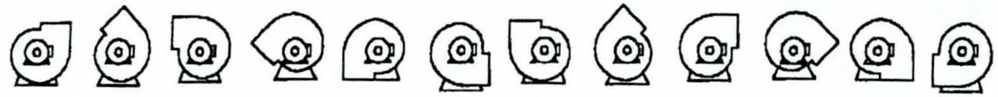

EUROVENT : LG0 LG45 LG90 LG135 LG180 LG270 RD0 RD45 RD90 RD135 RD180 RD270

dimension tolerance class: EN ISO 13920-CG

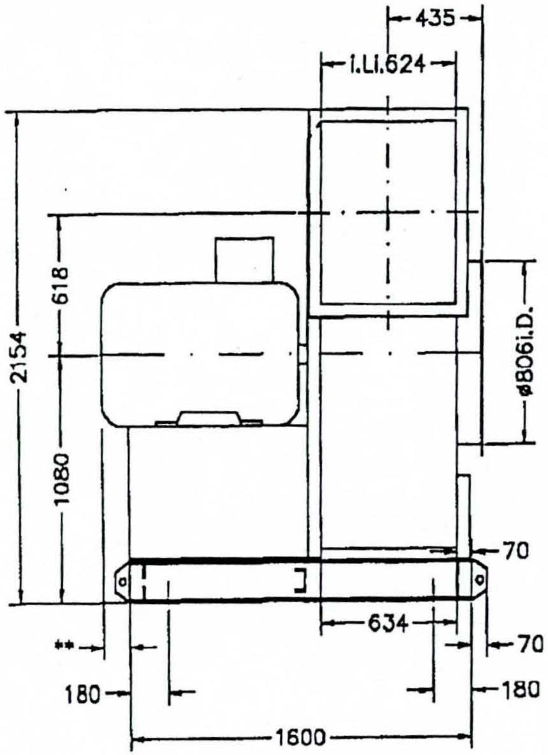

outlet flange :

inlet flange :

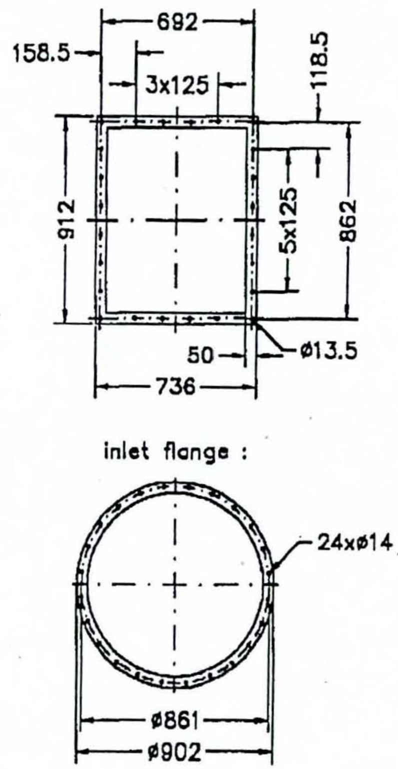

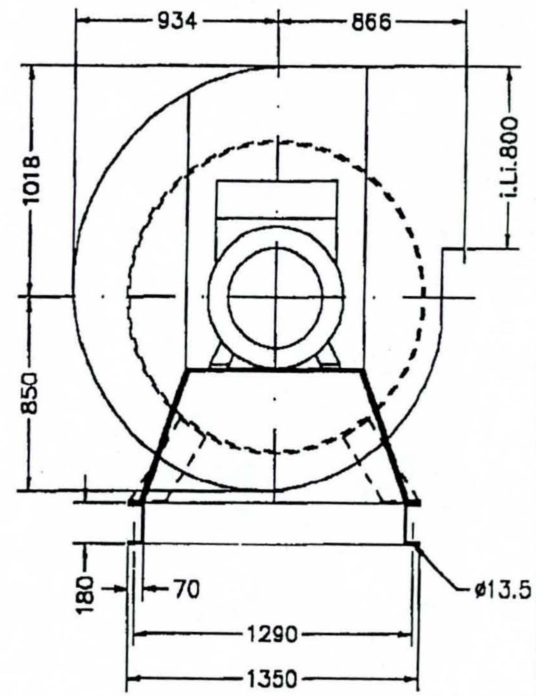

** motor excess with motor dimension k=1090 (ABB) ca.: 130

PROVISIONAL DRAWING
APPROX NET WT = 2350Kg

OUTLET POSITION : please inform	FAN TYPE : A-LRZ9/800/1250/1		DATE	NAME	DIMENSION SHEET	FAN SYSTEMS
MOTOR POSITION :	MOTOR TYPE: 315	DRAWN	25.11.02		UNCERTIFIED CENTRIFUGAL FAN DESIGN	
DESIGNATION : Drawing.dwg	SCALE : dimensioned parts 1:33	CHECK				NO. 25110201BMA-2 POS.

FAN SYSTEMS

Date: 25/11/02

DATA SHEET FOR CENTRIFUGAL FAN

Yorkshire HX48HB, Tel.: +44 (14 22) 378 131 Fax: +44 (14 22) 378 672

CUSTOMER:	ENQUIRY: from 25/11/02	Item:	TENDER No.:
dulas ltd Unit 1 Dyfi Eco Park Powys SY20 8RX	PROJECT: ??	3	25110201BMA
YOUR REF.: Conrad Trevelyan	Y/DESC.:	Units: 1	Handled by: B.Horrocks (+44) 1892 852520

Type : S-LRZ9D/800/1120/1

TECHNICAL DATA

Volume flow rate		V m³/h	32,400
Static pressure at ρ=1.2 kg/m³	Δp_{st}	Pa	4,095
Total pressure at ρ=1.2 kg/m³	Δp_t	Pa	4,288
Static pressure at ρ= kg/m³	Δp_{st}	Pa	
Total pressure at ρ= kg/m³	Δp_t	Pa	
Speed	n	1/min	1,478
Impeller power at ρ= 1.2 kg/m³	P_W	kW	44.01
Impeller power at ρ= kg/m³	P_W	kW	
Sound pressure,free field	L_p	dB(A)	82-1m
for installation type D (ISO) calculated acc. to VDI 3731			
Sound power level	L_W	dB(A)	108
Fan weight (without motor) approx.		kg	1,050
Operating temperature		°C	20
maximum temperature		°C	40

Flow medium ■ fresh air ■ dust free ☐

Ex-protection ☐ zone 0 ☐ zone 1 ☐ zone 2 ☐ shipbuilding rules

☐ for speed control : block resonance frequencies

INSTALLATION TYPE according to ISO 13349

- ☐ A -Free inlet, free outlet
- ☐ B -Free inlet, ducted outlet
- ☐ C -Ducted inlet, free outlet
- ■ D -Ducted inlet and outlet

Exhaust position according to EUROVENT **RD90**

MOTOR

Make		**Standard IEC Motor**
Type/Size		**/ 250M**
Rated voltage U/Frequency f	V/Hz	**3x400V / 50**
Rated speed n approx.	1/min	**1475**
Rated power P	kW	**55**
Design/protection class		**B3 / IP55**
Motor weight approx.	kg	**425**
Classification		**IEC**
Insulation class/utilised		**F/B**
Rated current I/ Starting current I approx.	A	**97 / 7.3-times**

- ☐ Ex-protection
- ☐ Multi speed
- ■ Direct-Connection
- ■ Thermistor protection 3-times
- ☐ Space heater
- ☐ without motor terminal box, with cable
- ☐ Drain in flange

CENTRIFUGAL FAN

- ■ Single inlet
- ■ Direct drive, impeller mounted on motor shaft
- ☐ Belt drive
- ☐ Drive through elastic coupling
- ☐ Blocklager Bearing Unit
- ■ Indoor installation
- ☐ Shaft seal
- ■ 1 x Split casing
- ■ 1 x Flanged Inlet spigot size 800 mild steel
- ■ 1 x Drain plug 1/2"
- ■ 1 x Inspection opening

MATERIAL

Impeller	S235JRG2=RSt37-2
Casing	S235JRG2=RSt37-2
Base frame/support	S235JRG2=RSt37-2
Inlet cone	S235JRG2=RSt37-2

SURFACE TREATMENT

Impeller	primer
Casing outside	Standard grey hammer
Casing inside	primer
Base frame/support	Standard grey hammer

PRICE PER UNIT EXCL. VAT

	£
■ Centrifugal fan base price	3,254.00
■ Motor	incl.
☐ Cooling disc	
☐ Protection grill inlet	
☐ Protection grill outlet	
☐ Anti-spark lining (brass)	
■ 1 x RSC Base	incl.

SEPARATE PARTS

- ☐ Vibration attenuators
- ☐ Counter flange inlet
- ☐ Counter flange outlet
- ☐ Flex.connect. Inlet
- ☐ Guide duct inlet
- ☐ Flex.connect. outlet
- ☐ Guide duct outlet

OTHER REQUIREMENTS

Total price/unit excl. VAT	**£**	**3,254.00**
Total price excl. VAT	**£**	**3,254.00**

Delivery time (EXW): To be agreed

Delivery conditions:

EXW (Incoterms'00), Hollybank Works

Payment conditions:

30 days net

Guarantee

12 months after delivery, wear and tear parts 6 months

Tender valid: 25/01/03

Documentation

Legal basis :2

Tolerance according to B. S. 848

Fan Systems Terms and Conditions

Payment terms conditional on positive credit rating

240

FANCURVE FOR CENTRIFUGAL FAN

Date: 25/11/02

CUSTOMER: dulas ltd Unit 1 Dyfi Eco Park Powys SY20 8RX	**ENQUIRY:** from 25/11/02	**Item:** 3	**TENDER No.:** 25110201BMA
YOUR REF.: Conrad Trevelyan	**PROJECT:** ?? **Y/DESC.:**	**Units:** 1	**Handled by: B.Horrocks** **(+44) 1892 852520**

V.2

Fan type : S-LRZ9D/800/1120/1 **Fan type: Centrifugal fans**

Total press. Pt, static press. Ps , dynamic press. Pd2 [Pa]

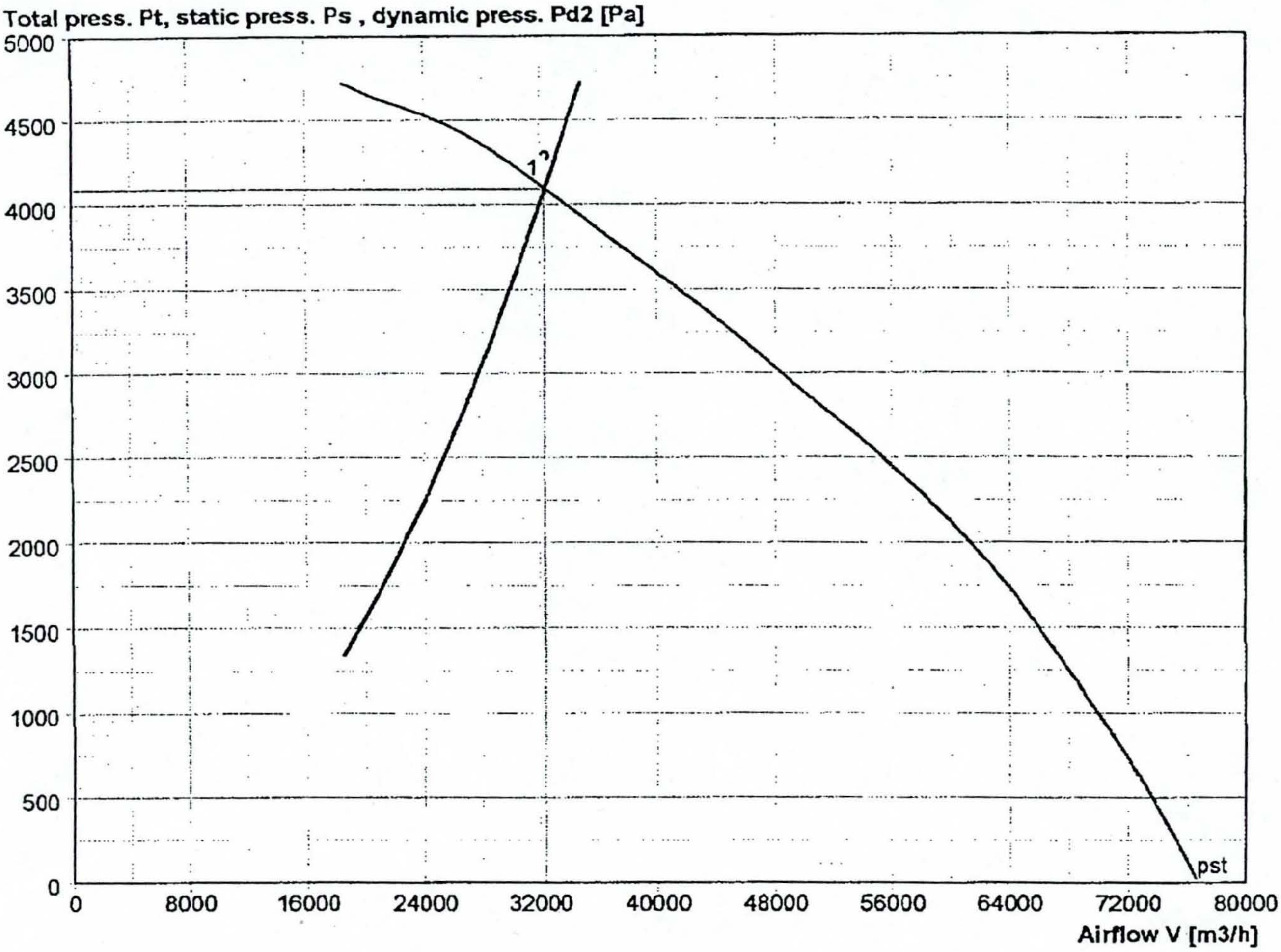

Impeller power Pw [kW]

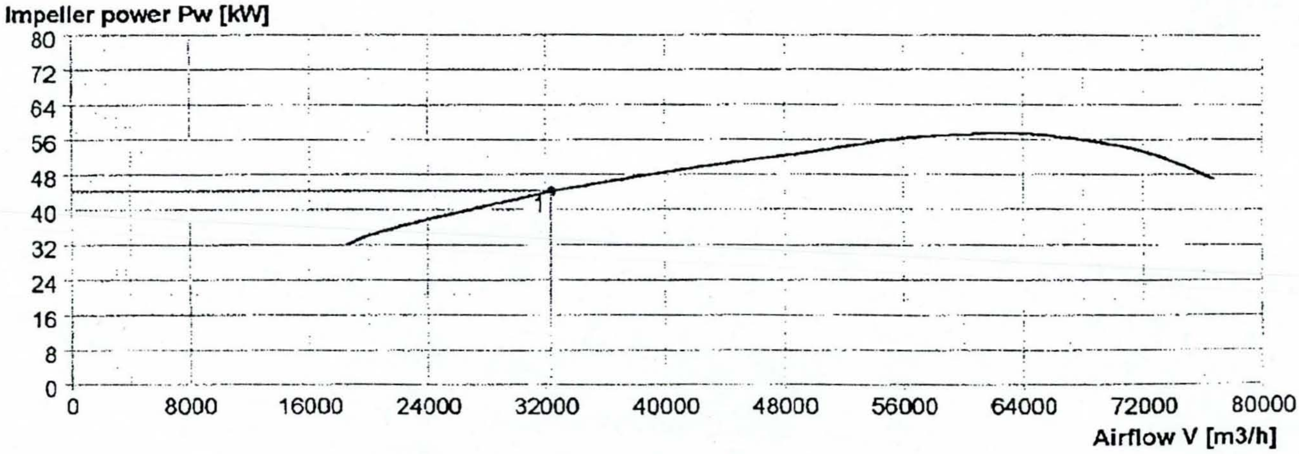

		1				
Air volume	V [m3/h]	32400.00				
Inlet density	Rho [kg/m3]	1.20				
Fan speed	N [1/min]	1478.00				

FAN SYSTEMS

STARTUP-/RUNDOWN CURVE

Date: 25/11/02lified

CUSTOMER:	ENQUIRY: from 25/11/02	Item:	TENDER No.:
dulas ltd Unit 1 Dyfi Eco Park Powys SY20 8RX		3	**25110201BMA**
	PROJECT: ??	Units:	Handled by: B.Horrocks (+44) 1892 852520
YOUR REF.: Conrad Trevelyan	Y/DESC.:	1	

Fan type : S-LRZ9D/800/1120/1 **Fan type: Centrifugal fans**

Flow rate	V [m3/h]:	32400.00
Inlet density	Rho [kg/m3]:	1.20
Fan speed	N [1/min]:	1478.00
Impeller power	Pw [kW]:	44.02
Rated motor power	PM [kW]:	55.00
Rough approximation of starting time :		
Appx. impeller weight	[kg]:	144.00
Appx. mass moment of inertia [kg m²]	[ ]:	26.29
Appx. starting time	ta [s]:	13
ca. Standard Rundown time	td [s]:	81

Run up time

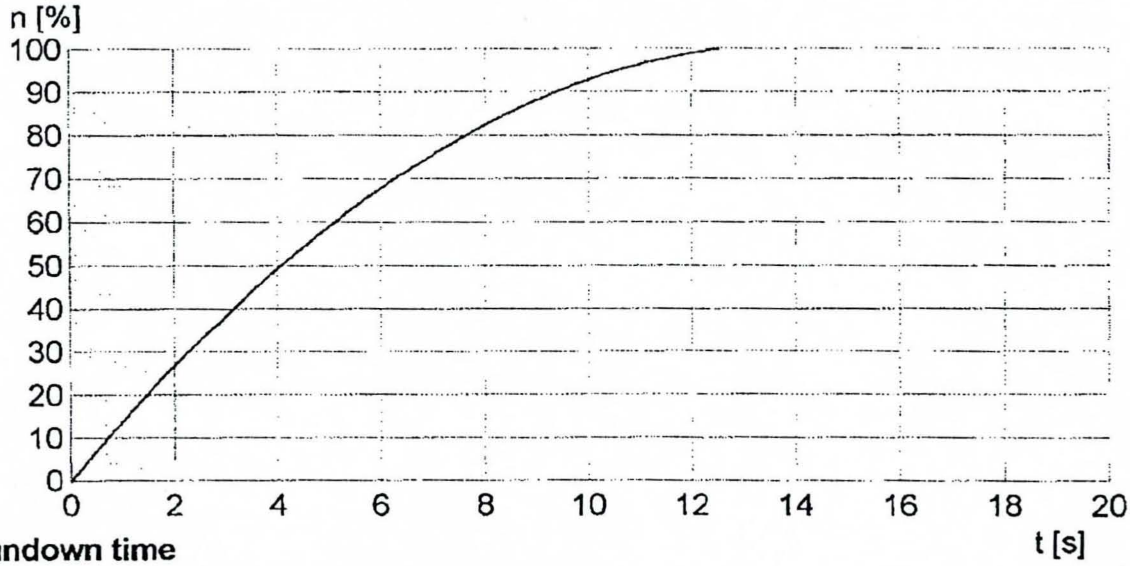

Rundown time

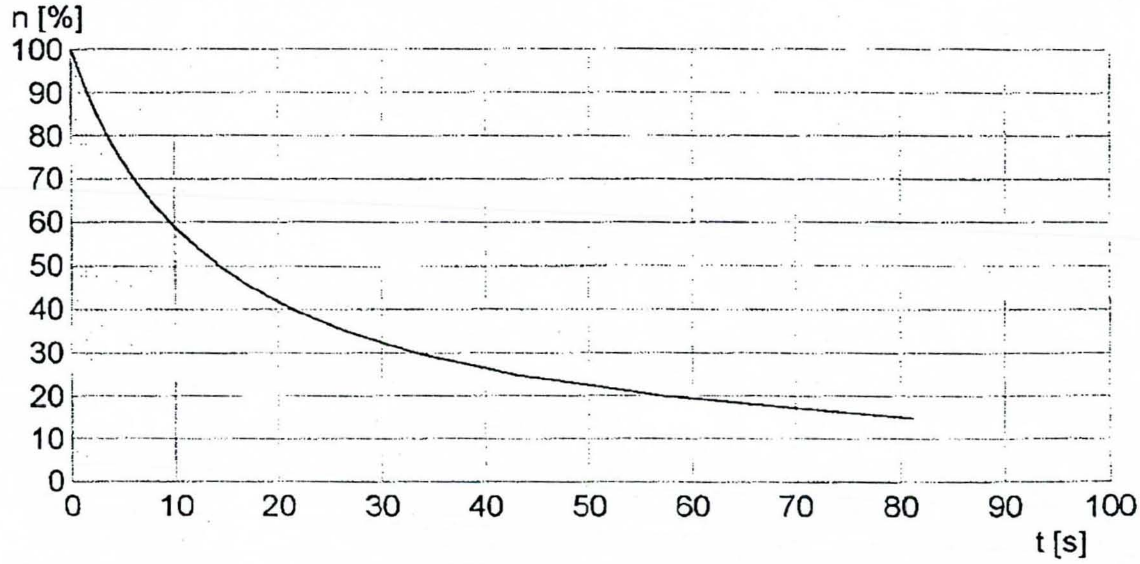

The stated times are a first approximation only. Significant variance for different motor suppliers due to diffe
motor-torque are to be expected. At start-up against closed damper 10 - 20 % faster times can be achieved.
The values only apply for direct on line start/ the given density, for star/delta start the switching time is relev

Appendix 5

Tjaerborg Turbine Model Validation Test Results

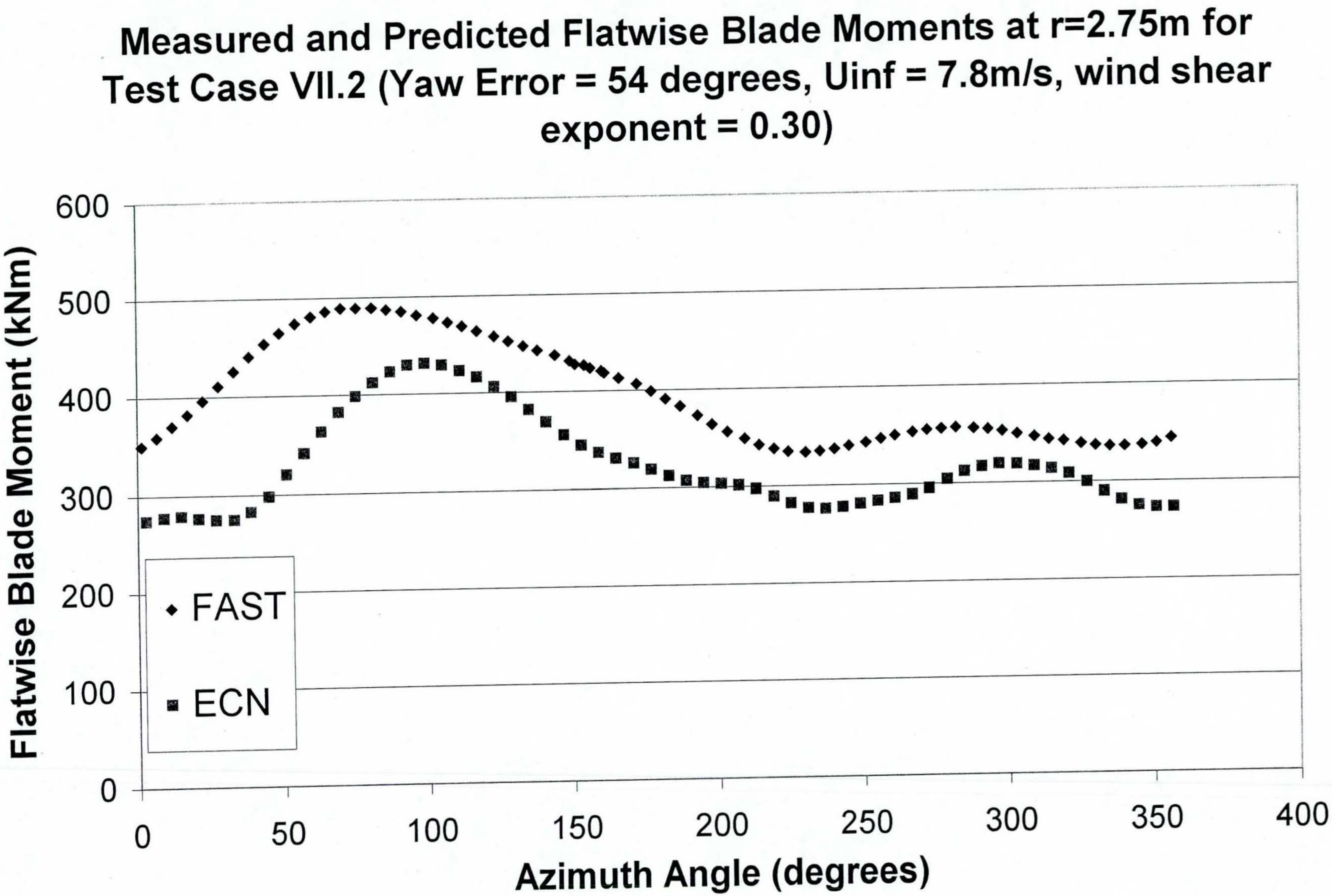
Measured and Predicted Flatwise Blade Moments at r=2.75m for Test Case VII.2 (Yaw Error = 54 degrees, Uinf = 7.8m/s, wind shear exponent = 0.30)
Flatwise Blade Moment (kNm)
600
500
400
300
200
100
0
0
50
100
150
200
250
300
350
400
Azimuth Angle (degrees)
FAST
ECN

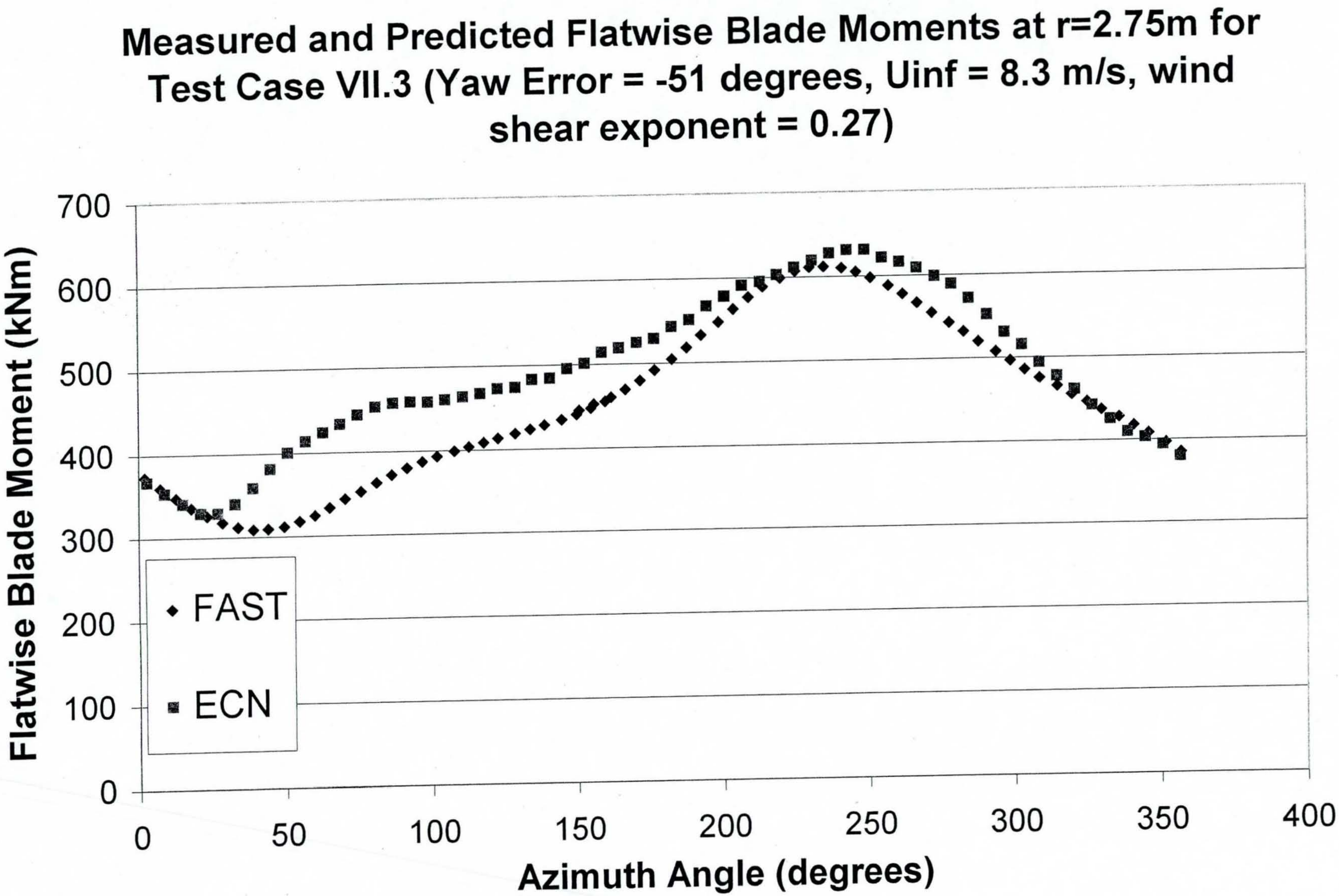
Measured and Predicted Flatwise Blade Moments at r=2.75m for Test Case VII.3 (Yaw Error = -51 degrees, Uinf = 8.3 m/s, wind shear exponent = 0.27)
Flatwise Blade Moment (kNm)
700
600
500
400
300
200
100
0
0
50
100
150
200
250
300
350
400
Azimuth Angle (degrees)
FAST
ECN

258

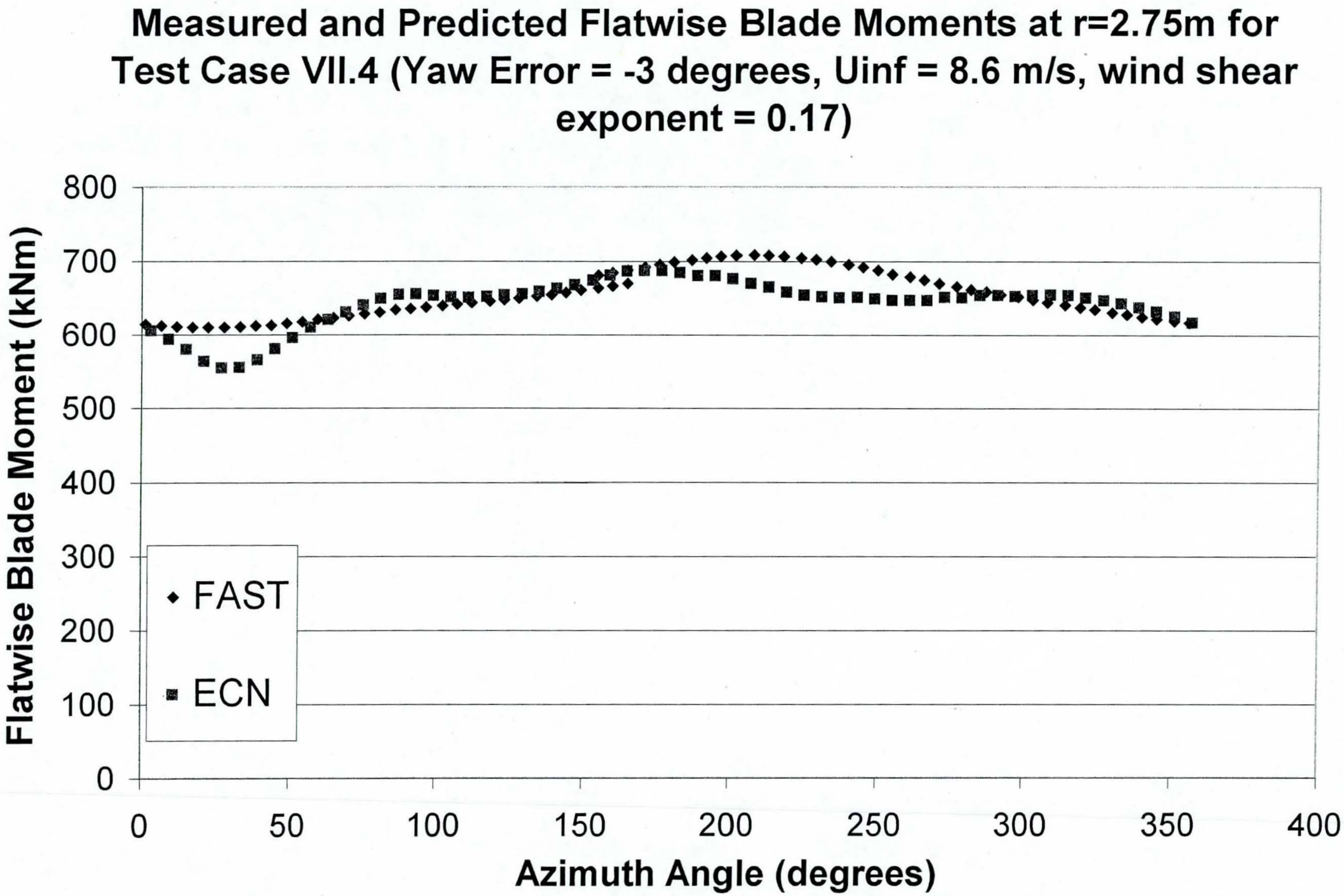

Measured and Predicted Flatwise Blade Moments at r=2.75m for Test Case VII.4 (Yaw Error = -3 degrees, Uinf = 8.6 m/s, wind shear exponent = 0.17)
Flatwise Blade Moment (kNm)
0
100
200
300
400
500
600
700
800
Azimuth Angle (degrees)
0
50
100
150
200
250
300
350
400
FAST
ECN